

A MICROWAVE RADIOMETER FOR INTERNAL BODY
TEMPERATURE MEASUREMENT

by

ROBERT PATTERSON SCHEELER

B.S., North Dakota State University, 2008

M.S., University of Colorado, 2011

A thesis submitted to the
Faculty of the Graduate School of the
University of Colorado in partial fulfillment
of the requirements for the degree of
Doctor of Philosophy
Department of Electrical, Computer, and Energy Engineering

2013

This thesis entitled:

A Microwave Radiometer for Internal Body Temperature Measurement

written by Robert Patterson Scheeler

has been approved for the Department of Electrical, Computer, and Energy Engineering

Zoya Popović

Erich Grossman

Date _____

The final copy of this thesis has been examined by the signatories, and we
Find that both the content and the form meet acceptable presentation standards
Of scholarly work in the above mentioned discipline.

Scheeler, Robert Patterson (Ph.D., Electrical Engineering)

A Microwave Radiometer for Internal Body Temperature Measurement

Thesis directed by Professor Zoya Popović

This thesis presents the analysis and design of a microwave radiometer for internal body temperature measurements. There is currently no available method for non-invasive temperature measurement inside the human body. However, knowledge of both relative and absolute temperature variations over time is important to a number of medical applications. The research presented in this thesis details a proof-of-concept near-field microwave radiometer demonstrating relative thermometry of a multi-layer phantom.

There are a number of technical challenges addressed in this thesis for radiometric determination of sub-degree temperature variations in the human body. A theoretical approach is developed for determining sensing depth from known complex layered tissues, which is defined as a figure of merit, and is shown to be dependent on frequency, electrical properties of the tissues, and the near-field probe. In order to obtain depth resolution, multiple frequency operation can be used, so multi-frequency probes are designed and demonstrated in this work.

The choice of frequencies is determined not only by the tissue material properties, but also by the ever increasing radio interference in the environment. In this work, quiet bands allocated to radio astronomy are investigated. The radiometer and probe need to be compact to be wearable, and several advancements are made towards a fully wearable device: multi-frequency low-profile probes are designed and fabricated on a flexible substrate and the process of on-chip integration is demonstrated by a GaAs MMIC cold noise source for radiometer calibration.

The implemented proof-of-concept device consists of two radiometers at 1.4 GHz and 2.7 GHz, designed with commercial inexpensive devices that can enable sufficient sensitivity. The device is tested on a phantom with two water layers whose temperatures are varied in a controlled manner, and focused on the human body temperature range. Measured results are discussed qualitatively as they relate to circadian rhythm monitoring. Finally, the thesis identifies future research that is required to make a practical wearable microwave thermometer for internal body temperature measurements.

DEDICATION

To my family.

PERSONAL ACKNOWLEDGMENTS

I owe my wife Jenna a debt of gratitude for her love, support, and patience. You are an inspiration. I am grateful to my parents for instilling an importance on education that has been the backbone of my motivation to pursue higher education.

To the current and former group members I extend many thanks for the technical discussions and advice that have helped me immensely in my studies and for making graduate school a fun experience. I have had the pleasure of working with an inspirational group of people: Maíra Batista, John Boudreaux, Dr. Jonathan Chisum, Mike Coffey, Dr. Evan Cullens, Gonzalo Expósito, Asmita Dani, Dr. Mike Elsbury, Dr. Erez Falkenstein, Dr. John Hoversten, Jennifer Imperial, Dr. Nicola Kinzie, Sean Korhummel, Dr. Dan Kuester, Gregor Lasser, Dr. Bradley Lindseth, Mike Litchfield, Dr. Joseph Mruk, Xavi Palomer, Ignacio Ramos, Dr. Michael Roberg, Parisa Roodaki, Dr. Luke Sankey, Scott Schafer, Frank Trang, and Andrew Zai.

PROFESSIONAL

ACKNOWLEDGMENTS

I wish to extend my sincerest gratitude to my advisor, Prof. Zoya Popović, whose guidance and support has enabled completion of this thesis. Prof. Popović has been a great source of knowledge and enthusiasm, which has been an integral part of my success. I also owe a debt of gratitude for her pursuit of funding in order to complete this thesis work. I would also like to thank my other committee members Profs. Edward Kuester, Dejan Filipović, Dana Anderson, Sean Shaheen, and Dr. Erich Grossman for their time and valuable feedback.

For financial support of this research I am grateful to Texas Instruments (formerly National Semiconductor), the NIST and University of Colorado Graduate Fellowship in Measurement Science and Engineering, and the National Science Foundation. I would also like to thank TriQuint Semiconductor for fabricating the GaAs MMIC designs presented in this thesis, and to Dr. David Walker and Rob Billinger of NIST for their help with the measurements of the active cold noise source presented in this thesis. I also wish to extend my thanks to Virginia Gurley, MD, whose helpful discussion of the circadian rhythm helped in the design of the system presented in this thesis.

Finally, I would like to thank my undergraduate advisor, Prof. Robert Nelson, who sparked my initial interest in electromagnetics and encouraged me to go to graduate school.

CONTENTS

1	INTRODUCTION	1
1.1	Overview	1
1.2	Radiometry concepts	3
1.2.1	Emissivity	6
1.3	Near-field Radiometry for Medical Applications	7
1.4	Electrical Properties of Tissues	9
1.4.1	Phantom Materials for Medical Applications	12
1.4.2	Probe Designs from the Literature	15
1.5	Thesis Outline	18
2	RADIOMETER DESIGN	19
2.1	Introduction	19
2.2	Receiver Definitions	20
2.3	Receiver Architectures	23
2.4	Receiver and Probe Designs for a Wearable Radiometer	25
2.4.1	Calibration	28
2.4.2	1.4 GHz System	30
2.4.3	2.7 GHz System	36
2.5	Multi-frequency Probe Designs	41
2.6	Conclusion	48
3	MMIC CIRCUITS FOR RADIOMETERS	49

3.1	Introduction	50
3.2	Tunable MMIC Coupler	50
3.2.1	Tunable Coupler Analysis	51
3.2.2	MMIC Coupler Implementation and Measured Scattering Parameters	56
3.2.3	Comparison to Simulation	59
3.2.4	Linearity Measurement	61
3.2.5	Comparison to Other Work	62
3.3	An Active MMIC Cold Noise Source	64
3.3.1	Noise Source Model	65
3.3.2	Minimized $T_{s,1}$ Example	67
3.3.3	GaAs MMIC Noise Source Design	68
3.3.4	GaAs MMIC Noise Source Experimental Results	71
3.4	Conclusions	71
4	NEAR-FIELD PROBE ANALYSIS	73
4.1	Introduction	73
4.2	Hertz Vector Potentials for a Stratified Medium	76
4.2.1	Spectral Domain Analysis of the Hertz Potentials	80
4.2.2	Input Impedance of a Dipole	85
4.3	Power Flow and Sensing Depth	87
4.4	Algorithm Verification	91
4.4.1	Comparison to Published Works	92
4.4.2	Theoretical Results	94
4.5	Dipole on Skin, Fat, and Muscle	99
4.6	Conclusion	104
5	RADIOMETRIC MEASUREMENTS	106
5.1	Overview	107

5.2	The Inverse Problem: Temperature Retrieval	107
5.3	Radiometric Estimation of Variable Temperature Single Layer Phantom	109
5.4	Single Frequency Estimation of Subsurface Temperature	113
5.5	Inverse Problems in Radiometry	117
5.5.1	Least-squares Method	118
5.5.2	Optimal Estimation Method	118
5.6	Multi-frequency Estimation of Subsurface Temperature	119
5.6.1	Least-Squares Solution to Three Layer Measurement	121
5.6.2	Optimal Estimation of Three Layer Measurement	125
5.6.3	Multi-frequency Estimates Discussion	126
5.7	Tissue Thickness Variability Analysis	129
5.8	Conclusion	135
6	SUMMARY AND FUTURE WORK	137
6.1	Summary	137
6.2	Future Work	138
6.3	Contributions	142
	Bibliography	146
A	VARIATIONAL SOLUTION TO THE INPUT IMPEDANCE	157
B	POWER FLOW IN A STRATIFIED MEDIUM	159
C	UNITS	161
D	PYTHON CODE FOR PROBE ANALYSIS	162

LIST OF TABLES

- 1.1 Formulas for different Debye models of pure water at temperature T in Celsius. **14**
- 1.2 Example probe designs from literature. **17**
- 2.1 Receiver frequencies for a wearable radiometer. The frequency bands chosen are protected for radio astronomy and remote sensing. **27**
- 2.2 Components for 1.4 GHz diode detector. **32**
- 2.3 Components for a 1.4 GHz receiver. **32**
- 2.4 1.4 GHz probe weighting functions on a water half-space. **35**
- 2.5 Components for a 2.7 GHz receiver. **39**
- 2.6 2.7 GHz probe weighting functions on a water half-space. **41**
- 2.7 Normalized weighting functions for the three frequency probe on a three layer medium of skin (1 mm), fat (2 mm), and muscle. **47**
- 3.1 Comparison of the tunable coupler from this work to others presented in the literature. **63**
- 4.1 Dielectric properties of human tissues at microwave frequencies. **75**
- 4.2 Dielectric properties of human skin at 1 GHz on various parts of the body. **76**
- 4.3 Sensing depth (mm) at various frequencies for sensitivity ratios of 0.2 and 0.1. Two different three layer media are considered: (a) 2 mm skin/10 mm fat/muscle, and (b) 1 mm skin/2 mm fat/muscle. **103**
- 5.1 1.4 GHz probe weighting functions on 10.3 mm water, 5 mm glass, and water. **115**
- 5.2 Results of non-linear regression analysis to determine unknowns in (5.7) from thermocouple T_{t3} and radiometric estimates T_{v3} . **117**

- 5.3 1.4 and 2.7 GHz probe weighting functions on 10.3 mm water, 5 mm glass, and water. **122**
- 5.4 Comparison of the error in the least-squares estimate of T_{v3} for two unknowns and one unknown. **124**
- 5.5 Comparison of the error in the fitted least-squares (LS) estimate and the fitted optimal estimation (OP) of T_{v1} with two unknowns. **127**
- 5.6 Comparison of the error in the fitted least-squares (LS) estimate and the fitted optimal estimation (OP) of T_{v3} with two unknowns and one unknown comparison. **127**
- 5.7 Dipole parameters for the variability study of the three layer problem of skin, fat, and muscle. **130**
- 5.8 Summary of analysis where various methods are used to invert the data using the nominal weighting function for radiometric observations generated by tissues properties varying 10% from the nominal values of 2 mm of skin and 10 mm of fat. The table presents the error in the estimates for the unknown muscle temperature parameters. **133**
- 5.9 Summary of analysis where various methods are used to invert the data using the correct weighting function for radiometric observations generated by tissues properties varying 10% from the nominal values of 2 mm of skin and 10 mm of fat. The table presents the error in the estimates for the unknown muscle temperature parameters. **135**
- C.1 Table of units for various quantities used in this document. **161**

LIST OF FIGURES

- 1.1 Radiometer receiving blackbody radiation in the form of propagating electromagnetic waves from an object with brightness temperature T_B that is proportional to the physical temperature times the emissivity. The power received by the antenna is proportional to the brightness temperature. **2**
- 1.2 Spectral brightness versus frequency for 3 K (cosmic background), 310 K (body temperature), 1500 K (campfire), 6000 K (sun). **4**
- 1.3 The power delivered by (a) an antenna placed inside a blackbody enclosure of temperature T is equal to that of (b) a resistor maintained at the same temperature. **5**
- 1.4 Emissivity and brightness temperature. **7**
- 1.5 Depiction of the weighting function where it is necessary to determine the contribution from a differential volume element V_i at a temperature T_i to the overall antenna temperature. **8**
- 1.6 Response of a dielectric material to a step electric field. The polarization have an initial nearly instantaneous response P_∞ . The polarization will then reach steady state (P_s) described by a first order process with a time constant τ . **11**
- 1.7 Comparison of three different Debye formulas for the complex permittivity of pure water vs. frequency (a) from of 100 MHz to 100 GHz at a temperature $T = 25^\circ\text{C}$ (77°F) and at 1.4 GHz vs. temperature (b) from 5° to 50°C . **14**
- 1.8 Real part of the relative dielectric constant (a) (ϵ'_r) and the conductivity (b) of pure water for the temperatures 25°C and 37°C (human body temperature) calculated using (1.44) to (1.47). **15**

- 2.1 Simplified block diagram of a total power radiometer along with important parameters such as gain (G) and bandwidth (B). The power is detected with a square-law detector (x^2) and integrated with an integration time (τ). **20**
- 2.2 Equivalent noise temperature definition where a noisy device (a) terminated in a fictitious 0 K load is replaced by a noiseless device (b) terminated in a resistor with an equivalent noise temperature. **21**
- 2.3 Noise figure for two cascaded two-port networks. **22**
- 2.4 Dicke radiometer block diagram where the input of the radiometer is periodically switched to a matched reference load at a stable temperature. **24**
- 2.5 Balanced noise injection Dicke radiometer block diagram. **25**
- 2.7 Post detection data conditioning and acquisition. The dc voltage is amplified and filtered before being measured with a DAQ. **29**
- 2.8 Raw measurement data used to determine antenna temperature. The raw hot, antenna, and cold voltages are averaged every τ_{cal} . To ensure an accurate estimate of the mean for each standard the first 10 low-pass filter time constants τ_{rc} shown in the inset are thrown out. **30**
- 2.9 Schematic (a) and photograph (b) of a 1.4 GHz diode square-law detector with lumped element match. **31**
- 2.10 Measured performance of the 1.4 GHz diode (SMS7630-079) square-law detector. The output voltage vs. input power at 1.4 GHz (a) demonstrates a sensitivity of $25 \text{ mV}/\mu\text{W}$. The narrowband (b) and broadband (c) frequency response is shown for an input power of -40 dBm. **31**
- 2.11 Predetection schematic of the 1.4 GHz radiometer. **32**
- 2.12 Measured performance of the 1.4 GHz receiver vs. RF input over frequency and power. The output voltage vs. input power at 1.4 GHz (a) demonstrates an output voltage of $127.6 \mu\text{V}$ for an input power of -100 dBm. The narrowband (b) and broadband (c) frequency response is shown for an input power of -80 dBm. **33**

- 2.13 1.4 GHz probe with a microstrip tapered balun feed (a), and its measured and simulated reflection coefficients (b). **35**
- 2.14 Receiver measurements on a constant temperature water bath. The water temperature T_t and room temperature T_{rm} were measured with a thermocouple (a). The calibrated receiver temperature (b) is 263.5 K, and the calibrated antenna temperature (c) demonstrates good agreement between the radiometer and thermocouple measurements. The receiver stability (d) demonstrates an Allan deviation less than 0.2 K for integration times of one second or greater. **36**
- 2.15 Measured performance of the 2.7 GHz diode (SMS7630-079) square-law detector (a). The output voltage vs. input power at 2.65 GHz (b) demonstrates a sensitivity of 10 mV/ μ W. The narrowband (c) and broadband (d) frequency response is shown for an input power of -40 dBm. **37**
- 2.16 Prediction schematic of the 2.7 GHz radiometer. **38**
- 2.17 Measured performance of the 2.7 GHz receiver vs. RF input over frequency and power. The output voltage vs. input power at 2.64 GHz (a) demonstrates an output voltage of 15.1 μ V for an input power of -96 dBm. The narrowband (b) and broadband (c) frequency response is shown for an input power of -80 dBm. **39**
- 2.18 2.7 GHz probe with a microstrip tapered balun feed (a), and its measured and simulated reflection coefficients (b). **40**
- 2.19 2.7 GHz receiver measurements on a constant temperature water bath. The water temperature T_t and room temperature T_{rm} were measured with a thermocouple (a). The calibrated receiver temperature (b) is 288.8 K, and the calibrated antenna temperature (c) demonstrates good agreement between the radiometer and thermocouple measurements. The receiver stability (d) demonstrates an Allan deviation less than 0.4 K for integration times of one second or greater. **42**
- 2.20 Detail of the front (a) and back (b) of the nested dipole probe with the 400 MHz (c) and 1.4 GHz (d) probes highlighted. **44**

- 2.21 Measured performance of the 400 MHz (a) and 1.4 GHz (b) probes, along with the isolation (c) between the probes. **45**
- 2.22 SAR for the 400 MHz (a) and 1.4 GHz (b) probes at the hear-cortical bone interface. Each plot is normalized to the peak value at that layer in the tissues as shown by the scale in (b). **45**
- 2.23 Three frequency probe with balun feed network. The overall dimensions of the probe are $30\text{ mm} \times 30\text{ mm}$ neglecting the balun. **46**
- 2.25 SAR at various depths in the tissues for each of the three probes. Each individual SAR plot is normalized to the peak value as demonstrated by the scale. It can be seen from the SAR plots close to the surface that the maximum occurs directly below the feed. Further into the tissues, however, the maximum begins to occur in the center of the entire probe footprint. **47**
- 3.1 Balanced noise injection Dicke radiometer block diagram. The two highlighted components are a fixed directional coupler and a variable attenuator. A variable directional coupler can replace these two circuit elements. **51**
- 3.2 Tunable directional coupler topology (a) with the even (b) and odd (c) mode equivalent circuits where Γ_e and T_e corresponds to the even mode reflection and transmission coefficients and Γ_o and T_o corresponds to the odd mode reflection and transmission coefficients. **52**
- 3.3 Comparison of $|S_{21}|$ and $|S_{31}|$ vs. tuning capacitance C at 2 GHz for both the exact solution (solid line) and the solution based on the Taylor series approximation (dashed line). **55**
- 3.4 Simulated results for S_{11} and S_{31} for the tunable coupler demonstrating a tuning range of 34 dB on S_{31} while maintaining a return loss of greater than 24 dB at 2 GHz. **55**
- 3.5 Simulated results for S_{21} and S_{41} for the tunable coupler. The insertion loss varies from 0.75 dB to 0 dB while the isolation is better than 23 dB. **55**
- 3.6 Tunable directional coupler topology. **56**

- 3.7 A quarter wavelength transmission line (a) and the lumped element π equivalent circuit (b). **57**
- 3.8 Photograph of the GaAs MMIC coupler. The chip occupies an area of $2.2 \text{ mm} \times 1.4 \text{ mm}$ neglecting probe pads and test structures. **57**
- 3.9 Measured S-Parameters for the coupled port demonstrating a tuning range of -6.6 dB to -60 dB at 2 GHz for $|S_{31}|$. The depletion mode diode was reverse biased so the coupling varies by decreasing the bias voltage from 0 V to -1.2 V. **58**
- 3.10 Measured input return loss for the tunable coupler demonstrating better than 12 dB return loss for all bias conditions at 2 GHz. The return loss improves to better than 20 dB over a wide coupling coefficient tuning range from 18 dB to 41 dB. **58**
- 3.11 Measured isolation greater than 17 dB for all bias conditions. The isolation of the coupler improves to 40 dB with decreasing bias. **59**
- 3.12 Measured tunable coupler scattering parameters at 2 GHz vs. DC bias from 0 V to -1.6 V. **59**
- 3.13 Comparison of measured (solid line) to simulated (dashed line) scattering parameters of the MMIC tunable coupler at two different bias points: 0 V (blue) and -0.8 V (red). **60**
- 3.14 Two-tone linearity measurement setup. **61**
- 3.15 Linearity measurements for the MMIC tunable directional coupler. The different traces correspond to: Blue (0 V), Red (-0.6 V), Green (-0.7 V), Orange (-0.8 V). **62**
- 3.16 Two-load radiometer with hot T_h and cold T_c standards. The highlighted portion could be an ACL in which T_c would be colder than its physical temperature. **64**
- 3.17 Two port noise source schematic with the amplifier represented by its two port scattering parameters. The noise temperature $T_{s,1}$ is incident on the input plane 1 and the noise temperature $T_{s,2}$ is incident on the output plane 2. **65**
- 3.18 Block diagram for the ACL design showing the input and output matching and bias networks necessary for the design in which the input of the device is presented with Γ_S and the output of the device is presented with Γ_L . **66**

- 3.19 Simulated $T_{s,1}$ and $|\Gamma_L|$ calculated from (3.36) for a TriQuint $0.5 \mu\text{m}$ pHEMT device. The transistor was biased at 1.7 V on the drain and the ideal source inductance was varied from 0.5 nH to 3 nH for two different gate biases corresponding to 0.5 V and 0.788 V . A minimum in $T_{s,1}$ is achieved when $|\Gamma_L|$ is minimized. **67**
- 3.20 The optimum noise match (Γ_{opt}) and conjugate of device input reflection coefficient vs. ideal source inductance ranging from 0.5 to 3 nH for two different gate bias points ($V_{GS} = 0.5 \text{ V}$ and $V_{GS} = 0.788 \text{ V}$) with the drain biased at $V_{DS} = 1.7$. For the gate bias $V_{GS} = 0.788 \text{ V}$ S_{11}^* and Γ_{opt} are approximately equal ($S_{11}^* \approx \Gamma_{\text{opt}} \approx 0.586 + j0.224$) for a source inductance of 1.03 nH . The Smith chart is normalized to 50Ω . **68**
- 3.21 Schematic of the active cold noise source. Additional source inductance was added such that the optimum load impedance is 50Ω such that no output matching network is needed. **69**
- 3.22 Simulated optimum noise match and the conjugate of the reflection coefficient looking into the device are shown along with the reflection coefficient looking towards the source (Γ_S) through the input match and bias network vs. frequency from 1 to 2 GHz . The input match is shown looking into the noise source (Γ'_{in}). The Smith chart is normalized to 50Ω , and the markers on the plot correspond to 1.4 GHz . **70**
- 3.23 Simulated $T_{s,1}$ and input match of the MMIC ACL demonstrating a $T_{s,1} = 70.9 \text{ K}$ with an input match of -27 dB at 1.4 GHz . **70**
- 3.24 Photo of the 1.4 GHz GaAs MMIC. The noise source with the input and output bias tees and input matching network is labeled by (1). The test circuits are a blocking capacitor (2), input matching network (3), and transistor test circuit (4). **71**
- 3.25 Measured $T_{s,1}$ and reflection coefficient of the packaged MMIC noise source demonstrating an equivalent noise temperature of approximately 90 K while maintaining an input reflection coefficient of less than -50 dB at 1.4 GHz . **72**

- 4.1 Dipole probe placed on the skin connected to a microwave radiometer to measure sub-surface tissue temperature. The tissues are represented by layers of complex permittivity dielectrics ($\epsilon = \epsilon' - j\epsilon''$). **75**
- 4.2 Stratified media consisting of layers of complex permittivity materials with current source $\mathbf{J}_s = J_x \mathbf{a}_x + J_y \mathbf{a}_y$ at $z = 0$. The source is embedded at the interface between layers $i = 1$ and $i = -1$. It is assumed that layers n and $-m$ extend to ∞ and $-\infty$ respectively. **77**
- 4.3 Source free boundary between two layers where $\mathbf{a}_n = s\mathbf{a}_z$. **82**
- 4.4 Definition of sensing depth z_s for a dipole on a lossy stratified half-space. Temperature changes with depth in the tissue layers while it is constant in the upper half-space. **89**
- 4.5 Flat dipole of length l and width W on a dissipative half-space. **91**
- 4.6 Real part of the relative dielectric constant (ϵ'_r) and the conductivity over the frequency range of 250 MHz to 5 GHz calculated using a single Debye model assuming the water temperature is 25°C. **92**
- 4.7 Comparison of the input impedance of a 10 GHz dipole on a GaAs half-space versus length for the method presented by Kominami et al. and the method presented in Section 4.2 of this work. **93**
- 4.8 Admittance (a) and impedance (b) of a quarter-wave monopole versus the loss tangent $\tan \delta$ at 114 MHz. Admittance (c) and impedance (d) of a half-wave monopole versus the loss tangent $\tan \delta$ at 114 MHz. **94**
- 4.9 Impedance vs. frequency for a $l = 0.6 \lambda_{\text{eff}}$ dipole at the interface of a lossy half-space characterized by a relative dielectric constant of conductivity from Fig. 4.6. **95**
- 4.10 Lower half-space efficiency, η_l , over frequency from theory, HFSS, and as calculated from $\eta_l = \epsilon_r^{3/2} / (\epsilon_r^{3/2} + 1)$ all of which showing $\eta_l > .996$. **96**
- 4.11 Summary of determining $P(z)$ from HFSS simulations. The volume loss density is integrated over each subvolume. From the power dissipated in each layer, $P(z)$ can be found. **98**

- 4.12 Comparison of theory to simulated results for the normalized power level $P(z)/P_{\text{tot}}$ vs. z of a dipole above a lossy half-space at (a) 500 MHz, (b) 1 GHz, (c) 1.5 GHz, (c) 2 GHz, (d) 2.5 GHz, and (d) 3 GHz. **99**
- 4.13 Comparison of the theoretical results for the normalized power level $P(z)/P_{\text{tot}}$ vs. z of a dipole above a lossy half-space for the following frequencies: 500 MHz 1.5 GHz, and 3 GHz. **100**
- 4.14 Sensing depth z_s as defined by (4.77) vs. frequency and the ratio of the receiver sensitivity σ to the incremental increase in temperature ΔT for a $0.6\lambda_{\text{eff}}$ dipole on a lossy half-space. **100**
- 4.15 Sensing depth z_s as defined by (4.77) vs. frequency and the ratio of the receiver sensitivity σ to the incremental increase in temperature ΔT for a plane wave propagating in a lossy medium. The power is normalized to 1 at the interface between the two media. **101**
- 4.16 Sensing depth z_s as defined by (4.77) vs. the ratio of the receiver sensitivity σ to the incremental increase in temperature ΔT for a $0.6\lambda_{\text{eff}}$ dipole on a lossy half-space. The three frequencies (1 GHz, 1.5 GHz, and 3 GHz) shown are compared to a plane wave assumption that the power decays as $\exp(-2\alpha z)$. **101**
- 4.17 Three layer tissue model consisting of skin, fat, and muscle. **102**
- 4.18 Comparison of theory to simulated results for the impedance of a $0.57\lambda_{\text{eff}}$ dipole above a three layer medium comprised of 2 mm of skin, 10 mm of fat, and muscle. **102**
- 4.19 Sensing depth z_s as defined by (4.77) vs. frequency and the ratio of the receiver sensitivity σ to the incremental increase in temperature ΔT for a $0.57\lambda_{\text{eff}}$ dipole above a three layer medium comprised of 2 mm of skin, 10 mm of fat, and muscle. **103**
- 4.20 Sensing depth z_s as defined by (4.77) vs. frequency and the ratio of the receiver sensitivity σ to the incremental increase in temperature ΔT for a $0.57\lambda_{\text{eff}}$ dipole above a three layer medium comprised of 1 mm of skin, 2 mm of fat, and muscle. **104**

- 5.1 Diagram of the inverse problem. The radiometer measures a temperature T_A'' which includes the contribution from the noise generated by the receiver (T_{rec}') due to reflection (Γ) from the available noise temperature T_A' . Additionally, any loss L through a cable which is assumed to be matched will change the antenna temperature T_A due to the physical temperature of the cable T_{rm} . The antenna temperature includes contributions from the feed (T_f, W_f), the upper half-space (T_u, W_u), and each volume in the layered media (T_{vn}, W_{vn}) or for the half-space problem the lower half-space (T_v, W_v). **108**
- 5.2 (a) Measured reflection coefficient of the probe at two different temperatures. (b) Radiometric estimate of the temperature of a water half-space T_v using the 1.4 GHz radiometer compared to the measured thermocouple temperature T_t vs. time. (c) A direct comparison of T_v vs. T_t showing how the radiometric estimate compares to the thermocouple measurements. **111**
- 5.3 (a) Measured reflection coefficient of the probe at two different temperatures. (b) Radiometric estimate of the temperature of a water half-space T_v using the 2.7 GHz radiometer compared to the measured thermocouple temperature T_t vs. time. (c) A direct comparison of T_v vs. T_t showing how the radiometric estimate compares to the thermocouple measurements. **113**
- 5.4 Three layer measurement with the 1.4 GHz radiometer of 10.3 mm water, 5 mm glass, and water. The measured and simulated reflection coefficient (a) of the 1.4 GHz probe. Thermocouple measurements of the two water layers and room temperature (b) along with a exponential fit for the top water layer T_{t1} . Radiometric estimate T_{v3} and thermocouple measurement T_{t3} of the subsurface water layer (c) along with the antenna temperature T_A and top water layer thermocouple measurement T_{t1} . Comparison of raw radiometer estimate and thermocouple measurement(d). Comparison of fitted radiometer thermocouple measurements (e). A comparison of the radiometer estimate vs. thermocouple temperature (f). **116**

- 5.5 Photograph of measurement setup (a), and block diagram (b) with the (1) 2.7 GHz probe, (2) 1.4 GHz probe, (3) 2.7 GHz radiometer, (4) Agilent noise source and power divider, (5) 1.4 GHz radiometer, and (6) PicoTech data logger. Both receivers were constantly calibrated and the unknown antenna temperatures measured. **120**
- 5.6 Three layer probe reflection coefficient for the (a) 1.4 GHz probe and (b) 2.7 GHz probe. **121**
- 5.7 Thermocouple measurements of room temperature (T_{rm}), the top water layer (T_{v1}), and the bottom water layer (T_{v3}) along with the fitted curve (dashed black line) for each thermocouple measurement. **122**
- 5.8 Least-squares raw estimate of the top (\hat{T}_{v1}) and bottom (\hat{T}_{v3}) water layers compared to fitted thermocouple measurements $T_{v1,\text{fit}}$ and $T_{v3,\text{fit}}$. The dashed black line shows the fit to the least-squares estimate. **123**
- 5.9 Absolute errors of the least-squares estimate for the top water ($\epsilon(\hat{T}_{v1})$) and bottom water ($\epsilon(\hat{T}_{v3})$), and the absolute error if the least-squares estimate are fitted to the exponential from (5.7) ($\epsilon(\hat{T}_{v1,\text{fit}})$, $\epsilon(\hat{T}_{v3,\text{fit}})$). **123**
- 5.10 Least-squares estimate and fit (a) of the bottom water (\hat{T}_{v3} , $\hat{T}_{v3,\text{fit}}$) compared to fitted the thermocouple measurement $T_{v3,\text{fit}}$. Error (b) in the least-squares estimate ($\epsilon(\hat{T}_{v3})$) and fit ($\epsilon(\hat{T}_{v3,\text{fit}})$). **124**
- 5.11 Optimal estimation of the top water (\hat{T}_{v1}) and bottom water (\hat{T}_{v3}) compared to fitted thermocouple measurements $T_{v1,\text{fit}}$ and $T_{v3,\text{fit}}$. **125**
- 5.12 Absolute errors of the optimal estimation for the top water ($\epsilon(\hat{T}_{v1})$) and bottom water ($\epsilon(\hat{T}_{v3})$), and the absolute error if the optimal estimations are fitted to the exponential from (5.7) ($\epsilon(\hat{T}_{v1,\text{fit}})$, $\epsilon(\hat{T}_{v3,\text{fit}})$). **126**
- 5.13 Optimal estimation and fit (a) of the bottom water (\hat{T}_{v3} , $\hat{T}_{v3,\text{fit}}$) compared to fitted the thermocouple measurement $T_{v3,\text{fit}}$. Error (b) in the optimal estimate ($\epsilon(\hat{T}_{v3})$) and fit ($\epsilon(\hat{T}_{v3,\text{fit}})$). **127**
- 5.14 Simulated temperatures of the skin, fat, and muscle over a 24 hour period. **131**
- 5.15 Code diagram for the tissue thickness variability analysis. **134**

- 6.1 Virtual family that may be used as guide for estimating tissue variability. **140**
- 6.2 Example PCB of a radiometer integrated on a single board. **141**

LIST OF ACRONYMS

ADC analog-to-digital converter

DAQ data acquisition unit

ENR excess noise ratio

F noise figure

FBW fractional bandwidth

FCC Federal Communications Commission

GaAs gallium arsenide

GCPW grounded coplanar waveguide

GI gastrointestinal

IF intermediate frequency

ITU International Telecommunication Union

LNA low-noise amplifier

MMIC monolithic microwave integrated circuit

NF noise figure (dB)

NMRI nuclear magnetic resonance imaging

PEC perfect electric conductor

PML perfectly matched layer

SAD seasonal affective disorder

SAR specific absorption rate

SNR signal-to-noise ratio

SoC system on chip

TE Transverse Electric

TEM Transverse Electromagnetic

TM Transverse Magnetic

WF weighting function

CHAPTER 1

INTRODUCTION

CONTENTS

1.1	Overview	1
1.2	Radiometry concepts	3
1.2.1	Emissivity	6
1.3	Near-field Radiometry for Medical Applications	7
1.4	Electrical Properties of Tissues	9
1.4.1	Phantom Materials for Medical Applications	12
1.4.2	Probe Designs from the Literature	15
1.5	Thesis Outline	18

1.1 OVERVIEW

The topic of the research presented in this thesis is the measurement of physical temperature using microwave radiometry receivers. The most common applications of microwave radiometry are in radio-astronomy, atmospheric sensing, earth sensing, and some industrial processes such as cement and brick manufacturing [1–3]. The radiometer instruments in these applications measure power radiated by astronomical objects, layers of the Earth’s atmosphere, and types of terrain, etc., which radiate power in accordance with blackbody radiation

laws. The received power is a function of frequency and bandwidth of the instrument, and temperature and physical properties of the radiating medium. In the common applications of radiometry, the incident power is in the form of plane waves and is received by an antenna as demonstrated in Fig. 1.1. In this thesis,

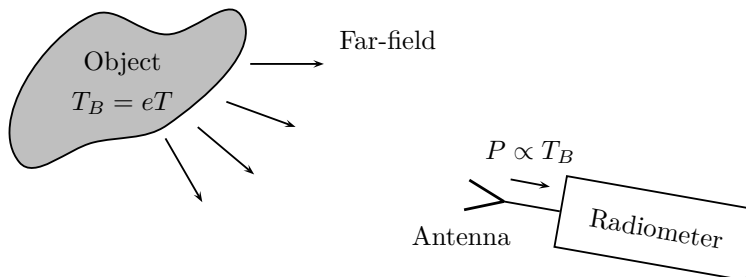


Figure 1.1: Radiometer receiving blackbody radiation in the form of propagating electromagnetic waves from an object with brightness temperature T_B that is proportional to the physical temperature times the emissivity. The power received by the antenna is proportional to the brightness temperature.

radiometry is applied to a different problem - that of measuring internal body temperature non-invasively. Since the power, in this case, is radiated from body parts located in the near field of the antenna, standard radiometry theory and instrument design does not apply and requires modifications.

Microwave radiometers are practical for addressing medical problems in which it is necessary to determine subsurface temperature because at microwave frequencies sensing depths of up to 3-7 cm are achievable [4, 5], and was first applied to sensing subsurface thermography in 1974 [4, 6]. Microwave radiometry for non-invasive temperature measurements is based on near-field power reception and holds promise to achieve the spatial resolution and sensing depth necessary for a variety of medical applications, including cancer detection [7, 8]. Monitoring drug delivery for cancer treatment [9], hyperthermia temperature control [10], hypothermic neural rescue of infants suffering from hypoxia-ischemia [11, 12], and detection of vesicoureteral reflux in children [13, 14] also utilize non-invasive near-field radiometric measurements. Measurement of elevated joint temperature to detect arthritis by non-invasive microwave thermometry has also been investigated [5, 15]. Quantification of *in vivo* inflammation in atherosclerotic plaques by means of non-invasive microwave radiometry has been applied to the area of vascular pathology [16, 17]. Additionally, near-field applicators are used in microwave hyperthermia treatment [18] and non-medical applications such as food processing [19].

This introductory chapter briefly reviews radiometry concepts and defines the antenna temperature in terms of objects in the near-field. This antenna temperature will be a weighted average of the temperature

of the surrounding objects, and therefore weighting functions (WFs) will be used to define the antenna temperature as a weighted average of the temperature of objects close to the antenna. Next, the electrical properties of tissues are discussed, and in what manner these properties may be mimicked for experimental purposes. Finally, an overview of the remainder of the thesis is given.

1.2 RADIOMETRY CONCEPTS

This section presents definitions that are important to understanding the operation of a radiometer. The concepts and definitions can be found in any number of radiometry and remote sensing books such as [1, 2]. The material in Ulaby et al. [2] was the source of the material presented in this introductory chapter, and knowledge of the basic radiometry concepts is necessary to understand the contributions of this thesis. A radiometer is a device that measures incoherent radiation. Matter emits electromagnetic energy based on its temperature in all directions with spectral brightness described by Planck's blackbody radiation law as

$$B_f = \frac{2hf^3}{c^2} \frac{1}{e^{hf/kT} - 1} \quad [\text{W}\cdot\text{m}^{-2}\cdot\text{sr}^{-1}\cdot\text{Hz}^{-1}], \quad (1.1)$$

where h is Planck's constant (6.63×10^{-34} J·sec), c is the speed of light in vacuum (m/sec), k is the Boltzmann constant (1.38×10^{-23} J/K), and T is the temperature in Kelvin. Fig. 1.2 shows the spectral brightness versus frequency for temperatures ranging from the cosmic microwave background (3 K) to the temperature of the sun (6000 K). The term brightness for microwave terminology differs from the optical terminology which is radiance [20], however, in this work the term brightness will be used.

At "low frequencies" $hf/kT \ll 1$, and as a result, the quantity $(e^{hf/kT} - 1)$ may be approximated by a truncated Taylor series such that $e^x - 1 \approx x$. Therefore Planck's blackbody radiation law reduces to the low frequency approximation known as the Rayleigh-Jeans law:

$$B_f = \frac{2kTf^2}{c^2} = \frac{2kT}{\lambda^2}. \quad (1.2)$$

For body temperature (≈ 310 K) the Rayleigh-Jeans law deviates less than one percent from Planck's law up to 127 GHz and therefore is valid in the microwave frequency range. The radiant electromagnetic energy described by Planck's blackbody radiation law may be received by an antenna which converts electromagnetic energy propagating in free space to a guided wave in a transmission line. The power that the antenna

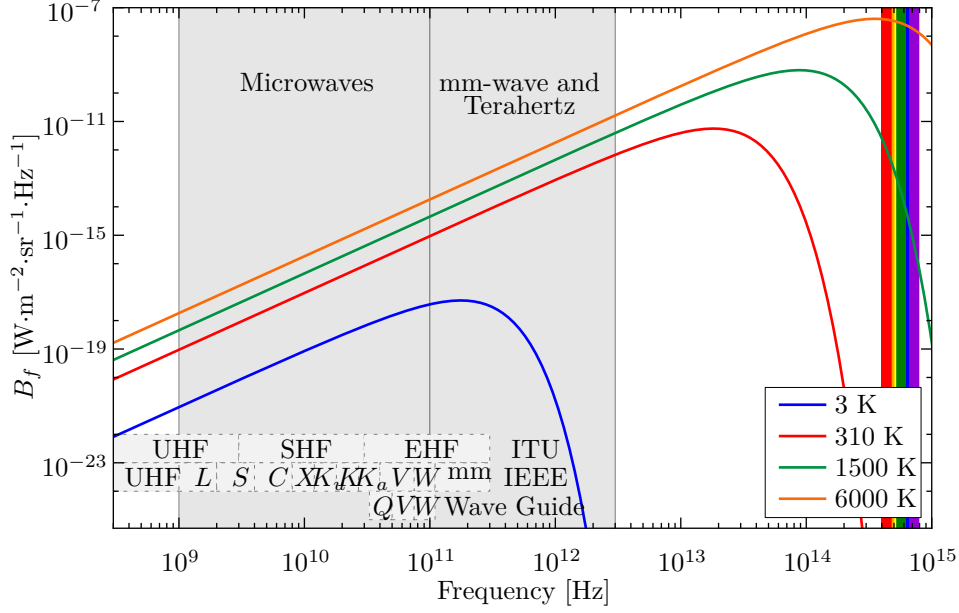


Figure 1.2: Spectral brightness versus frequency for 3 K (cosmic background), 310 K (body temperature), 1500 K (campfire), 6000 K (sun).

would receive from a spatial distribution of spectral brightness given by $B_f(\theta, \phi)$ will only be half of the total power incident since the antenna is polarized and the electromagnetic radiation has two independent polarizations [21]. In general, the power received by an antenna P_A is given from the power spectral density S ($\text{W}\cdot\text{m}^{-2}\text{Hz}^{-1}$) and the effective area of the antenna A (m^2) which are functions of position and frequency. The thermal power received by the antenna in a narrow bandwidth Δf is given by integrating the power received through a differential solid angle $d\Omega$ over all 4π steradians. The power received by the antenna is:

$$P_A = \frac{1}{2} \int_f^{f+\Delta f} \iint_{4\pi} B_f(\theta, \phi) A(f, \theta, \phi) d\Omega df \quad [\text{W}] \quad (1.3)$$

Using the relation between the gain $G(f, \theta, \phi)$ and the effective area $A(f, \theta, \phi)$ ¹ where

$$G(f, \theta, \phi) = \frac{4\pi}{\lambda^2} A(f, \theta, \phi), \quad (1.4)$$

the power received by the antenna may be written in terms of the gain as

$$P_A = \frac{\lambda^2}{8\pi} \int_f^{f+\Delta f} \iint_{4\pi} B_f(\theta, \phi) G(f, \theta, \phi) d\Omega df \quad (1.5)$$

¹ This relation can be derived from thermodynamic considerations [21] for an antenna in a constant thermal enclosure where the antenna, load, and enclosure are all the same temperature. Ensuring thermal equilibrium the power received by the antenna must be equal to the power radiated by the antenna results in the relation given in (1.4).

Next, consider a lossless antenna is placed in an enclosure with absorber that is kept at a constant temperature T as shown in figure Fig. 1.3a. Substituting in the Rayleigh-Jeans law from (1.2) into (1.5), and noting that for a lossless antenna

$$\iint_{4\pi} G(f, \theta, \phi) d\Omega = 4\pi, \quad (1.6)$$

yields an expression for the power received by the antenna:

$$P_A = kT\Delta f. \quad (1.7)$$

It may be noted at this point that the result is the same found by Nyquist for a resistor at a finite temperature [22]. This concept is illustrated by considering a matched resistor maintained at a temperature T as seen in Fig. 1.3b. The power received by the antenna is the same as that received by the matched resistor.

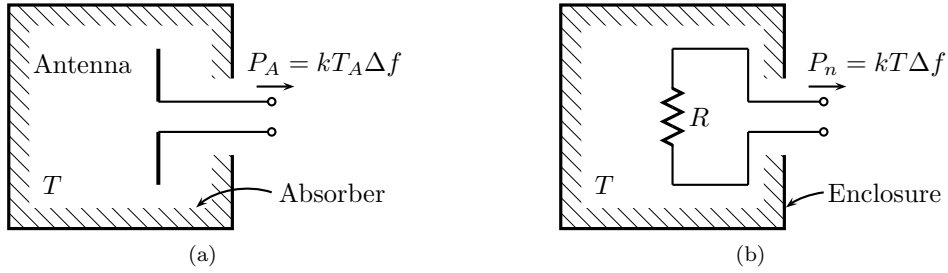


Figure 1.3: The power delivered by (a) an antenna placed inside a blackbody enclosure of temperature T is equal to that of (b) a resistor maintained at the same temperature.

Next, consider the antenna is observing a temperature distribution that is spatially dependent. Substitution of the Rayleigh-Jeans law with a spatially dependent temperature $T(\theta, \phi)$ into (1.5) yields an expression for the power received by the antenna. If the bandwidth Δf is narrow G is considered to be constant over the frequency and the power received by the antenna is

$$P_A = k\Delta f \left(\frac{1}{4\pi} \iint_{4\pi} G(f, \theta, \phi) T(\theta, \phi) d\Omega \right). \quad (1.8)$$

It can be seen that the portion in parentheses in (1.8) has the units of Kelvins. Thus, the expression is similar to that for the resistor ($kT\Delta f$), and the power received by the antenna is proportional to the temperature distribution weighted by the gain. The portion in parentheses in (1.8) is referred to as the resistor-equivalent

antenna temperature T_A or just antenna temperature given by

$$T_A = \frac{1}{4\pi} \iint_{4\pi} G(f, \theta, \phi) T(\theta, \phi) d\Omega. \quad (1.9)$$

This is a powerful result as the antenna power relation states there is a direct relation between the power received by the antenna and the spatial temperature distribution. Therefore, an antenna and receiver can be used to determine the physical temperature observed by the antenna by inverting (1.9).

1.2.1 EMISSIVITY

To this point only blackbodies have been considered as they are ideal emitters and absorbers of radiation. In reality objects are *grey bodies*. A grey body will emit or absorb less than that of a perfect blackbody. Thus, for grey bodies, the term brightness temperature T_B is used as this is the observed temperature of the object which is less than its physical temperature. The equations in the previous section used the physical temperature T in for the Rayleigh-Jeans law, however for grey bodies, the brightness temperature must be used. The ratio of the brightness temperature to physical temperature is defined as the *emissivity* and is given by

$$e(\theta, \phi) = \frac{T_B(\theta, \phi)}{T}. \quad (1.10)$$

In this expression, the brightness temperature T_B is the brightness temperature of the object, and does not include scattered brightness temperature from the environment. The emissivity is essentially a plane wave power transmission coefficient which can be illustrated by considering the interface between a homogeneous dielectric and free space as seen in Fig. 1.4. The observed brightness temperature of the object neglecting scattered temperature from the background is given by

$$T_B = (1 - |\Gamma|^2) T_{AP}(0^-), \quad (1.11)$$

where $T_{AP}(0^-)$ is the apparent temperature just below the surface, and Γ is the Fresnel reflection coefficient. Also T_{AP} and Γ are dependent on the angle of incidence θ_2 and the polarization as illustrated in Fig. 1.4. The Fresnel reflection coefficient is given by

$$\Gamma = \frac{Z_{c2} - Z_{c1}}{Z_{c2} + Z_{c1}}. \quad (1.12)$$

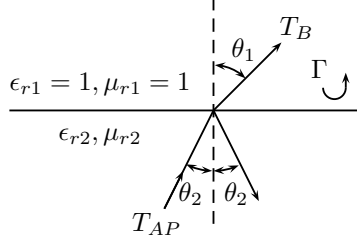


Figure 1.4: Emissivity and brightness temperature.

The characteristic impedance for TE and TM polarization is

$$Z_{ci} = \begin{cases} \eta_i \sec \theta_1, & \text{TE} \\ \eta_i \cos \theta_1, & \text{TM}, \end{cases} \quad (1.13)$$

with $i = 1$ or 2 , and η_i is the wave impedance in the medium. Also the angle θ_2 is given by Snell's law as $k_1 \sin \theta_1 = k_2 \sin \theta_2$, $k = \omega \sqrt{\mu \epsilon}$. The emissivity is related to the reflection coefficient by

$$e = 1 - |\Gamma|^2. \quad (1.14)$$

It may also be noted that for a material to remain in thermodynamic equilibrium, the emissivity is equal to the absorptivity. This result is utilized to analyze the probe in the reciprocal case where it is transmitting.

1.3 NEAR-FIELD RADIOMETRY FOR MEDICAL APPLICATIONS

In the previous section, emissivity was defined as the ratio of observed temperature T_B to the actual temperature T . The emissivity was defined as a power transmission coefficient which assumes propagating plane electromagnetic waves. In general for radio astronomy or atmospheric and earth sensing, the antenna is electrically far from the sensing target such that the received electromagnetic power is in the form of propagating plane waves. For the medical applications detailed in the Overview of this chapter, the spatial sensitivity requires balancing sensing depth with transverse selectivity. As a result, the antenna must be very close to the target or even in direct contact with the body in the case of a wearable device. For this application it is more appropriate to think of the antenna as a transducer or probe. In Section 1.2, the radiometric antenna temperature was determined from the far-field parameters of the antenna as given in (1.9). For objects placed in the near-field of the antenna, the antenna temperature cannot be determined assuming plane waves, and

therefore far-field parameters are no longer applicable. As a result, the expression for emissivity in (1.14) is no longer applicable.

To determine the antenna temperature, it is necessary to find the portion of power received by the antenna from a differential volume, relative to the total received thermal power as seen in Fig. 1.5 for an arbitrary stack of homogeneous complex permittivity materials such as human tissues. The total power received by the antenna will be a weighted volume average of the spatial temperature distribution. To determine the antenna temperature, weighting functions (WFs) will be used, which are found using the antenna reciprocity theorem as the power absorption rate. The antenna measures a weighted volume average brightness temperature within the sensing volume V . The spatial temperature distribution is defined as $T(\mathbf{r})$ at point \mathbf{r} , and the antenna brightness temperature T_A is given by

$$T_A = \iiint_V W(\mathbf{r})T(\mathbf{r})dV. \quad (1.15)$$

The weighting functions may also be given from discrete differential subvolumes V_i [23, Chapter 17], [24] as

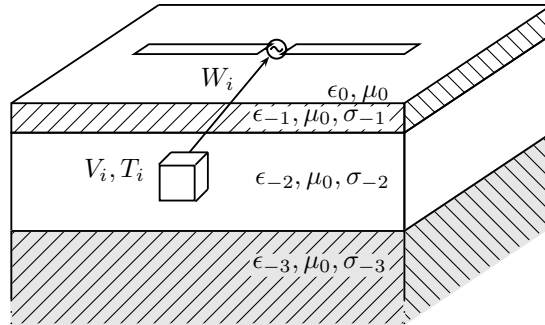


Figure 1.5: Depiction of the weighting function where it is necessary to determine the contribution from a differential volume element V_i at a temperature T_i to the overall antenna temperature.

seen in Fig. 1.5 as

$$T_A = \sum_{i=1}^{\infty} W_i(f)T_i, \quad i = 1, 2, \dots, \infty. \quad (1.16)$$

The weighting functions are dependent on the dielectric properties the antenna is receiving thermal radiation from. For medical applications these dielectrics are human tissues. The weighting functions are only valid for a specific probe, tissue combination, and frequency. To view how power is received from the tissues, the specific absorption rate (SAR) from the transmitting antenna may be calculated from simulation software

such as Ansys HFSS. The SAR is defined as

$$\text{SAR} = \frac{\sigma|E|^2}{2\rho} \quad [\text{W/kg}], \quad (1.17)$$

where σ is the effective conductivity, and ρ is the mass density. The SAR is proportional to the weighting function, and is often calculated for transmitting applications such as mobile handsets.

1.4 ELECTRICAL PROPERTIES OF TISSUES

In the previous section near-field weighting functions were used to define the antenna temperature. The weighting functions were dependent on the dielectric properties of the materials close to the antenna, which for medical applications, are human tissues. The dielectric properties of tissues have been widely studied, and the standard resource is a series of articles from S. Gabriel and C. Gabriel that include a literature survey [25], measurements [26], and models [27] for various human tissues. For the designer, there are several resources where these tissue properties are available. For dielectric properties of various tissues in the frequency range of 10 Hz to 100 GHz, “An Internet Resource for the Calculation of the Dielectric Properties of Body Tissues” from the Italian National Research Council [28] is a great resource. Additionally, the “Tissue Properties Database” from IT’IS Foundation [29] has not only the dielectric properties of the tissues, but also physical properties such as density and thermal conductivity. IT’IS also has a virtual population of body models [30] that can be used to estimate tissue thicknesses for different people to account for inter-subject variability. Knowledge of the dielectric properties is essential for design of the probe, frequency selection, and inversion of the radiometric observations to determine the physical temperature of the tissues.

The electromagnetic properties of tissues are given by the complex permittivity

$$\epsilon = \epsilon' - j\epsilon'', \quad (1.18)$$

where the imaginary part accounts for loss in the medium due to damping. This damping converts electromagnetic energy into heat (loss). Often the dielectric loss tangent $\tan \delta$ is specified as

$$\tan \delta = \frac{\epsilon''}{\epsilon'}, \quad (1.19)$$

or in terms of the effective conductivity σ as

$$\tan \delta = \frac{\sigma}{\omega \epsilon'}. \quad (1.20)$$

Therefore the complex permittivity can be written in terms of $\tan \delta$ as

$$\epsilon = \epsilon' (1 - j \tan \delta). \quad (1.21)$$

Care should be taken, however, in the the meaning of σ for the loss tangent [31, Chapter 2], [32]. Using the terminology from [31, Chapter 2] it may be considered that the conductivity σ is the effective conductivity including both the static frequency independent conductivity and alternating field conductivity which is sometimes given by $\omega \epsilon''$, however, here ϵ'' will be equivalent to σ/ω where σ is the effective conductivity including the static and frequency dependent loss. Therefore, the conductivity or loss tangent are only valid at a given frequency.

It is often useful to express the complex permittivity in terms of the relative permittivity as

$$\epsilon = \epsilon_0 \epsilon_r, \quad (1.22)$$

where ϵ_0 is the free space permittivity (8.854×10^{-12} Farad/m), and

$$\epsilon_r = \epsilon'_r - j \epsilon''_r. \quad (1.23)$$

When analyzing a problem that requires knowledge of the dielectric constant it is necessary to have a model to predict the dielectric constant across frequencies. These models are generally fit to experimental data. A simple model to predict the frequency dependent complex permittivity with a single relaxation process is the Debye model [32–37]. Consider an electric field that is suddenly applied to polar dielectric such as water, there will be an instantaneous polarization response due to the ionic and electronic polarization (P_∞). The dipole polarization will not happen as fast as the ionic and electronic polarization taking some relaxation time τ to reach steady state P_s [32, 37]. The response of the polarization to a step electric field ($E_s u(t)$) as shown in Fig. 1.6 is then given by

$$P(t) = P_\infty + (P_s - P_\infty) \left(1 - e^{-t/\tau}\right), \quad t > 0. \quad (1.24)$$

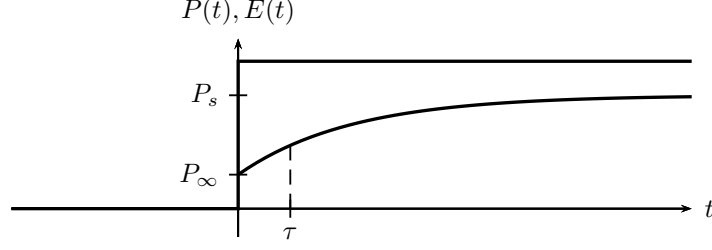


Figure 1.6: Response of a dielectric material to a step electric field. The polarization have an initial nearly instantaneous response P_∞ . The polarization will then reach steady state (P_s) described by a first order process with a time constant τ .

Taking the Laplace transform (as time $t > 0$ is of interest) defined by

$$F(s) = \int_0^\infty f(t)e^{-st} dt, \quad t > 0, \quad (1.25)$$

of the polarization $P(t)$ and simplifying yields

$$P(s) = \frac{1}{s} \left(P_\infty + \frac{P_s - P_\infty}{1 + s\tau} \right). \quad (1.26)$$

Using the Laplace transform once again, the electric field is given by

$$E(s) = \frac{E_s}{s}. \quad (1.27)$$

For a linear medium such as human tissues², the polarization is related to the electric field through the electric susceptibility χ (dimensionless), and the free space permittivity ϵ_0 (Farad/m). The polarization in the transform domain is

$$P(s) = \epsilon_0 \chi(s) E(s). \quad (1.28)$$

Using (1.26) to (1.28), and solving for the susceptibility yields

$$\chi(s) = \chi_\infty + \frac{\chi_s - \chi_\infty}{1 + s\tau}. \quad (1.29)$$

The relative dielectric constant is related to the susceptibility as follows

$$\epsilon_r = \chi + 1. \quad (1.30)$$

² The electromagnetic properties of tissues are linear when interacting with weak fields. However under high field strengths non-linear effects may occur [37]. For this thesis the fields produced by thermal radiation are weak and the dielectric response will be linear.

Substituting (1.29) into (1.30), using $s = j\omega$, and multiplying by ϵ_0 , yields the Debye equation for the complex permittivity

$$\epsilon = \epsilon_\infty + \frac{\epsilon_s - \epsilon_\infty}{1 + j\omega\tau}. \quad (1.31)$$

The real and imaginary parts of (1.31) can easily be shown to be

$$\epsilon' = \epsilon_\infty + \frac{\epsilon_s - \epsilon_\infty}{1 + (\omega\tau)^2} \quad (1.32)$$

$$\epsilon'' = \frac{(\epsilon_s - \epsilon_\infty)\omega\tau}{1 + (\omega\tau)^2}. \quad (1.33)$$

This expression for the permittivity does not take into account conduction current. For a static conductivity σ_s the Debye model is [37]

$$\epsilon = \epsilon_\infty + \frac{\epsilon_s - \epsilon_\infty}{1 + j\omega\tau} - j \frac{\sigma_s}{\omega\epsilon_0}. \quad (1.34)$$

Another useful model for predicting complex permittivity of materials is the Cole-Cole model [38]

$$\epsilon = \epsilon_\infty + \frac{\epsilon_s - \epsilon_\infty}{1 + (j\omega\tau)^{(1-\alpha)}}. \quad (1.35)$$

The Cole-Cole model is similar to the Debye model, however, it includes a distribution parameter that describes the distribution of relaxation times [27, 38]. The Cole-Cole model reduces to the Debye model for $\alpha = 0$.

If multiple relaxations processes are present, the material properties can be described as a sum of multiple Debye or Cole-Cole relaxations. For tissues, three relaxations are generally considered (α , β , γ) [25]. The α dispersion is the low-frequency relaxation due to ionic diffusion at the cell membrane [25]. Polarization cell membranes, proteins, and other macro-molecules leads to the β dispersion in the hundreds of kilohertz range, while water molecules lead to the γ dispersion at gigahertz frequencies [25]. These relaxations can be described as a sum of multiple Cole-Cole type relaxations [27]

1.4.1 PHANTOM MATERIALS FOR MEDICAL APPLICATIONS

In a laboratory environment it is essential to demonstrate a concept with a well controlled test setup. For this reason, it is convenient to use *phantoms*, whose electromagnetic properties mimic those of human tissues. A

common phantom material is water, which is easily controlled in a laboratory environment, and is a standard phantom material, dielectric reference, and calibration standard [37, 39–41]. Consequently, the dielectric properties of pure water have been widely investigated with a thorough summary provided by Ellison et al. [42]. A select few will be summarized and compared here. In 1971, Stogryn [34] presented expressions for the three unknowns in the Debye model as a function of temperature and salinity. The expressions were compared to measured data from the literature at frequencies ranging from 3.25 GHz to 23.7 GHz. Kaatze et al. in 1989 [43] used their own measured data from 0°C to 50°C over the frequency range of 1.1 GHz to 57 GHz in combination with data from the literature to determine a Debye model which is valid up to 100 GHz and over the temperature range of -4°C to 60°C. In 1991 Liebe et al. [44] presented models fit to experimental data compiled from literature. They presented a single term Debye model that is valid up to 100 GHz. Beyond 100 GHz and up to 30 THz a double Debye model was used to account for both primary and secondary relaxations. Additional double Debye models have been presented such as that by Buchner et al. [45].

The formulas of the three single Debye models discussed in the previous paragraph were compared over the frequency range of 100 MHz to 10 GHz at a temperature $T = 25^\circ\text{C}$ (77°F) and at 1.4 GHz over the temperature range of 5° to 50°C. The results are summarized in Fig. 1.7 showing good agreement between all of the methods. The formulas are reproduce here³ as a function of temperature T in Celsius for the readers' convenience in (1.47).

In this work, the frequency range of interest is between 100 MHz and 10 GHz. The model presented by Liebe et al. [44] will be used to determine the dielectric properties of water. The dielectric properties will then be used in various simulations. For convenience, the conductivity σ is often specified. As mentioned previously, this conductivity is an effective conductivity including both frequency independent and dependent losses. Fig. 1.8 shows the real part of the relative dielectric constant (ϵ'_r) and the conductivity at a temperature of 25°C. The real part of the relative dielectric constant is relatively constant (78.3-62.9), however, the conductivity changes notably from 0.002 S/m to 16.6 S/m over the frequency range of 100 MHz to 10 GHz.

Although water is a useful phantom material, other phantoms that more closely mimic the dielectric

³ It should be noted that the expression for ϵ_s presented by Stogryn [34] has a typographical error. The formula is reproduced from Malmberg et al. [46] formula (5). Additionally, the first order term in (5) from [46] differs slightly from the equation in the abstract ($-0.4008T$ as apposed to $-0.40008T$). Equation (5) from [46] will be presented here for ϵ_s .

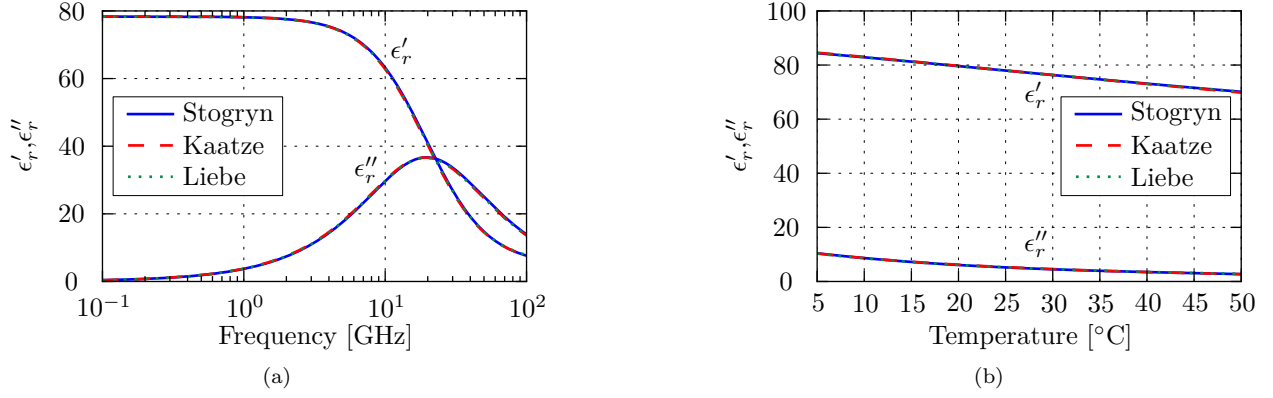


Figure 1.7: Comparison of three different Debye formulas for the complex permittivity of pure water vs. frequency (a) from of 100 MHz to 100 GHz at a temperature $T = 25^\circ\text{C}$ (77°F) and at 1.4 GHz vs. temperature (b) from 5° to 50°C .

Table 1.1: Formulas for different Debye models of pure water at temperature T in Celsius.

Source	Debye Paramters
Stogryn [34]	$\epsilon_s = 87.74 - 0.4008T + 9.398 \times 10^{-4}T^2 + 1.41 \times 10^{-6}T^3$ (1.36)
	$\epsilon_\infty = 4.9$ (1.37)
	$\tau = \frac{1}{2\pi}(1.1109 \times 10^{-10} - 3.824 \times 10^{-12}T$ (1.38)
	$+ 6.938 \times 10^{-14}T^2 - 5.096 \times 10^{-16}T^3)$ (1.39)
Kaatze et al. [43]	$\epsilon_s = 10^{1.94404 - 1.991 \times 10^{-3}T}$ (1.40)
	$\epsilon_\infty = 5.77 - 2.74 \times 10^{-2}T$ (1.41)
	$\tau = 3.745 \times 10^{-15}(1 + 7 \times 10^{-5}(T - 27.5)^2)$ (1.42)
	$\times \exp((2.2957 \times 10^3)/(T + 273.15))$ (1.43)
Liebe et al. [44]	$\theta = 1 - 300/(T + 273.15)$ (1.44)
	$\epsilon_s = 77.66 - 103.3\theta$ (1.45)
	$\epsilon_\infty = 0.066\epsilon_s$ (1.46)
	$\tau = \frac{1 \times 10^{-9}}{2\pi(20.27 + 146.5\theta + 314\theta^2)}$ (1.47)

properties of various human tissues may be necessary for specific scientific experiments. Recipes for producing these phantoms are published in the literature(e.g. [47–49]).

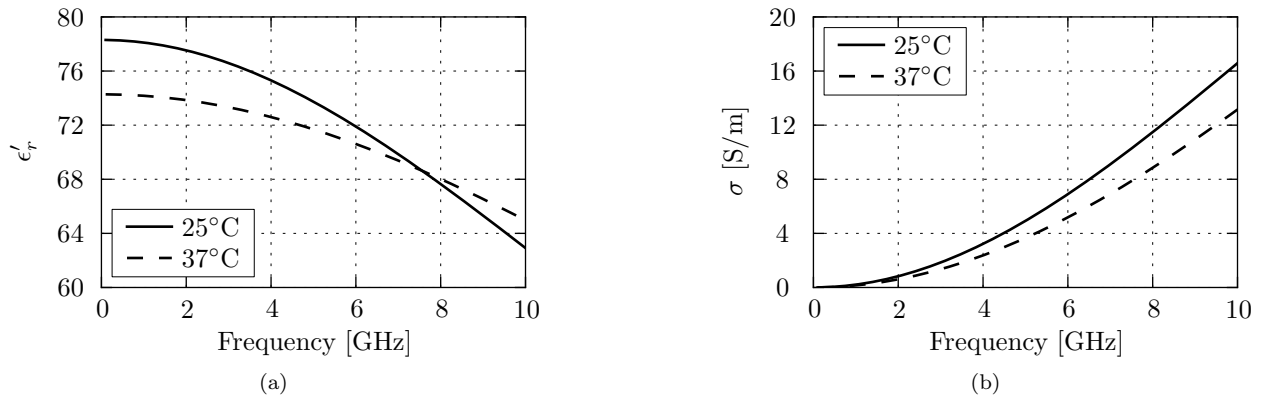


Figure 1.8: Real part of the relative dielectric constant (a) (ϵ'_r) and the conductivity (b) of pure water for the temperatures 25°C and 37°C (human body temperature) calculated using (1.44) to (1.47).

1.4.2 PROBE DESIGNS FROM THE LITERATURE

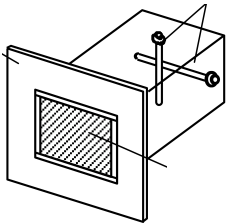
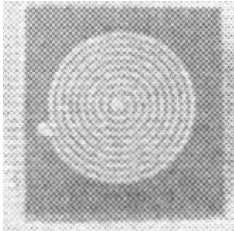
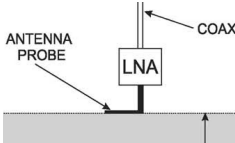
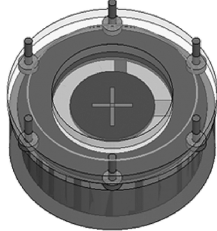
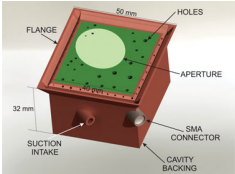
The inverse problem of determining the physical temperature of tissues from radiometric observations will require multiple independent measurements at different frequencies e.g. [11] or different angles [50]. Multiple frequencies are used as the weighting functions will be a function of frequency, thus resulting in independent measurements. The challenge in using multiple frequencies is that the probe must be measuring the same tissues at each frequency which has led researchers to develop broadband waveguide apertures that are filled with a high dielectric constant to achieve the bandwidth necessary (utilizing two polarizations) for using a single aperture over 1 to 4 GHz [41]. Additional broadband designs such as a spiral have been presented [18]. These broadband designs utilize the same aperture to ensure the antenna is receiving thermal power from the same tissues across the frequency bands of interest.

For applications where determining absolute temperature at a depth is not required, single frequencies may be used. Such single frequency applications as detecting a buried hot object with a monopole [39] or determining body temperature that includes contributions from the core temperature with a cavity back slot [51] utilize antennas designed for a single frequency. Another single frequency design was presented for *in vivo* measurements that utilized suction to mount the antenna [52]. A comparison of these example probes is summarized in Table 1.2 comparing the size, frequency, and application.

The aim of this thesis is to address some of the challenges related to making a wearable compact device that may be operated in an open and possibly congested RF environment. Multiple discrete frequencies with

narrow bandwidths less than 5% will be used to determine subsurface temperature. What is different in this work is separate antennas that are located in close proximity will be used to receive thermal power from the same part of the body rather than a single antenna matched over a broad band. The antenna impedance in this case will also aid in filtering. To ensure the antenna will be lightweight and flexible so that it is easily worn, printed dipoles will be used. This differs from some of the probes presented in Table 1.2.

Table 1.2: Example probe designs from literature.

Probe Type	Dielectric Filled Waveguide [41]	Archimedean Spiral [18]	L-Shaped Monopole [39]	Cavity Backed Slot [51]	Elliptical Antenna [52]
Photograph					
Frequency [GHz]	1-3.8 (5) 400 MHz bands	1-3.5	1.393 - 1.757	1.2-1.6	3.5
Dimensions [cm]	2.1×2.8	3.5×3.5	2.8	$9 \times 9 \times 2.7$	$5 \times 5 \times 3.2$
Designed for	Water	Water	Water	Adjustable air gap (skin, muscle, fat/blood phantom)	Human tissues (hand, chest, belly, and hip)

1.5 THESIS OUTLINE

In this thesis, radiometry is applied to measuring internal body temperature non-invasively using a wearable microwave radiometer. The outline of the thesis is summarized for each Chapter by the following:

Chapter 2 Receiver architectures are discussed, and 1.4 GHz and 2.7 GHz radiometers are designed and characterized. The system also includes the probe used to receive the thermal radiation. Two single frequency probes are presented that were designed for a water phantom, and two other multi-frequency probes are presented that were designed for human tissues.

Chapter 3 To address the goal of developing a compact system. Two monolithic microwave integrated circuit (MMIC) circuits for a compact radiometer are presented - a tunable coupler and an active cold noise source. The design methodologies for both circuits are detailed and applied to a TriQuint 0.5 μm commercial GaAs process. The measured results of each MMIC are also presented.

Chapter 4 The analysis of a dipole in a stratified lossy medium is presented using a spectral domain technique. The analysis is done to determine the sensing limitations for a dipole used as the transducer to receive thermal radiation from tissues. An improved sensing depth metric is presented and analyzed for a water phantom, and a three layer tissue model of skin, fat, and muscle.

Chapter 5 Utilizing the radiometers presented in Chapter 2, Chapter 5 demonstrates the detection of subsurface temperature changes using a water, glass, water phantom. Additionally, the question of weighting function model validity is addressed by simulation of a radiometer measuring thermal emission from a three layer tissue medium of skin, fat, and muscle. The results are interpreted for medical applications.

Chapter 6 Summarizes the contributions of this work and presents a path forward for future work.

CHAPTER 2

RADIOMETER DESIGN

CONTENTS

2.1	Introduction	19
2.2	Receiver Definitions	20
2.3	Receiver Architectures	23
2.4	Receiver and Probe Designs for a Wearable Radiometer	25
2.4.1	Calibration	28
2.4.2	1.4 GHz System	30
2.4.3	2.7 GHz System	36
2.5	Multi-frequency Probe Designs	41
2.6	Conclusion	48

2.1 INTRODUCTION

In the previous chapter, basic radiometry concepts were introduced, and the blackbody power received by an antenna was defined in terms of both near-field and far-field parameters. This power is delivered to a sensitive microwave receiver called a radiometer. The output of the radiometer is generally a dc voltage that is proportional to the antenna temperature. In this chapter, the fundamental definitions essential for the

design of the radiometer are presented, and a few radiometer architectures are discussed. Two receivers and probes designed for 1.4 and 2.7 GHz operation are presented along with their measured performance. Finally, additional multi-frequency probes are presented that have been designed for interaction with human tissues.

2.2 RECEIVER DEFINITIONS

A simple block diagram of a radiometer is shown in Fig. 2.1. Power is received through the antenna at an equivalent noise temperature T'_A . The gain (G) is dictated by the number of amplifiers in the receiver chain, and the losses in the receiver from passive elements such as transmission lines and filters. The bandwidth (B) is generally dictated by the filters used in the predetection section of the receiver, but is also a function of the bandwidth of the active components such as the amplifiers and square-law (x^2) detector. The output is then integrated with a time constant τ to improve the radiometric resolution. Next, the definitions necessary to characterize the noise performance of the receiver will be presented. The definitions in this section are widely published, and the following references are examples: [2, Chapter 6], [53, Chapters 10, 13], [1].

A radiometer must amplify a very low level signal while introducing minimal noise. Amplifier noise is measured by the signal-to-noise ratio (SNR), defined as the ratio of the signal power P_s to the noise power P_n or $\text{SNR} = P_s/P_n$. For a linear two port device or system, the noise figure (F) is a measure of the degradation of the SNR by noise added from the device or system. The noise figure is the ratio of the input SNR to the output SNR given as

$$F = \frac{P_{si}/P_{ni}}{P_{so}/P_{no}}, \quad (2.1)$$

where the input noise power is the power provided by a matched resistor at a temperature $T_0 = 290$ K

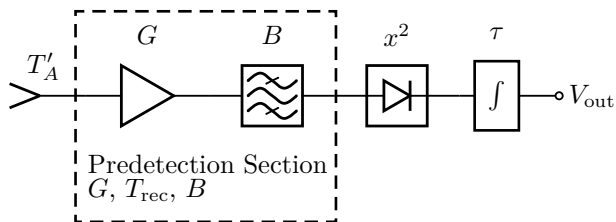


Figure 2.1: Simplified block diagram of a total power radiometer along with important parameters such as gain (G) and bandwidth (B). The power is detected with a square-law detector (x^2) and integrated with an integration time (τ).

($P_{ni} = kT_0B$). The linear quantity for noise figure is also referred to as noise factor while the value in decibels is referred to as noise figure (dB) (NF) defined as

$$\text{NF} = 10 \log_{10} F. \quad (2.2)$$

The equivalent input noise temperature is used to define the noise performance of a device as an equivalent noise source that is placed at the input of an ideal noise-free device. Consider the two networks shown in Fig. 2.2. The network in Fig. 2.2a is a noisy amplifier with a fictitious 0 K load at the input such that $P_{ni} = 0$. For this case, P_{no} represents the output noise power generated by the device when the input is connected to a noise-free termination. This network is replaced with an equivalent noiseless network shown in Fig. 2.2b, where T_e represents an equivalent temperature of a matched resistor referred to the input of the noise free device that would generate the same output power P_{no} , given by

$$T_e = \frac{P_{no}}{GkB}, \quad (2.3)$$

where the gain of the device is G , and the bandwidth considered is B . The equivalent input noise temperature is related to the noise figure (F) as

$$T_e = (F - 1)T_0. \quad (2.4)$$

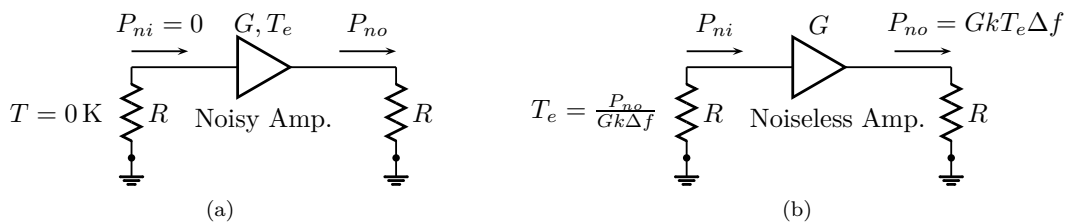


Figure 2.2: Equivalent noise temperature definition where a noisy device (a) terminated in a fictitious 0 K load is replaced by a noiseless device (b) terminated in a resistor with an equivalent noise temperature.

The noise performance of a system can be expressed in terms of the noise parameters and gains of the individual stages. The output noise power of a single stage (assuming the input noise power is given from a match resistor at T_0) in a small frequency band is given by

$$P_{no} = Gk(T_0 + T_e)B \quad (2.5)$$

The available output noise power for the cascaded system shown in Fig. 2.3 is

$$P_{no} = \underbrace{G_1 G_2 k T_0 B}_{\text{due to source } T_0} + \underbrace{G_1 G_2 k T_{e1} B}_{\text{due to noise in first network}} + \underbrace{G_2 k T_{e2} B}_{\text{due to noise in second network}} \quad (2.6)$$

Using this expression, the effective input temperature of the two networks cascaded can be written as

$$T_{e1,2} = \frac{k G_2 (G_1 T_{e1} + T_{e2}) B}{G_1 G_2 k B} = T_{e1} + \frac{T_{e2}}{G_1}, \quad (2.7)$$

which can be generalized for n networks in cascade to find the overall effective temperature equal to

$$T_e = T_{e1} + \frac{T_{e2}}{G_1} + \dots + \frac{T_{en}}{G_1 G_2 \dots G_{n-1}} \quad (2.8)$$

Using (2.4), the overall noise figure is given by

$$F = F_1 + \frac{F_2 - 1}{G_1} + \dots + \frac{F_n - 1}{G_1 G_2 \dots G_{n-1}} \quad (2.9)$$

Inspection of (2.9) reveals the cascaded noise figure is dominated by the noise figures of the first few stages provided the overall receiver has adequate gain. If the first component is a passive network, e.g. a lossy cable, G is replaced by the loss L . Therefore to design a receiver with a low system noise figure, a low-noise amplifier (LNA) with a low noise figure and reasonable gain should be placed as close to the antenna as possible.

Using the noise performance of the receiver, in addition to knowledge of the bandwidth and integration time, the sensitivity of the receiver can be determined. The voltage at the output of the square-law detector (x^2) is integrated with a time constant τ as seen in Fig. 2.1. The final output voltage will have a dc component that corresponds to the mean value of the input power, and the ac or fluctuating component which limits the resolution of the radiometer. For a total power radiometer, such as the one shown in Fig. 2.1, the radiometric resolution is given by

$$\Delta T = \frac{T'_A + T_{\text{rec}}}{\sqrt{B\tau}}, \quad (2.10)$$

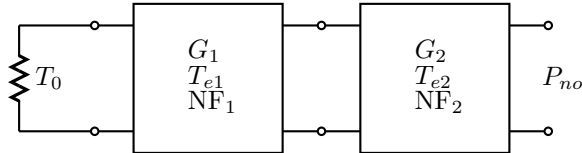


Figure 2.3: Noise figure for two cascaded two-port networks.

where the receiver temperature and gain are assumed to be constant. T'_A is the antenna temperature including the ohmic losses. This is the precision with which T_A can be recovered from the output voltage of the square law detector after integration.

The definitions presented in this section are essential for designing a radiometer. Design requirements such as sensitivity, expected temperatures that will be measured, and the EM environment in which the radiometer will be operated all determine the receiver temperature, bandwidth, and integration time. These requirements dictate the choice of LNAs, filters, detectors, and interconnect losses. In the subsequent sections, the choice of parts for a specific application are presented and the receiver temperatures and sensitivities estimated. First, a few receiver architectures are presented to motivate the architecture choice for the microwave thermometer.

2.3 RECEIVER ARCHITECTURES

The fundamental receiver architecture is the total power radiometer shown in Fig. 2.1, and serves as the reference for the various other architectures: Dicke, radiation balance, noise injection, and two-load radiometers detailed in many texts and articles such as [1, 2, 54, 55]. The expression for sensitivity from (2.10) assumes no gain variations. If the fluctuations in the gain are considered, the sensitivity must be modified [2, 55] as follows

$$\Delta T = (T'_A + T_{\text{rec}}) \sqrt{\frac{1}{B\tau} + \left(\frac{\Delta G}{G}\right)^2}, \quad (2.11)$$

where G is the average power gain of the radiometer, and ΔG is the rms value of the gain fluctuation.

To reduce the effect of gain variations, Dicke [56] proposed a radiometer that is periodically compared to a matched reference load at a stable temperature T_{ref} as shown in Fig. 2.4. The output is then synchronously demodulated resulting in the following radiometric resolution

$$\Delta T = \sqrt{\frac{2(T'_A + T_{\text{rec}})^2}{B\tau} + \frac{2(T_{\text{ref}} + T_{\text{rec}})^2}{B\tau} + (T'_A - T_{\text{ref}})^2 \left(\frac{\Delta G}{G}\right)^2}. \quad (2.12)$$

This equation is easily interpreted as contributions from the noise variations of the antenna measurement for a period of $1/\tau$ and the reference measurement for a period of $1/\tau$ in addition to fluctuations in the gain. The rate at which the reference load is compared should be fast enough such that the gain is considered to be constant over the switching interval. It is seen that variations due to gain can be minimized if $T'_A = T_{\text{ref}}$. In

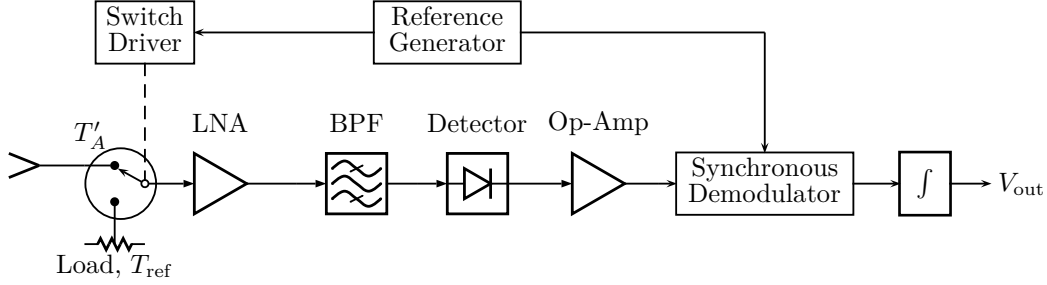


Figure 2.4: Dicke radiometer block diagram where the input of the radiometer is periodically switched to a matched reference load at a stable temperature.

this case the radiometer is said to be *balanced*, and the radiometric resolution is twice that of the ideal total power radiometer as the antenna input is only received half of the time.

Methods for balancing include varying the reference load with a variable attenuator until the reference temperature is equal to the antenna temperature. Another method of balancing a radiometer is to inject a variable amount of noise (from a noise source with a variable attenuator) by means of a coupler into the antenna path to raise the antenna temperature to be equal to the reference temperature as seen in Fig. 2.5. Balancing techniques require feedback to control the attenuators until a balanced mode of operation is achieved.

To determine the unknown antenna temperature T'_A , the receiver must be calibrated with known temperature standards. Assuming the output voltage is linear with respect to input power, there is a linear relation between the input temperature and output voltage as shown in Fig. 2.6a. The temperature standard may either be a matched microwave load with a known temperature, or a target observed by the antenna with a known temperature.

A two-load radiometer shown in Fig. 2.6b is constantly calibrated against a hot and cold load. Goodberlet et al [57] proposed a two-load radiometer as a way to improve the radiometric resolution. The optimal time to measure each standard during the calibration cycle for a two-load architecture is presented in [57]. Fig. 2.6a shows the calibration line associated with the two-load radiometer.

The architectures presented here have advantages in terms of insensitivity to variations in gain and disadvantages such as hardware complexity for the synchronous modulator/de-modulator. However, with the advent of improved data acquisition unit (DAQ) units, the synchronous demodulation can be done in

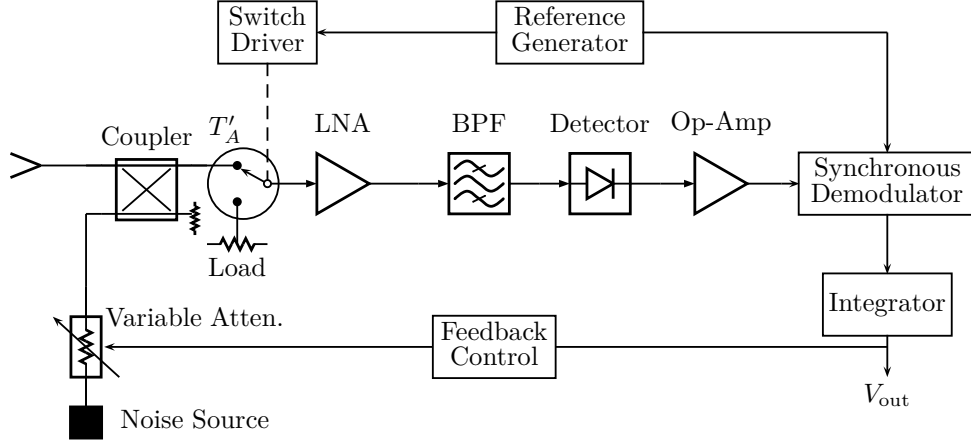


Figure 2.5: Balanced noise injection Dicke radiometer block diagram.

software and switching frequencies and dwell times may be easily varied through computer control. A two-load radiometer along with a computer controlled DAQ allows for flexibility in the mode of operation. The receiver is calibrated constantly which is advantageous as a wearable radiometer’s receiver temperature may drift, and will need to be regularly calibrated which the two-load radiometer is capable of. For these reasons, the two-load radiometer is the architecture of choice for the radiometers in presented in this chapter.

2.4 RECEIVER AND PROBE DESIGNS FOR A WEARABLE RADIOMETER

As stated in the introductory chapter, the goal of this thesis is to not only design a radiometer capable of determining subsurface temperature, but for the radiometer to be wearable e.g. not necessarily operated in a well controlled environment. The ambient radio frequency spectrum is congested, degrading the achievable signal-to-noise ratio (SNR) at many frequencies that might otherwise be optimal for passive sensing. Therefore, allocated quiet bands for remote sensing and radio astronomy that will minimally degrade the SNR are chosen for this application. The protected frequency bands are regulated by both the Federal Communications Commission (FCC) and International Telecommunication Union (ITU) [58], and several frequency bands are detailed in Table 2.1. The frequency bands will be referred to as 1.4 GHz and 2.7 GHz for ease of reference, and shall correspond to the frequency bands detailed in Table 2.1.

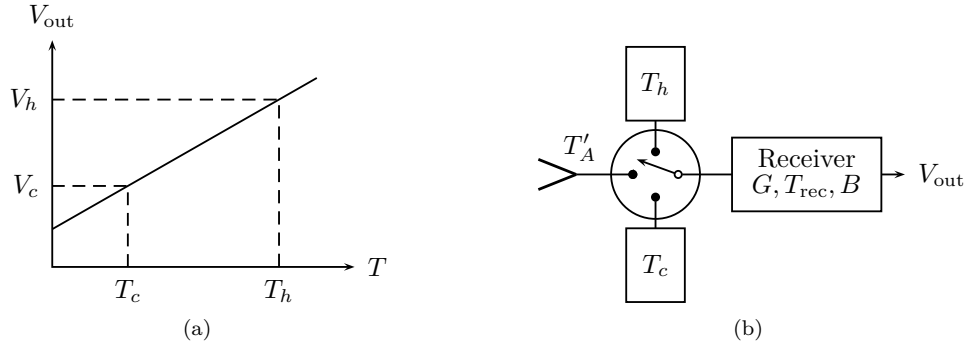


Figure 2.6: General calibration line (a) of a radiometer where V_h and V_c are the hot and cold output voltages corresponding to the input temperatures T_h and T_c , and a two-load radiometer (b) in which the radiometer is constantly calibrated using an RF switch at the front of the receiver.

In this chapter, only receivers for the 1.4 GHz and 2.7 GHz bands are presented. The 4.9 GHz frequency does not penetrate very deep into a lossy medium and may be used to sense the surface skin temperature. Additionally, if very deep sensing is required, the 400 MHz band may also be used.

Up to this point the choice of direct detection or superheterodyne has not been discussed. Either architectures may be used in the predetection section of the receiver. To reduce the complexity of the receiver, direct detection is the architecture chosen for the radiometers presented in this chapter. Generally, conversion to an intermediate frequency (IF) frequency is done to spread the required gain across different frequencies as large gain can easily be achieved as frequency decreases. Additionally, conversion to an IF can make improving the selectivity easier. One advantage of not converting to an IF is that a diode square-law detector can be matched over the narrow RF bandwidth increasing the sensitivity of the detector which decreases the required RF gain. This small dc signal can then be amplified by a low-noise op-amp circuit rather than at the IF. The following design procedure is used for the receivers:

- Design a matched detector and determine sensitivity.
- Given the square-law detector sensitivity, design the receiver front-end or predetection section that will have the required gain to stay above the noise floor of the detector, but still within the square-law region of the diode.
- Ensure the noise figure of the system meets the design requirements for receiver sensitivity by proper selection of components.

Table 2.1: Receiver frequencies for a wearable radiometer. The frequency bands chosen are protected for radio astronomy and remote sensing.

Passive Sensing Frequency Band [MHz]	Abbreviated Name
406.1-410 ^a	400 MHz
1400-1427 ^b	1.4 GHz
2650-2700 ^{b,c}	2.7 GHz
4800-5000 ^{c,d}	4.9 GHz

^a Reserved for radio astronomy at specific locations (footnotes US74 and US385 [58])

^b Emissions are prohibited at the frequencies of 1.4-1.427 GHz, 2.69-2.7 GHz for both the FCC (footnote US246 of [58]) and ITU (footnote 5.430 of [58]).

^c Part of the frequency band is shared with transmitters.

^d Emissions are prohibited by the FCC in the frequency range of 4.99-5.0 GHz FCC (footnote US246 of [58]).

The receiver also includes the near-field probe or transducer, designed for the specific materials being measured. For the purpose of demonstration, water is the medium used, and the probes are designed to be matched when placed in contact with water. In this thesis, a dipole probe is used as it is more useful than a waveguide when size, flexibility, and cost are requirements, as is the case for a portable microwave thermometer. The dipole also has the advantage of being directional when placed at the interface between a high dielectric constant half space and free space as the ratio of power radiated into the lower and upper half-spaces varies approximately as $\epsilon_r^{3/2}$ [59, 60].

The stability of the radiometer is characterized by determining the Allan deviation. Allan deviation has been developed as a statistical tool for frequency standard metrology [61] where classical variance can give misleading results for long-term variations. Allan variance has been proposed for characterizing radiometer stability [57, 62], and for a discrete time series y_k spaced τ_0 apart is given by

$$\sigma_y^2(\tau) = \frac{1}{2(N - 2n + 1)} \sum_{k=1}^{N-2n+1} \left(\frac{1}{n} \sum_{j=k+n}^{k+2n-1} y_j - \frac{1}{n} \sum_{j=k}^{k+n-1} y_j \right)^2, \quad (2.13)$$

where $\tau = n\tau_0$. The Allan deviation is simply the square-root of the Allan variance. The formula for the Allan deviation may look complicated, but it has a simple interpretation: it is the standard deviation of the differences between adjacent measurements, where a measurement consists of enough samples to take up time τ .

2.4.1 CALIBRATION

To determine the unknown antenna temperature, the receivers must be calibrated. For the two-load radiometer, calibration is performed continuously by regularly switching the receiver between the antenna and two loads of known temperatures. The measurements in this thesis are calibrated with an SMA microwave load at room temperature for the cold calibration standard, and an Agilent 346A noise source for the hot calibration standard. The Agilent 346A noise source has an excess noise ratio (ENR) of between 4.5 dB and 6 dB. The ENR is defined in terms of its on and off noise states, and is generally expressed in dB as

$$\text{ENR} = 10 \log_{10} \left(\frac{T_S^{\text{ON}} - T_S^{\text{OFF}}}{T_0} \right). \quad (2.14)$$

The calibrated ENR of a noise source is always referenced to $T_S^{\text{OFF}} = T_0 = 290$ K. If the physical temperature of the noise source is not 290 K the ENR must be corrected [63]:

$$\text{ENR}_{\text{corr}} = 10 \log_{10} \left(10^{\text{ENR}_{\text{cal}}/10} + \frac{T_0 - T_S^{\text{OFF}}}{T_0} \right), \quad (2.15)$$

where ENR_{cal} is the calibrated value given by the manufacturer. The noise source temperature when it is on is determined from the value of the ENR. For example, a noise source with an ENR of 5 dB at 290 K would have an on temperature $T_S^{\text{ON}} = 1207$ K. The data provided by the manufacturer is only specified at discrete frequencies and for the Agilent 346A noise source, it is estimated to be 5.14 dB and 5.17 dB at 1.4 GHz and 2.7 GHz, respectively.

The noise temperature of the source may be reduced by use of an attenuator, for the purpose of ensuring the output is still within the square-law region of the diode detector. A precision matched attenuator of 2.88 dB was used to reduce the noise temperature of the source where the temperature of the output is given by

$$T_{\text{out}} = \frac{T_{\text{in}}}{L} + \left(1 - \frac{1}{L} \right) T_p, \quad (2.16)$$

where T_p is the physical temperature of the attenuator, and L is the loss in the attenuator. This corresponds to a hot temperature standard of 778 K and 781 K at 1.4 GHz and 2.7 GHz respectively.

The output voltage from the square-law detector is amplified by a low-noise op-amp, filtered, and then measured by an analog-to-digital converter (ADC). The AD620 from Analog Devices is a low-noise

instrumentation amplifier requiring only one resistor to set a gain between 1 and 10,000. After the amplifier a RC low-pass filter is used, then the voltage is measured by a National Instruments PCI-6143 16-Bit, 250 kS/s/ch, simultaneous sampling multifunction DAQ. The DAQ is also used to control the RF front-end switch for calibration. This setup is illustrated in Fig. 2.7 including a temperature data logger (TC-08) from Pico Technology to monitor the load temperature and experimental test setup temperatures.

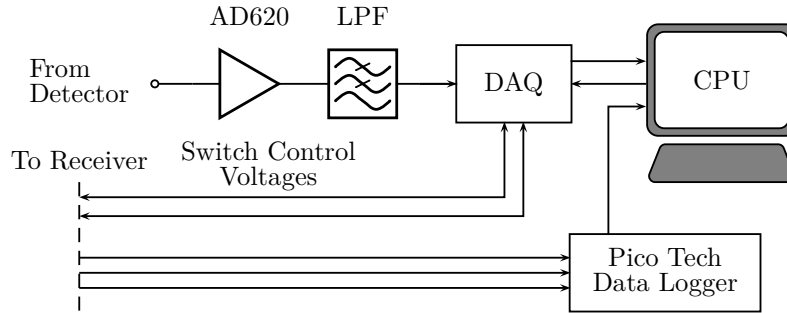


Figure 2.7: Post detection data conditioning and acquisition. The dc voltage is amplified and filtered before being measured with a DAQ.

The RC low-pass filter has a time constant of $\tau_{rc} = 825 \mu\text{s}$, therefore the DAQ is used to sample the output voltages every 1 ms. The raw data from the output of the diode detector is measured by the DAQ along with the control voltages. Calibration is done every 1 second ($\tau_{cal} = 1 \text{ s}$) with an equal dwell time on each load (0.333 s). The raw data is processed by determining the mean output voltage from each load over 1/3 of the calibration cycle. Since an RC low-pass filter is used, it takes time for the capacitor to charge and discharge such that the measured voltage has reached steady state. To ensure the estimate of the average is not affected by the low-pass filter time constant, the first 10 filter time constants (8.25 ms) of data at the beginning of each load measurement is not used in estimating the mean. A summary of the calibration is shown for an example case of raw data in Fig. 2.8. This calibration procedure will be used throughout the rest of this thesis.

For the long measurements (up to an hour) done in this thesis, post processing all the data is not feasible. Therefore, custom code was written in Python to periodically process the data, and re-write the raw time series data. This was done every 30 seconds without interrupting the data sampling so that the data used for calculations is continuous.

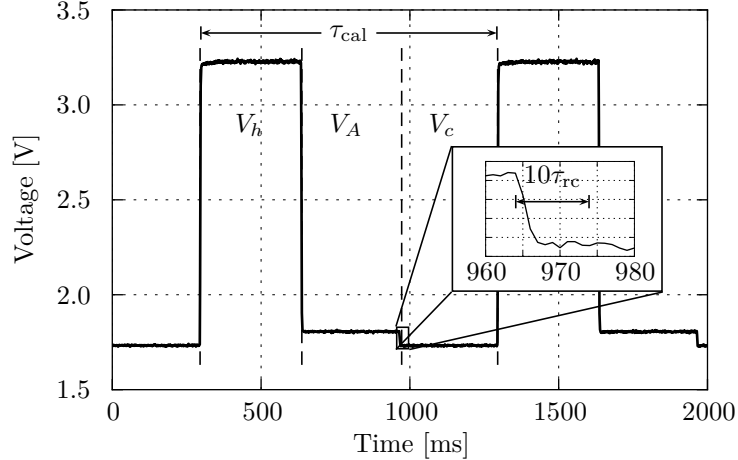


Figure 2.8: Raw measurement data used to determine antenna temperature. The raw hot, antenna, and cold voltages are averaged every τ_{cal} . To ensure an accurate estimate of the mean for each standard the first 10 low-pass filter time constants τ_{rc} shown in the inset are thrown out.

2.4.2 1.4 GHz SYSTEM

The receiver and detector sensitivities were measured using a Lock-in Amplifier (SR-830 from Stanford Research Systems). The lock-in amplifier uses phase sensitive detection to characterize very small signals that may be obscured by noise. The square-law diode detector is a Schottky diode SMS7630-079 from Skyworks Inc. The Schottky diode is matched with a lumped element LC match shown in Fig. 2.9a, with the corresponding elements shown in Table 2.2. A photograph of the square-law detector is shown in Fig. 2.9b.

To characterize the performance of the square-law detector, a RF sweeper was used to drive the detector at different power levels and at different frequencies. Fig. 2.10 shows the measured performance of the square-law detector. The sensitivity as seen in Fig. 2.10a is $25 \text{ mV}/\mu\text{W}$ when driven with a 1.4 GHz signal. The frequency performance is shown in Figs. 2.10b and 2.10c showing the detector is matched best at 1.4 GHz when driven with an RF input power of -40 dBm. The broadband response shown in Fig. 2.10c demonstrates a factor of 1000 difference from the peak voltage over the range of 2.35 GHz to 4.5 GHz. A factor of 1000 difference in dc voltage corresponds to a 30 dB rejection in RF power for the square-law detector.

The next step in the receiver design procedure is to determine the necessary gain and receiver sensitivity requirements. To determine the necessary gain, the RF power is calculated from (1.7). Using the 27 MHz bandwidth and normal body temperature ($\approx 310 \text{ K}$) the power level is -99.4 dBm. If the desired output voltage is $100 \mu\text{V}$, which places the input power within the square-law region of the detector, 45 dB of gain is required.

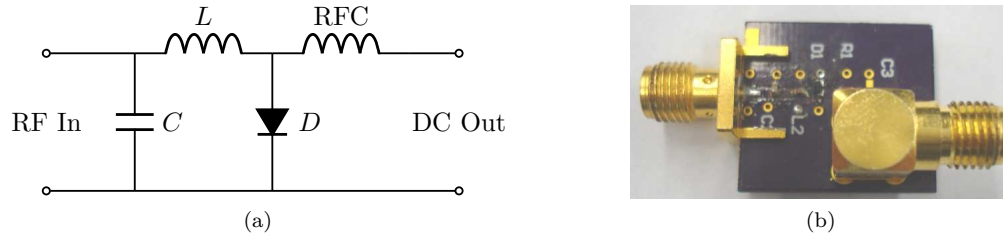


Figure 2.9: Schematic (a) and photograph (b) of a 1.4 GHz diode square-law detector with lumped element match.

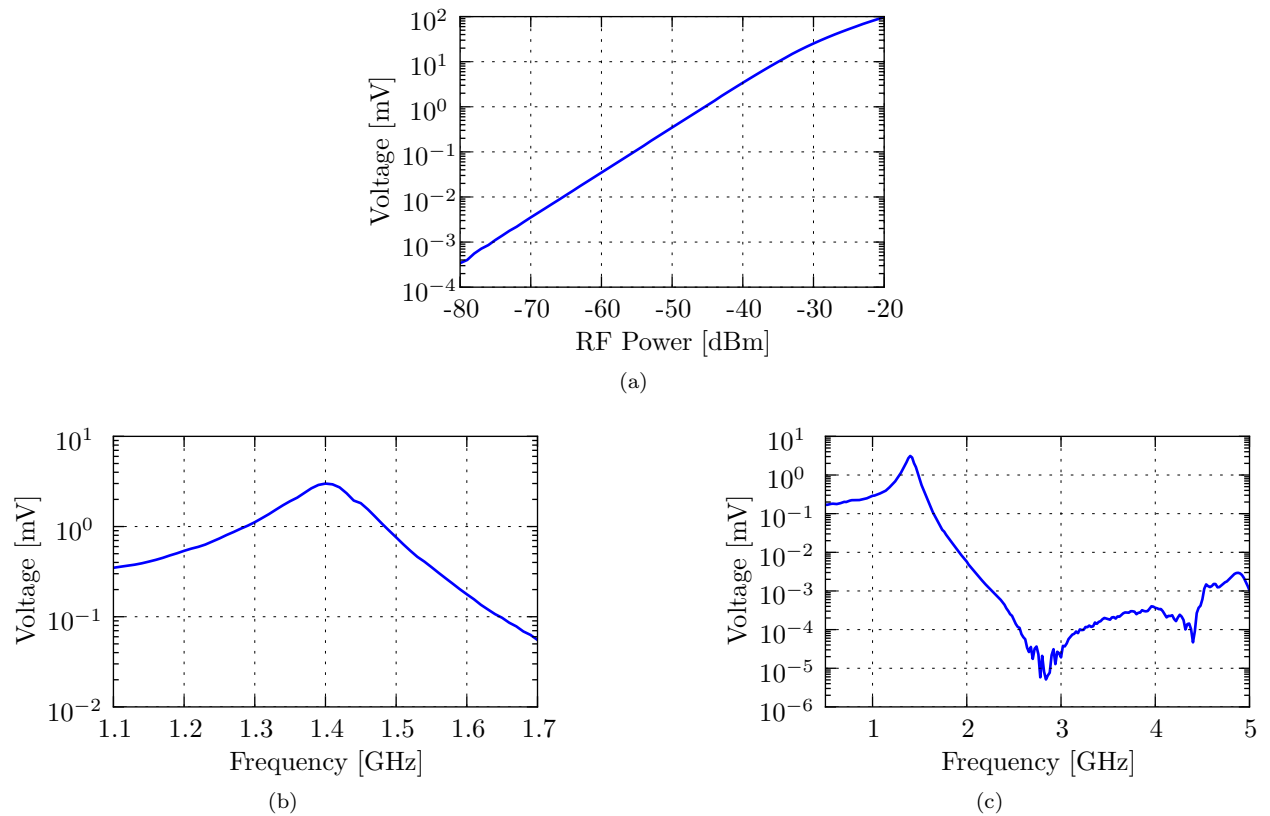


Figure 2.10: Measured performance of the 1.4 GHz diode (SMS7630-079) square-law detector. The output voltage vs. input power at 1.4 GHz (a) demonstrates a sensitivity of $25 \text{ mV}/\mu\text{W}$. The narrowband (b) and broadband (c) frequency response is shown for an input power of -40 dBm .

For a receiver sensitivity of 0.2 K , (2.10) is used to determine the required receiver temperature assuming $\tau = 0.333 \text{ s}$. Next, (2.4) is used to determine the corresponding noise figure which is $\text{NF} = 3 \text{ dB}$. With this information, parts are selected that achieve the appropriate gain and cascaded noise figure.

Fig. 2.11 shows the schematic of the 1.4 GHz radiometer. The radiometer consists of a switch at the input for calibration, then a series of LNAs are cascaded with bandpass filters to achieve the required gain and

Table 2.2: Components for 1.4 GHz diode detector.

Schematic Element	Manufacturer	Part Number	Value
C	ATC	600L4R7CT	4.7 pF
L	Coilcraft	0402CS-15NX	15 nH
D	Skyworks	SMS7630-079LF	
RFC	Coilcraft	0603CS-R12X	120 nH

filter outside of the band of interest. The elements in the schematic are summarized in Table 2.3. Using the formula for cascaded noise figure (2.9), the noise figure of the receiver is calculated to be 3.1 dB with a gain of 45.6 dB. This is a large amount of gain and stability is an issue to be concerned with, however the band-pass filters help as they reduce the gain at low frequencies.

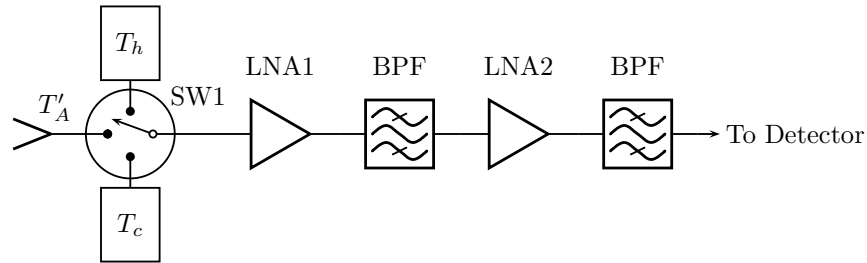


Figure 2.11: Predetection schematic of the 1.4 GHz radiometer.

Table 2.3: Components for a 1.4 GHz receiver.

Schematic Element	Manufacturer	Part Number	G [dB]	NF [dB]
SW1	Hittite	HMC345LP3	-2	2
LNA1	Mini-Circuits	RAMP-33LN	16.7	1
BPF	Mini-Circuits	VBFZ-1400	-2	2
LNA2	Mini-Circuits	TAMP	34.9	0.6

The measured receiver detection sensitivity vs. input power and frequency is summarized in Fig. 2.12. In a bandwidth of 27 MHz, the power delivered from an antenna temperature equal to that of the human body is approximately -100 dBm, and the corresponding output voltage of the receiver at 1.4 GHz is 127.6 μ V, as seen in Fig. 2.12a. The narrowband frequency response is shown in Fig. 2.12b for an input power of -80 dBm, showing the receiver outputs the highest voltage (12 mV) at 1.39 GHz. The broadband response is shown in Fig. 2.12c, demonstrating a factor of 10^4 difference in output voltage compared to the peak for frequencies above 1.8 GHz. This corresponds to an RF power rejection of 40 dB. It should be noted, however, that the

measurement appears to have reached the noise floor of the detector which is approximately 220 nV. Therefore the dynamic range in RF power is 40 dB. The receiver actually has more rejection out of band.

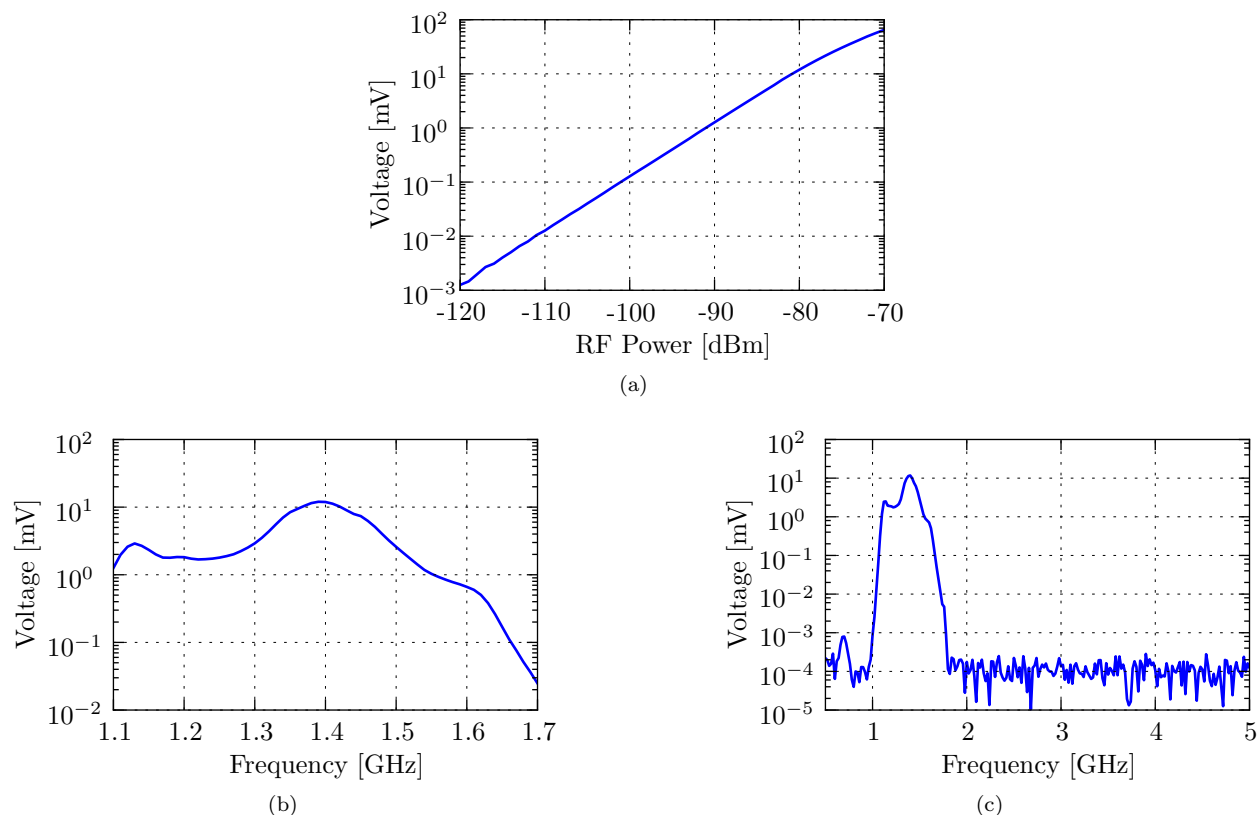


Figure 2.12: Measured performance of the 1.4 GHz receiver vs. RF input over frequency and power. The output voltage vs. input power at 1.4 GHz (a) demonstrates an output voltage of 127.6 μ V for an input power of -100 dBm. The narrowband (b) and broadband (c) frequency response is shown for an input power of -80 dBm.

The final part to design for the 1.4 GHz system is the probe or transducer. As was stated previously, a dipole probe is used. To feed the dipole, which is a balanced structure, a microstrip tapered balun (*balanced* to *unbalanced*) is used. A tapered balun was first presented to transition from a coaxial line to a two-wire transmission line, and was designed to be broadband (100:1 bandwidth) [64]. This was extended to a stripline balun by Gans et al. [65]. Microstrip tapered baluns have been analyzed with various tapers such as circular, linear, and exponential demonstrating wideband microstrip baluns [66, 67].

The 1.4 GHz balun with an exponentially tapered ground plane and linearly tapered top conductor was designed and simulated in Ansys HFSS on a Rogers 4350B ($\epsilon_r = 3.66$) 30 mil thick substrate. The length of the balun is $\lambda_g/2$ at 1.4 GHz transitioning from microstrip on the unbalanced end (towards the receiver)

to balanced stripline on the end that connects to the dipole. The width of the bottom conductor on the unbalanced or microstrip end is truncated at five board thicknesses away from the top conductor trace. The bottom conductor is exponentially tapered, while the top conductor is linearly tapered. The antenna and feed are composed of two pieces of substrate that are orthogonal to one another. To connect the dipole to the balun, a hole is drilled in the antenna portion of the substrate, while a notch is made in the balun such that the two conductors in the balanced stripline could pass through the hole in the antenna substrate and be soldered to the dipole.

For increased impedance, a folded dipole is designed. The shape of the printed dipole and width of the traces are optimized to achieve an impedance match to a $50\ \Omega$ system when fed with the balun. The probe is simulated on a water half-space that is $\lambda_0/4$ away from any radiating edge in extent, and the temperature of the water is assumed to be 21°C . The dielectric properties of the water are estimated using the Debye model from [44]. A photo of the manufactured probe is shown in Fig. 2.13a. To measure the probe, the water half-space is approximated by using a plastic container with water with an approximate depth of 10 cm ($\approx 0.47\lambda_0$). The reflection coefficient is measured using a an Agilent Technologies E8364C network analyzer with an short-open-load-through calibration up to the plane of the connector. The measured and simulated reflection coefficients are shown in Fig. 2.13b demonstrating a return loss greater than 20 dB in the band of interest.

In addition to the reflection coefficient of the probe, it is also necessary to determine the near-field weighting functions for the probe to determine the temperature of the water from raw radiometric observations. To do this, the reciprocal case of a transmitting antenna is analyzed, and the power dissipated in each region around the antenna is determined. For the half-space problem, three regions are considered: upper half-space, lower half-space, and the feed. The desired performance is to have the most power dissipated (received in the reciprocal case for the radiometer) in the lower half-space. Power dissipated in the feed is due to conductor and dielectric losses, while upper half-space loss is due to radiated power. If these values are normalized to the power accepted into the antenna, they can be considered to be the normalized weighting functions. Table 2.4 summarizes the upper half-space (W_u), feed (W_f), and lower half-space (W_l) weighting functions at 1.4 GHz. It is important to note that these weighting functions are specific to the probe and water half-space that it is

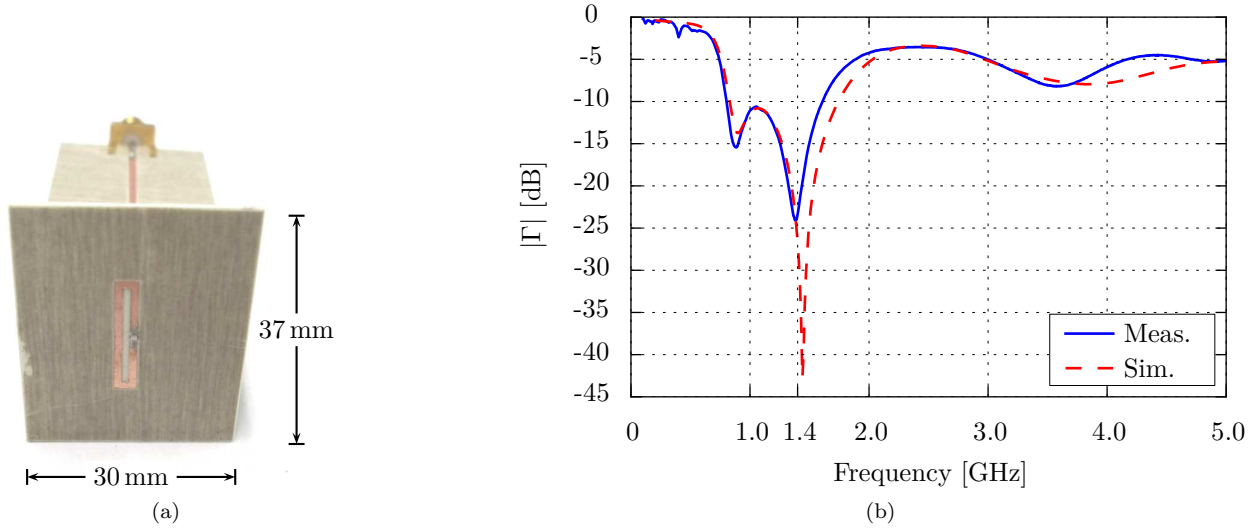


Figure 2.13: 1.4 GHz probe with a microstrip tapered balun feed (a), and its measured and simulated reflection coefficients (b).

in contact with. The power dissipation is a function of the complex permittivity of the water and the physical dimensions of the probe. The 1.4 GHz probe receives 93.9% of its total power from the water half-space.

Table 2.4: 1.4 GHz probe weighting functions on a water half-space.

Upper (W_u)	Feed (W_f)	Lower (W_l)
0.008	0.053	0.939

To characterize the stability of the 1.4 GHz radiometer, the Allan deviation was determined by placing the probe on water in a plastic container. The entire measurement setup was done in an anechoic chamber to ensure there is no outside interference. The depth of the water was approximately 10 cm. A 60 minute measurement was taken, and the radiometer was constantly calibrated every second with equal dwell time on the hot standard, cold standard, and the antenna (0.333 sec.). The Allan deviation was calculated using (2.13). The measurements are summarized in Fig. 2.14. The room temperature T_{rm} (ambient temperature of the calibration load) and water temperature T_t were measured using a temperature data logger (TC-08) from Pico Technology and the measurements are shown in Fig. 2.14a. The initial estimate of the receiver noise figure from data provided by the manufacturer results in a receiver temperature of 302 K, while the measured receiver temperature was 263.5 K as shown in Fig. 2.14b. The antenna temperature T'_A is shown in Fig. 2.14c, and demonstrates an error of 2.2 K between the measured antenna temperature and the thermocouple

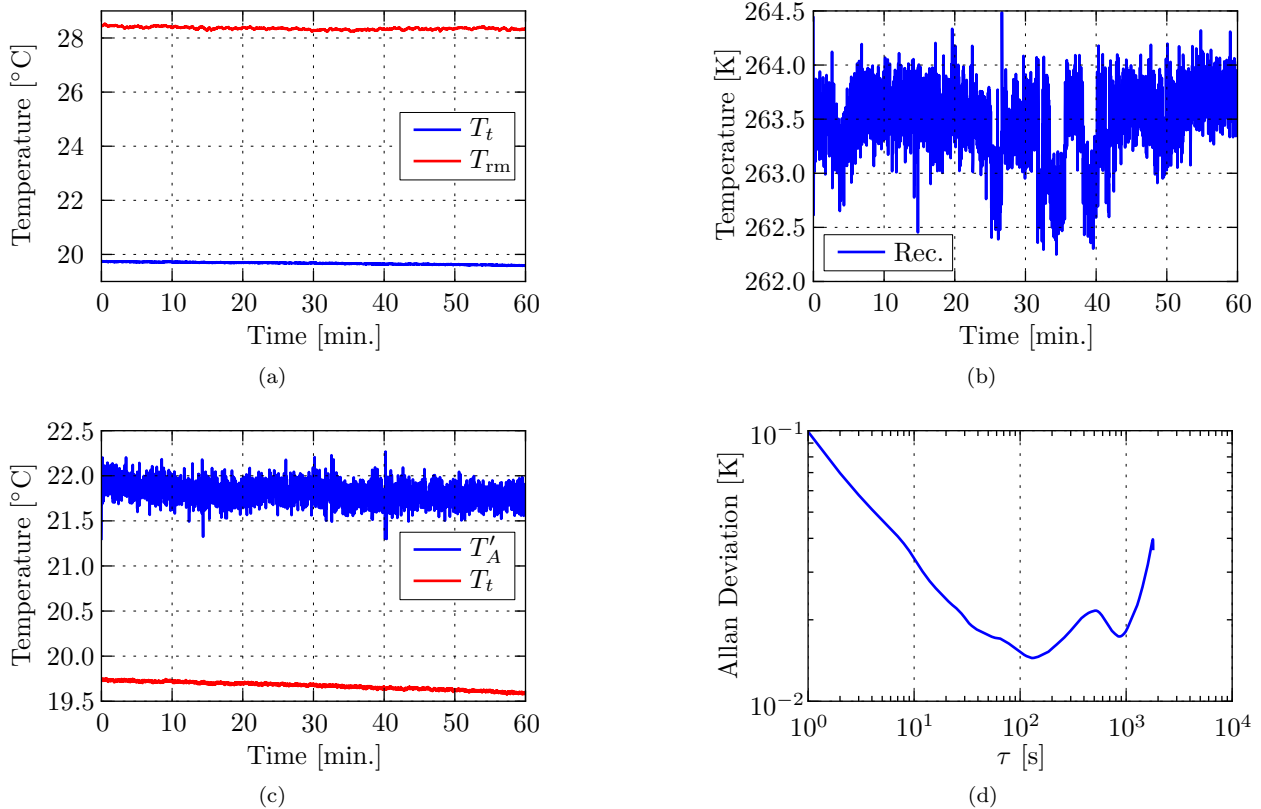


Figure 2.14: Receiver measurements on a constant temperature water bath. The water temperature T_t and room temperature T_{rm} were measured with a thermocouple (a). The calibrated receiver temperature (b) is 263.5 K, and the calibrated antenna temperature (c) demonstrates good agreement between the radiometer and thermocouple measurements. The receiver stability (d) demonstrates an Allan deviation less than 0.2 K for integration times of one second or greater.

measurement. The Allan deviation is shown in Fig. 2.14d demonstrating an improvement in the variance of the output for integration times up to 100 seconds.

The measured temperature T'_A is not corrected for error due to mismatch in this particular case. The temperature inversion process will be discussed in more detail in Chapter 5, where the measurements will be corrected for mismatch and loss in the feed network. Weighting functions will then be used to determine the temperature of the water.

2.4.3 2.7 GHz SYSTEM

The 2.7 GHz receiver was designed using the same method as the 1.4 GHz receiver design. First, the detector was built. Then, knowing the sensitivity of the detector, the receiver front-end was designed with enough gain

and adequate noise figure.

The 2.7 GHz detector was designed using a single stub match with grounded coplanar waveguide (GCPW) transmission lines on an FR4 substrate. The RF choke was designed by meandering an RF shorted (through a capacitor) $\lambda_g/4$ GCPW line. The same Skyworks Inc. Schottky SMS7630-079LF diode was used. To characterize the performance of the square-law detector, a RF sweeper was used to drive the detector at different power levels and at different frequencies. Fig. 2.15 shows the measured performance of the square-law detector. The sensitivity as seen in Fig. 2.15b is 10 mV/ μ W when driven with a 2.65 GHz signal. The frequency performance is shown in Figs. 2.15c and 2.15d showing the detector is matched best at 2.65 GHz when driven with an RF input power of -40 dBm. The broadband response shown in Fig. 2.15d demonstrates a factor of 10 difference from the peak voltage over the range of 2.8 to 5 GHz. A factor of 10 difference in voltage corresponds to a 10 dB rejection in RF power.

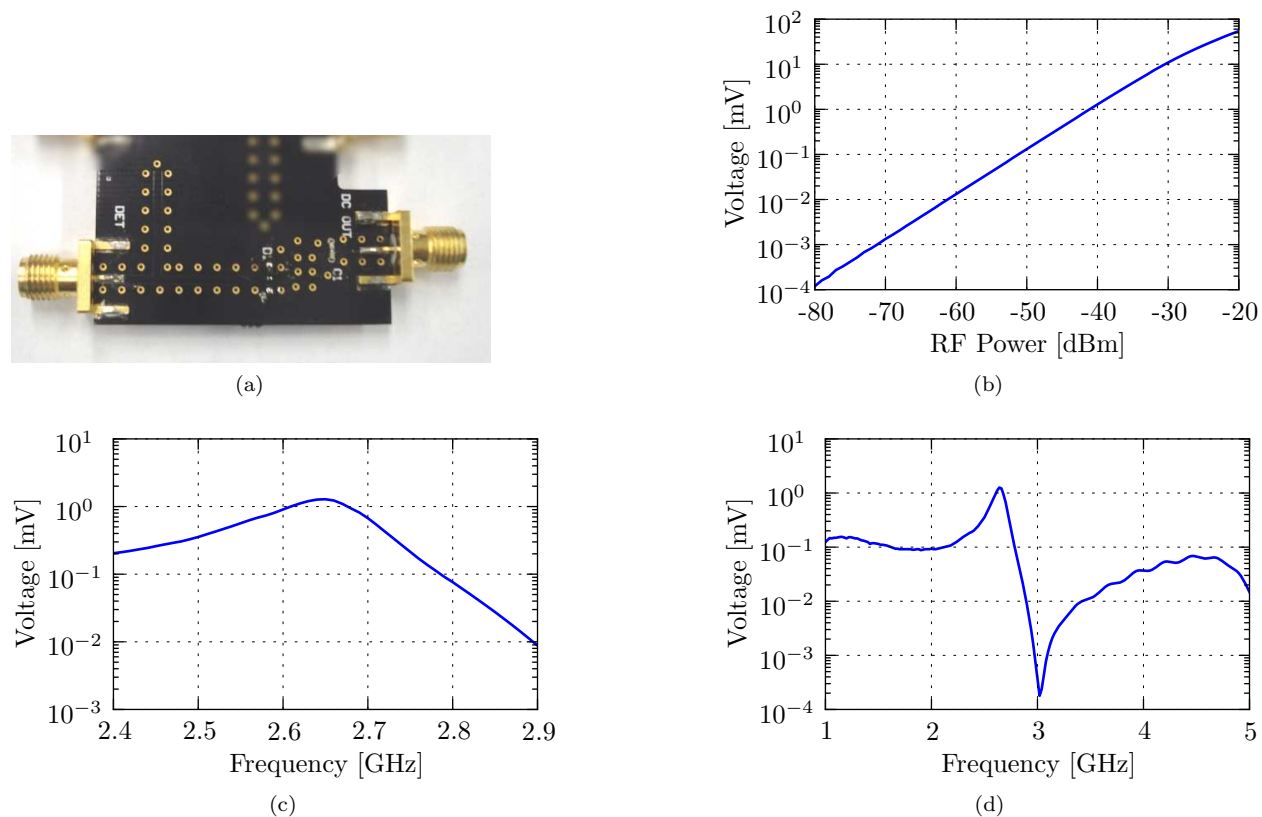


Figure 2.15: Measured performance of the 2.7 GHz diode (SMS7630-079) square-law detector (a). The output voltage vs. input power at 2.65 GHz (b) demonstrates a sensitivity of 10 mV/ μ W. The narrowband (c) and broadband (d) frequency response is shown for an input power of -40 dBm.

The next step in the receiver design procedure is to determine the necessary gain and receiver sensitivity requirements. To determine the necessary gain, first the RF power is calculated from (1.7). Using the 50 MHz bandwidth and normal body temperature (≈ 310 K), the power level is -96.7 dBm. If the desired output voltage is $10 \mu\text{V}$, which places the input power within the square-law region of the detector, 36.7 dB of gain is required. For a receiver sensitivity of 0.2 K, (2.10) is used to determine the required receiver temperature assuming $\tau = 0.333$ s. Next, (2.4) is used to determine the corresponding noise figure which is $\text{NF} = 4.4$ dB. With this information, parts can be selected that will achieve the appropriate gain and cascaded noise figure.

Fig. 2.16 shows the schematic of the 2.7 GHz radiometer. The radiometer consists of a switch at the input for calibration, then a series of LNA's are cascaded with bandpass filters to achieve the required gain and filter outside of the band of interest. The elements in the schematic are summarized in Table 2.5. Using the formula for cascaded noise figure (2.9), the noise figure of the receiver is calculated to be 3 dB with a gain of 36.7 dB.

The measured receiver detection sensitivity vs. input power and frequency are summarized in Fig. 2.17. As stated previously, in a bandwidth of 50 MHz the power delivered from an antenna temperature equal to that of the human body to the receiver is approximately -96 dBm. The output voltage of the receiver for an input power of -96 dBm at 2.64 GHz is $15.1 \mu\text{V}$. The narrow band frequency response is shown in Fig. 2.17b for an input power of -80 dBm showing the receiver outputs the highest voltage ($633 \mu\text{V}$) at 2.64 GHz. The broadband response is shown in Fig. 2.17c, demonstrating a factor of 10^4 difference in output voltage compared to the peak for frequencies above 3 GHz and below 2.35 GHz. This corresponds to an RF power rejection of 40 dB. It should be noted, however, that the measurement appears to have reached the noise floor of the detector which is approximately 80 nV. The receiver actually has more rejection out of band.

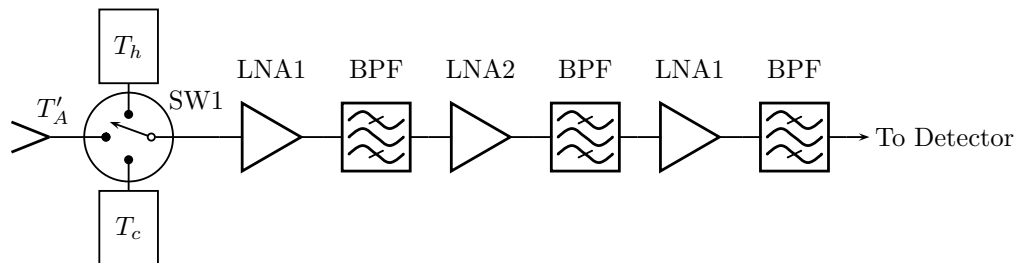
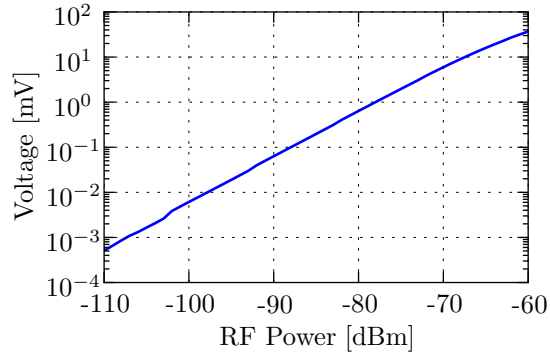


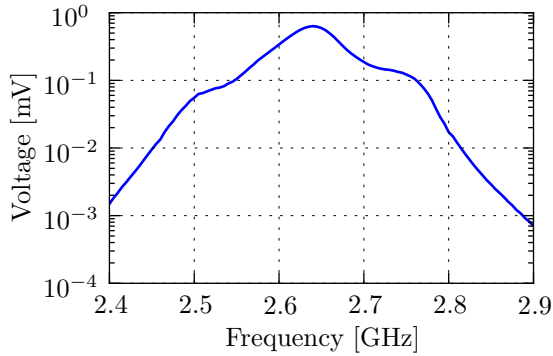
Figure 2.16: Pre-detection schematic of the 2.7 GHz radiometer.

Table 2.5: Components for a 2.7 GHz receiver.

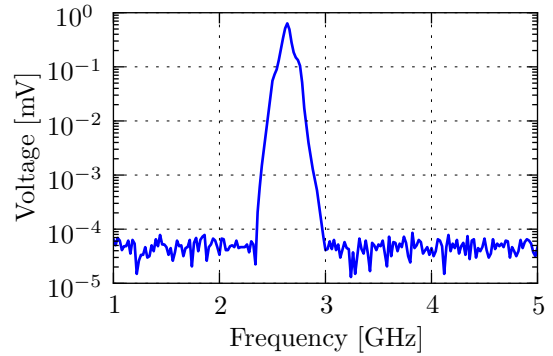
Schematic Element	Manufacturer	Part Number	G [dB]	NF [dB]
SW1	Hittite	HMC345LP3	-2	2
LNA1	Mini-Circuits	TAMP-272LN	13.7	0.8
BPF	Mini-Circuits	BCFN-2700	-2.25	2.25
LNA2	Hittite	HMC667LP2	18	0.75



(a)



(b)



(c)

Figure 2.17: Measured performance of the 2.7 GHz receiver vs. RF input over frequency and power. The output voltage vs. input power at 2.64 GHz (a) demonstrates an output voltage of $15.1 \mu\text{V}$ for an input power of -96 dBm . The narrowband (b) and broadband (c) frequency response is shown for an input power of -80 dBm .

The final part to design for the 2.7 GHz system is the probe or transducer. The same design procedure for the 1.4 GHz probe was used for the 2.7 GHz probe. A folded dipole with a microstrip tapered balun was designed to be matched to a 50Ω system. The microstrip tapered balun and folded dipole structure was designed and simulated in Ansys HFSS on a Rogers 4350B ($\epsilon_r = 3.66$) 30 mil thick substrate. The length of the balun was $\lambda_g/2$ at 2.7 GHz transitioning from microstrip on the unbalanced end (towards the receiver) to balanced stripline on the end that connects to the dipole. The width of the bottom conductor on the

unbalanced or microstrip end was truncated at 5 board thicknesses away from the top conductor trace. The bottom conductor was exponentially tapered, while the top conductor was linearly tapered. The antenna and feed are composed of two pieces of substrate that are orthogonal to one another. To connect the dipole to the balun, a hole was drilled in the antenna portion of the substrate, while a notch was made in the balun such that the two conductors in the balanced stripline could pass through the hole in the antenna substrate and be soldered to the dipole. To increase the impedance of the dipole, a folded dipole design was used. The spacing of the folds and width of the traces were optimized to achieve an impedance match to a $50\ \Omega$ when fed with the balun.

The probe was simulated on a water half-space that was $\lambda_0/4$ away from any radiating edge in extent, and the temperature of the water was assumed to be 21°C . The dielectric properties of the water were estimated using the Debye model from [44]. A photo of the manufactured probe is shown in Fig. 2.18a. To measure the probe, the water half-space was approximated by using a plastic container with water that had an approximate depth of 10 cm ($\approx 0.9\lambda_0$). The reflection coefficient was measured using a Network Analyzer. The measured and simulated reflection coefficients are shown in Fig. 2.18b demonstrating a return loss greater than 17 dB in the band of interest.

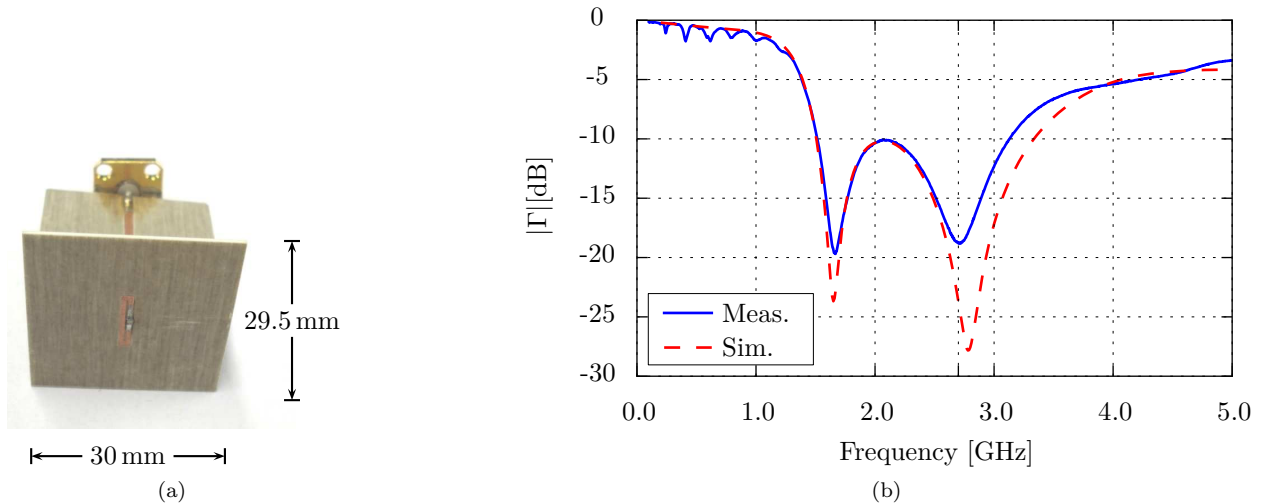


Figure 2.18: 2.7 GHz probe with a microstrip tapered balun feed (a), and its measured and simulated reflection coefficients (b).

The probe weighting functions were also determined in the same manner as described for the 1.4 GHz

probe. Table 2.6 summarizes the upper half-space (W_u), feed (W_f), and lower half-space (W_l) weighting functions at 2.7 GHz. It is important to note, that these weighting functions are specific to the probe and water half-space that it is in contact with. The power dissipation is a function of the complex permittivity of the water and the physical dimensions of the probe. The 2.7 GHz probe receives 93.5% of its total power from the water half-space.

Table 2.6: 2.7 GHz probe weighting functions on a water half-space.

Upper (W_u)	Feed (W_f)	Lower (W_l)
0.01	0.055	0.935

Similar to the 1.4 GHz radiometer, the Allan deviation of the 2.7 GHz radiometer was determined by placing the probe on water in a plastic container. The entire measurement setup was done in an anechoic chamber to ensure there is no outside interference. The depth of the water was approximately 10 cm deep. A 60 minute measurement was taken. The radiometer was constantly calibrated every second with equal dwell time on the hot standard, cold standard, and the antenna (0.333 s). The Allan deviation was calculated using (2.13). The measurements are summarized in Fig. 2.19. The room temperature T_{rm} (ambient temperature of the calibration load) and water temperature were measured using a temperature data logger (TC-08) from Pico Technology and the measurements are shown in Fig. 2.19a. The initial estimate of the receiver noise figure from data provided by the manufacturer results in a receiver temperature of 283 K, while the measured receiver temperature was 303 K as shown in Fig. 2.19b. The antenna temperature T'_A is shown in Fig. 2.19c, and demonstrates an error of 3.6 K between the measured antenna temperature and the thermocouple measurement. The Allan deviation is shown in Fig. 2.19d demonstrating an improvement in the variance of the output for integration times up to 200 seconds.

2.5 MULTI-FREQUENCY PROBE DESIGNS

While for the scope of this thesis temperature estimates will be done with a water phantom, it is necessary to demonstrate that hardware can be designed for the actual application of non-invasive medical radiometry. A few examples of probes were shown in Section 1.4.2, however, these designs were either bulky, or designed only

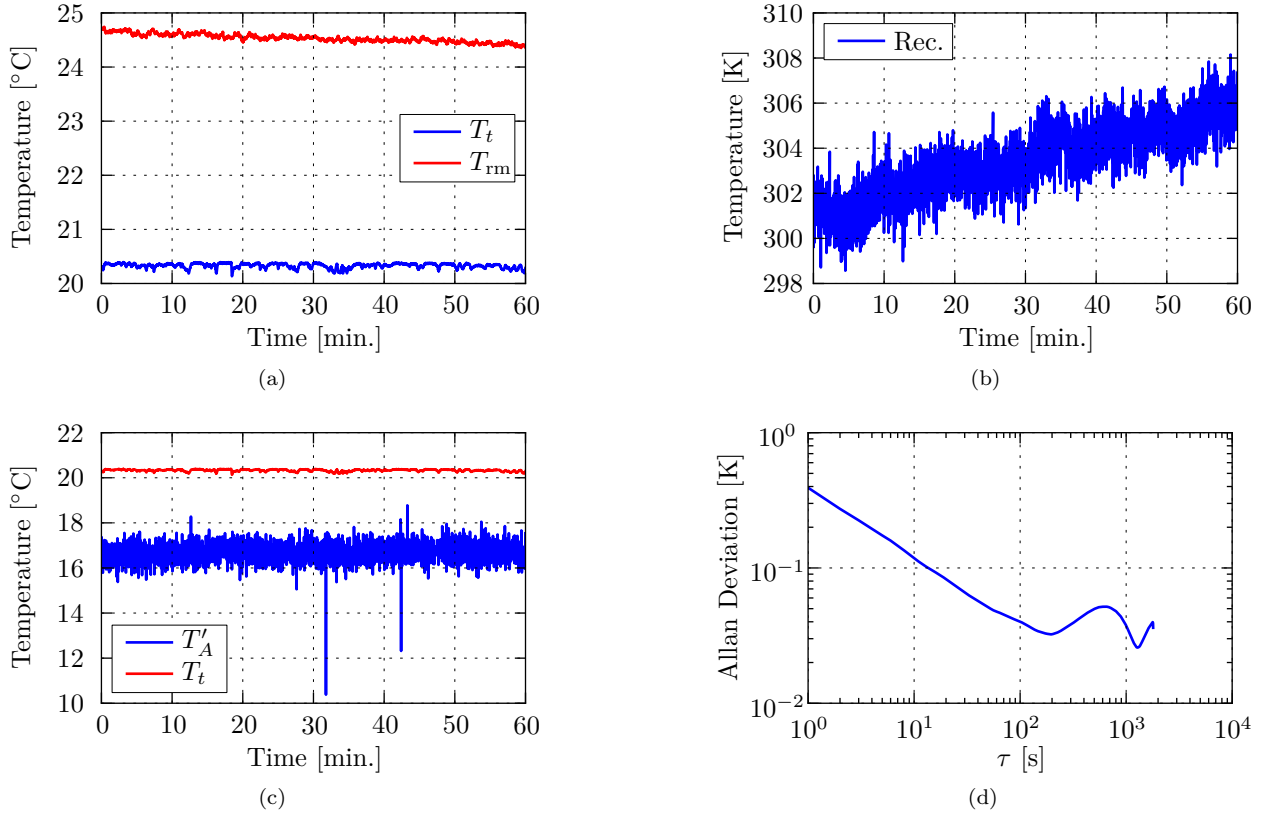


Figure 2.19: 2.7 GHz receiver measurements on a constant temperature water bath. The water temperature T_t and room temperature T_{rm} were measured with a thermocouple (a). The calibrated receiver temperature (b) is 288.8 K, and the calibrated antenna temperature (c) demonstrates good agreement between the radiometer and thermocouple measurements. The receiver stability (d) demonstrates an Allan deviation less than 0.4 K for integration times of one second or greater.

for a single frequency. Multiple frequencies must be used to differentiate temperature received from various depths within the tissues. An additional challenge is that the probes must be receiving power from the same parts of the tissues, or at least in a manner that ensures the model is still valid. This model assumption is that the tissues are a stack of homogeneous tissue layers that are infinite in extent in the transverse direction with uniform temperature in the transverse direction. For this assumption to be valid, the probes must be collocated and the power must be dissipated in a narrow field of view within the tissues. To view how power is dissipated within the tissues, the specific absorption rate (SAR) will be calculated at various depths in the tissues. The SAR is defined as

$$\text{SAR} = \frac{\sigma |E|^2}{2\rho} \quad [\text{W/kg}], \quad (2.17)$$

where σ is the effective conductivity, and ρ is the mass density. The design requirements are thus two-fold: impedance matched and collocated power dissipation pattern.

DUAL FREQUENCY STERNUM PROBE

The first multi-frequency probe design is a dual frequency probe designed for 400 MHz and 1.4 GHz matched on the human sternum. The tissue stack was 1.2 mm skin/ 4 mm fat/ 2 mm cortical bone/ 7 mm cancellous bone / 2 mm cortical bone/ heart. The frequency dependent dielectric properties of the tissues were downloaded from [28]. The probe was simulated in Ansys HFSS to determine the input impedance and power dissipation pattern. The high frequency probe is nested in the low frequency probe as shown in Fig. 2.20 to ensure power dissipation patterns are collocated. The probe was printed on Rogers 3010 ($\epsilon_r = 10$) 25 mil board material, which is somewhat flexible.

The probe was measured *in vivo* on the human sternum with the author serving as a volunteer. The measured results show good agreement with simulation maintaining a return loss greater than 20 dB for each probe at their respective design frequencies as demonstrated in Fig. 2.21. The measured isolation is also shown in Fig. 2.21 demonstrating an isolation of better than 20 dB.

The SAR was determined at the interface between the heart and cortical bone. Fig. 2.22 shows the SAR normalized to the peak value at that layer in the tissues. It can be seen for both probes that the maximum is located underneath the footprint of the probe.

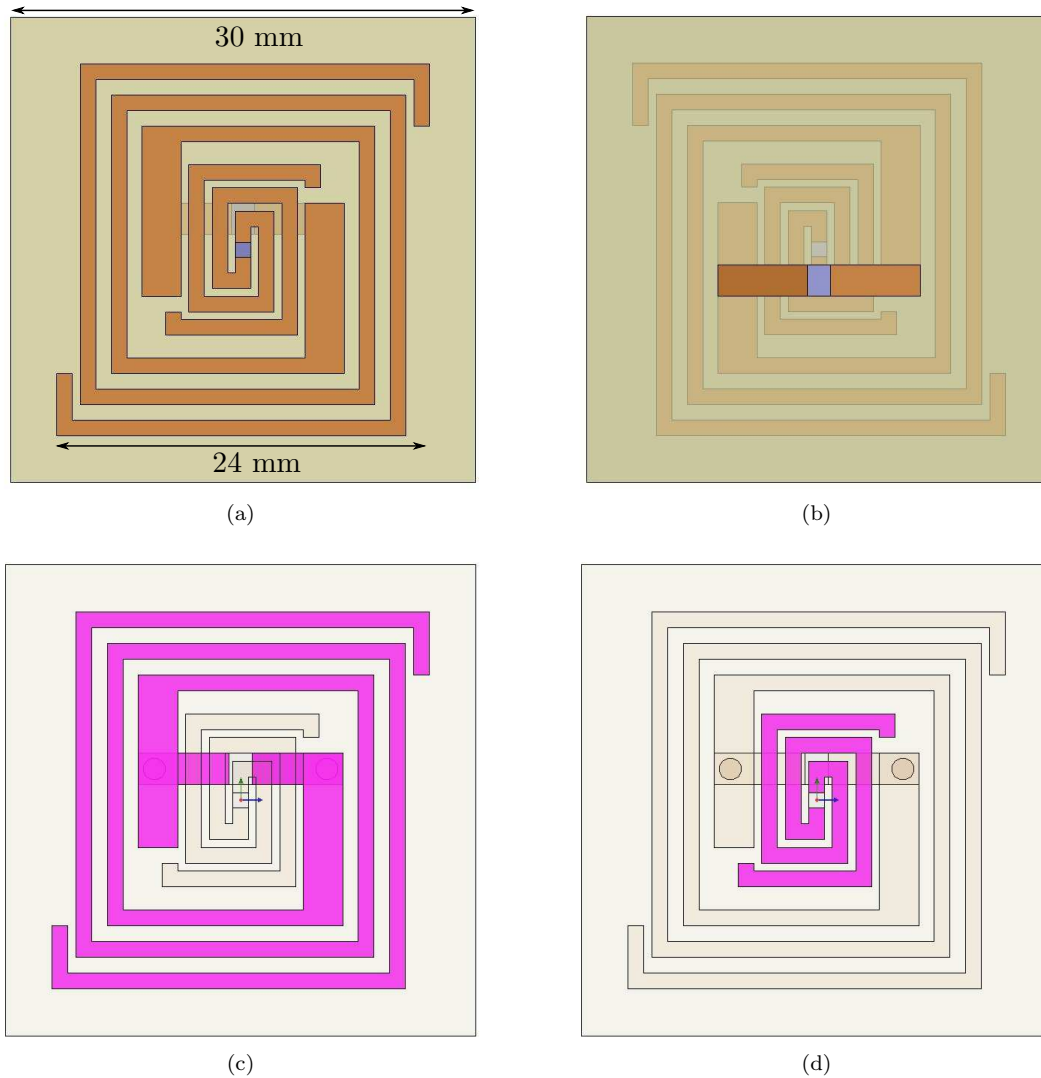


Figure 2.20: Detail of the front (a) and back (b) of the nested dipole probe with the 400 MHz (c) and 1.4 GHz (d) probes highlighted.

THREE FREQUENCY ABDOMEN PROBE

A second probe design was made to be placed on the human abdomen assuming assuming a 1-mm thick skin layer, 2-mm thick fat layer, and infinitely thick muscle layer. The three frequencies used were the 1.4, 2.7, and 4.9 GHz bands. The probe design is shown in Fig. 2.23. The probes are designed to be as collocated as possible so that their power dissipation patterns coincide spatially in the tissue stack. For this reason the two lower frequency probes are bent as shown in the photograph. The probes are made on a Rogers RO-4350B 0.762-mm thick substrate with $\epsilon_r=3.66$, and each dipole is fed with a microstrip tapered balun.

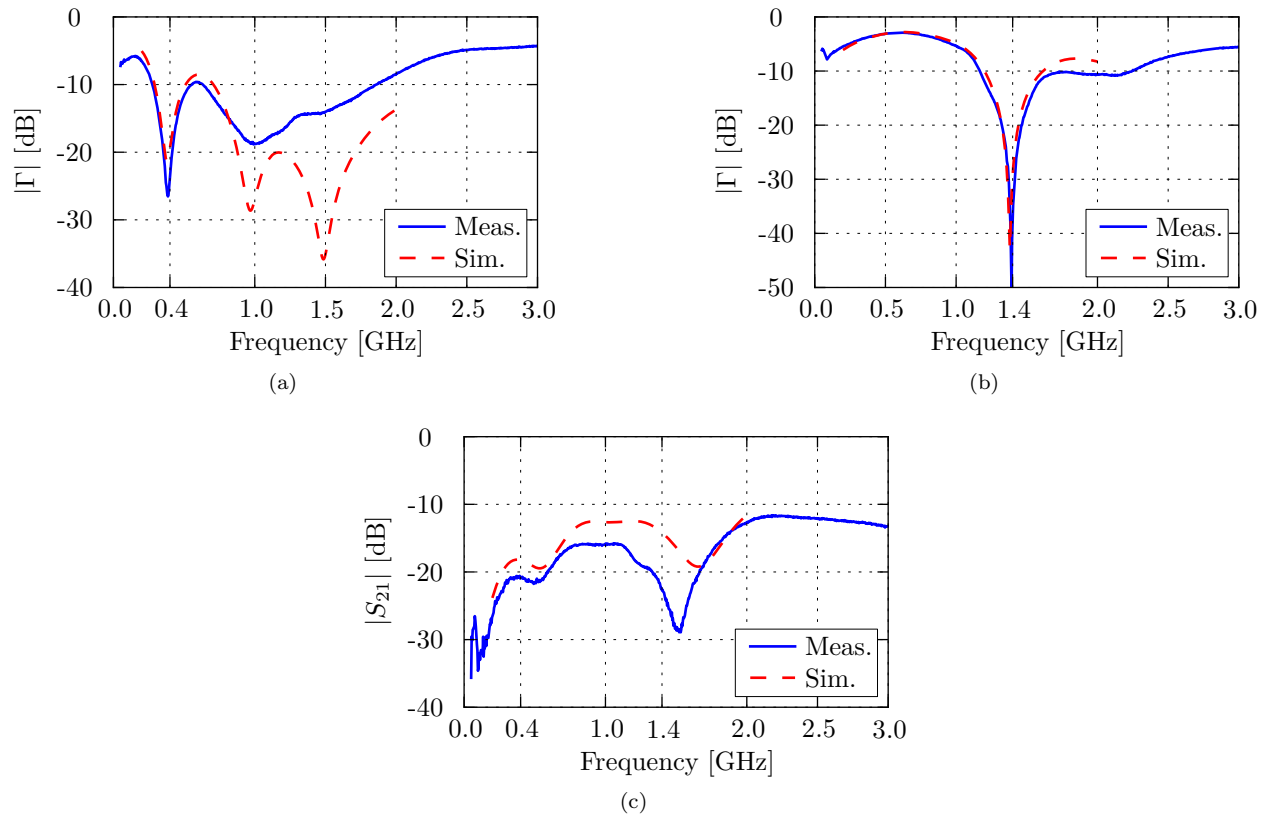


Figure 2.21: Measured performance of the 400 MHz (a) and 1.4 GHz (b) probes, along with the isolation (c) between the probes.

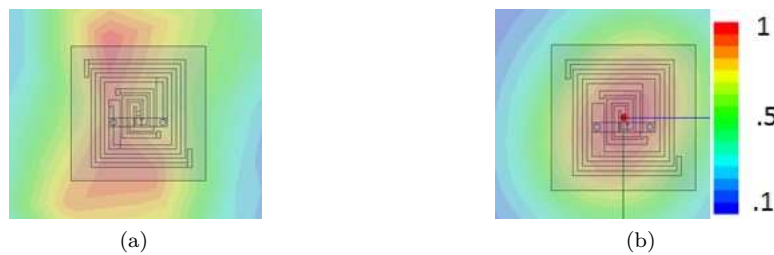


Figure 2.22: SAR for the 400 MHz (a) and 1.4 GHz (b) probes at the hear-cortical bone interface. Each plot is normalized to the peak value at that layer in the tissues as shown by the scale in (b).

The dipoles are measured *in vivo* on the abdomen with the author serving as a volunteer. The measured results for the three probes are shown in Fig. 2.24 demonstrating a match better than -15 dB for each probe at the respective design frequencies. The measured results are compared to HFSS simulations in Fig. 2.24, and agree well over the entire frequency range from 0.5 to 7 GHz.

The simulated normalized weighting functions are shown in Table 2.7. In each case, over 50% of the power

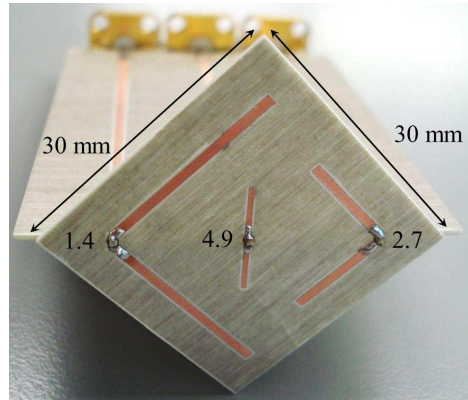


Figure 2.23: Three frequency probe with balun feed network. The overall dimensions of the probe are 30 mm \times 30 mm neglecting the balun.

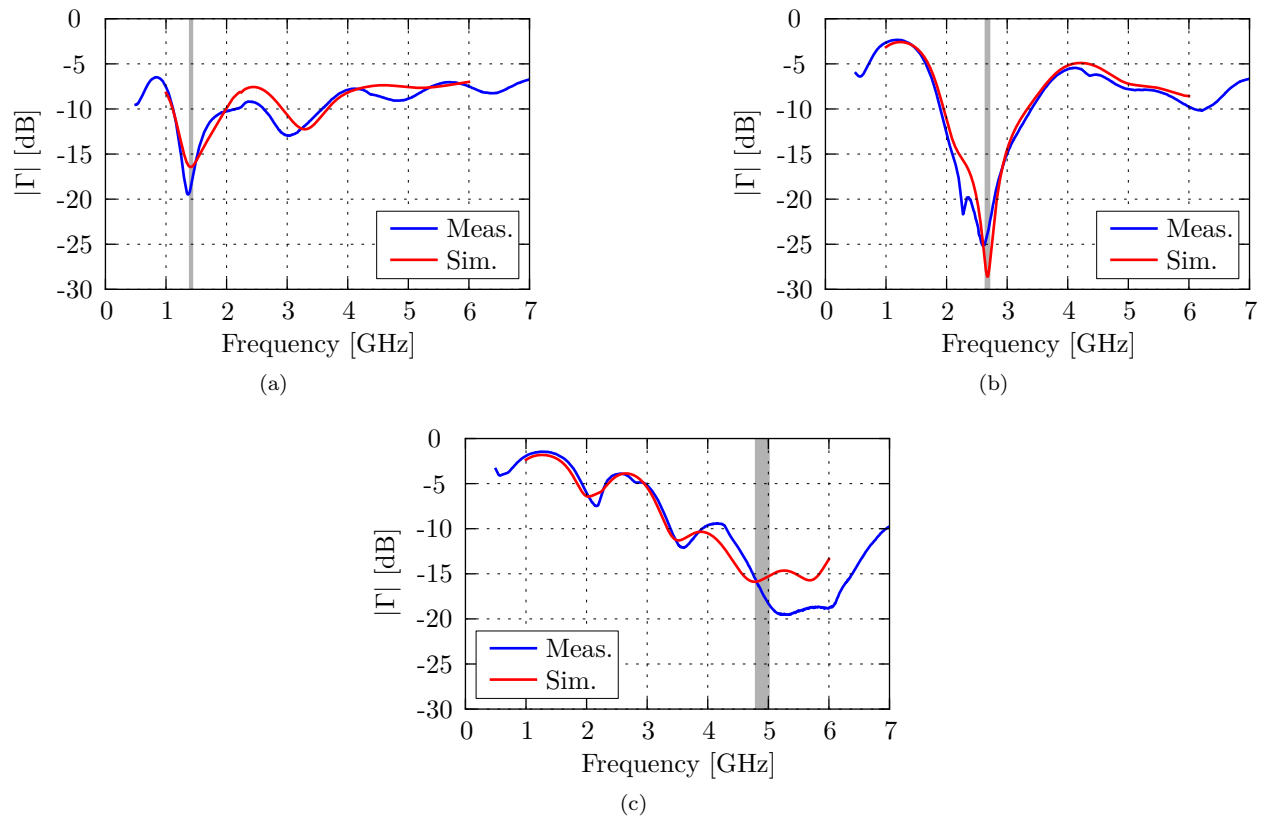


Figure 2.24: Comparison of measured input match to HFSS simulations for the (a) 1.4 GHz, (b) 2.7 GHz, and (c) 4.9 GHz probes.

accepted into the probe is dissipated in the 1-mm thick skin layer. The lowest frequency probe dissipates the most power in the muscle. Less than 10% of the power is dissipated in the fat layer, and this percentage decreases with increasing frequency in this particular case.

Table 2.7: Normalized weighting functions for the three frequency probe on a three layer medium of skin (1 mm), fat (2 mm), and muscle.

f [GHz]	W				
	Skin	Fat	Muscle	Feed	Radiated
1.4	0.511	0.071	0.388	0.013	0.017
2.7	0.550	0.058	0.350	0.022	0.020
4.9	0.602	0.049	0.276	0.040	0.033

In addition to calculating the dissipated power, the SAR is shown at three depths in the tissues for each probe in Fig. 2.25. Each individual SAR plot is normalized to the peak value (red). It can be seen from the SAR plots close to the surface that the maximum occurs directly below the feed. Further into the tissues, however, the maximum begins to occur in the center of the entire probe footprint.

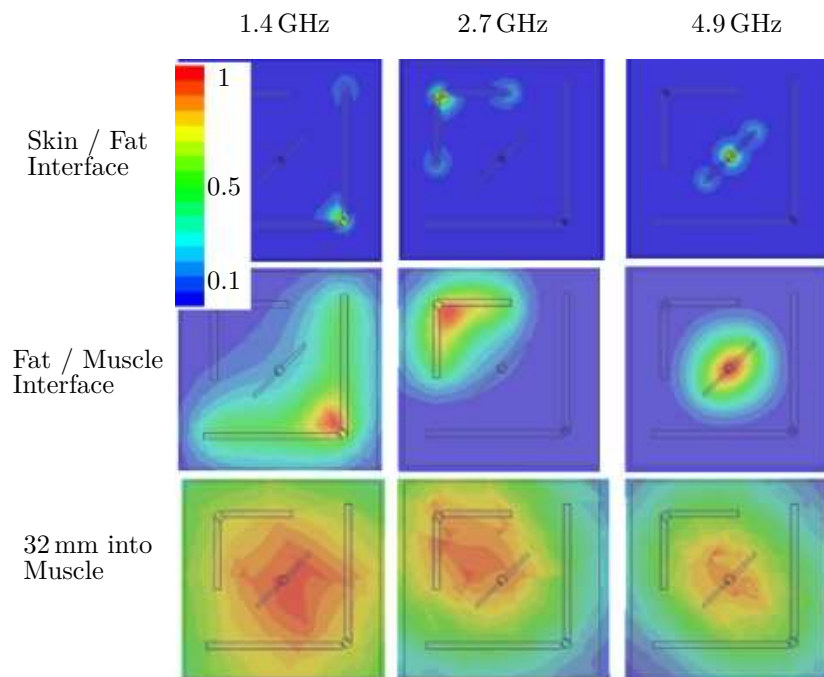


Figure 2.25: SAR at various depths in the tissues for each of the three probes. Each individual SAR plot is normalized to the peak value as demonstrated by the scale. It can be seen from the SAR plots close to the surface that the maximum occurs directly below the feed. Further into the tissues, however, the maximum begins to occur in the center of the entire probe footprint.

2.6 CONCLUSION

This chapter has presented the necessary receiver architectures and relevant design equations for designing a radiometer for non-invasive microwave thermography. To address the problem of operation in a congested RF environment, narrow frequency bands allocated for remote sensing and radio astronomy were utilized. Two radiometers were presented and their performance characterized. In addition, probes for use with a water phantom were shown. Additional multi-frequency probes for medical applications were characterized and their measured and simulated performance compared.

CHAPTER 3

MMIC CIRCUITS FOR RADIOMETERS

CONTENTS

3.1	Introduction	50
3.2	Tunable MMIC Coupler	50
3.2.1	Tunable Coupler Analysis	51
3.2.2	MMIC Coupler Implementation and Measured Scattering Parameters	56
3.2.3	Comparison to Simulation	59
3.2.4	Linearity Measurement	61
3.2.5	Comparison to Other Work	62
3.3	An Active MMIC Cold Noise Source	64
3.3.1	Noise Source Model	65
3.3.2	Minimized $T_{s,1}$ Example	67
3.3.3	GaAs MMIC Noise Source Design	68
3.3.4	GaAs MMIC Noise Source Experimental Results	71
3.4	Conclusions	71

3.1 INTRODUCTION

Design of a microwave radiometer capable of being a wearable device requires miniaturization of circuit elements. A path for integration must be presented with the ultimate goal being the development of a compact system on chip (SoC). There has been increased interest for integrating multiple components on a single chip. The feasibility of developing SoC radiometer components at 13 GHz for monitoring emergency operators [68] and other optically masked targets such as forest fire detection [69] has been investigated. The studies presented simulations of the following radiometer components in a 90 nm CMOS process: LNA, mixer, IF amplifier, and square-law detector. The IF section of the radiometer was developed in a 90 nm CMOS process demonstrating a gain, noise figure, and bandwidth of 45 dB, 10 dB, and 58 MHz respectively while occupying an area of 1 mm². Additionally, integration of MMIC technology to reduce the overall size and weight while maintaining performance has been demonstrated for a K-band tropospheric water vapor profiling radiometer [70].

This chapter presents two new circuit elements that could aid in the design of a radiometer on a single chip. The first circuit combines two circuit elements (a variable attenuator and a fixed directional coupler) of a balanced Dicke radiometer into one MMIC tunable coupler made in a 0.5 μm TriQuint gallium arsenide (GaAs) process. The second part of this chapter presents a 0.5 μm GaAs MMIC calibration standard capable of achieving cold equivalent temperatures when the physical temperature of the device is at ambient temperature. Such a device minimizes the need for a bulky cryogenic load. The noise source section also presents a design procedure to achieve a minimum equivalent noise temperature.

3.2 TUNABLE MMIC COUPLER

A balanced Dicke radiometer seen in Fig. 3.1, is an appropriate architecture for these applications, and a conventional approach uses a variable attenuator and fixed directional coupler. Alternatively, a MMIC variable coupler can replace these two components highlighted in Fig. 3.1, thus making the wearable radiometer more compact. Additional applications include tunable impedance transformers [71].

Couplers with tunable coupling ratios have been presented in [71–77], with a thorough comparison of

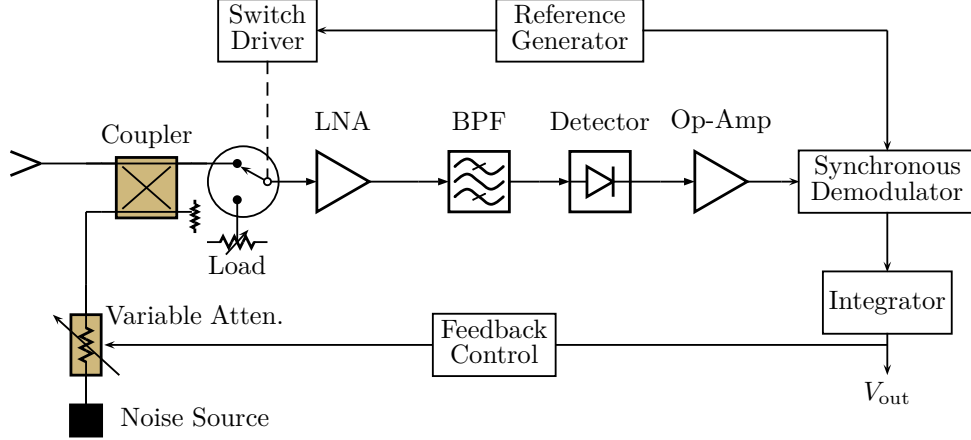


Figure 3.1: Balanced noise injection Dicke radiometer block diagram. The two highlighted components are a fixed directional coupler and a variable attenuator. A variable directional coupler can replace these two circuit elements.

variable directional couplers presented in [75]. In this section, the simplified coupler model analysis is first presented using even and odd mode analysis. Next, the analysis is applied to a $0.5 \mu\text{m}$ TriQuint GaAs process, and the measured coupler performance is presented and compared to simulation. Finally, a two-tone linearity measurement is presented to further characterize the device performance for various applications.

3.2.1 TUNABLE COUPLER ANALYSIS

Consider the simplified directional coupler circuit with ideal variable capacitors shown in Fig. 3.2a. The even and odd mode circuits are shown in Figs. 3.2b and 3.2c respectively.

To find the even and odd mode transmission and reflection coefficient, the two port transmission matrix or $ABCD$ matrix [53] is defined

$$\begin{bmatrix} V_1 \\ I_1 \end{bmatrix} = \begin{bmatrix} A & B \\ C & D \end{bmatrix} \begin{bmatrix} V_2 \\ I_2 \end{bmatrix}. \quad (3.1)$$

The corresponding $ABCD$ matrix for the even mode excitation is

$$\begin{bmatrix} A & B \\ C & D \end{bmatrix}_e = \begin{bmatrix} 0 & jZ_0\sqrt{2} \\ j/Z_0\sqrt{2} & 0 \end{bmatrix} \begin{bmatrix} 0 & jZ_0\sqrt{2} \\ j/Z_0\sqrt{2} & 0 \end{bmatrix} = \begin{bmatrix} -1 & 0 \\ 0 & -1 \end{bmatrix}, \quad (3.2)$$

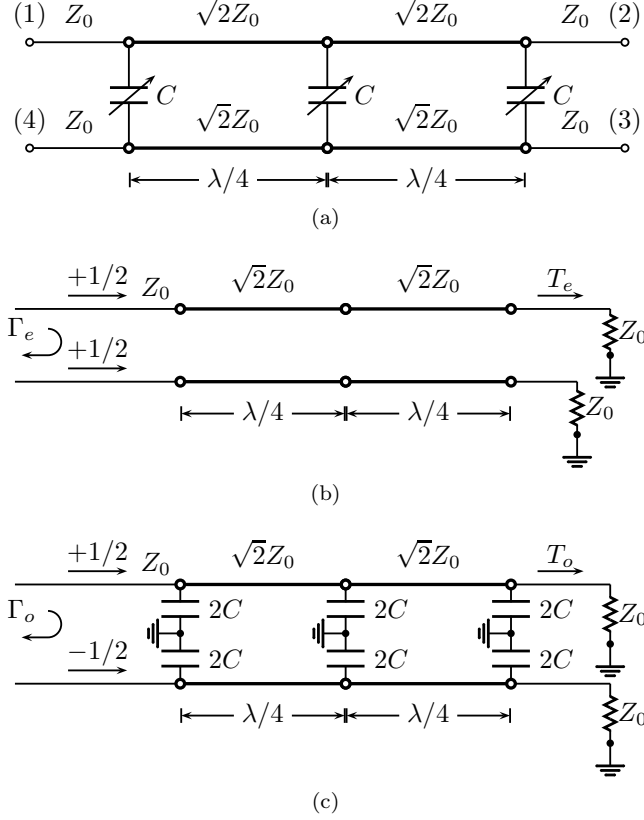


Figure 3.2: Tunable directional coupler topology (a) with the even (b) and odd (c) mode equivalent circuits where Γ_e and T_e corresponds to the even mode reflection and transmission coefficients and Γ_o and T_o corresponds to the odd mode reflection and transmission coefficients.

and the odd mode $ABCD$ matrix is given by

$$\begin{aligned}
 \begin{bmatrix} A & B \\ C & D \end{bmatrix}_o &= \begin{bmatrix} 1 & 0 \\ jB & 1 \end{bmatrix} \begin{bmatrix} 0 & jZ_0\sqrt{2} \\ j/Z_0\sqrt{2} & 0 \end{bmatrix} \begin{bmatrix} 1 & 0 \\ jB & 1 \end{bmatrix} \begin{bmatrix} 0 & jZ_0\sqrt{2} \\ j/Z_0\sqrt{2} & 0 \end{bmatrix} \begin{bmatrix} 1 & 0 \\ jB & 1 \end{bmatrix} \\
 &= \begin{bmatrix} 2B^2Z_0^2 - 1 & -j2BZ_0^2 \\ j2B(B^2Z_0^2 - 1) & 2B^2Z_0^2 - 1 \end{bmatrix}. \tag{3.3}
 \end{aligned}$$

The reflection and transmission coefficients can then be found from Table 4.2 of [53]

$$\Gamma = \frac{A + B/Z_0 - CZ_0 - D}{A + B/Z_0 + CZ_0 + D} \tag{3.4}$$

$$T = \frac{2}{A + B/Z_0 + CZ_0 + D}. \tag{3.5}$$

Substituting (3.2) and (3.3) into (3.4) and (3.5) yields the even mode reflection and transmission coefficients

given by

$$\Gamma_e = 0 \quad , \quad T_e = -1, \quad (3.6)$$

and the odd mode reflection and transmission coefficients given by

$$\Gamma_o = \frac{-B^3 Z_0^3}{B^3 Z_0^3 - j2B^2 Z_0^2 - 2BZ_0 + j} \quad (3.7)$$

$$T_o = \frac{-j}{B^3 Z_0^3 - j2B^2 Z_0^2 - 2BZ_0 + j}, \quad (3.8)$$

where $B = 4\pi fC$. The four port scattering parameters are now found from the even and odd mode transmission and reflection coefficients. Using even and odd mode analysis, if port 1 is driven the emerging wave B_n seen at the n th port is defined as

$$B_1 = \frac{1}{2}\Gamma_e + \frac{1}{2}\Gamma_o \quad (3.9)$$

$$B_2 = \frac{1}{2}T_e + \frac{1}{2}T_o \quad (3.10)$$

$$B_3 = \frac{1}{2}T_e - \frac{1}{2}T_o \quad (3.11)$$

$$B_4 = \frac{1}{2}\Gamma_e - \frac{1}{2}\Gamma_o. \quad (3.12)$$

If restrictions are imposed that the coupler be matched and isolated, the following conditions must be met

$$S_{11} = \frac{1}{2}\Gamma_o = 0 \quad (3.13)$$

$$S_{41} = -\frac{1}{2}\Gamma_o = 0. \quad (3.14)$$

This implies $B = 0$ and $T_o = -1$, however, this trivial solution does not allow for tuning the coupling given by

$$S_{21} = \frac{1}{2}(T_o - 1) = -1 \quad (3.15)$$

$$S_{31} = -\frac{1}{2}(T_o + 1) = 0 \quad (3.16)$$

The zero of the odd mode reflection coefficient from the match and isolation requirement is of third order.

Therefore, the even mode reflection coefficient can be approximated by a Taylor series expansion about $B = 0$

to second order and still satisfy the match and isolation condition approximated by

$$S_{11} = -S_{41} \approx \frac{1}{2} \left(\Gamma_o(0) + B\Gamma_o'(0) + \frac{B^2}{2}\Gamma_o''(0) \right) = 0. \quad (3.17)$$

Next, the odd mode transmission coefficient is also expanded in a Taylor series about $B = 0$ to second order.

Applying this approximation to the through and coupled port yields

$$\begin{aligned} S_{21} &\approx \frac{1}{2} \left(-1 + T_o(0) + BT'_o(0) + \frac{B^2}{2} T''_o(0) \right) \\ &= -1 + jBZ_0 + B^2 Z_0^2 \end{aligned} \quad (3.18)$$

$$\begin{aligned} S_{31} &\approx -\frac{1}{2} \left(1 + T_o(0) + BT'_o(0) + \frac{B^2}{2} T''_o(0) \right) \\ &= -jBZ_0 - B^2 Z_0^2, \end{aligned} \quad (3.19)$$

which results in a dependence on B with the requirement that B is small. Finally, the phase difference from the coupled port to the through port is given by the following approximation

$$\arg(S_{21}) = \tan^{-1} \left(\frac{BZ_0}{B^2 Z_0^2 - 1} \right) \approx \tan^{-1} (-BZ_0) \quad (3.20)$$

$$\begin{aligned} \arg(S_{31}) - \arg(S_{21}) &= \tan^{-1} \left(\frac{1}{BZ_0} \right) - \tan^{-1} (-BZ_0) \\ &= \frac{\pi}{2}. \end{aligned} \quad (3.21)$$

Equation (3.17) demonstrates the coupler is matched and isolated while the coupled and through ports are dependent on B and thus can be varied if B can be varied. Additionally, the phase difference between the coupled and through ports is 90° . These conditions are valid for B close to zero.

TUNABLE COUPLING COEFFICIENT

Solving (3.19) for B and using $C = B/4\pi f$ gives two solutions for C as a function of the magnitude of coupling, the positive solution is chosen for a capacitance

$$C = \frac{\sqrt{2 \left(\sqrt{4|S_{31}|^2 + 1} - 1 \right)}}{8\pi f Z_0}. \quad (3.22)$$

Using (3.22) for a desired tuning range of $|S_{31}|$ between -40 and -5 dB corresponds to $C = 8 - 400$ fF respectively. The accuracy of making an approximation based on a Taylor series expansion to second order is shown in Fig. 3.3. The approximation is within 0.01 dB for small values of C and is within 1 dB of the exact value for $|S_{31}|$. With an estimation on what value of C will result in the desired tuning range for

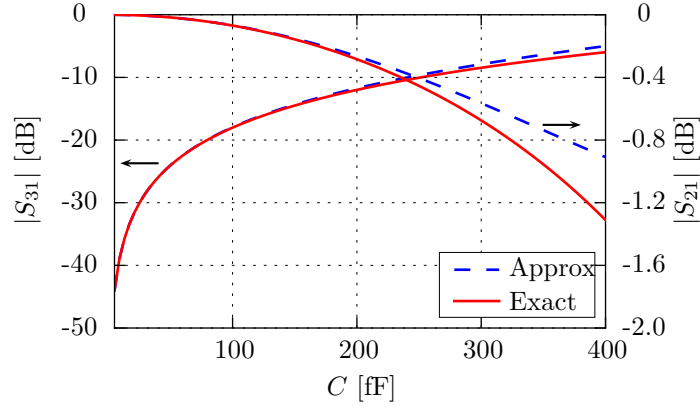


Figure 3.3: Comparison of $|S_{21}|$ and $|S_{31}|$ vs. tuning capacitance C at 2 GHz for both the exact solution (solid line) and the solution based on the Taylor series approximation (dashed line).

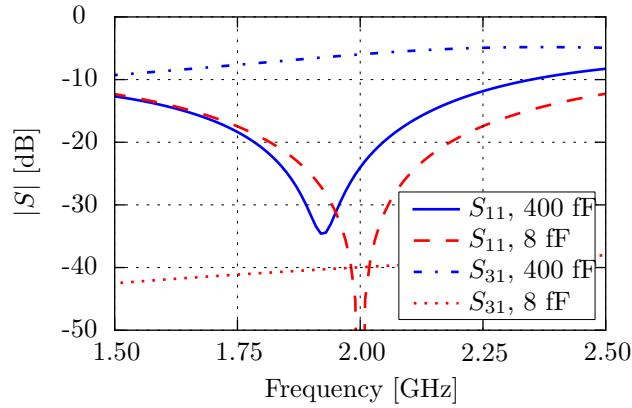


Figure 3.4: Simulated results for S_{11} and S_{31} for the tunable coupler demonstrating a tuning range of 34 dB on S_{31} while maintaining a return loss of greater than 24 dB at 2 GHz.

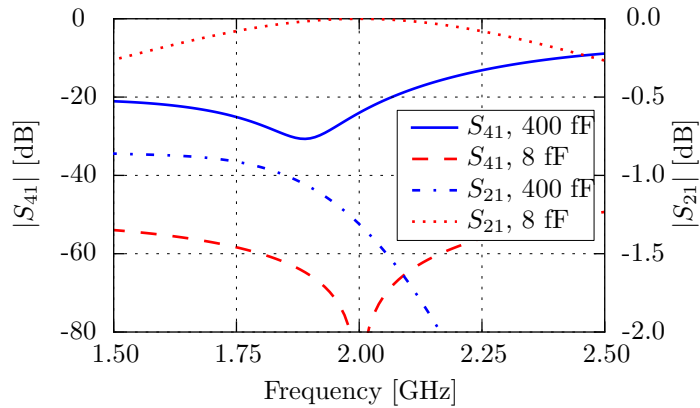


Figure 3.5: Simulated results for S_{21} and S_{41} for the tunable coupler. The insertion loss varies from 0.75 dB to 0 dB while the isolation is better than 23 dB.

the coupled port, the full four-port scattering parameters for the tunable coupler can be determined. The ideal tunable coupler was analyzed over a frequency range of 1.5 to 2.5 GHz for $C = 8$ fF and $C = 400$ fF. Fig. 3.4 demonstrates a coupling coefficient from -6 dB to -40 dB for a capacitance from 400 fF to 8 fF, while maintaining a return loss greater than 24 dB at 2 GHz.

3.2.2 MMIC COUPLER IMPLEMENTATION AND MEASURED SCATTERING PARAMETERS

The proposed MMIC tunable directional coupler schematic is shown in Fig. 3.6. Due to size constraints the $\lambda/4$ transmission lines are implemented using π -equivalent networks as seen in Fig. 3.7 with C_π and L_π to synthesize a 70.71Ω $\lambda/4$ line at 2 GHz. The values for the π -equivalent circuit are

$$C_\pi = \frac{1}{\omega_0 Z_0} \quad (3.23)$$

$$L_\pi = \frac{Z_0}{\omega_0}. \quad (3.24)$$

The variable capacitance is obtained by applying a varying bias to three depletion mode Schottky diodes (D_{var}). To reduce circuit size, on-chip bias tees were realized using an inductor and a shunt capacitor. The bias network is simplified by applying the same bias to each of the three Schottky diodes so only two DC bias lines are needed. There are four DC blocking capacitors on each port to block the DC bias from the output. This simplified bias network aids in reducing the overall size and complexity of the circuit. The tunable directional coupler was fabricated in a $0.5 \mu\text{m}$ GaAs commercial (TQS TQPED pHEMT) process. A

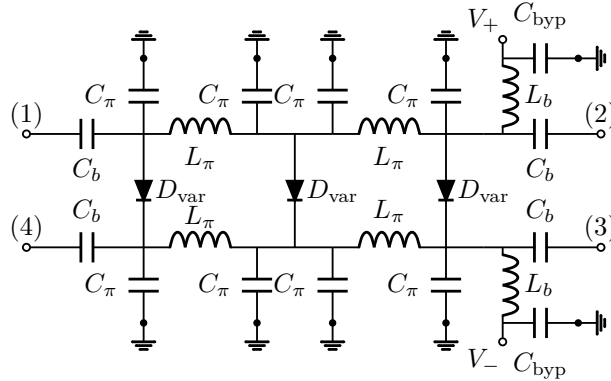


Figure 3.6: Tunable directional coupler topology.



Figure 3.7: A quarter wavelength transmission line (a) and the lumped element π equivalent circuit (b).

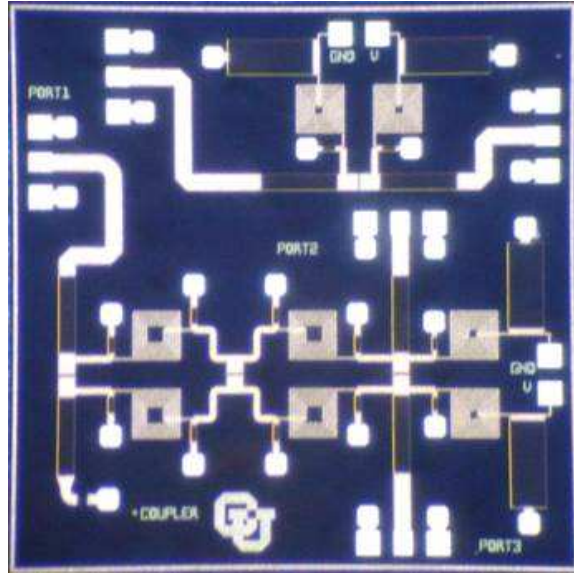


Figure 3.8: Photograph of the GaAs MMIC coupler. The chip occupies an area of $2.2 \text{ mm} \times 1.4 \text{ mm}$ neglecting probe pads and test structures.

photograph of the coupler is shown in Fig. 3.8. The chip occupies an area of $2.2 \text{ mm} \times 1.4 \text{ mm}$ neglecting probe pads and test structures. The $\lambda/4$ 70.71Ω lines were realized with two shunt metal-insulator-metal (MIM) capacitors (C_π) connected with a spiral inductor (L_π).

The MMIC tunable directional coupler was characterized by doing three separate measurements on a two-port network analyzer. The die was probed using $150 \mu\text{m}$ pitch probes with an SOLT calibration using an impedance standard substrate (ISS). The four port tunable coupler was characterized with an assumption of symmetry. The fourth or isolated port was terminated on-chip with a 50Ω resistor, the coupler was then characterized by taking three separate two port measurements with the third port terminated with a load connected to an RF probe. Three measurements were done to characterize the through port ($|S_{21}|$), coupling coefficient ($|S_{31}|$), and isolation ($|S_{41}|$). Figs. 3.9 to 3.11 shows the coupling, input match, and isolation across frequency over the bias voltage range of 0 to -1.2 V with the following conclusions of its performance at 2 GHz:

- the coupling coefficient varies from 6.6 dB to 60 dB, corresponding to a dynamic range of 53.4 dB,
- the input match of the coupler is better than 12 dB for all bias points, improving to better than 20 dB for large coupling coefficients,
- the isolation ranges from 17 dB to 40 dB as the bias decreases.

To demonstrate the performance versus the diode bias, the scattering parameters are plotted versus bias at 2 GHz as seen in Fig. 3.12.

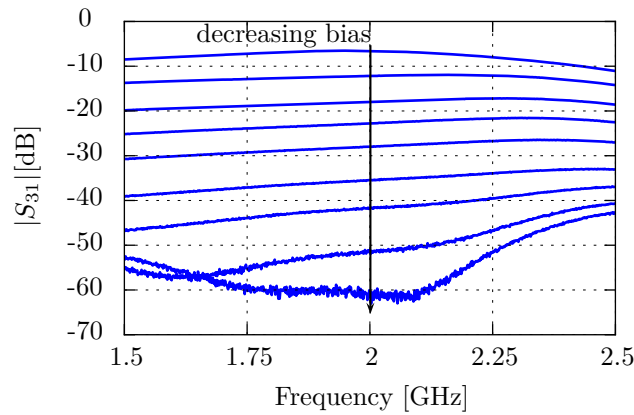


Figure 3.9: Measured S-Parameters for the coupled port demonstrating a tuning range of -6.6 dB to -60 dB at 2 GHz for $|S_{31}|$. The depletion mode diode was reverse biased so the coupling varies by decreasing the bias voltage from 0 V to -1.2 V.

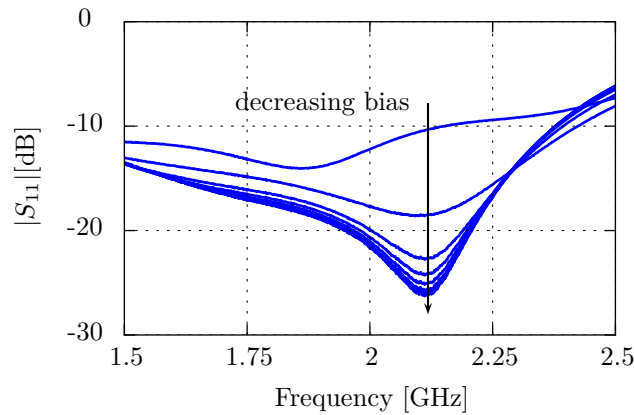


Figure 3.10: Measured input return loss for the tunable coupler demonstrating better than 12 dB return loss for all bias conditions at 2 GHz. The return loss improves to better than 20 dB over a wide coupling coefficient tuning range from 18 dB to 41 dB.

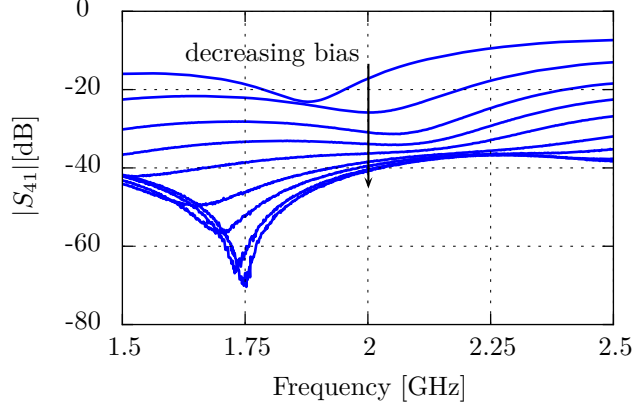


Figure 3.11: Measured isolation greater than 17 dB for all bias conditions. The isolation of the coupler improves to 40 dB with decreasing bias.

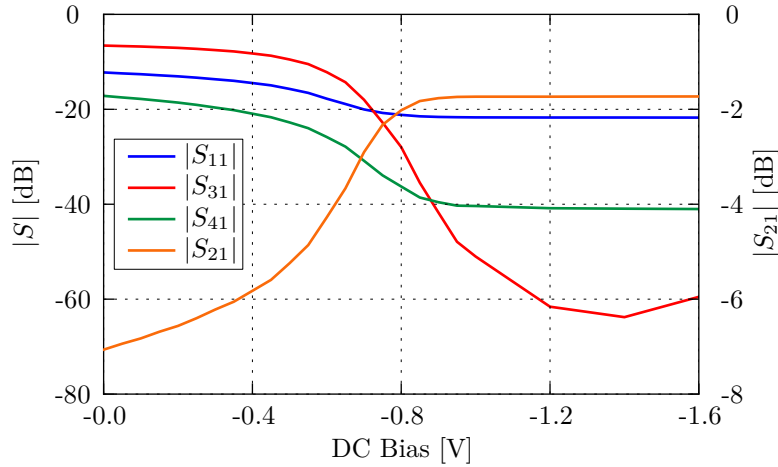


Figure 3.12: Measured tunable coupler scattering parameters at 2 GHz vs. DC bias from 0 V to -1.6 V.

3.2.3 COMPARISON TO SIMULATION

The measured results are compared to simulation at two separate bias points (0 V, and -0.8 V) in Fig. 3.13. The simulated data is determined in AWR Microwave Office from a combination of linear circuit models, 3D planar Method of Moments solver AXIEM, and non-linear circuit models. The DC blocking capacitor, π -equivalent 90° network, and bias line were simulated using AXIEM. These networks were then connected together using linear circuit models for short microstrip lines and tee junctions. Finally the diode was modeled with a non-linear model from TriQuint. The input match shown in Fig. 3.13a demonstrates simulation and measurement are within approximately 5 dB across the frequency range of 1 to 3 GHz. The through port shown in Fig. 3.13b is within 1 dB across the frequency range for the two bias points, and the coupled port is

within 2.5 dB as seen in Fig. 3.13c. Finally, the isolated port shown in Fig. 3.13d demonstrates a discrepancy between measured and simulated of 20 dB. However, the difference between -30 dB and -50 dB is a difference of 0.03.

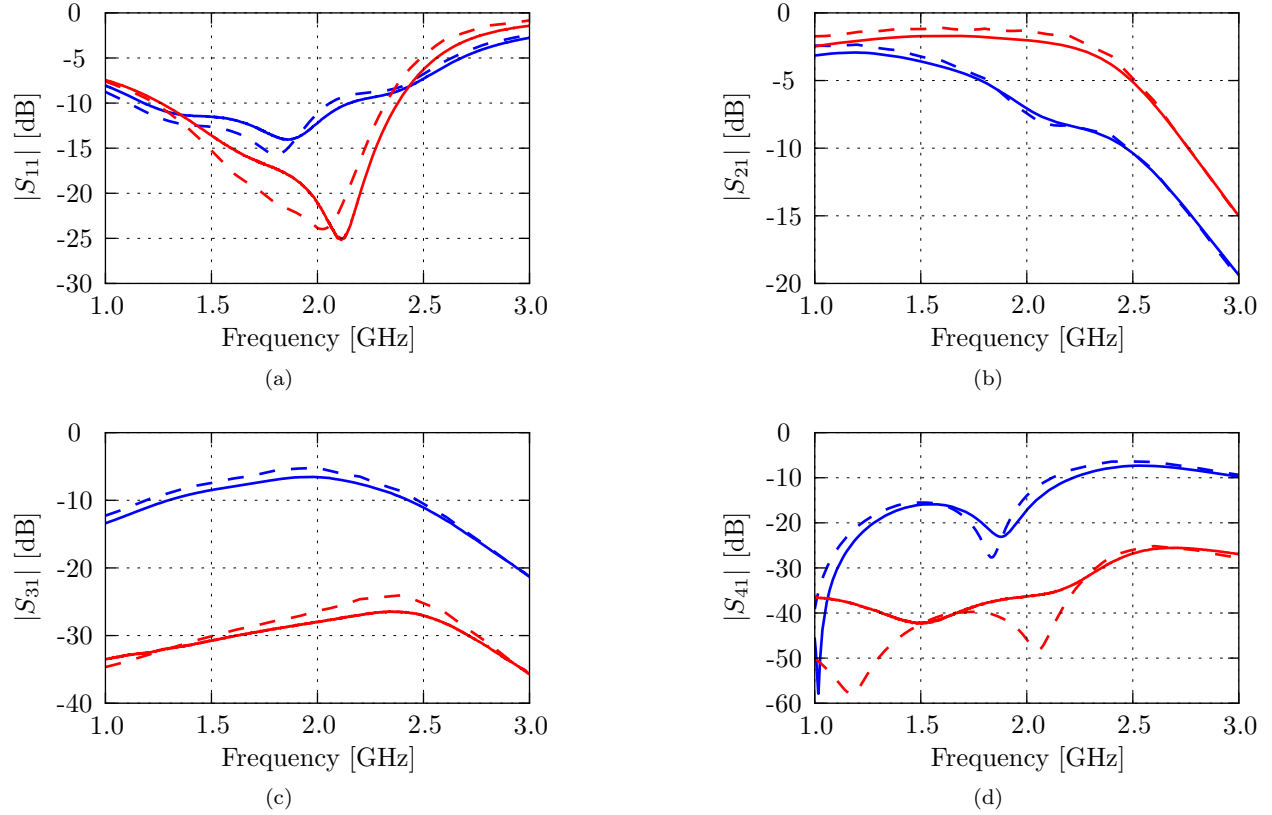


Figure 3.13: Comparison of measured (solid line) to simulated (dashed line) scattering parameters of the MMIC tunable coupler at two different bias points: 0 V (blue) and -0.8 V (red).

3.2.4 LINEARITY MEASUREMENT

A two-tone measurement was performed to characterize the linearity of the MMIC tunable directional coupler. The linearity measurement performed on the coupled path, while the isolated port was terminated on chip and the through port was terminated with a load connected to an RF GSG probe landed on the MMIC. Fig. 3.14 shows the measurement setup.

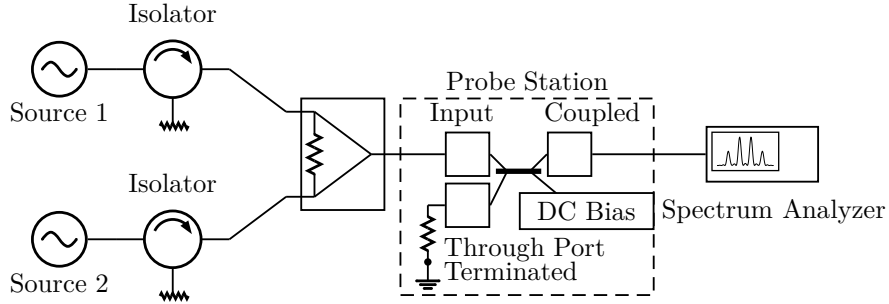


Figure 3.14: Two-tone linearity measurement setup.

Two tones spaced 1 MHz apart were injected into the coupler via RF probes. The tones were given by

$$f_1 = 1.9995 \text{ [GHz]} \quad (3.25)$$

$$f_2 = 2.0005 \text{ [GHz]}. \quad (3.26)$$

The third order products are given by

$$2f_2 - f_1 \quad (3.27)$$

$$2f_1 - f_2. \quad (3.28)$$

The IMD_3 is the ratio of the power of the third order product to the fundamental given in dBc as

$$\text{IMD}_3 = P_{o3} - P_o \text{ [dBc]}, \quad (3.29)$$

where P_o and P_{o3} are the power level at the output for the fundamental tone and third order product respectively. Using the IMD_3 , the output third-order intercept point can be calculated by

$$\text{OIP}_3 = P_o - \frac{\text{IMD}_3}{2} = \frac{1}{2}(3P_o - P_{o3}) \text{ [dBm]}. \quad (3.30)$$

The input third-order intercept point is defined as

$$\text{IIP}_3 = \text{OIP}_3 - G \text{ [dBm]}, \quad (3.31)$$

where G is the gain of the device under test. The linearity measurements are shown in Fig. 3.15 for four different DC bias points (0 V, -0.6 V, -0.7 V, and -0.8 V). It can be seen from Fig. 3.15a that the 1 dB compression point is a function of DC bias, and for larger coupling coefficients the compression happens at a lower input power level. By inspection of Fig. 3.15b the IMD3 products are much lower for smaller coupling coefficients (more power through coupled port). Finally, Figs. 3.15c and 3.15d show both the output and input third-order intercept points. The intercept points are higher for smaller coupling coefficients.

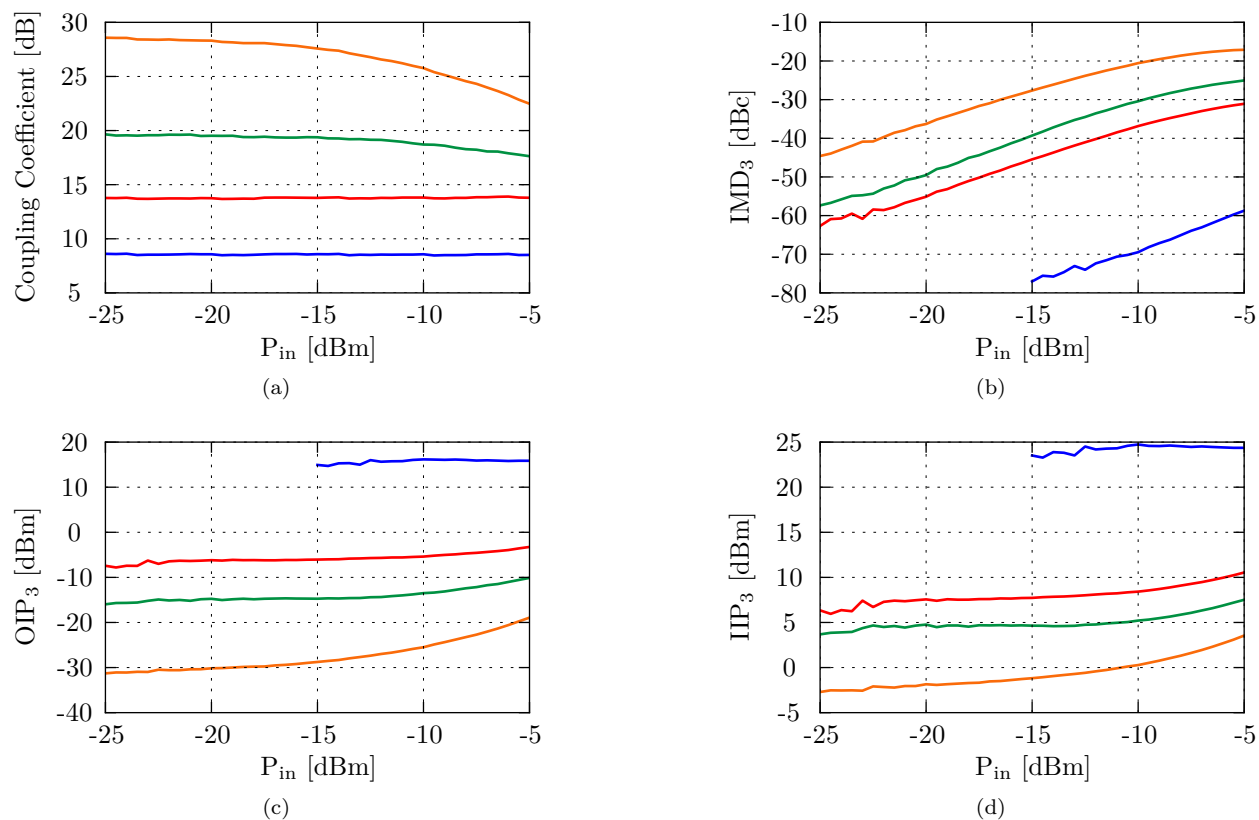


Figure 3.15: Linearity measurements for the MMIC tunable directional coupler. The different traces correspond to: Blue (0 V), Red (-0.6 V), Green (-0.7 V), Orange (-0.8 V).

3.2.5 COMPARISON TO OTHER WORK

The performance of the tunable coupler is summarized and compared to other published couplers in Table 3.1. The comparison includes two hybrid couplers [71, 72], two other MMIC CMOS couplers [75, 76], and a MEMS coupler [77]. The coupler from this work presents the largest dynamic range.

Table 3.1: Comparison of the tunable coupler from this work to others presented in the literature.

Specification	[72] 1982	[71] 2007	[75] 2008	[76] 2013	[77] 2013 ^a	This Work ([78] 2012) ^b
Technology	Hybrid	Hybrid	0.13 μm CMOS	130 nm CMOS	MEMS	0.5 μm GaAs
Frequency [GHz]	4.5	2	2.1 \Rightarrow 3.1	6.7	14	2
Coupling Range [dB]	4 \Rightarrow 20	6 \Rightarrow 10	1.4 \Rightarrow 7	-3 \Rightarrow 6	11.31 \Rightarrow 18.57	6.6 \Rightarrow 60
Input Return Loss [dB]	13 \Rightarrow 19	16.5 \Rightarrow 17.5	12.6 \Rightarrow 32	> 19	16 \Rightarrow 18	12 \Rightarrow 22
Isolation [dB]	19 \Rightarrow 49	16 \Rightarrow 35.4	41 \Rightarrow 51	15 \Rightarrow 24	48 \Rightarrow 57	17 \Rightarrow 40
Through Port [dB]	-0.15 \Rightarrow -0.5	-	-	> -1.2	-2 \Rightarrow -3	-3.6 \Rightarrow -1.7
Power Consumption [mW]	0	0	208	1 \Rightarrow 22	0	0
Size [mm ²]	12 \times 12 ^c	14.8 \times 2.3	0.73 \times 0.6	0.47 \times 0.25	1.71 \times 1.29	2.2 \times 1.4

^a This paper presented two concepts, here concept two from Table II of [77] is compared. Additionally, performance is specified based on its performance at 14 GHz not across the bandwidth from 10-18 GHz.

^b The values represent the performance at 2 GHz.

^c From [75] estimated for $\lambda/4 \times \lambda/4$ for an $\epsilon_r = 2.2$ substrate.

3.3 AN ACTIVE MMIC COLD NOISE SOURCE

This section presents an active noise source developed for a compact 1.4 GHz radiometer. Radiometers are calibrated by switching the receiver from the antenna to a load of a known temperature [1]. The calibration is demonstrated in Fig. 3.16, showing a block diagram of a two-load radiometer with hot and cold calibration standards. Cold standards are often cooled absorber loads, which tend to be large. An avalanche diode may be used as a more compact noise source. However, avalanche diodes result in a very high equivalent noise temperature, and are generally used as a hot calibration standards. A cold equivalent noise temperature can be achieved by using an active cold load (ACL), which is represented by the cold standard T_c highlighted in Fig. 3.16. An ACL noise source using a MESFET device demonstrated a temperature of 48 K at 1.4 GHz [79]. Other hybrid designs have been done utilizing GaAs and InP FETs [80] and SiGe HBT [81]. MMIC designs of active cold loads from 2 GHz to 26 GHz are presented in [82]. In addition to presenting designs that achieve a cold equivalent noise temperature, the stability of ACLs has also been investigated. Long term drift of two X-band ACLs ranging in absolute temperature from 55 K to 77 K was estimated to be 1.5 K/year [83]. An 18 GHz ACL with an equivalent noise temperature of 126 K demonstrated a measured drift of 2 K/year [84]. Finally, intermediate term stability has been measured for an 83 K L-band ACL demonstrating a drift of 1.1 mK/day [85]. Although hybrid designs have been done below 2 GHz, to the author's knowledge no MMIC designs have been presented at these frequencies.

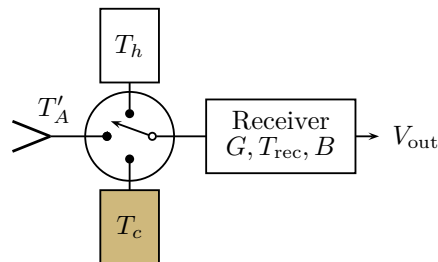


Figure 3.16: Two-load radiometer with hot T_h and cold T_c standards. The highlighted portion could be an ACL in which T_c would be colder than its physical temperature.

3.3.1 NOISE SOURCE MODEL

The theory presented in [86] gives an expression for the output noise power seen at the input of the transistor and is given here for completeness. The incident noise temperature at plane 1 of Fig. 3.17 can be expressed as

$$T_{s,1} = T_b + [(T_1 (1 - |\Gamma_S|^2) + T_a) G_{21} |\Gamma_L|^2 + T_2 (1 - |\Gamma_L|^2)] G_{12} \quad [\text{K}], \quad (3.32)$$

where T_2 is the temperature of the termination and T_1 is the temperature of the system connected to the

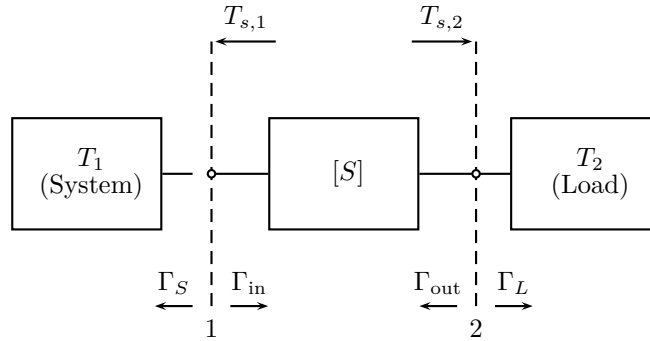


Figure 3.17: Two port noise source schematic with the amplifier represented by its two port scattering parameters. The noise temperature $T_{s,1}$ is incident on the input plane 1 and the noise temperature $T_{s,2}$ is incident on the output plane 2.

input of the transistor. G_{12} and G_{21} are power gains calculated from the S -parameters of the transistor. The alternate noise parameters T_a and T_b are given by [86]

$$T_a = T_{e(\min)} + \frac{T_k |\Gamma'_{\text{opt}}|^2}{1 - |\Gamma'_{\text{opt}}|^2} \quad [\text{K}] \quad (3.33)$$

$$T_b = \frac{T_k}{1 - |\Gamma'_{\text{opt}}|^2} - T_{e(\min)} \quad [\text{K}], \quad (3.34)$$

where $T_{e(\min)} = T_0(F_{\min} - 1)$ and $T_k = 4T_0 R_n G_{\text{opt}}$ where R_n is the equivalent noise resistance and G_{opt} is the optimum noise conductance for the transistor. Γ'_{opt} for an unmatched load is related to Γ_{opt} by

$$\Gamma'_{\text{opt}} = \frac{\Gamma_{\text{in}}^* - \Gamma_{\text{opt}}}{\Gamma_{\text{opt}} \Gamma_{\text{in}} - 1}. \quad (3.35)$$

The input and output matching/bias networks as seen in Fig. 3.18 must be designed to transform source and load impedances to present the necessary Γ_S and Γ_L to the device. The noise power $T_{s,1}$ incident on plane 1 given in (3.32) will be minimized by appropriate circuit design. To minimize $T_{s,1}$, first the optimum noise

match condition is utilized by designing an input matching network such that $\Gamma_S = \Gamma_{\text{opt}}$. The input power match condition is satisfied then by $\Gamma_{\text{in}} = \Gamma_{\text{opt}}^*$. To achieve the input power match condition the reflection coefficient at the output of the transistor must be

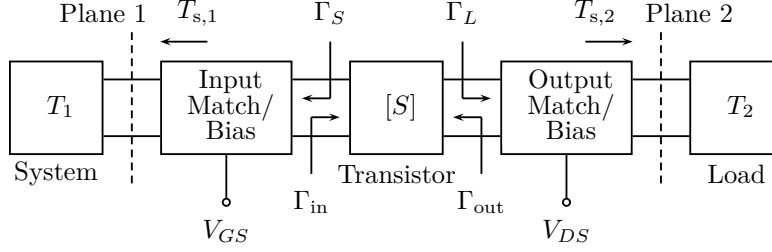


Figure 3.18: Block diagram for the ACL design showing the input and output matching and bias networks necessary for the design in which the input of the device is presented with Γ_S and the output of the device is presented with Γ_L .

$$\Gamma_L = \frac{\Gamma_{\text{opt}}^* - S_{11}}{S_{12}S_{21} + S_{22}(\Gamma_{\text{opt}}^* - S_{11})} \quad (3.36)$$

The input power match condition will result in $\Gamma'_{\text{opt}} = 0$ which can be used to simplify (3.32) to

$$T_{s,1} = T_k - T_{e(\text{min})} + [(T_1(1 - |\Gamma_S|^2) + T_{e(\text{min})})G_{21}|\Gamma_L|^2 + T_2(1 - |\Gamma_L|^2)]G_{12}. \quad (3.37)$$

The simplified expression is minimized with respect to $|\Gamma_L|$ by solving $\partial T_{s,1}/\partial |\Gamma_L| = 0$ where

$$\frac{\partial T_{s,1}}{\partial |\Gamma_L|} = 2 [(T_1(1 - |\Gamma_S|^2) + T_{e(\text{min})})G_{21} + T_2]G_{12}|\Gamma_L| \quad (3.38)$$

Therefore, minimizing $T_{s,1}$ under the conditions of optimum noise match and input power match is done by minimizing $|\Gamma_L|$. The minimum will occur as $|\Gamma_L| \rightarrow 0$. Under this condition, the reflection coefficient looking into the transistor is $\Gamma_{\text{in}} = S_{11}$. When $\Gamma_L = 0$ the input power match condition dictates that $\Gamma_{\text{opt}} = S_{11}^*$. This can be satisfied by altering the S -parameters of the device which can be done by changing the bias point or varying the source inductance. Therefore the minimum achievable temperature $T_{s,1(\text{min})}$ is

$$T_{s,1(\text{min})} = T_k - T_{e(\text{min})} + T_2G_{12}, \quad (3.39)$$

demonstrating the minimum depends on the device noise parameters, the load temperature T_2 and G_{12} of the device. It must be noted, however, that in the actual implementation the loss in the input network will also contribute to the noise temperature.

3.3.2 MINIMIZED $T_{s,1}$ EXAMPLE

To demonstrate $T_{s,1}$ is minimized when the input power match condition requirement on $|\Gamma_L| \rightarrow 0$, two separate bias points were considered for a TriQuint $0.5 \mu\text{m}$ GaAs pHEMT device. Simulations were carried out using AWR Microwave Office and the device was modeled with TriQuint's nonlinear TOM3 model. A $300 \mu\text{m}$ gate periphery TriQuint device was biased at two different gate bias points ($V_{GS} = 0.5 \text{ V}$, $V_{GS} = 0.788 \text{ V}$) while the drain was biased at $V_{DS} = 1.7 \text{ V}$. An ideal inductor was placed on the source of the transistor and its inductance was varied. The device, source, and load temperatures are assumed to be at 298 K . The input is assumed to be matched to Γ_{opt} and the output reflection coefficient is given in (3.36) to achieve an input power match. Fig. 3.19 demonstrates a minimum in $T_{s,1}$ is achieved when the magnitude of the load reflection coefficient Γ_L from (3.36) is minimized. For a gate bias of $V_{GS} = 0.788 \text{ V}$ a minimum occurs with a source inductance of 1.03 nH corresponding to $T_{s,1} = 19 \text{ K}$ and $|\Gamma_L| = -58.4 \text{ dB}$ which is approximately zero. If $|\Gamma_L| = 0$ then the following relation is true $\Gamma_{\text{opt}} \approx S_{11}^*$. If Γ_L is not zero, a minimum in $T_{s,1}$ will still occur when $|\Gamma_L|$ is minimized. This is demonstrated in Fig. 3.19 for a gate bias of $V_{GS} = 0.5 \text{ V}$ and a source inductance of 1.95 nH corresponding to $T_{s,1} = 304.4 \text{ K}$ and $|\Gamma_L| = -13.3 \text{ dB}$.

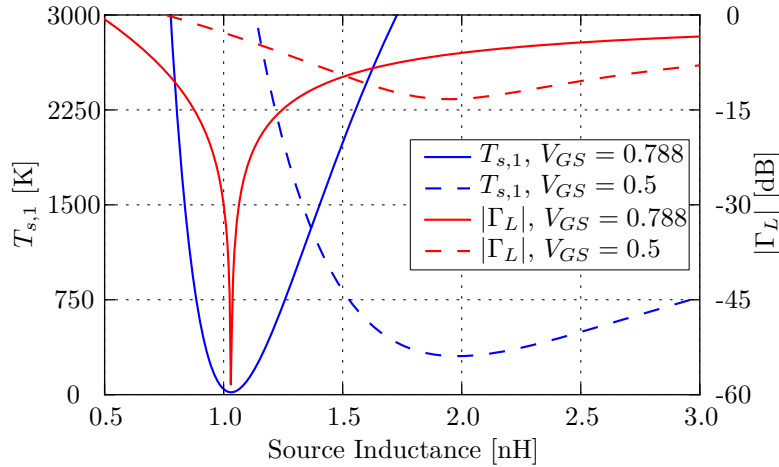


Figure 3.19: Simulated $T_{s,1}$ and $|\Gamma_L|$ calculated from (3.36) for a TriQuint $0.5 \mu\text{m}$ pHEMT device. The transistor was biased at 1.7 V on the drain and the ideal source inductance was varied from 0.5 nH to 3 nH for two different gate biases corresponding to 0.5 V and 0.788 V . A minimum in $T_{s,1}$ is achieved when $|\Gamma_L|$ is minimized.

The lowest value for $T_{s,1}$ was achieved for the gate bias point of $V_{GS} = 0.788 \text{ V}$ by varying the source inductance such that $\Gamma_{\text{opt}} \approx S_{11}^*$. The conjugate of the device input reflection coefficient S_{11}^* along with

the optimum noise reflection coefficient for the two bias points vs. source inductance from 0.5 nH to 3 nH are plotted on a Smith chart shown in Fig. 3.20. It is seen that S_{11}^* and Γ_{opt} are approximately equal ($S_{11}^* \approx \Gamma_{\text{opt}} \approx 0.586 + j0.224$) at a point corresponding to 1.03 nH which is the source inductance corresponding to a minimum in $T_{s,1}$. If the two are equal the input to the noise source is matched and the load should be terminated in a matched load. This is not the case for a gate bias of $V_{GS} = 0.5$ V and therefore Γ_L is not zero for an input power match.

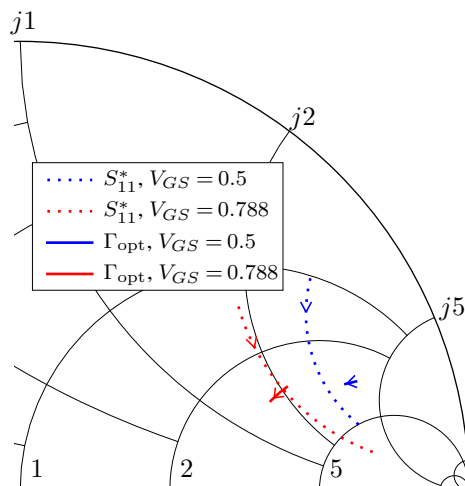


Figure 3.20: The optimum noise match (Γ_{opt}) and conjugate of device input reflection coefficient vs. ideal source inductance ranging from 0.5 to 3 nH for two different gate bias points ($V_{GS} = 0.5$ V and $V_{GS} = 0.788$ V) with the drain biased at $V_{DS} = 1.7$. For the gate bias $V_{GS} = 0.788$ V S_{11}^* and Γ_{opt} are approximately equal ($S_{11}^* \approx \Gamma_{\text{opt}} \approx 0.586 + j0.224$) for a source inductance of 1.03 nH. The Smith chart is normalized to 50Ω .

3.3.3 GAAS MMIC NOISE SOURCE DESIGN

To design an ACL with a minimum noise temperature the following procedure is applied:

1. Select a bias point for the transistor and determine the scattering and noise parameters for the biased transistor.
2. Calculate Γ_L from (3.36) and vary the source inductance to find a minimum for the calculated value of $T_{s,1}$ and $|\Gamma_L|$.
3. Design output matching network to meet the condition for Γ_L given by (3.36).
4. Design the input matching network such that $\Gamma_S = \Gamma_{\text{opt}}$.

The design procedure can be iterated for different bias points such that a minimum in $T_{s,1}$ and $|\Gamma_L|$ can be attained.

To develop a compact cold calibration load for a 1.4 GHz wearable microwave radiometer system, the design procedure above was applied to a TriQuint 0.5 μm GaAs pHEMT with 300 μm gate periphery using TriQuint's nonlinear TOM3 model biased at $V_{GS} = 0.72\text{ V}$ and $V_{DS} = 1.7\text{ V}$. The source inductance was varied to achieve a minimum in $|\Gamma_L|$. An inductor was designed and simulated using the 3D planar Method of Moments solver AXIEM available in AWR Microwave Office. Once a minimum in $|\Gamma_L|$ was achieved the cold noise source could be designed by matching the input and placing bias tees at the input and output as seen in Fig. 3.21. The input network and bias tee were simulated in AXIEM. The match was achieved using a shunt capacitor and series inductor. The bias line consisted of a shunt capacitor and series inductor to achieve a 90° phase shift and an RF shorting capacitor, and finally a series capacitor was placed to block DC.

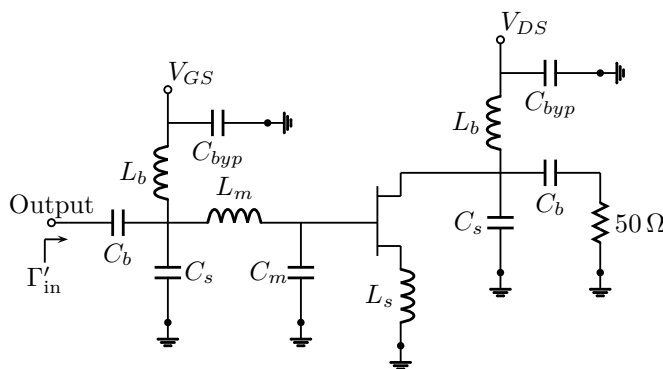


Figure 3.21: Schematic of the active cold noise source. Additional source inductance was added such that the optimum load impedance is $50\ \Omega$ such that no output matching network is needed.

Fig. 3.22 shows the source reflection coefficient, optimum noise match, and transistor S_{11}^* . The input network is designed as a compromise between input power match and noise match which can be seen by the markers placed at 1.4 GHz. Additionally, the reflection coefficient looking into the noise source (Γ'_{in}) is plotted to demonstrate the input match is better than 25 dB at 1.4 GHz denoted by the marker. The output was terminated in a $50\ \Omega$ bias tee.

To determine the value of $T_{s,1}$ at the output of the MMIC, (3.32) was used. After placing the simulated input and output networks on the transistor biased at $V_{GS} = 0.72\text{ V}$ and $V_{DS} = 1.7\text{ V}$, the whole ACL is considered as a 2 port network characterized by its S -parameters and noise parameters (same as that depicted

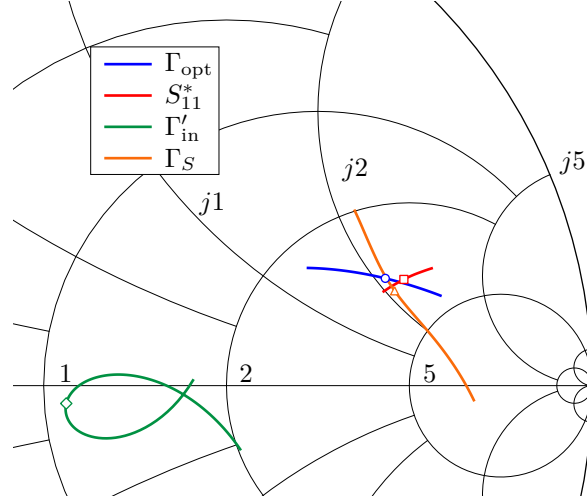


Figure 3.22: Simulated optimum noise match and the conjugate of the reflection coefficient looking into the device are shown along with the reflection coefficient looking towards the source (Γ_S) through the input match and bias network vs. frequency from 1 to 2 GHz. The input match is shown looking into the noise source (Γ'_{in}). The Smith chart is normalized to 50Ω , and the markers on the plot correspond to 1.4 GHz.

in Fig. 3.17). These are determined in simulation by combining the AXIEM simulations with the nonlinear TOM3 model. $T_{s,1}$ is determined assuming the source and load are terminated in the system impedance ($\Gamma_S = \Gamma_L = 0$). The resulting equivalent noise temperature and input match of the MMIC ACL are shown in Fig. 3.23 demonstrating a $T_{s,1} = 70.9 \text{ K}$ with an input match of -27 dB at 1.4 GHz. The final layout of the chip is shown in Fig. 3.24 where the dimensions of the chip are $2.5 \text{ mm} \times 2.5 \text{ mm}$.

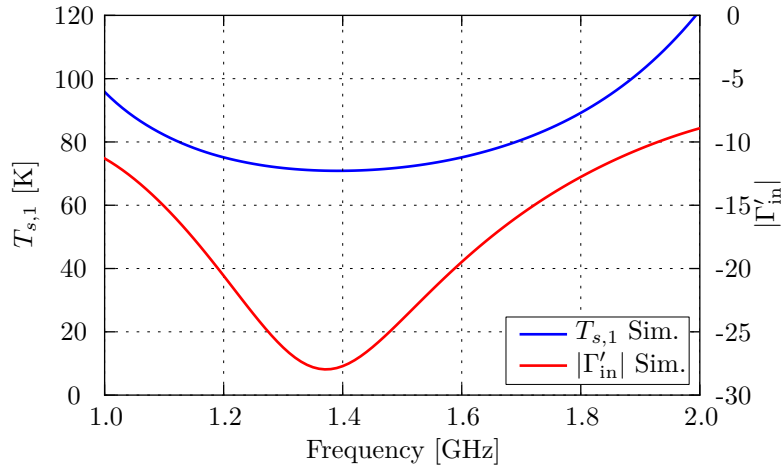


Figure 3.23: Simulated $T_{s,1}$ and input match of the MMIC ACL demonstrating a $T_{s,1} = 70.9 \text{ K}$ with an input match of -27 dB at 1.4 GHz.

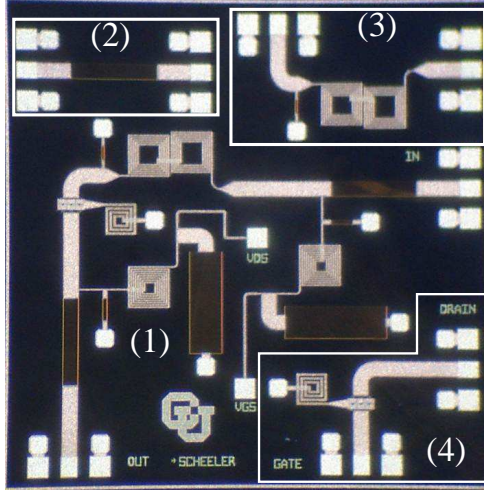


Figure 3.24: Photo of the 1.4 GHz GaAs MMIC. The noise source with the input and output bias tees and input matching network is labeled by (1). The test circuits are a blocking capacitor (2), input matching network (3), and transistor test circuit (4).

3.3.4 GAAS MMIC NOISE SOURCE EXPERIMENTAL RESULTS

The MMIC shown in Fig. 3.24 was placed on a microwave substrate carrier and connected with bond wires. The board was then placed in a shielded box and the input of the cold noise source was connect to an SMA connector. The MMIC was measured at the National Institute for Standards and Technology (NIST) using an automated coaxial radiometer system (NFRad). First, the input match of the noise source was measured to correct the raw noise measurements due to mismatch. The noise source demonstrated a measured equivalent noise temperature of less than 90 K from 1.3 GHz to 1.5 GHz. Some of the temperature increase is due to parasitics from placing the MMIC on a carrier. If the packaging parasitics are accounted for along with an additional 220 pF of source inductance the simulated temperature is approximately 75 K as opposed to the original simulation without parasitics which was 71 K. The comparison between simulated and measured equivalent noise temperature and input reflection coefficient is shown in Fig. 3.25. The measured input match is better than simulation, and the temperature $T_{s,1}$ is within 6 to 15 K (8% to 17%) of simulation.

3.4 CONCLUSIONS

This chapter presented two new circuit elements that could aid in the design of a radiometer on a single chip. The first circuit design was a MMIC tunable directional coupler with 53 dB of dynamic range for the

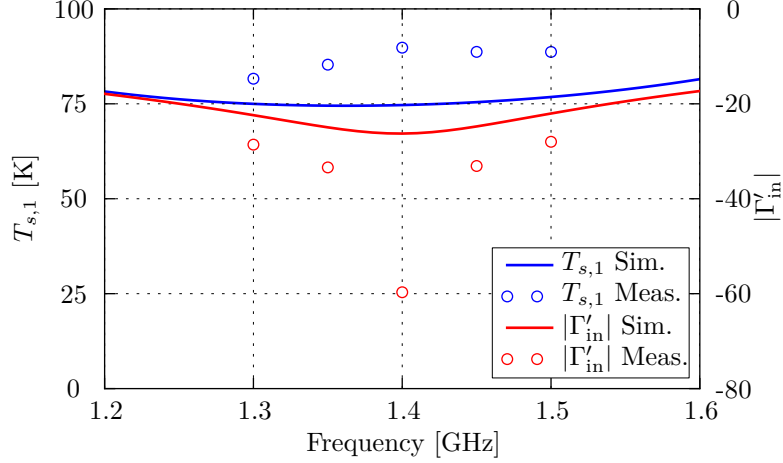


Figure 3.25: Measured $T_{s,1}$ and reflection coefficient of the packaged MMIC noise source demonstrating an equivalent noise temperature of approximately 90 K while maintaining an input reflection coefficient of less than -50 dB at 1.4 GHz.

coupling coefficient over a voltage supply range of 1.2 V. The coupler was first analyzed with ideal elements to determine the range of capacitances necessary to achieve a desired tuning range. The chip occupies a total area of $2.2 \text{ mm} \times 1.4 \text{ mm}$. The chip was comprised of three Schottky diodes to achieve tuning and π -equivalent $\lambda/4$ transmission lines. The input match and isolation of the coupler was better than 12 dB and 17 dB respectively for all bias points. The second circuit was an active cold noise source. A design procedure for obtaining a minimum equivalent noise temperature of an active cold load was presented utilizing the equations given in [86]. An example was shown demonstrating a minimum in $T_{s,1}$ for two different bias points of a TriQuint $0.5 \mu\text{m}$ GaAs pHEMT device using TriQuint's nonlinear TOM3 model. The procedure was applied to a 1.4 GHz GaAs MMIC designed for a wearable microwave radiometer for core body temperature measurement. The packaged MMIC demonstrated an equivalent noise temperature of less than 90 K from 1.3 GHz to 1.5 GHz while maintaining a return loss greater than 28 dB.

CHAPTER 4

NEAR-FIELD PROBE ANALYSIS

CONTENTS

4.1	Introduction	73
4.2	Hertz Vector Potentials for a Stratified Medium	76
4.2.1	Spectral Domain Analysis of the Hertz Potentials	80
4.2.2	Input Impedance of a Dipole	85
4.3	Power Flow and Sensing Depth	87
4.4	Algorithm Verification	91
4.4.1	Comparison to Published Works	92
4.4.2	Theoretical Results	94
4.5	Dipole on Skin, Fat, and Muscle	99
4.6	Conclusion	104

4.1 INTRODUCTION

Of critical importance for both receiving and transmitting near-field medical applications is accurate knowledge of the power within a few wavelengths of the antenna. The dipole antenna receives thermal power radiated by the tissue layers situated in the near field, and therefore it is more appropriate to think of the dipole as

a transducer. The received power is filtered by the dipole impedance with a pre-detection bandwidth Δf , and in this Chapter we are considering a narrowband response where the fractional bandwidth (FBW) is less than four percent. The dipole feed is connected to a total power radiometer as shown in Fig. 4.1. The signal is received using a square-law detector and an integrator with an integration time τ . To measure the temperature of, e.g., a portion of the muscle, it is necessary to find the portion of the power received by the antenna due to the specific heated muscle, relative to the total received thermal power. This in turn will depend on the imaginary part of the permittivity of the tissues, as well as on the thicknesses and real part of the permittivity. To this end, an improved *sensing depth* metric is defined, and its dependence on tissue parameters is shown. Typical values for the dielectric properties of human tissues are given in Table 4.1. The values presented in Table 4.1 are gathered from the IFAC-CNR online resource for dielectric properties of human tissues [28]. This data is generated using a four dispersion Cole-Cole model [27] that was fitted for various tissues using data from literature [25, 26]. As an example of the variability of human tissues, two sources of measured dielectric properties of human skin will be compared. The dielectric properties of skin were measured by Gabriel et al. [87] on the ventral (towards the abdomen) part of the forearm, and on various parts of the human body using the coaxial probe method by Grant et al. [88]. The data is compared in Table 4.2 at 1 GHz. Grant et al. also mentioned 95% confidence intervals of less than 0.6 for both the real and imaginary parts of the relative complex permittivity. The motivation for measuring the dielectric properties of skin at different places on the body was for the application of hyperthermia treatment. The variation in the data (up to 26% for ϵ'_r and 30% for $\tan \delta$) from one part of the body to another is most likely due to the subcutaneous tissues as the probe penetration is approximately 7 mm [88]. For the neck and abdomen, fat is located below the skin and has a low water content thus a lower ϵ'_r , where as the palm is vascular and muscle is located below the skin leading to a higher ϵ'_r and a higher loss [88].

In the literature, simplified models of electromagnetic waves propagating through tissues are used that assume a plane wave with an exponentially decaying field [18, 39], or are determined by a 3-D electromagnetic simulation software. Here, a spectral domain analysis is applied to this problem of a dipole for passive near-field radiometry, and it is demonstrated that simple propagation models cannot be used to accurately predict the physical temperature through inversion of the radiometric measurements.

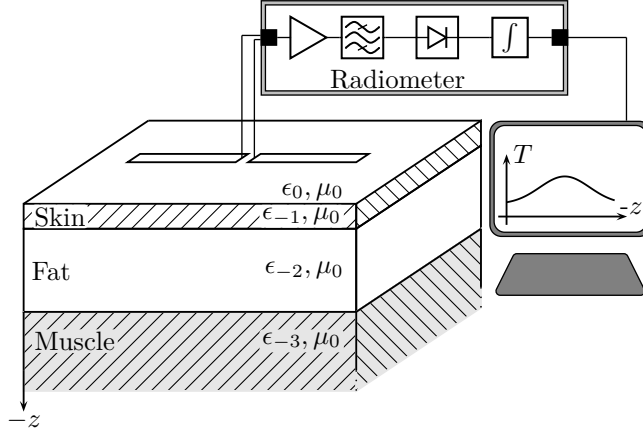


Figure 4.1: Dipole probe placed on the skin connected to a microwave radiometer to measure sub-surface tissue temperature. The tissues are represented by layers of complex permittivity dielectrics ($\epsilon = \epsilon' - j\epsilon''$).

Table 4.1: Dielectric properties of human tissues at microwave frequencies [25, 26, 28].

Tissue	Dielectric Property	Frequency [GHz]				
		0.5	1	1.5	2	2.5
Skin	ϵ_r	44.92	40.94	39.43	38.57	37.95
	$\tan \delta$	0.58	0.40	0.33	0.29	0.28
Fat	ϵ_r	5.54	5.45	5.38	5.33	5.27
	$\tan \delta$	0.28	0.18	0.15	0.14	0.15
Muscle	ϵ_r	56.45	54.81	53.96	53.29	52.67
	$\tan \delta$	0.52	0.32	0.26	0.25	0.24

A common antenna for near-field microwave thermometry is a waveguide aperture and has widely been investigated for radiating into stratified biological tissues [24, 89, 90]. In near-field microwave radiometry for temperature measurements, multiple frequencies are used to achieve spatial resolution. The sensing depth is dictated by the frequency that achieves the deepest sensing, which is often assumed to be the lowest frequency. This assumption is accurate for plane waves propagating in a lossy medium, however, this is not always the case for near-field antennas as demonstrated by Cheever et al. [40] for small waveguide apertures. A printed dipole probe is more useful than a waveguide when size, flexibility, and cost are requirements as for a portable microwave thermometer.

Human tissues are often approximated by multi-layer planar dielectrics [24, 50, 89, 90]. It is important to note that the tissue thicknesses will vary from person to person, especially the thickness of the fat layer. This variability is a challenge that must be overcome not only for impedance matching the probe, but also for the inverse problem of determining the temperature. One method to deal with the problem of tissue variability

Table 4.2: Dielectric properties of human skin at 1 GHz on various parts of the body [87,88].

Location	ϵ'_r	$\tan \delta$
Forearm (ventral) [87]	44.56	0.41
Palm [88]	43.5	0.41
Temple (forehead) [88]	34.7	0.31
Neck (thyroid) [88]	30.2	0.28
Abdomen (liver) [88]	31.7	0.28

would be to have a library of probes that would be used on subjects with specific tissue thicknesses. There would be a finite set of categories in which subjects would be placed into, and a probe would be selected based on this categorization.

Previously developed spectral domain analysis methods are adapted to the case of a receiving dipole in the presence of a stratified tissue medium. Assuming the dipole is matched to a radiometer with a finite sensitivity, sensing limitations are determined as a function of frequency, tissue properties, and thickness. The analysis of dipoles in stratified media have been investigated in the context of multi-substrate microstrip antennas and transmission lines [91, 92]. Spectral domain methods to determine the fields as a superposition of TE and TM fields have been used to investigate dipoles in stratified media [91–93] and dipoles on a lossy half-space [60]. Galejs [93, 94] and Dvorak et al. [95] utilized Hertz vector potentials to determine the fields, and are used in this paper since they are appropriate for inhomogeneous lossy dielectrics.

In the next section, the problem of a dipole in a stratified medium is defined, and the fields are determined by a spectral domain analysis. The input impedance of a dipole is determined by a variational method using an approximate current density. This enables finding the Poynting vector, used to define a sensing depth for the purpose of a medical microwave radiometer.

4.2 HERTZ VECTOR POTENTIALS FOR A STRATIFIED MEDIUM

Consider the idealized stratified medium describing tissue layers in Fig. 4.2 that consists of layers of constant-thickness complex dielectrics that are infinite in x and y and bounded in z . A current element denoted by the surface current density \mathbf{J}_s is located at the interface between two layers ($i = 1$ and $i = -1$). The spectral domain Hertz vector potentials used in [93–96] will be applied to this problem. This stratified approximation

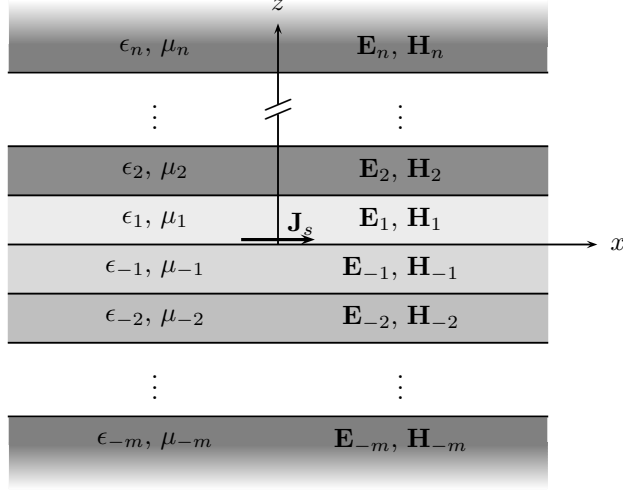


Figure 4.2: Stratified media consisting of layers of complex permittivity materials with current source $\mathbf{J}_s = J_x \mathbf{a}_x + J_y \mathbf{a}_y$ at $z = 0$. The source is embedded at the interface between layers $i = 1$ and $i = -1$. It is assumed that layers n and $-m$ extend to ∞ and $-\infty$ respectively.

is an appropriate approximation as the dipoles will only be receiving power from a narrow field of view as demonstrated by the SAR plots in Section 2.5.

The derivation of the Hertz vector potentials follows that of [96, Chapter 1], and is presented here (with different notation) for completeness. In radiation problems consisting of layered media it is convenient to use higher order Transverse Electric (TE) and Transverse Magnetic (TM) modes rather than the fundamental Transverse Electromagnetic (TEM) mode as the fundamental mode cannot satisfy all the boundary conditions [31, pp. 269], [96, pp. 34]. The solution of the fields will be given in terms of a superposition of TE and TM (to z) modes. The TE to z mode will have no electric field in the z direction, likewise, the TM to z mode will have no magnetic field in the z direction. For this reason Whittaker potentials (Hertz vectors with only z -components) will be used. The Whittaker potentials are defined as

$$\mathbf{\Pi}_e = \mathbf{a}_z V, \quad \mathbf{\Pi}_m = \mathbf{a}_z U, \quad (4.1)$$

where the subscripts e and m denote the electric and magnetic Hertz potentials respectively. Since $\nabla \cdot \mathbf{H} = 0$, \mathbf{H} can be written in terms of the curl of an arbitrary vector potential $\mathbf{\Pi}_e$ as

$$\mathbf{H} = j\omega\epsilon\nabla \times \mathbf{\Pi}_e. \quad (4.2)$$

Substituting (4.2) into Maxwell's equation gives

$$\nabla \times \mathbf{E} = k^2 \nabla \times \mathbf{\Pi}_e, \quad (4.3)$$

where $k^2 = \omega^2 \mu \epsilon$. Grouping terms of (4.3) yields the following form

$$\nabla \times (\mathbf{E} - k^2 \mathbf{\Pi}_e) = 0. \quad (4.4)$$

Noting the curl of the gradient of a scalar (ϕ_e) is equal to zero and solving for \mathbf{E} gives

$$\mathbf{E} = k^2 \mathbf{\Pi}_e + \nabla \phi_e. \quad (4.5)$$

Next, taking the curl of both sides of (4.2) yields

$$\nabla \times \mathbf{H} = \nabla \times \nabla \times (j\omega \epsilon \mathbf{\Pi}_e). \quad (4.6)$$

Applying the vector identity $\nabla \times \nabla \times \mathbf{A} = \nabla(\nabla \cdot \mathbf{A}) - \nabla^2 \mathbf{A}$ to (4.6) gives

$$\nabla \times \mathbf{H} = j\omega \epsilon (\nabla(\nabla \cdot \mathbf{\Pi}_e) - \nabla^2 \mathbf{\Pi}_e). \quad (4.7)$$

Also, substituting (4.5) into Ampère's law gives

$$\begin{aligned} \nabla \times \mathbf{H} &= j\omega \epsilon \mathbf{E} + \mathbf{J} \\ &= j\omega \epsilon (k^2 \mathbf{\Pi}_e + \nabla \phi_e) + \mathbf{J}, \end{aligned} \quad (4.8)$$

for an electric current density \mathbf{J} . Substitution of the right hand side of (4.8) into the left hand side of (4.7) yields

$$\nabla(\nabla \cdot \mathbf{\Pi}_e) - \nabla^2 \mathbf{\Pi}_e = k^2 \mathbf{\Pi}_e + \nabla \phi_e + \frac{\mathbf{J}}{j\omega \epsilon}. \quad (4.9)$$

The definition of a vector requires the specification of both its curl and divergence. Since both $\nabla \cdot \mathbf{\Pi}_e$ and ϕ_e are both arbitrary, a Lorenz type gauge condition may be introduced such that $\nabla \cdot \mathbf{\Pi}_e = \phi_e$ which yields the homogeneous vector Helmholtz equation

$$\nabla^2 \mathbf{\Pi}_e + k^2 \mathbf{\Pi}_e = -\frac{\mathbf{J}}{j\omega \epsilon}. \quad (4.10)$$

Additionally, by introduction of the gauge, the electric field may be written in terms of the electric Hertz vector potential as

$$\mathbf{E} = \nabla(\nabla \cdot \mathbf{\Pi}_e) + k^2 \mathbf{\Pi}_e. \quad (4.11)$$

The magnetic Hertz vector potential is defined in a similar manner as

$$\mathbf{E} = -j\omega\mu\nabla \times \mathbf{\Pi}_m. \quad (4.12)$$

By satisfying the Lorenz gauge, the homogeneous vector Helmholtz equation for the magnetic Hertz potential is shown in a similar manner to that of the electric potential to be

$$\nabla^2 \mathbf{\Pi}_m + k^2 \mathbf{\Pi}_m = -\frac{\mathbf{M}}{j\omega\mu}, \quad (4.13)$$

for a magnetic current density \mathbf{M}^1 . The magnetic field may be written in terms of the magnetic Hertz potential as

$$\mathbf{H} = \nabla(\nabla \cdot \mathbf{\Pi}_m) + k^2 \mathbf{\Pi}_m. \quad (4.14)$$

For a general medium with both electric and magnetic current sources, the total field is a superposition of the partial fields given in (4.2), (4.11), (4.12) and (4.14) [94,95] related to the potentials by

$$\begin{aligned} \mathbf{E} &= \nabla(\nabla \cdot \mathbf{\Pi}_e) + k^2 \mathbf{\Pi}_e - j\omega\mu\nabla \times \mathbf{\Pi}_m \\ \mathbf{H} &= \nabla(\nabla \cdot \mathbf{\Pi}_m) + k^2 \mathbf{\Pi}_m + j\omega\epsilon\nabla \times \mathbf{\Pi}_e. \end{aligned} \quad (4.15)$$

Substitution of the Whittaker potentials from (4.1) into (4.15) yields expressions for the electric and magnetic

¹ The notation \mathbf{M} for the magnetic current density should not be confused with the magnetization vector which is generally denoted by \mathbf{M} and is not used in this work.

fields

$$\begin{aligned}
E_{xi} &= \frac{\partial^2 V_i}{\partial x \partial z} - j\omega\mu_i \frac{\partial U_i}{\partial y} \\
E_{yi} &= \frac{\partial^2 V_i}{\partial y \partial z} + j\omega\mu_i \frac{\partial U_i}{\partial x} \\
E_{zi} &= \left(\frac{\partial^2}{\partial z^2} + k_i^2 \right) V_i \\
H_{xi} &= \frac{\partial^2 U_i}{\partial x \partial z} + j\omega\epsilon_i \frac{\partial V_i}{\partial y} \\
H_{yi} &= \frac{\partial^2 U_i}{\partial y \partial z} - j\omega\epsilon_i \frac{\partial V_i}{\partial x} \\
H_{zi} &= \left(\frac{\partial^2}{\partial z^2} + k_i^2 \right) U_i,
\end{aligned} \tag{4.16}$$

where the subscript i represents the fields in the i -th layer. Additionally, U_i and V_i represent solutions to the following scalar Helmholtz equations in the i -th layer by substitution of (4.1) into (4.10) and (4.13)

$$(\nabla^2 + k_i^2)U_i = 0, \quad (\nabla^2 + k_i^2)V_i = 0. \tag{4.17}$$

Therefore, it is seen that terms containing U_i represent TE fields and those containing V_i represent TM fields.

4.2.1 SPECTRAL DOMAIN ANALYSIS OF THE HERTZ POTENTIALS

To simplify the analysis and avoid spatial derivatives with respect to x and y , the Fourier transform is introduced as the problem is continuous in the x and y directions. The Fourier transform of a function $f(x, y, z)$ is defined as

$$\tilde{f}(\alpha, \beta, z) = \frac{1}{(2\pi)^2} \int_{-\infty}^{\infty} \int_{-\infty}^{\infty} f(x, y, z) e^{j(\alpha x + \beta y)} dx dy, \tag{4.18}$$

and the inverse Fourier transform is

$$f(x, y, z) = \int_{-\infty}^{\infty} \int_{-\infty}^{\infty} \tilde{f}(\alpha, \beta, z) e^{-j(\alpha x + \beta y)} d\alpha d\beta, \tag{4.19}$$

which leads to the following transform pair definitions

$$\frac{\partial f}{\partial x} \Leftrightarrow -j\alpha \tilde{f} \tag{4.20}$$

$$\frac{\partial f}{\partial y} \Leftrightarrow -j\beta \tilde{f}. \tag{4.21}$$

Taking the Fourier transform of the wave equations in (4.17) yields the transform of the Helmholtz equation

$$\left(\frac{\partial^2}{\partial z^2} - \gamma_i^2\right)\tilde{U}_i = 0, \quad \left(\frac{\partial^2}{\partial z^2} - \gamma_i^2\right)\tilde{V}_i = 0, \quad (4.22)$$

where

$$\gamma_i^2 = (\alpha^2 + \beta^2) - k_i^2. \quad (4.23)$$

Next, the Fourier transform of the fields in (4.16) is taken yielding

$$\begin{aligned} \tilde{E}_{xi} &= -\omega\mu_i\beta\tilde{U}_i - j\alpha\frac{\partial\tilde{V}_i}{\partial z} \\ \tilde{E}_{yi} &= \omega\mu_i\alpha\tilde{U}_i - j\beta\frac{\partial\tilde{V}_i}{\partial z} \\ \tilde{E}_{zi} &= \left(\frac{\partial^2}{\partial z^2} + k_i^2\right)\tilde{V}_i \\ \tilde{H}_{xi} &= -j\alpha\frac{\partial\tilde{U}_i}{\partial z} + \omega\epsilon_i\beta\tilde{V}_i \\ \tilde{H}_{yi} &= -j\beta\frac{\partial\tilde{U}_i}{\partial z} - \omega\epsilon_i\alpha\tilde{V}_i \\ \tilde{H}_{zi} &= \left(\frac{\partial^2}{\partial z^2} + k_i^2\right)\tilde{U}_i. \end{aligned} \quad (4.24)$$

The solution to the differential equation (4.22) can be expressed as a superposition of plane waves propagating in the positive and negative z directions. Therefore, the spectral domain Whittaker potentials expressed in terms of the forward and reflected waves are

$$\begin{aligned} \tilde{U}_i &= A_i \left(e^{-s\gamma_i z} + \Gamma_{ai} e^{s\gamma_i z} \right) \\ \tilde{V}_i &= B_i \left(e^{-s\gamma_i z} + \Gamma_{bi} e^{s\gamma_i z} \right), \end{aligned} \quad (4.25)$$

where $s = \text{sgn}(i)$. The source free boundary conditions dictate the continuity of the tangential electric and magnetic fields which will be utilized to determine the unknown amplitude constants and reflection coefficients.

In the spectral domain the boundary conditions are

$$\begin{aligned} \mathbf{a}_n \times \left(\tilde{\mathbf{E}}_{i+s} - \tilde{\mathbf{E}}_i \right) &= 0 \\ \mathbf{a}_n \times \left(\tilde{\mathbf{H}}_{i+s} - \tilde{\mathbf{H}}_i \right) &= 0, \end{aligned} \quad (4.26)$$

where $\mathbf{a}_n = s\mathbf{a}_z$ as seen in Fig. 4.3. In the source free region the boundary conditions at z_i for TE and TM fields are decoupled and the unknowns can be determined. The boundary conditions for the TE fields are found by substitution of (4.24) into (4.26) yielding

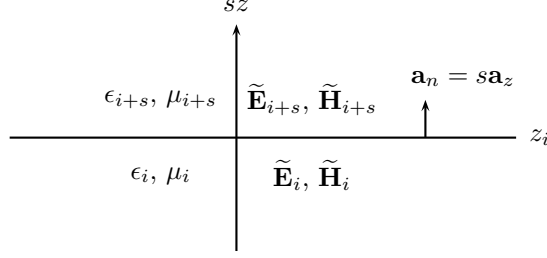


Figure 4.3: Source free boundary between two layers where $\mathbf{a}_n = s\mathbf{a}_z$.

$$\mu_{i+s}\tilde{U}_{i+s}(\alpha, \beta, z_i) = \mu_i\tilde{U}_i(\alpha, \beta, z_i) \quad (4.27)$$

$$\left. \frac{\partial \tilde{U}_{i+s}(\alpha, \beta, z)}{\partial z} \right|_{z=z_{i+s}} = \left. \frac{\partial \tilde{U}_i(\alpha, \beta, z)}{\partial z} \right|_{z=z_i}. \quad (4.28)$$

Substituting in the transformed Whittaker potentials from (4.25)

$$A_{i+s}\mu_{i+s}e^{s\gamma_{i+s}z_i} (e^{-2s\gamma_{i+s}z_i} + \Gamma_{a,i+s}) = A_i\mu_i e^{s\gamma_i z_i} (e^{-2s\gamma_i z_i} + \Gamma_{ai}) \quad (4.29)$$

$$A_{i+s}\gamma_{i+s}e^{s\gamma_{i+s}z_i} (e^{-2s\gamma_{i+s}z_i} - \Gamma_{a,i+s}) = A_i\gamma_i e^{s\gamma_i z_i} (e^{-2s\gamma_i z_i} - \Gamma_{ai}), \quad (4.30)$$

then dividing (4.29) by (4.30) yields an expression for the TE reflection coefficient

$$\Gamma_{ai} = e^{-2s\gamma_i z_i} \frac{(e^{-2s\gamma_{i+s}z_i} + \Gamma_{a,i+s}) - \frac{\mu_i\gamma_{i+s}}{\mu_{i+s}\gamma_i} (e^{-2s\gamma_{i+s}z_i} - \Gamma_{a,i+s})}{(e^{-2s\gamma_{i+s}z_i} + \Gamma_{a,i+s}) + \frac{\mu_i\gamma_{i+s}}{\mu_{i+s}\gamma_i} (e^{-2s\gamma_{i+s}z_i} - \Gamma_{a,i+s})}. \quad (4.31)$$

Similarly for the TM fields, application of the boundary conditions yields the following expressions

$$\epsilon_{i+s}\tilde{V}_{i+s}(\alpha, \beta, z_i) = \epsilon_i\tilde{V}_i(\alpha, \beta, z_i) \quad (4.32)$$

$$\left. \frac{\partial \tilde{V}_{i+s}(\alpha, \beta, z)}{\partial z} \right|_{z=z_{i+s}} = \left. \frac{\partial \tilde{V}_i(\alpha, \beta, z)}{\partial z} \right|_{z=z_i}. \quad (4.33)$$

Substituting in the transformed Whittaker potentials from (4.25)

$$B_{i+s}\epsilon_{i+s}e^{s\gamma_{i+s}z_i} (e^{-2s\gamma_{i+s}z_i} + \Gamma_{b,i+s}) = B_i\epsilon_i e^{s\gamma_i z_i} (e^{-2s\gamma_i z_i} + \Gamma_{bi}) \quad (4.34)$$

$$B_{i+s}\gamma_{i+s}e^{s\gamma_{i+s}z_i} (e^{-2s\gamma_{i+s}z_i} - \Gamma_{b,i+s}) = B_i\gamma_i e^{s\gamma_i z_i} (e^{-2s\gamma_i z_i} - \Gamma_{bi}), \quad (4.35)$$

then dividing (4.34) by (4.35) yields an expression for the TM reflection coefficient

$$\Gamma_{bi} = e^{-2s\gamma_i z_i} \frac{(e^{-2s\gamma_{i+s}z_i} + \Gamma_{b,i+s}) - \frac{\epsilon_i\gamma_{i+s}}{\epsilon_{i+s}\gamma_i} (e^{-2s\gamma_{i+s}z_i} - \Gamma_{b,i+s})}{(e^{-2s\gamma_{i+s}z_i} + \Gamma_{b,i+s}) + \frac{\epsilon_i\gamma_{i+s}}{\epsilon_{i+s}\gamma_i} (e^{-2s\gamma_{i+s}z_i} - \Gamma_{b,i+s})}. \quad (4.36)$$

The unknown TE and TM amplitude coefficients are found by solving (4.29) and (4.34) for A_{i+s} and B_{i+s}

respectively

$$A_{i+s} = A_i \frac{\mu_i}{\mu_{i+s}} \frac{e^{s\gamma_i z_i}}{e^{s\gamma_{i+s} z_i}} \frac{e^{-2s\gamma_i z_i} + \Gamma_{ai}}{e^{-2s\gamma_{i+s} z_i} + \Gamma_{a,i+s}} \quad (4.37)$$

$$B_{i+s} = B_i \frac{\epsilon_i}{\epsilon_{i+s}} \frac{e^{s\gamma_i z_i}}{e^{s\gamma_{i+s} z_i}} \frac{e^{-2s\gamma_i z_i} + \Gamma_{bi}}{e^{-2s\gamma_{i+s} z_i} + \Gamma_{b,i+s}}. \quad (4.38)$$

Next, the boundary conditions at $z = 0$ will be solved to determine the unknown amplitude coefficients A_1 , A_{-1} , B_1 , and B_{-1} . First, it is assumed that there is no magnetic current ($\mathbf{M} = 0$) and the surface current is from a thin sheet so current only flows in the x and y directions. The boundary conditions are

$$\begin{aligned} \mathbf{a}_z \times (\tilde{\mathbf{E}}_1 - \tilde{\mathbf{E}}_{-1}) &= 0 \\ \mathbf{a}_z \times (\tilde{\mathbf{H}}_1 - \tilde{\mathbf{H}}_{-1}) &= \tilde{\mathbf{J}}_s. \end{aligned} \quad (4.39)$$

The continuity of the tangential electric field gives

$$-\omega\mu_1\beta A_1(1 + \Gamma_{a1}) + j\alpha\gamma_1 B_1(1 - \Gamma_{b1}) = -\omega\mu_{-1}\beta A_{-1}(1 + \Gamma_{a,-1}) + j\alpha\gamma_{-1} B_{-1}(1 - \Gamma_{b,-1}) \quad (4.40)$$

$$\omega\mu_1\alpha A_1(1 + \Gamma_{a1}) + j\beta\gamma_1 B_1(1 - \Gamma_{b1}) = \omega\mu_{-1}\alpha A_{-1}(1 + \Gamma_{a,-1}) - j\beta\gamma_{-1} B_{-1}(1 - \Gamma_{b,-1}). \quad (4.41)$$

Multiplying (4.40) by $-\beta/\alpha$ and adding it to (4.41) yields a relation between A_1 and A_{-1}

$$\begin{aligned} \omega\mu_1 \frac{\beta^2}{\alpha} A_1(1 + \Gamma_{a1}) + \omega\mu_1\alpha A_1(1 + \Gamma_{a1}) &= \omega\mu_{-1} \frac{\beta^2}{\alpha} A_{-1}(1 + \Gamma_{a,-1}) + \omega\mu_{-1}\alpha A_{-1}(1 + \Gamma_{a,-1}) \\ \left(\frac{\beta^2}{\alpha} + \alpha\right) \omega\mu_1 A_1(1 + \Gamma_{a1}) &= \left(\frac{\beta^2}{\alpha} + \alpha\right) \omega\mu_{-1} A_{-1}(1 + \Gamma_{a,-1}) \\ \mu_1 A_1(1 + \Gamma_{a1}) &= \mu_{-1} A_{-1}(1 + \Gamma_{a,-1}). \end{aligned} \quad (4.42)$$

Similarly, multiplying (4.40) by α/β and adding it to (4.41) yields a relation between B_1 and B_{-1}

$$\begin{aligned} \left(\frac{\alpha^2}{\beta} + \beta\right) B_1\gamma_1(1 - \Gamma_{b1}) &= -\left(\frac{\alpha^2}{\beta} + \beta\right) \gamma_{-1} B_{-1}(1 - \Gamma_{b,-1}) \\ B_1\gamma_1(1 - \Gamma_{b1}) &= -\gamma_{-1} B_{-1}(1 - \Gamma_{b,-1}). \end{aligned} \quad (4.43)$$

Applying the boundary conditions on the tangential magnetic fields yields

$$j\alpha\gamma_1 A_1(1 - \Gamma_{a1}) + \omega\epsilon_1\beta B_1(1 + \Gamma_{b1}) + j\alpha\gamma_{-1} A_{-1}(1 - \Gamma_{a,-1}) - \omega\epsilon_{-1}\beta B_{-1}(1 + \Gamma_{b,-1}) = \tilde{\mathcal{J}}_y \quad (4.44)$$

$$j\beta\gamma_1 A_1(1 - \Gamma_{a1}) - \omega\epsilon_1\alpha B_1(1 + \Gamma_{b1}) + j\beta\gamma_{-1} A_{-1}(1 - \Gamma_{a,-1}) + \omega\epsilon_{-1}\alpha B_{-1}(1 + \Gamma_{b,-1}) = -\tilde{\mathcal{J}}_x. \quad (4.45)$$

Multiplying (4.44) by α/β and adding it to (4.45) yields a relation between A_1 and A_{-1}

$$\begin{aligned} \left(\frac{\alpha^2}{\beta} + \beta\right) j\gamma_1 A_1 (1 - \Gamma_{a1}) + \left(\frac{\alpha^2}{\beta} + \beta\right) j\gamma_{-1} A_{-1} (1 - \Gamma_{a,-1}) &= -\tilde{J}_x + \frac{\alpha}{\beta} \tilde{J}_y \\ \gamma_1 A_1 (1 - \Gamma_{a1}) + \gamma_{-1} A_{-1} (1 - \Gamma_{a,-1}) &= \frac{-\beta \tilde{J}_x + \alpha \tilde{J}_y}{j(\alpha^2 + \beta^2)}. \end{aligned} \quad (4.46)$$

Similarly, multiplying (4.44) by $-\beta/\alpha$ and adding it to (4.45) yields a relation between B_1 and B_{-1}

$$\begin{aligned} \left(\frac{\beta^2}{\alpha} + \alpha\right) \omega \epsilon_1 B_1 (1 + \Gamma_{b1}) - \left(\frac{\beta^2}{\alpha} + \alpha\right) \omega \epsilon_{-1} B_{-1} (1 + \Gamma_{b,-1}) &= \tilde{J}_x + \frac{\beta}{\alpha} \tilde{J}_y \\ \epsilon_1 B_1 (1 + \Gamma_{b1}) - \epsilon_{-1} B_{-1} (1 + \Gamma_{b,-1}) &= \frac{\alpha \tilde{J}_x + \beta \tilde{J}_y}{\omega(\alpha^2 + \beta^2)}. \end{aligned} \quad (4.47)$$

Combining (4.42) with (4.46) yields a result for the amplitude coefficient A_1

$$A_1 = \left(\frac{\gamma_1(1 - \Gamma_{a1})}{\mu_1(1 + \Gamma_{a1})} + \frac{\gamma_{-1}(1 - \Gamma_{a,-1})}{\mu_{-1}(1 + \Gamma_{a,-1})} \right)^{-1} \frac{-\beta \tilde{J}_x + \alpha \tilde{J}_y}{j\mu_1(1 + \Gamma_{a1})(\alpha^2 + \beta^2)}. \quad (4.48)$$

Combining (4.43) with (4.47) yields a result for the amplitude coefficient B_1

$$B_1 = \left(\frac{\epsilon_1(1 + \Gamma_{b1})}{\gamma_1(1 - \Gamma_{b1})} + \frac{\epsilon_{-1}(1 + \Gamma_{b,-1})}{\gamma_{-1}(1 - \Gamma_{b,-1})} \right)^{-1} \frac{\alpha \tilde{J}_x + \beta \tilde{J}_y}{\omega \gamma_1(1 - \Gamma_{b1})(\alpha^2 + \beta^2)}, \quad (4.49)$$

where A_{-1} and B_{-1} are related to (4.48) and (4.49) by solving (4.42) and (4.43) respectively, and are given by

$$A_{-1} = A_1 \frac{\mu_1(1 + \Gamma_{a1})}{\mu_{-1}(1 + \Gamma_{a,-1})} \quad (4.50)$$

$$B_{-1} = -B_1 \frac{\gamma_1(1 - \Gamma_{b1})}{\gamma_{-1}(1 - \Gamma_{b,-1})}. \quad (4.51)$$

Thus, the fields can be solved if the current distribution is known. Also, it is assumed that the stratified medium has a finite number of layers n in the positive z direction and m in the negative z direction such that $\Gamma_{an} = \Gamma_{bn} = 0$ and $\Gamma_{a,-m} = \Gamma_{b,-m} = 0$. To solve for the fields, the following procedure is used

- Assume a surface current distribution \mathbf{J}_s along the dipole.
- Determine the fields in terms of the Whittaker potentials, and to avoid spatial derivatives, take the spatial Fourier transform.
- The resulting transformed Whittaker potentials will be in terms of unknown amplitude and reflection coefficients in the spatial transform domain which must be determined by applying boundary conditions.

- Calculate the reflection coefficients Γ_{ai} and Γ_{bi} from (4.31) and (4.36) starting with the outermost layers ($\Gamma_{an} = \Gamma_{bn} = 0$ and $\Gamma_{a,-m} = \Gamma_{b,-m} = 0$) and recursively calculate until the reflection coefficients at layers $i = 1$ and $i = -1$ are determined.
- Calculate the amplitude coefficients in layers $i = 1$ and $i = -1$ from (4.48) to (4.51) using the calculated reflection coefficients.
- Finally, calculate the amplitude coefficients in each layer from (4.37) and (4.38).

This procedure can easily be implement in software. For this work, Python was used to calculate the unknown TE and TM reflection and amplitude coefficients. The code is listed in Appendix D. The functions are recursive and perform the same function as the detailed procedure. Additionally, for the purpose of checking units of the quantities derived in subsequent sections, the units of the TE and TM amplitude coefficients are given in Appendix C.

4.2.2 INPUT IMPEDANCE OF A DIPOLE

Having determined the fields of a current element in the presence of a stratified medium, the driving point impedance of the dipole can be determined by use of the induced EMF method [97]. A thin linear dipole of length l and width W will be considered. If the dipole is narrow such that $W \ll l$, it is assumed that current only flows in the x direction such that $\mathbf{J}_s = J_x \mathbf{a}_x$

$$Z_{\text{in}} = -\frac{1}{I_{\text{in}}^2} \int_{-W/2}^{W/2} \int_{-l/2}^{l/2} J_x(x, y, z = 0) E_{x1}(x, y, z = 0) dx dy, \quad (4.52)$$

where I_{in} is the current at the input terminals. Writing in terms of the Fourier integral representation for the electric field yields

$$Z_{\text{in}} = -\frac{1}{I_{\text{in}}^2} \int_{-W/2}^{W/2} \int_{-l/2}^{l/2} J_x \left[\int_{-\infty}^{\infty} \int_{-\infty}^{\infty} \tilde{E}_{x1} e^{-j(\alpha x + \beta y)} d\alpha d\beta \right] dx dy. \quad (4.53)$$

Next, the order of integration is changed and J_x is assumed to be an even function about $x = 0$, $y = 0$ yielding

$$Z_{\text{in}} = -\frac{(2\pi)^2}{I_{\text{in}}^2} \int_{-\infty}^{\infty} \int_{-\infty}^{\infty} \tilde{E}_{x1} \left[\frac{1}{(2\pi)^2} \int_{-W/2}^{W/2} \int_{-l/2}^{l/2} J_x \cos(\alpha x) \cos(\beta y) dx dy \right] d\alpha d\beta \quad (4.54)$$

The portion in brackets of (4.54) represents the Fourier transform of J_x given by \tilde{J}_x . Next, a function of the ratio of the transformed electric field from (4.24) to the transformed current density is defined by

$$\begin{aligned}
\tilde{E}_{x1} &= -\omega\mu_1\beta\tilde{U}_1|_{z=0} - j\alpha\left.\frac{\partial\tilde{V}_1}{\partial z}\right|_{z=0} \\
\tilde{E}_{x1} &= -j\omega\left(\frac{\gamma_1(1-\Gamma_{a1})}{\mu_1(1+\Gamma_{a1})} + \frac{\gamma_{-1}(1-\Gamma_{a,-1})}{\mu_{-1}(1+\Gamma_{a,-1})}\right)^{-1}\frac{\beta^2\tilde{J}_x}{\alpha^2+\beta^2} \\
&\quad + \frac{j}{\omega}\left(\frac{\epsilon_1(1+\Gamma_{b1})}{\gamma_1(1-\Gamma_{b1})} + \frac{\epsilon_{-1}(1+\Gamma_{b,-1})}{\gamma_{-1}(1-\Gamma_{b,-1})}\right)^{-1}\frac{\alpha^2\tilde{J}_x}{\alpha^2+\beta^2} \\
\tilde{F}(\alpha,\beta) &= -\frac{\tilde{E}_{x1}}{j\omega\tilde{J}_x} \\
\tilde{F}(\alpha,\beta) &= \left(\frac{\gamma_1(1-\Gamma_{a1})}{\mu_1(1+\Gamma_{a1})} + \frac{\gamma_{-1}(1-\Gamma_{a,-1})}{\mu_{-1}(1+\Gamma_{a,-1})}\right)^{-1}\frac{\beta^2}{\alpha^2+\beta^2} \\
&\quad - \frac{1}{\omega^2}\left(\frac{\epsilon_1(1+\Gamma_{b1})}{\gamma_1(1-\Gamma_{b1})} + \frac{\epsilon_{-1}(1+\Gamma_{b,-1})}{\gamma_{-1}(1-\Gamma_{b,-1})}\right)^{-1}\frac{\alpha^2}{\alpha^2+\beta^2}, \tag{4.55}
\end{aligned}$$

and if $\mu_1 = \mu_{-1} = \mu$, (4.55) can be simplified to

$$\begin{aligned}
\tilde{F}(\alpha,\beta) &= -\frac{\tilde{E}_{x1}}{j\omega\mu\tilde{J}_x} \\
\tilde{F}(\alpha,\beta) &= \left(\gamma_1\frac{1-\Gamma_{a1}}{1+\Gamma_{a1}} + \gamma_{-1}\frac{1-\Gamma_{a,-1}}{1+\Gamma_{a,-1}}\right)^{-1}\frac{\beta^2}{\alpha^2+\beta^2} \\
&\quad - \left(\frac{k_1^2}{\gamma_1}\frac{1+\Gamma_{b1}}{1-\Gamma_{b1}} + \frac{k_{-1}^2}{\gamma_{-1}}\frac{1+\Gamma_{b,-1}}{1-\Gamma_{b,-1}}\right)^{-1}\frac{\alpha^2}{\alpha^2+\beta^2}. \tag{4.56}
\end{aligned}$$

The impedance is now written as

$$Z_{\text{in}} = \frac{4j\omega\pi^2}{I_{\text{in}}^2} \int_{-\infty}^{\infty} \int_{-\infty}^{\infty} \tilde{F}(\alpha,\beta)\tilde{J}_x(\alpha,\beta)^2 d\alpha d\beta \tag{4.57}$$

A variational solution for the impedance is given in Appendix A that follows the method presented by Galejs [93,94]. The solution uses a two term trial function that consists of a sine and shifted cosine with unknown amplitudes. The amplitudes are determined by imposing the stationary character of the input impedance such that a small change in the current about its correct value gives a zero first order change in the impedance.

It may be noted at this point that the derivations presented in Section 4.2 are similar to that presented by [93–95], but are presented here for completeness as these formulas will be necessary in following section regarding power flow in this arbitrary stratified medium.

4.3 POWER FLOW AND SENSING DEPTH

The aim of this analysis is to determine the power density profile for a transmitting dipole into a lossy stratified medium, which results in a metric for the sensing depth of the same dipole in receive mode. First, the time-average power flow through a plane of infinite extent in the x and y directions is determined from Poynting's theorem as

$$P(z) = \frac{1}{2} \text{Re} \left\{ \int_{-\infty}^{\infty} \int_{-\infty}^{\infty} \mathbf{E} \times \mathbf{H}^* \cdot d\mathbf{s} \right\}. \quad (4.58)$$

Utilizing Parseval's formula for the Fourier transform, the time average power flow can be written in terms of the transformed fields as

$$P(z) = s2\pi^2 \text{Re} \left\{ \int_{-\infty}^{\infty} \int_{-\infty}^{\infty} \tilde{E}_x \tilde{H}_y^* - \tilde{E}_y \tilde{H}_x^* d\alpha d\beta \right\}, \quad (4.59)$$

where the transformed fields are given in (4.24) of Section 4.2. The goal of this analysis is to determine the sensing limit for a dipole when utilized as an antenna for a near-field medical microwave radiometer. The principal of operation for a microwave radiometer is to measure blackbody radiated power emitted by all matter based on its temperature. This radiation is defined by Planck's blackbody radiation law for spectral brightness B_f , given by the Rayleigh-Jeans approximation for the microwave region:

$$B_f = \frac{2kT}{\lambda^2} \quad [\text{W} \cdot \text{sr}^{-1} \cdot \text{m}^{-2} \cdot \text{Hz}^{-1}], \quad (4.60)$$

where

k = Boltzmann's constant [1.38×10^{-23} joule/ K]

T = Absolute temperature [K]

λ = Wavelength [m].

The emitted power over a bandwidth Δf is given by $kT\Delta f$. Thus, by measuring the power radiated in a bandwidth Δf , the temperature of a body can be measured. A near-field probe or antenna placed in contact with a lossy medium (human tissues) couples the blackbody radiation into the receiver. The antenna measures a weighted volume average brightness temperature within the sensing volume V . The spatial temperature

distribution is defined as $T(\mathbf{r})$ at point \mathbf{r} , and the antenna brightness temperature T_A is given by

$$T_A = \eta_l \iiint_V W(\mathbf{r})T(\mathbf{r})dV + \eta_u T_{Bu} \quad (4.61)$$

where η_l and η_u are the lower and upper half-space efficiencies defined below. The weighting function $W(\mathbf{r})$ defines the contribution from point \mathbf{r} at a temperature $T(\mathbf{r})$ to the overall antenna brightness temperature.

The weighting function is obtained from the antenna reciprocity theorem as the power absorption rate

$$W(\mathbf{r}) = \frac{P_d(\mathbf{r})}{\iiint_V P_d(\mathbf{r})dV} \quad (4.62)$$

for a transmitting antenna, where $P_d(\mathbf{r})$ is the power dissipation at point \mathbf{r} . Additionally, η_l and η_u are the lower and upper half-space efficiencies, where the lower half-space corresponds to the tissues. The efficiencies are defined from (4.59) as

$$\eta_l = \frac{P(0^-)}{P(0^-) + P(0^+)}, \quad \eta_u = \frac{P(0^+)}{P(0^-) + P(0^+)}. \quad (4.63)$$

Thus, it can be seen that the term $\eta_u T_{Bu}$ is the contribution from the upper half-space of a constant temperature T_{Bu} . Given the geometry assumed in Fig. 4.2 which assumes a stratified medium that is infinite in extent in the x and y directions and assuming the tissues under test will be characterized by a constant temperature in the x and y directions [12], (4.61) can be reduced to a one-dimensional expression

$$T_A = \eta_l \int_{-\infty}^0 W(z)T(z)dz + \eta_u T_{Bu} \quad (4.64)$$

where

$$W(z) = \iint_S W(\mathbf{r})dS. \quad (4.65)$$

For a non-ideal antenna with radiation efficiency η_r the antenna noise temperature at the terminals of the antenna T'_A is given in terms of the physical antenna temperature T_p as

$$T'_A = \eta_r T_A + (1 - \eta_r)T_p. \quad (4.66)$$

Using the definition of the antenna temperature, a metric for the sensing depth of the receiver will be defined in a similar manner as that presented by Bocquet et al. [24].

Consider an antenna placed at the interface between free-space and the human body. The human body is approximated by a stratified medium characterized by a temperature distribution $T(z)$ as shown in Fig. 4.4.

The antenna temperature is given by (4.64) and (4.66) as

$$T'_A = \eta_r \left[\eta_l \int_{-\infty}^0 W(z)T(z)dz + \eta_u T_{Bu} \right] + (1 - \eta_r)T_p. \quad (4.67)$$

Next, suppose that at a depth z_s the tissues below this depth are subjected to a uniform increase in temperature ΔT as shown in Fig. 4.4, then the antenna temperature is given by

$$T'_A + \Delta T'_A = \eta_r \left[\eta_l \left(\int_{-\infty}^0 W(z)T(z)dz + \Delta T \int_{-\infty}^{z_s} W(z)dz \right) + \eta_u T_{Bu} \right] + (1 - \eta_r)T_p \quad (4.68)$$

or the change in antenna temperature contributed by the layers deeper than z_s due to a uniform increase in

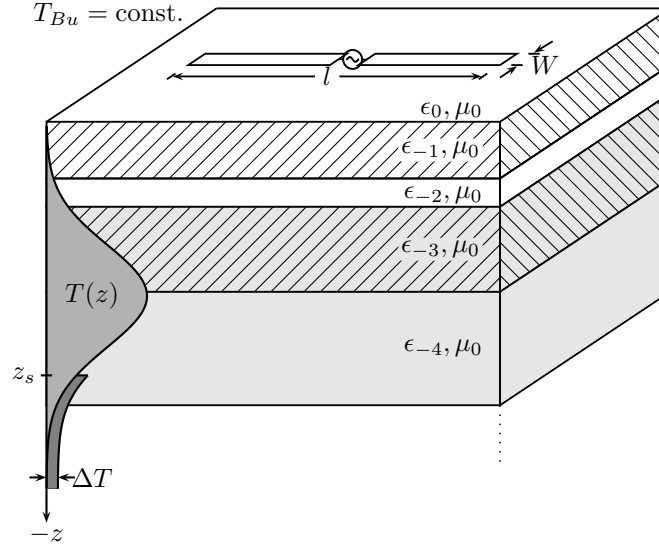


Figure 4.4: Definition of sensing depth z_s for a dipole on a lossy stratified half-space. Temperature changes with depth in the tissue layers while it is constant in the upper half-space.

temperature from $T(z)$ to $(T(z) + \Delta T)$ is

$$\Delta T'_A = \Delta T \eta_r \eta_l \int_{-\infty}^{z_s} W(z)dz. \quad (4.69)$$

The signal sensitivity to the ΔT change in the layers situated below z_s is

$$\frac{\Delta T'_A}{\Delta T} = \eta_r \eta_l \int_{-\infty}^{z_s} W(z)dz \quad (4.70)$$

Each individual measurement has uncertainty associated with it. This uncertainty is given for a total power radiometer as [2]

$$\sigma = \frac{T'_A + T_{\text{rec}}}{\sqrt{\Delta f \tau}} \quad (4.71)$$

where T_{rec} is the receiver noise temperature, Δf is the pre-detection bandwidth, and τ is the integration time. Thus, the uncertainties in the first and second measurements are

$$\sigma_1 = \frac{T'_A + T_{\text{rec}}}{\sqrt{\Delta f \tau}}, \quad \sigma_2 = \frac{T'_A + \Delta T'_A + T_{\text{rec}}}{\sqrt{\Delta f \tau}}. \quad (4.72)$$

Assuming that each measurement is statistically independent, the uncertainty in the estimate of $\Delta T'_A$ is

$$\sigma_{\text{tot}} = \sqrt{\sigma_1^2 + \sigma_2^2}. \quad (4.73)$$

If $\Delta T'_A$ is very small, then $\sigma_1 \approx \sigma_2$ resulting in the the total uncertainty

$$\sigma_{\text{tot}} = \sqrt{2}\sigma. \quad (4.74)$$

Therefore, to resolve a temperature change ΔT at a depth z_s the temperature contribution must be greater than $\sqrt{2}\sigma$. The maximum sensing depth z_s is then defined by

$$\int_{-\infty}^{z_s} W(z) dz = \frac{\sqrt{2}\sigma}{\eta_r \eta_l \Delta T}. \quad (4.75)$$

The left hand side of (4.75) represents the power absorbed by the material below z_s normalized to the total power absorbed. This quantity is also equal to the real power flowing through a plane located at z_s . Therefore, (4.75) is simplified by using the definition for the real power passing through a plane given by (4.59), resulting in the following sensing depth expression

$$\frac{P(z_s)}{P(0^-)} = \frac{\sqrt{2}\sigma}{\eta_r \eta_l \Delta T} \quad (4.76)$$

or

$$\frac{P(z_s)}{P(0^-) + P(0^+)} = \frac{\sqrt{2}\sigma}{\eta_r \Delta T} \quad (4.77)$$

To summarize, detecting a temperature change depends upon the probe and the receiver. Therefore, it is essential to consider the power flow from the probe ($W(z)$), the non-ideal receiver sensitivity (σ), and the

desired incremental temperature resolution (ΔT). It may also be noted that the probe is assumed to be matched to the receiver. If this is not the case, mismatched components may be accounted for in a standard way such as pp. 404-412 of [2] or [98]. In the following sections the sensing depth is determined assuming the probe is perfectly matched to the receiver.

4.4 ALGORITHM VERIFICATION

To illustrate the properties of a dipole in the presence of a lossy stratified medium, the spectral domain technique will first be applied to a dipole of length l and width W at the interface between free space and a lossy medium as shown in Fig. 4.5. In research for medical applications a water bath is often used to demonstrate temperature detection because the dielectric properties of water are similar to those of human tissues. Water is a medium that is easily controlled in a laboratory environment, and is a standard phantom

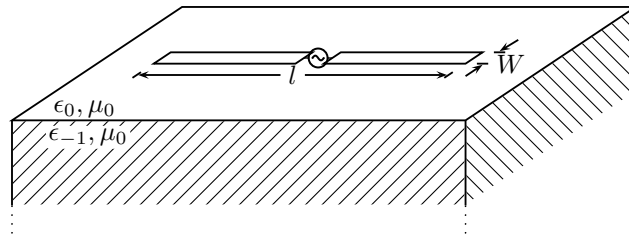


Figure 4.5: Flat dipole of length l and width W on a dissipative half-space.

material [39–41]. The dispersive electrical properties of water can be represented by a Debye model [33, 42, 44] and Fig. 4.6 shows the real part of the relative dielectric constant (ϵ'_r) and the conductivity over the frequency range of 250 MHz to 5 GHz. The values were calculated using the single Debye model in [44] assuming the temperature of the water is 25°C. These values are used in subsequent simulations.

For the two layer problem, the function (4.56) appearing in (A.9) simplifies to

$$\begin{aligned} \tilde{F}(\alpha, \beta) &= (\gamma_1 + \gamma_{-1})^{-1} \frac{\beta^2}{\alpha^2 + \beta^2} \\ &\quad - \left(\frac{k_1^2}{\gamma_1} + \frac{k_{-1}^2}{\gamma_{-1}} \right)^{-1} \frac{\alpha^2}{\alpha^2 + \beta^2}. \end{aligned} \quad (4.78)$$

Using Appendix A the input impedance of a dipole on a half space can be found. The propagation constant k along a dipole situated at the interface between two media used in the expression for the current density (A.1)

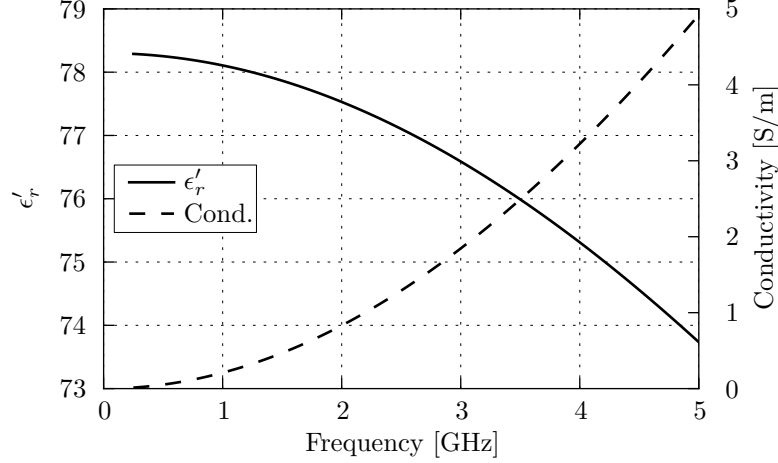


Figure 4.6: Real part of the relative dielectric constant (ϵ'_r) and the conductivity over the frequency range of 250 MHz to 5 GHz calculated using the single Debye model in [44] assuming the water temperature is 25°C.

to (A.4) will be given by an effective complex propagation constant k_{eff} [99, 100]

$$k_{\text{eff}} = \sqrt{\frac{k_1^2 + k_{-1}^2}{2}}. \quad (4.79)$$

Therefore, $\lambda_{\text{eff}} = 2\pi/\text{Re}\{k_{\text{eff}}\}$ will be used to determine the electrical length of the dipole.

4.4.1 COMPARISON TO PUBLISHED WORKS

The spectral domain approach with a variational solution for the input impedance will be validated first by comparison to other published works. Kominami et al. [60] investigated printed dipoles and slots on semi-infinite GaAs substrates. The application was for millimeter wave imaging or phased arrays where the lens is electrically large. Kominami et al. presented a moment method solution using Galerkin's method applied in the Fourier transform domain to determine the input impedance of dipoles and slots at the interface of two different dielectric half-spaces. The fields were described in terms of two scalar functions that appear to be the same as the Whittaker potentials, however, this is not explicitly stated in their work. In [60], a numerical simulation was done to determine the input impedance of an antenna of width $W = 0.02l$ versus the length l of the antenna using two entire domain expansion modes. Using the method presented in Section 4.2 the input impedance was calculated from (4.57). Since this is a half-space problem (4.78) was used as the auxiliary function $\tilde{F}(\alpha, \beta)$ appearing in (4.57), and the effective propagation constant from (4.79) was used in the expression for the current density. The method in [60] is compared to the method presented in Section 4.2

demonstrating good agreement as shown in Fig. 4.7.

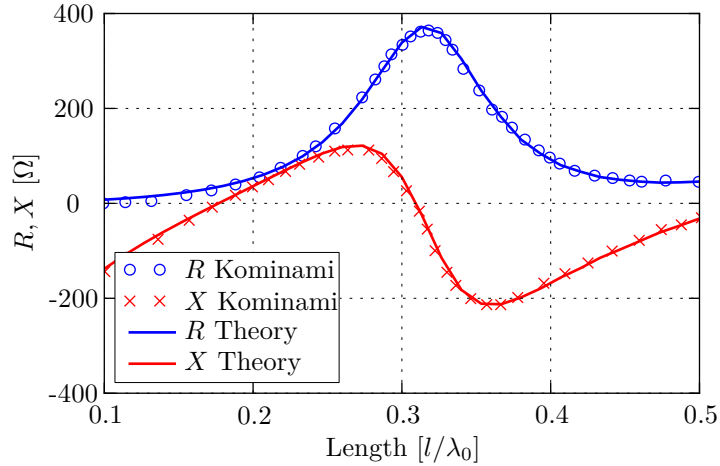


Figure 4.7: Comparison of the input impedance of a 10 GHz dipole on a GaAs half-space versus length for the method presented by Kominami et al. and the method presented in Section 4.2 of this work.

Next, this method was applied to the problem of a half-wave and quarter-wave monopole at the interface between air and water. The data presented was measured by Iizuka and presented in a Cruft lab report in 1963 [101]. The data presented here was taken from [100]. Measurements were made of a quarter-wave and half-wave monopole at 114 MHz on a lossy dielectric half-space where the wavelength was taken in the conducting medium. Measurements versus loss tangent $\tan \delta$ of the lower half-space of water ($\epsilon'_r = 77$) were made. To calculate the impedance, the previously presented method was used. The equivalent strip width is $W = 4a$ where $a = 0.318$ cm. The impedance of a half and full wave dipole was calculated, which is related to the monopole impedance by [102]

$$Z_{\text{monopole}} = \frac{Z_{\text{dipole}}}{2} \quad (4.80)$$

Fig. 4.8 shows the comparison between the theory presented here and measurements made by Iizuka. Both impedance and admittance are shown, however, the data taken from [100] was admittance. Comparing theory and measurement in Fig. 4.8 shows conductances and susceptances that are within approximately 20 mS of each other for both the half and quarter wave monopole as seen in Figs. 4.8a and 4.8c. Similarly, the resistances and reactances are within approximately 5 Ω of each other as seen in Figs. 4.8b and 4.8d

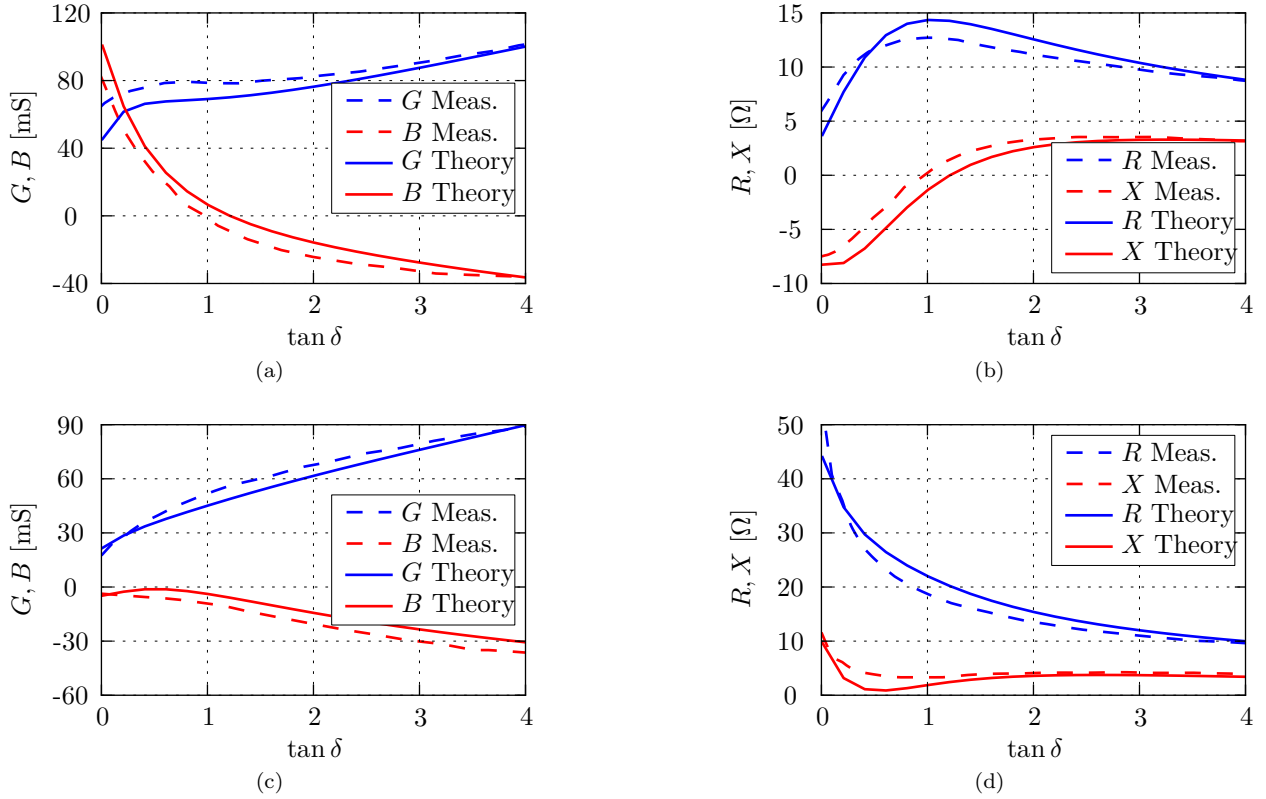


Figure 4.8: Admittance (a) and impedance (b) of a quarter-wave monopole versus the loss tangent $\tan \delta$ at 114 MHz. Admittance (c) and impedance (d) of a half-wave monopole versus the loss tangent $\tan \delta$ at 114 MHz.

4.4.2 THEORETICAL RESULTS

In the previous section, the method presented in Section 4.2 was compared to simulated and measured half-space problem results for GaAs (Fig. 4.7) and also for water (Fig. 4.8). Next, a water half-space will be investigated in depth with the theory presented, and the results will be compared to commercially available full wave electromagnetic software.

First, the spectral domain technique is applied to a dipole on a lossy half-space and the results are compared to Finite Element Method simulations using Ansys' commercially available HFSS software. The lower half-space medium is characterized by the dielectric properties shown in Fig. 4.6. To achieve an input match $|\Gamma| < -7.4$ dB the length of the dipole was chosen to be $0.6\lambda_{\text{eff}}$. Additionally, to maintain the assumption of current being uniformly distributed in y , the width of the dipole was chosen to be $W = l/100$. To numerically evaluate the integrals in (A.9) a Gauss-Legendre quadrature integration routine available in

the *mpmath* [103] Python library was used. The integration was carried out along the real axis as the complex poles are removed from the real axis, and the upper bound on the infinite integration was truncated at $500k_0$. The antenna driving point impedance was determined using the induced EMF method from 250 MHz to 3 GHz and using HFSS. The results are shown in Fig. 4.9. Results from HFSS are within 4.7Ω for the resistance and within 1.1Ω for the reactance as compared to theory.

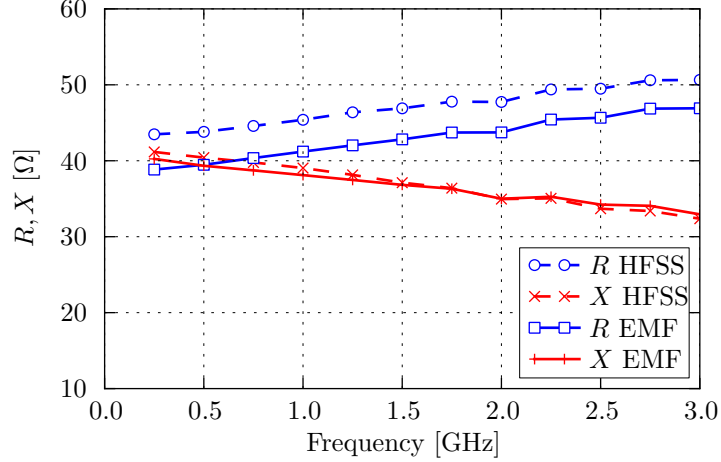


Figure 4.9: Impedance vs. frequency for a $l = 0.6 \lambda_{\text{eff}}$ dipole at the interface of a lossy half-space characterized by a relative dielectric constant of conductivity from Fig. 4.6.

Next, the sensing depth for a $0.6\lambda_{\text{eff}}$ dipole on a lossy half-space is determined by first finding the power flowing in the lower half-space. The power flow is a function of the current density in (A.1) for which only the ratio A/B is known from (A.11). Normalizing the current density to the current at the input yields an expression in terms of the ratio A/B . A z -dependent effective transfer resistance (similar to that defined by Galejs [104] and Sec. 12.3 of [94]) may be defined as

$$\begin{aligned}
 R(z) &= \frac{2P(z)}{|I(0)|^2} \\
 &= -\frac{4k^2\omega\mu_0}{\pi^2} \text{Im} \left\{ \int_0^\infty \int_0^\infty \text{sinc}^2\left(\frac{\beta W}{2}\right) \left[\gamma_{-1}^* |\gamma_1 + \gamma_{-1}|^{-2} \frac{\beta^2}{\alpha^2 + \beta^2} \right. \right. \\
 &\quad \left. \left. - \frac{(k_{-1}^*)^2}{\gamma_{-1}^*} \left| \frac{k_1^2}{\gamma_1} + \frac{k_{-1}^2}{\gamma_{-1}} \right|^{-2} \frac{\alpha^2}{\alpha^2 + \beta^2} \right] e^{2\text{Re}\{\gamma_{-1}\}z} \left| \left[\frac{\sqrt{\frac{A}{B}}g_A(\alpha) + \sqrt{\frac{B}{A}}g_B(\alpha)}{\sqrt{\frac{A}{B}}f_A(0) + \sqrt{\frac{B}{A}}f_B(0)} \right] \right|^2 d\alpha d\beta \right\}. \quad (4.81)
 \end{aligned}$$

The real power passing through a plane in the lower half-space is normalized to the total power radiated by the antenna which may be written in terms of the ratio of the distance dependent effective transfer resistance

to the input resistance as

$$\frac{P(z)}{P_{\text{tot}}} = \frac{R(z)}{R_{\text{in}}} \quad (4.82)$$

where R_{in} is the input resistance. It may also be noted that a dipole placed in contact with a high dielectric constant half-space is very directive towards the dielectric such that the ratio of power radiated into the lower and upper half-spaces varies approximately as $\epsilon_r^{3/2}$ [59, 60]. As a result, $\eta \approx 1$ or in other words $R(0^-) \approx R_{\text{in}}$. This is demonstrated in Fig. 4.10 showing the lower half-space efficiency (η_l) over frequency from theory, HFSS, and as calculated from $\eta_l = \epsilon_r^{3/2}/(\epsilon_r^{3/2} + 1)$ all of which showing $\eta_l > .996$.

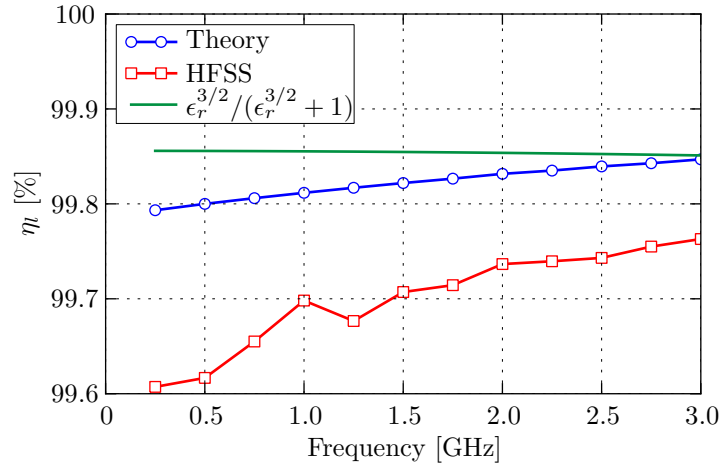


Figure 4.10: Lower half-space efficiency, η_l , over frequency from theory, HFSS, and as calculated from $\eta_l = \epsilon_r^{3/2}/(\epsilon_r^{3/2} + 1)$ all of which showing $\eta_l > .996$.

The integrals in (4.81) are calculated using the same method described for the input impedance. To determine the power flow in the lower half-space from HFSS, the lower half-space is composed of 20 discrete layers of water with logarithmic spacing all of which have same dielectric properties. The purpose for having many volume objects that have the same material properties is so that the power dissipation can be determined as a function of depth. It is not possible to determine this from a single volume. The power dissipation is determined using the Fields Calculator in HFSS. The *volume loss density* quantity is integrated over each subvolume to determine the power dissipated (P_n) in the n th subvolume. The volume loss density can be calculated by first considering the point form of the complex Poynting vector as

$$\rho_v = -\frac{1}{2} \text{Re}\{\nabla \cdot (\mathbf{E} \times \mathbf{H}^*)\}$$

Making use of the vector identity the point form of the complex Poynting vector is $\nabla \cdot (\mathbf{A} \times \mathbf{B}) = \mathbf{B} \cdot (\nabla \times \mathbf{A}) - \mathbf{A} \cdot (\nabla \times \mathbf{B})$:

$$\begin{aligned}\nabla \cdot (\mathbf{E} \times \mathbf{H}^*) &= \mathbf{H}^* \cdot (\nabla \times \mathbf{E}) - \mathbf{E} \cdot (\nabla \times \mathbf{H}^*) \\ &= -j\omega \mathbf{B} \cdot \mathbf{H}^* - \mathbf{E} \cdot (\mathbf{J}^* - j\omega \mathbf{D}^*) \\ &= -j\omega \mathbf{B} \cdot \mathbf{H}^* - \mathbf{E} \cdot \mathbf{J}^* - j\omega \mathbf{E} \cdot \mathbf{D}^*.\end{aligned}$$

If Ampère's law is written in terms of the effective conductivity σ as discussed in the introduction which includes both static and ac loss, then $j\omega \mathbf{E} \cdot \mathbf{D}^* = j\omega \epsilon' |\mathbf{E}|^2$ which is purely imaginary and may be left out of the volume loss density expression resulting in

$$\rho_v = \frac{1}{2} \text{Re} \{ \mathbf{E} \cdot \mathbf{J}^* + j\omega \mathbf{B} \cdot \mathbf{H}^* \}, \quad (4.83)$$

which is the form presented in the HFSS documentation. From the power dissipated in each layer P_n , $P(z)$ can be found by

$$\frac{P(z_n)}{P_{\text{tot}}} = 1 - \frac{P_{\text{up}}}{P_{\text{tot}}} - \sum_{i=1}^n \frac{P_i}{P_{\text{tot}}}, \quad (4.84)$$

which is illustrated in Fig. 4.11.

Numerical simulation and theory are compared in Fig. 4.12 demonstrating very good agreement (within 3%) over the frequency range of 500 MHz to 3 GHz. The theoretical results for the normalized power level $P(z)/P_{\text{tot}}$ as a function of depth is shown in Fig. 4.13 for the frequencies of 500 MHz 1.5 GHz, and 3 GHz, demonstrating power is dissipated closer to the antenna for an increase in frequency.

To determine the limitations for this particular example, the sensing depth is calculated from (4.77) and shown vs. frequency as a function of the ratio of the receiver sensitivity σ to the incremental increase in temperature ΔT . The sensing depth is shown on a contour plot in Fig. 4.14, and a plane wave attenuation is shown in Fig. 4.15. The plane wave assumption is that the power decays as $\exp(-2\alpha z)$, and all the power accepted into the antenna is radiated into the lower half-space. Fig. 4.16 shows the sensing depth for the $0.6\lambda_{\text{eff}}$ dipole on a dispersive lossy half-space compared to the case of an incident plane wave on the same half space. From Fig. 4.16 it can be seen that for larger sensitivity ratios the sensing depth is much lower for the near-field case as compared to a plane wave. The frequency dependence of the sensing depth is different for

the two cases, but increases with decreasing frequency. The near-field behavior differs greatly from the plane wave case for large sensitivity ratios. The results have important implications in the design of microwave radiometer for near-field temperature measurements that utilize a dipole in contact with a lossy medium. It is also demonstrated that theory and HFSS agree well, thus, if HFSS is more convenient, it can be used. However, to determine the power dissipated close to the antenna, the half-space must be comprised of many individual layers for which the volume loss density is calculated and integrated over the subvolume.

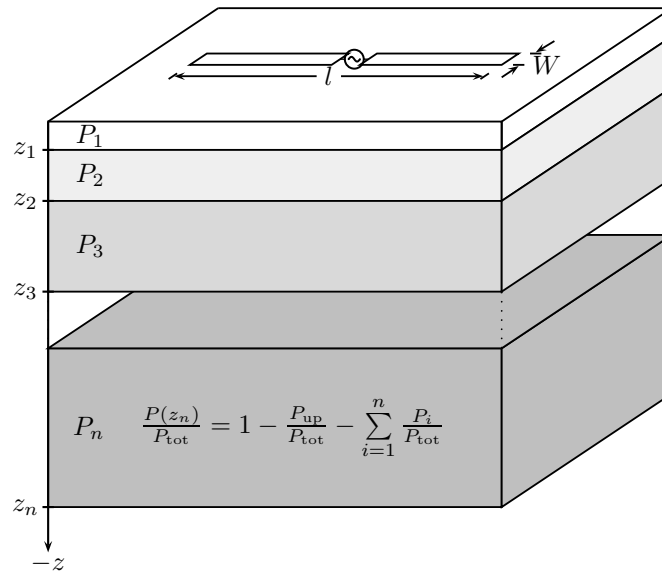


Figure 4.11: Summary of determining $P(z)$ from HFSS simulations. The volume loss density is integrated over each subvolume. From the power dissipated in each layer, $P(z)$ can be found.

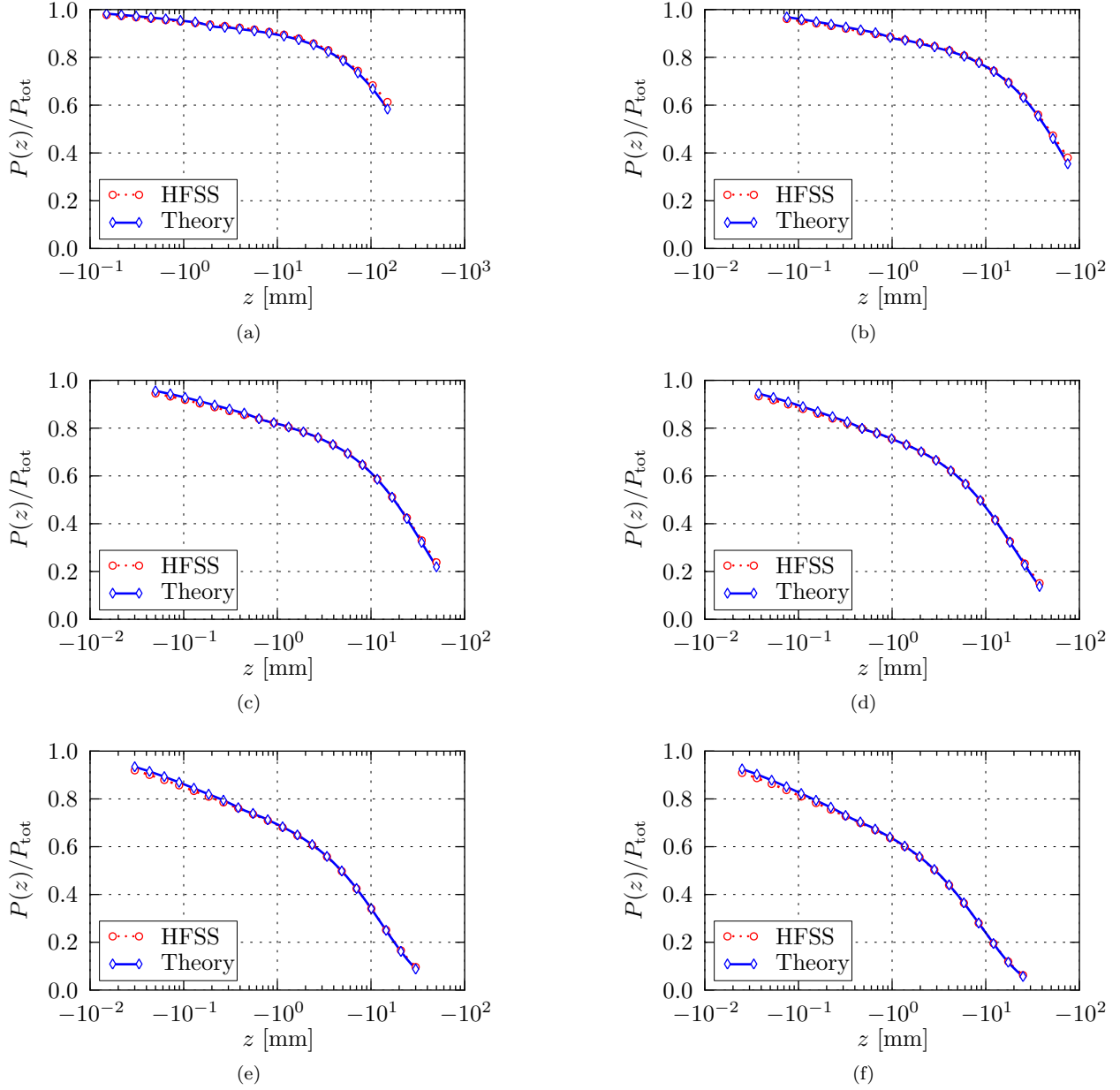


Figure 4.12: Comparison of theory to simulated results for the normalized power level $P(z)/P_{\text{tot}}$ vs. z of a dipole above a lossy half-space at (a) 500 MHz, (b) 1 GHz, (c) 1.5 GHz, (c) 2 GHz, (d) 2.5 GHz, and (d) 3 GHz.

4.5 DIPOLE ON SKIN, FAT, AND MUSCLE

After validation with numerical simulation for a simple phantom, the sensing depth of a dipole above a three layer medium consisting of skin, fat, and muscle is quantified. As in the previous section, the dipole is assumed to be in contact with the skin layer. The thickness of the skin is assumed to be 2 mm, fat 10 mm, and the muscle is assumed to be infinite in extent as seen in Fig. 4.17. In the previous section the relative permittivity

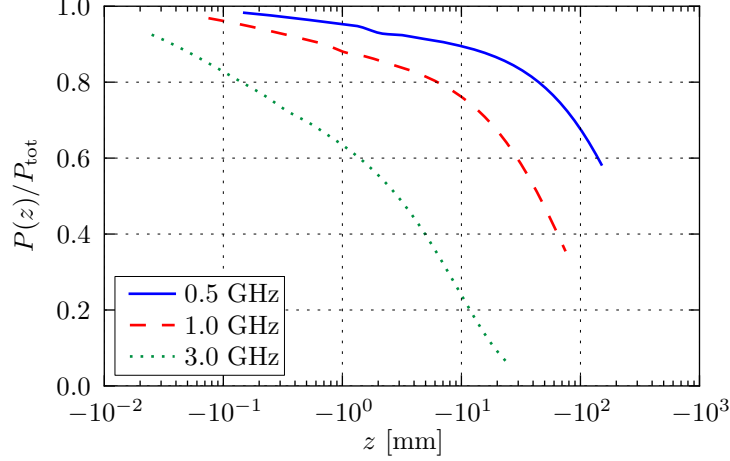


Figure 4.13: Comparison of the theoretical results for the normalized power level $P(z)/P_{\text{tot}}$ vs. z of a dipole above a lossy half-space for the following frequencies: 500 MHz, 1.5 GHz, and 3 GHz.

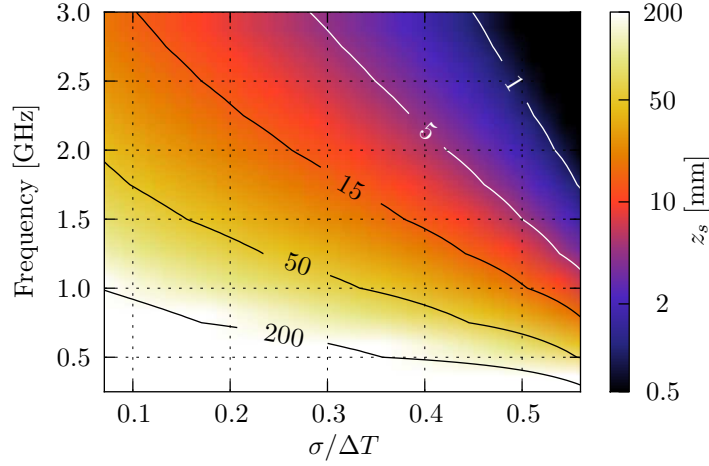


Figure 4.14: Sensing depth z_s as defined by (4.77) vs. frequency and the ratio of the receiver sensitivity σ to the incremental increase in temperature ΔT for a $0.6\lambda_{\text{eff}}$ dipole on a lossy half-space.

and conductivity were assumed to be constant over frequency. In this section the electromagnetic properties of the tissues are given in [25,26], and the dielectric properties at a few frequencies are shown in Table 4.1. To compare dipoles on the surface of a lossy dielectric, the electric length of the dipoles are chosen to be $0.57\lambda_{\text{eff}}$, as this length is matched well to a $50\ \Omega$ generator. The input impedance is found using the variational solution method from Appendix A. The input impedance is shown in Fig. 4.18. The simulated results from HFSS are within $6\ \Omega$ of the theoretical values for both the resistance and reactance from 500 MHz to 3 GHz.

Next, the sensing depth is determined. The general equation for the power flowing in a stratified medium is given in Appendix B, and was used to determine the power flowing through a transverse plane at some

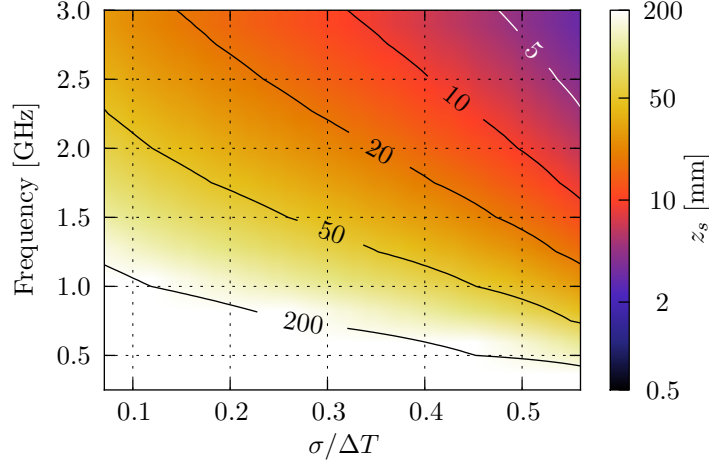


Figure 4.15: Sensing depth z_s as defined by (4.77) vs. frequency and the ratio of the receiver sensitivity σ to the incremental increase in temperature ΔT for a plane wave propagating in a lossy medium. The power is normalized to 1 at the interface between the two media.

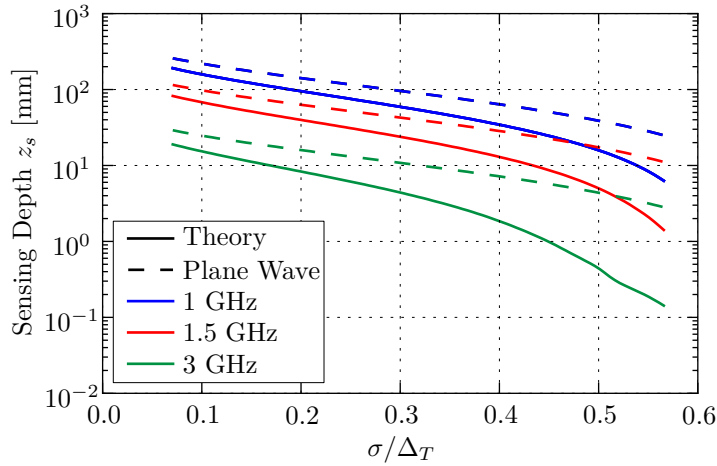


Figure 4.16: Sensing depth z_s as defined by (4.77) vs. the ratio of the receiver sensitivity σ to the incremental increase in temperature ΔT for a $0.6\lambda_{\text{eff}}$ dipole on a lossy half-space. The three frequencies (1 GHz, 1.5 GHz, and 3 GHz) shown are compared to a plane wave assumption that the power decays as $\exp(-2\alpha z)$.

depth in the layered medium. The Python code in Appendix D was used to determine the unknown reflection and amplitude coefficients in each layer using the procedure given at the end of Section 4.2.1. The sensing depth z_s is shown in Fig. 4.19, demonstrating a decrease in sensing depth for an increase in frequency over a sensitivity ratio ($\sigma/\Delta T$) from 0.15 to 0.35. However, between the sensitivity ratio 0.1 to 0.15 the sensing depth is greater at 1.5 GHz than 500 MHz. This demonstrates the inaccuracy in assuming a plane wave propagation. Additionally, it is important to know the sensitivity ratio when choosing frequencies that will achieve a desired sensing depth.

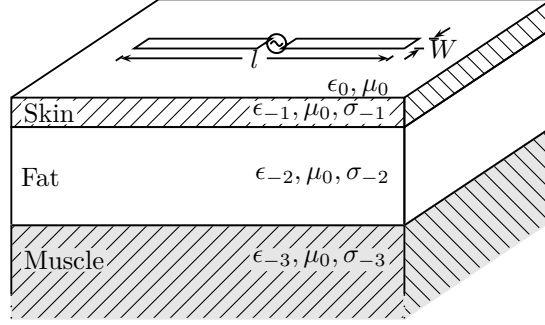


Figure 4.17: Three layer tissue model consisting of skin, fat, and muscle.

The three layer medium was repeated for 1 mm of skin and 2 mm of fat for a $0.57\lambda_{\text{eff}}$ dipole. The results shown in Fig. 4.20 demonstrate similar sensing depth behavior if the sensitivity ratio $\sigma/\Delta T$ is close to 0.1. However, there is a greater sensing depth if the sensitivity ratio is greater than 0.2. It is also observed that the sensing depth is greater as frequency increases when compared to the 2 mm of skin and 10 mm of fat medium. These two cases were examined to give an example of how the sensing depth may change due to tissue variability between subjects. Inter-subject variability can be estimated using a virtual population such as that provided by the IT'IS Foundation [30].

To illustrate the dependence of sensing depth on the sensitivity ratio ($\sigma/\Delta T$), an example will be given for the two tissue stacks previously considered: (a) 2 mm skin/10 mm fat/muscle; and (b) 1 mm skin/ 2 mm fat/muscle. Consider a receiver sensitivity $\sigma = 0.2\text{K}$. If the desired detectable temperature change $\Delta T = 1\text{K}$,

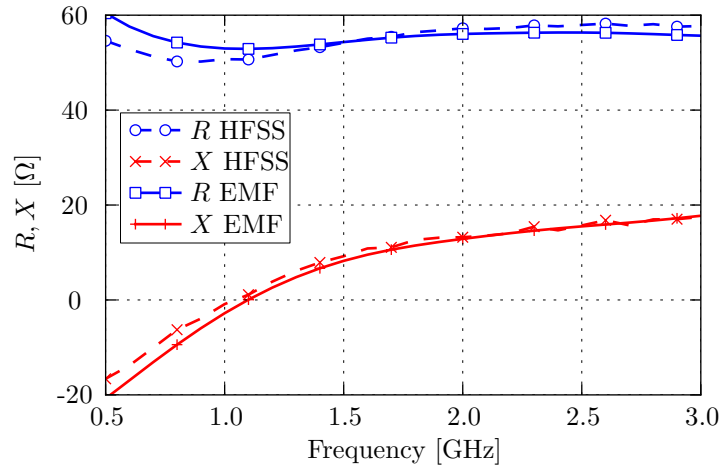


Figure 4.18: Comparison of theory to simulated results for the impedance of a $0.57\lambda_{\text{eff}}$ dipole above a three layer medium comprised of 2 mm of skin, 10 mm of fat, and muscle.

then the sensitivity ratio seen in the right hand side of (4.77) will be 0.2. The problem may be analyzed in the reciprocal case where the antenna is transmitting. Thus, the goal is to find where the signal radiated by the antenna has decayed by 80% assuming $\eta_r = 1$. The sensing depth for a few frequencies from 500 MHz to 2.5 GHz are listed in Table 4.3 showing a decreasing sensing depth as frequency increases for tissue stack (a). For tissue stack (b) the sensing depth increase slightly from 500 MHz to 1 GHz then decreases.

Next, consider the receiver sensitivity improving to $\sigma = 0.1$ K, resulting in a sensitivity ratio of 0.1. Note that the same sensing depth could be achieved for $\sigma = 0.2$ K and $\Delta T = 2$ K yielding a sensitivity ratio of 0.1. This can be seen in (4.77) as the sensing depth is a function of the ratio of receiver sensitivity to change in temperature. In the case of a sensitivity ratio of 0.1, Table 4.3 demonstrates an increase in the sensing depth from 500 MHz to 1 GHz for tissue stack (a). However, for tissue stack (b) the sensing depth decreases across the whole frequency range. Table 4.3 demonstrates how sensing depth is a function of receiver sensitivity,

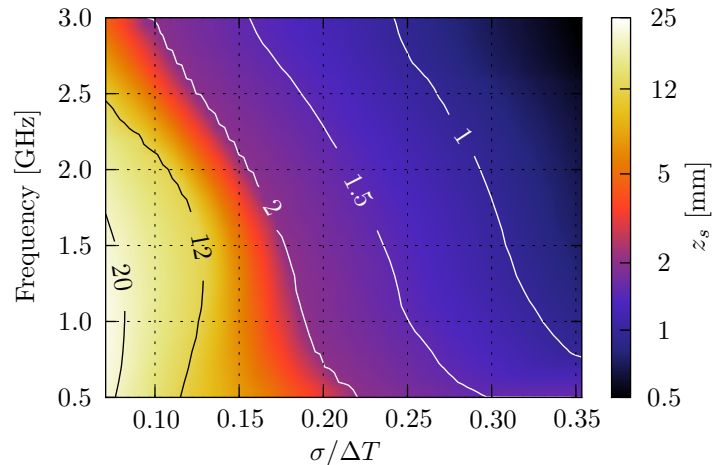


Figure 4.19: Sensing depth z_s as defined by (4.77) vs. frequency and the ratio of the receiver sensitivity σ to the incremental increase in temperature ΔT for a $0.57\lambda_{\text{eff}}$ dipole above a three layer medium comprised of 2 mm of skin, 10 mm of fat, and muscle.

Table 4.3: Sensing depth (mm) at various frequencies for sensitivity ratios of 0.2 and 0.1. Two different three layer media are considered: (a) 2 mm skin/10 mm fat/muscle, and (b) 1 mm skin/2 mm fat/muscle.

Stack	$\sigma/\Delta T$	z_s [mm]				
		0.5 GHz	1 GHz	1.5 GHz	2 GHz	2.5 GHz
a	0.2	8.2	8	7.4	3.5	1.8
a	0.1	21.7	22.7	21.3	17.6	11.1
b	0.2	10.7	11.0	10.2	8.7	7.4
b	0.1	22.9	22.6	19.9	16.8	14.1

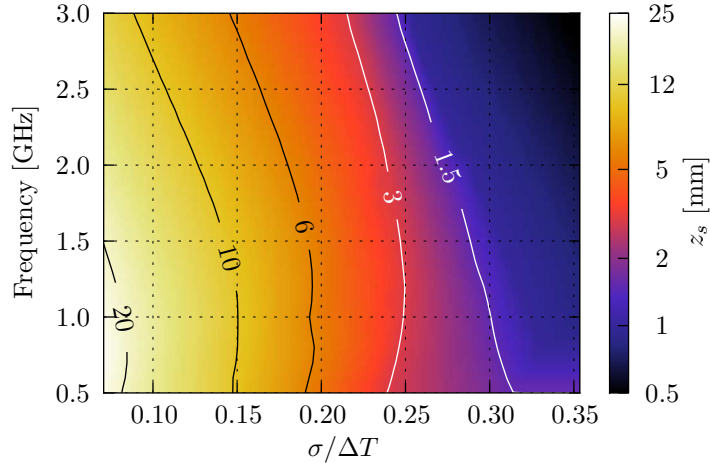


Figure 4.20: Sensing depth z_s as defined by (4.77) vs. frequency and the ratio of the receiver sensitivity σ to the incremental increase in temperature ΔT for a $0.57\lambda_{\text{eff}}$ dipole above a three layer medium comprised of 1 mm of skin, 2 mm of fat, and muscle.

change in temperature, and near field weighting functions.

4.6 CONCLUSION

This chapter detailed the analysis of a dipole in a lossy stratified medium, with a goal to determine the sensitivity limitations for thermal radiation measurement of deep seated tissues in the body and in the near field of the dipole. The results are important for designing a dipole probe to achieve a desired sensing depth for near-field microwave thermometry. An improved sensing depth metric is defined to determine the sensitivity limitations for thermal radiation measurement of deep seated tissues in the body and in the near field of the dipole. The sensing depth is not only a function of the near field power dissipation, but is also dependent on the receiver sensitivity σ and the desired temperature resolution ΔT .

To analyze the frequency dependent behavior of a dipole used for near-field microwave radiometry, a simplified model of a dipole in a lossy stratified medium is used. The medium is assumed to be uniform and infinite in extent in the x and y transverse planes while discontinuous in z . A finite number of layers are assumed where the outermost layers extend to infinity. A spectral-domain technique is applied to determine the input impedance and sensing depth, defined in terms of the dipole near-field weighting functions, the total power radiometer sensitivity, and the desired temperature resolution.

The technique is verified for the general case of a dipole on a water half-space by comparing impedance and normalized power dissipation to commercial FEM software, Ansys HFSS, with good agreement. The results enable design of other types of probes for a desired sensing depth by extending the theory to a three layer human tissue model of skin, fat, and muscle. The input impedance is validated with Ansys HFSS.

From the presented model, an optimal frequency can be determined for a desired sensing depth and tissue stack. However, a number of practical constraints will also affect the frequency choice. For example, the ambient radio frequency spectrum is congested, degrading the achievable signal to noise ratio (SNR) at many frequencies that might otherwise be optimal for passive sensing. Overall size and location of probe dictated by the application will also impose constraints on the choice of frequency. Additionally, bodies vary from patient to patient changing the performance of the probe. For this reason, two examples were given of different skin and fat thicknesses. Inter-subject variability can be estimated using a virtual population such as that provided by the IT'IS Foundation [30].

CHAPTER 5

RADIOMETRIC MEASUREMENTS

CONTENTS

- 5.1 Overview 107
- 5.2 The Inverse Problem: Temperature Retrieval 107
- 5.3 Radiometric Estimation of Variable Temperature Single Layer Phantom 109
- 5.4 Single Frequency Estimation of Subsurface Temperature 113
- 5.5 Inverse Problems in Radiometry 117
 - 5.5.1 Least-squares Method 118
 - 5.5.2 Optimal Estimation Method 118
- 5.6 Multi-frequency Estimation of Subsurface Temperature 119
 - 5.6.1 Least-Squares Solution to Three Layer Measurement 121
 - 5.6.2 Optimal Estimation of Three Layer Measurement 125
 - 5.6.3 Multi-frequency Estimates Discussion 126
- 5.7 Tissue Thickness Variability Analysis 129
- 5.8 Conclusion 135

5.1 OVERVIEW

Passive radiometry estimates of the antenna temperature seen at the input of the radiometer require inverse techniques in order to determine the unknown subsurface temperature from temperatures measurements by radiometry, an inverse problem needs to be solved. The inversion process uses near-field weighting functions defined in Chapter 1. The model of the inverse problem is defined, and used to determine temperature from the 1.4 GHz and 2.7 GHz radiometers measurements. The first measurements utilize a single radiometer at a time to track the temperature change of a homogeneous approximate half-space. Next, the 1.4 GHz radiometer is used to determine the subsurface temperature of a three layer volume consisting of water, glass, and water.

The single frequency measurements simply solve a single equation for a particular unknown. For multiple measurements and unknowns, inversion techniques such as least-squares and optimal estimation may be used to determine the unknown temperature profile. These techniques are applied to a two frequency measurement of a three layer phantom consisting of water, glass, and water. Measured results and a comparison of the techniques are given, followed by a discussion relating the measured results to parameters necessary for monitoring the circadian rhythm.

Finally, a variability analysis is done to demonstrate how error in the weighting functions affect the inverse problem, and how different inverse methods may be used. This variability analysis is extended to estimate the feasibility of using this system for monitoring the circadian rhythm.

5.2 THE INVERSE PROBLEM: TEMPERATURE RETRIEVAL

The inverse problem for a probe measuring a half-space that may be stratified is depicted in Fig. 5.1. The thermal model considered is layers of constant temperature. Models of the temperature profile are often used as a way improve spatial resolution while reducing the number of unknown parameters [10, 11, 105–107]. The first task in the inversion procedure is to estimate the antenna temperature at the feed of the antenna T_A from the radiometric observation at the plane of calibration on the radiometer T_A'' . The effects of mismatch

must be treated in a standard manner [2, Chaper 6], [98], and for the purpose of simplifying the inversion a few assumptions are made:

- The cable is assumed to be perfectly match and low loss (<0.5 dB);
- Γ seen at the input to the radiometer is assumed to be the measured Γ at the feed of the probe;
- The temperature of the cable is assumed to be a constant temperature equal to the room temperature, which is also the temperature of the load used for calibration.
- The noise temperature generated by the receiver towards the antenna is assumed to be 150 K.

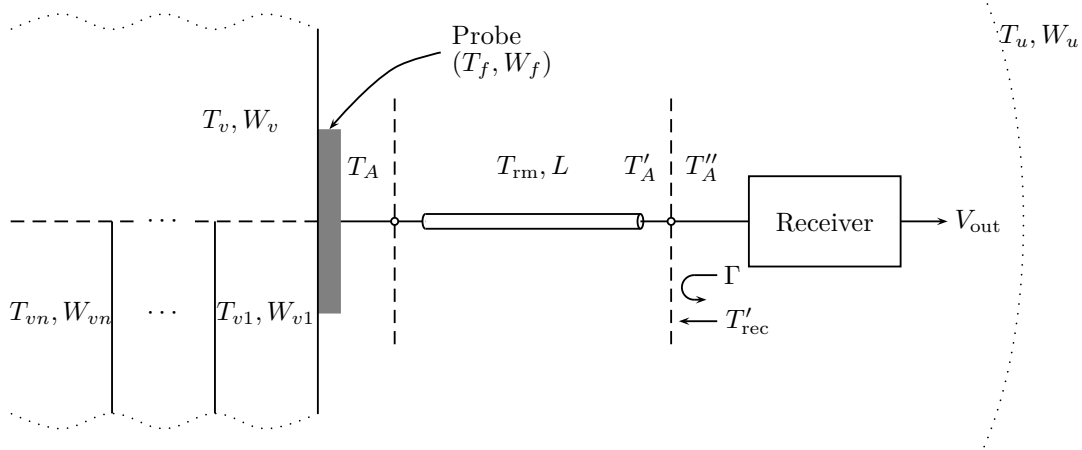


Figure 5.1: Diagram of the inverse problem. The radiometer measures a temperature T''_A which includes the contribution from the noise generated by the receiver (T'_{rec}) due to reflection (Γ) from the available noise temperature T'_A . Additionally, any loss L through a cable which is assumed to be matched will change the antenna temperature T_A due to the physical temperature of the cable T_{rm} . The antenna temperature includes contributions from the feed (T_f, W_f), the upper half-space (T_u, W_u), and each volume in the layered media (T_{vn}, W_{vn}) or for the half-space problem the lower half-space (T_v, W_v).

With these assumptions in mind, the antenna temperature is first corrected due to reflection as

$$T'_A = \frac{T''_A - T'_{rec} |\Gamma|^2}{1 - |\Gamma|^2}. \quad (5.1)$$

Next, the antenna temperature is corrected due to the loss in the cable as

$$T_A = T'_A L - (L - 1) T_{rm}. \quad (5.2)$$

This procedure corrects the radiometric observations up to the plane of the feed of the antenna. The goal of the inverse problem is to determine the temperature of an object or layer that the antenna is receiving thermal

radiation from. The antenna temperature may be expressed in terms of the weighting functions in (1.16). For the half-space problem shown in the upper half of the volume in Fig. 5.1 the antenna temperature is

$$T_A = T_u W_u + T_f W_f + T_v W_v. \quad (5.3)$$

Therefore if the temperature of the feed T_f and the upper half-space temperature T_u is known along with the weighting functions from simulation, the unknown half-space temperature may be solved for. This inversion is explored in the next section to determine one unknown layer.

5.3 RADIOMETRIC ESTIMATION OF VARIABLE TEMPERATURE SINGLE LAYER PHANTOM

The radiometers and probes presented in Chapter 2 are used to determine the temperature of a variable temperature half-space. This initial measurement is to demonstrate the radiometer's ability to detect temperature from a lossy material half-space. Later this will be extended to determining subsurface temperature, as the lossy half-space problem is a volume average of the temperature. To demonstrate this temperature detection, the test setup was placed in an anechoic chamber to reduce interference.

The 1.4 GHz receiver was calibrated using the method described in Section 2.4.1 with the hot calibration standard being the Agilent 346A noise source, and the cold temperature is a room temperature microwave load. The temperature of the load was measured with a thermocouple connected to the PicoTech TC-08 data logger. The calibration was performed every second with an equal dwell time on each of the standards and the unknown antenna temperature. The antenna was placed so that it was just touching the surface of the water. The antenna was connected to the radiometer through a 30 cm cable. To ensure air bubbles would not form on the surface of the probe and effecting the impedance match, the water was heated using an immersion heating coil. Once the water was heated to above 40°C the measurement was started. The water was allowed to cool off over a period of two hours, and the calibrated estimate of the antenna temperature seen at the plane of the radiometer (T_A'' in Fig. 5.1) was determined.

The raw estimate of the antenna temperature at the plane of the radiometer T_A'' was first corrected due to reflection. As was discussed in Chapter 1 the dielectric properties of water are temperature dependent.

The input reflection coefficient of the probe was measured at two separate temperatures: 40°C and 20°C. The reflection coefficient is compared in Fig. 5.2a demonstrating a slight difference. However, at the design frequency of 1.4 GHz, they are essentially the same. In the inversion process, the magnitude of the reflection coefficient was assumed to be $|\Gamma| = -23$ dB. The correction due to impedance mismatch was done using (5.1) to determine T'_A which is the available temperature at the input to the receiver. This estimate involves the following assumptions:

- The reflection coefficient of the probe is constant over the predetection bandwidth and constant over temperature;
- Since the cable is assumed to be perfectly matched and the input to the receiver is assumed to be 50Ω , the measured reflection coefficient of the probe at the design frequency of 1.4 GHz was used as the Γ in (5.1);
- The temperature generated towards the antenna at the input of the receiver T'_{rec} is estimated to be 150 K;

If these assumptions are incorrect, the result will be an error in the estimate of the available temperature T'_A . However, since the probe is well matched ($|\Gamma| = -23$ dB), only 0.5% of the temperature is due to reflection from the receiver. Therefore, even if the receiver temperature is really 300 K rather than 150 K, the contribution from the receiver would be 1.5 K rather than 0.75 K and does not significantly affect the estimate of the volume.

Next, the temperature is corrected due to loss in the matched cable using (5.2). At 1.4 GHz the loss in the cable is approximately 0.3 dB and the temperature of the cable is assumed to be room temperature, or the same temperature as the “cold” calibration standard. To estimate the actual temperature of the water, (5.3) is solved for T_v assuming the feed temperature T_f is the same as the temperature of the water T_v as the probe is placed in contact with the water resulting in

$$T_v = \frac{T_A - T_u W_u}{W_f + W_v}. \quad (5.4)$$

The upper half-space temperature is assumed to be equal to the room temperature T_{rm} .

The weighting functions are determined in simulation for room temperature water (20°C) and used to invert the data and are listed in Table 2.4. The radiometric temperature estimate is shown in Fig. 5.2b along with a thermocouple measurement of the water temperature T_t . To show the discrepancy between the radiometric estimate through the inversion process and the thermocouple measurement, every one minute of data was averaged and the radiometric estimate is shown vs. the thermocouple measurement in Fig. 5.2b. This demonstrates an error of about 0.4°C to 1.1°C. Discrepancy from the radiometric estimate and the thermocouple over time is probably due to incorrect assumption of the feed temperature T_f and possibly changes in the weighting function over time due to the changing dielectric properties.

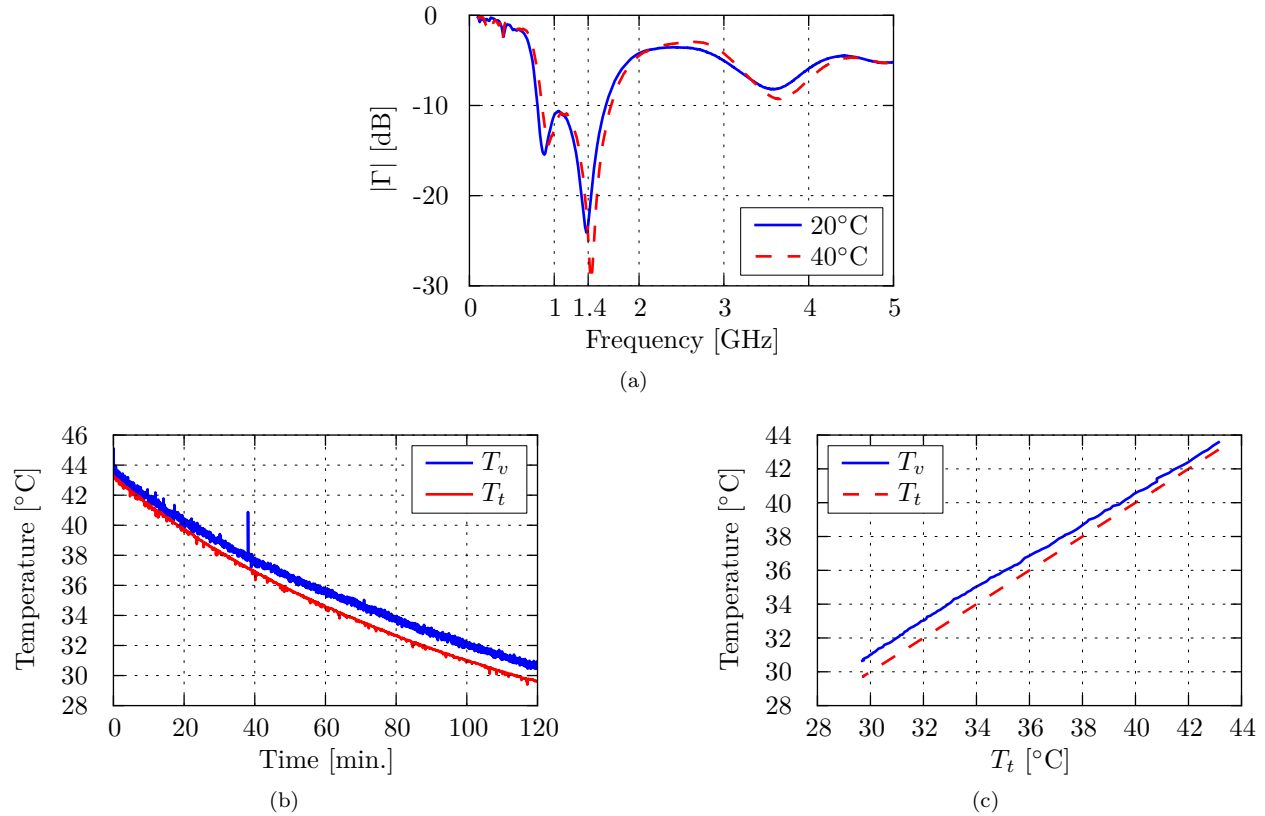


Figure 5.2: (a) Measured reflection coefficient of the probe at two different temperatures. (b) Radiometric estimate of the temperature of a water half-space T_v using the 1.4 GHz radiometer compared to the measured thermocouple temperature T_t vs. time. (c) A direct comparison of T_v vs. T_t showing how the radiometric estimate compares to the thermocouple measurements.

The same measurement was duplicated for the 2.7 GHz receiver using the same calibration process previously described. The water was heated with an immersion heating coil to ensure no air bubbles would form on the probe changing the reflection coefficient. The reflection coefficient of the probe was measured at

the hot (40°C) and cold (20°C) temperatures, and are compared in Fig. 5.3a. It can be seen that the probe reflection coefficient differs for the two temperatures. At the design frequency of 2.7 GHz this corresponds to a difference of -21 to -18 dB for 40°C and 20°C respectively.

The raw estimate of the antenna temperature at the plane of the radiometer T''_A was first corrected due to reflections using (5.1) to determine T'_A which is the available temperature at the input to the receiver. This estimate involves the following assumptions:

- The reflection coefficient of the probe is constant over the predetection bandwidth and linearly changes from -21 to -18 dB over the temperature change of the test setup (45°C to 31°C).
- Since the cable is assumed to be perfectly matched and the input to the receiver is assumed to be 50 Ω, the reflection coefficient of the probe at the design frequency of 2.7 GHz was used as the Γ in (5.1) with the temperature dependence previously stated.
- The temperature generated towards the antenna at the input of the receiver T'_{rec} is estimated to be 150 K.

The temperature was corrected due to loss in the cable (0.3 dB at 2.7 GHz) in the same manner as the 1.4 GHz measurements were corrected. The weighting functions are determined in simulation for room temperature water (20°C) and used to invert the data and are listed in Table 2.6. The radiometric temperature estimate is shown in Fig. 5.3b along with a thermocouple measurement of the water temperature T_t . To show the discrepancy between the radiometric estimate through the inversion process and the thermocouple measurement, every one minute of data was averaged and the radiometric estimate is shown vs. the thermocouple measurement in Fig. 5.3c. This demonstrates an error of about 1.4°C. Discrepancy from the radiometric estimate and the thermocouple over time is probably due to incorrect assumption of the feed temperature T_f and possibly changes in the weighting function over time due to the changing dielectric properties.

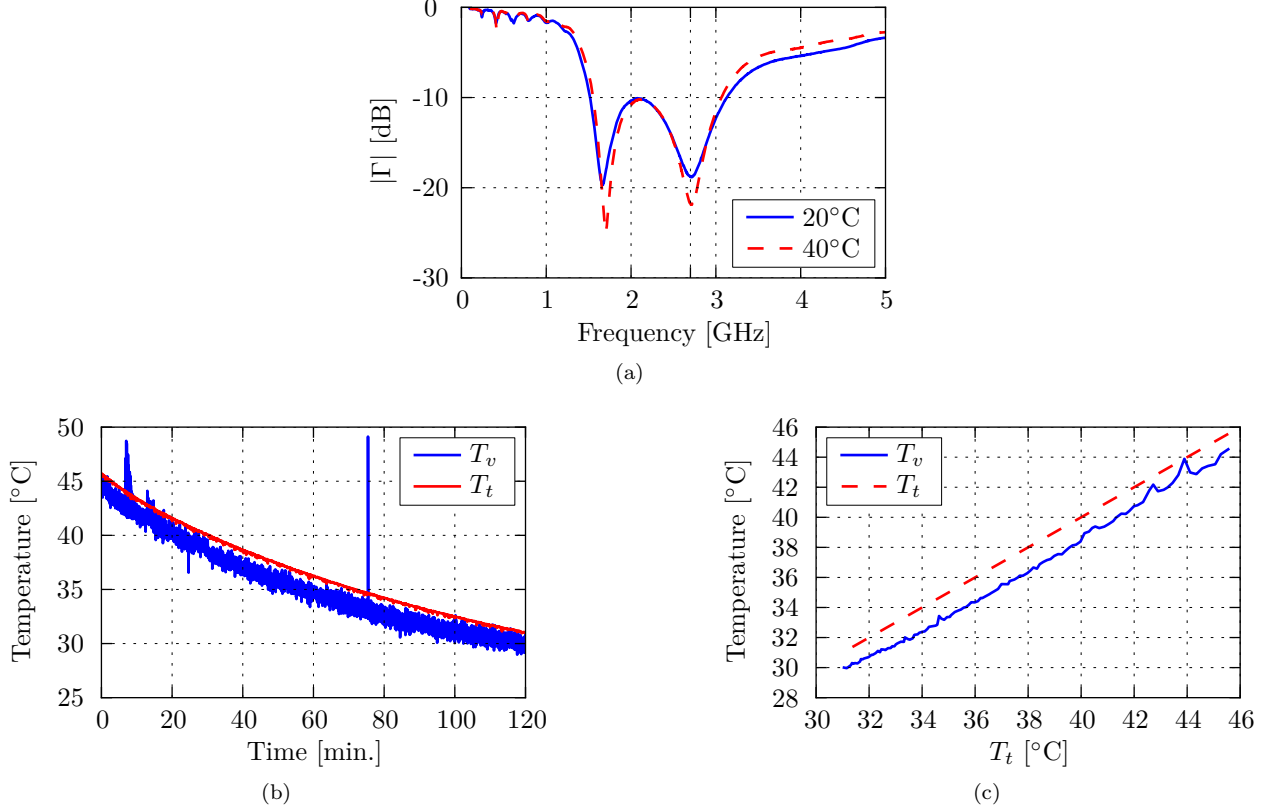


Figure 5.3: (a) Measured reflection coefficient of the probe at two different temperatures. (b) Radiometric estimate of the temperature of a water half-space T_v using the 2.7 GHz radiometer compared to the measured thermocouple temperature T_t vs. time. (c) A direct comparison of T_v vs. T_t showing how the radiometric estimate compares to the thermocouple measurements.

5.4 SINGLE FREQUENCY ESTIMATION OF SUBSURFACE TEMPERATURE

Having demonstrated the ability to detect temperature changes of a water half-space with both receivers, a three layer phantom is investigated next. The three layers are water, glass (Pyrex), and water. The reason for choosing glass is that the dielectric constant ($\epsilon'_r = 5.5$) is close to that of fat ($\epsilon'_r = 5.4$ at 1.4 GHz). Utilizing a glass pyrex baking dish with a lip, three layers were created by putting a small amount of water ≈ 10.3 mm in depth in the glass dish, then the dish was placed in the plastic bin filled with water. The thickness of the glass is 5 mm. The bottom layer was heated and the top layer started at room temperature. The glass Pyrex dish was placed in the heated water, thus producing two layers of water. The lower layer of water decreased in temperature over time, and the top layer of water increased in temperature over time.

The 1.4 GHz radiometer and probe were used to measure the three layer problem. The calibration procedure was done in the same manner previously described. The inverse problem now takes the form of determining the third layer temperature. This is depicted in the lower half of Fig. 5.1. The procedure for correcting the measured temperature T_A'' to the plane of the antenna was done by assuming 0.3 dB loss in the cable feeding the antenna. Additionally, the antenna reflection coefficient was measured using two layers of 20°C water. The thicknesses were 10.3 mm water, 5 mm glass, 10 cm water. A comparison of measured and simulated reflection coefficient is shown in Fig. 5.4a demonstrating good agreement across frequency with a better measured match than was simulated. The correction due to mismatch and loss through the cable was performed with the following assumptions:

- The reflection coefficient of the probe is constant over the predetection bandwidth and constant over temperature.
- Since the cable is assumed to be perfectly matched and the input to the receiver is assumed to be 50Ω , the measured reflection coefficient of the probe at the design frequency of 1.4 GHz was used as the Γ in (5.1).
- The temperature generated towards the antenna at the input of the receiver T_{rec}' is estimated to be 150 K.

The antenna temperature is a weighted volume average of the temperature of objects in the near-field and far-field of the antenna. The antenna temperature for the three layer problem is

$$T_A = T_u W_u + T_f W_f + T_{v1} W_{v1} + T_{v2} W_{v2} + T_{v3} W_{v3}, \quad (5.5)$$

where, referring to Fig. 5.1, T_{v1}, W_{v1} refers to the temperature and weighting function of the first 10.3 mm layer of water. T_{v2}, W_{v2} corresponds to the temperature and weighting function of the 5 mm glass layer, and T_{v3}, W_{v3} corresponds to the subsurface water layer. The weighting functions from simulation, described in detail in Chapter 4, are given in Table 5.1. The goal for the inverse problem is to determine the temperature of the subsurface water layer. To do this, however, the temperature contribution from all the other layers must be known. The unknown temperature is determined by solving (5.5) for T_{v3} yielding

$$T_{v3} = \frac{T_A - T_u W_u - T_f W_f - T_{v1} W_{v1} - T_{v2} W_{v2}}{W_{v3}}. \quad (5.6)$$

The weighting functions are assumed to be constant over temperature. The top and bottom water temperatures were measured with thermocouples denoted by T_{t1}, T_{t3} and the data recorded with the PicoTech data logger. Since the data logger sampling rate is faster than the calibration time, the top water layer is fitted to an exponential of the form

$$A \exp^{-t/b} + C, \quad (5.7)$$

using `curve_fit` a non-linear least squares regression tool available in the Python library SciPy. The raw thermocouple data is shown along with the fit $T_{v1,\text{fit}}$ in Fig. 5.4b. In the inverse problem, the feed and glass are assumed to be equal to the top layer temperature $T_{v1,\text{fit}}$ simplifying (5.6) to

$$T_{v3} = \frac{T_A - T_u W_u - T_{v1,\text{fit}}(W_f + W_{v1} + W_{v2})}{W_{v3}}. \quad (5.8)$$

The upper half-space is again assumed to be at room temperature. The result of the inversion is shown in Fig. 5.4c along with the thermocouple measurements of the water layers and the antenna temperature T_A which is between the two temperatures as expected as the antenna temperature is a weighted volume average. The thermocouple measurement T_{t3} and radiometric estimate T_{v3} are shown together in Fig. 5.4d showing good agreement. It is evident from Fig. 5.4c that the variance of the estimate of T_{v3} is larger than T_A which is to be expected as the weighting function from the third layer is only 0.385. This is easily seen by considering the fact that the combined uncertainty [108] of (5.8) assuming the random variables are independent is

$$\sigma_c^2(T_{v3}) = \sum_{i=1}^N \left(\frac{\partial T_{v3}}{\partial x_i} \right)^2 \sigma^2(x_i), \quad (5.9)$$

for estimates x_1, x_2, \dots, x_N . Assuming the variance in the estimates of T_u and $T_{v1,\text{fit}}$ are zero, the combined uncertainty is

$$\sigma_c(T_{v3}) = \frac{\sigma(T_A)}{W_{v3}}. \quad (5.10)$$

Table 5.1: 1.4 GHz probe weighting functions on 10.3 mm water, 5 mm glass, and water.

Upper (W_u)	Feed (W_f)	Top Water (W_{v1})	Glass (W_{v2})	Bottom Water (W_{v3})
0.014	0.056	0.543	0.002	0.385

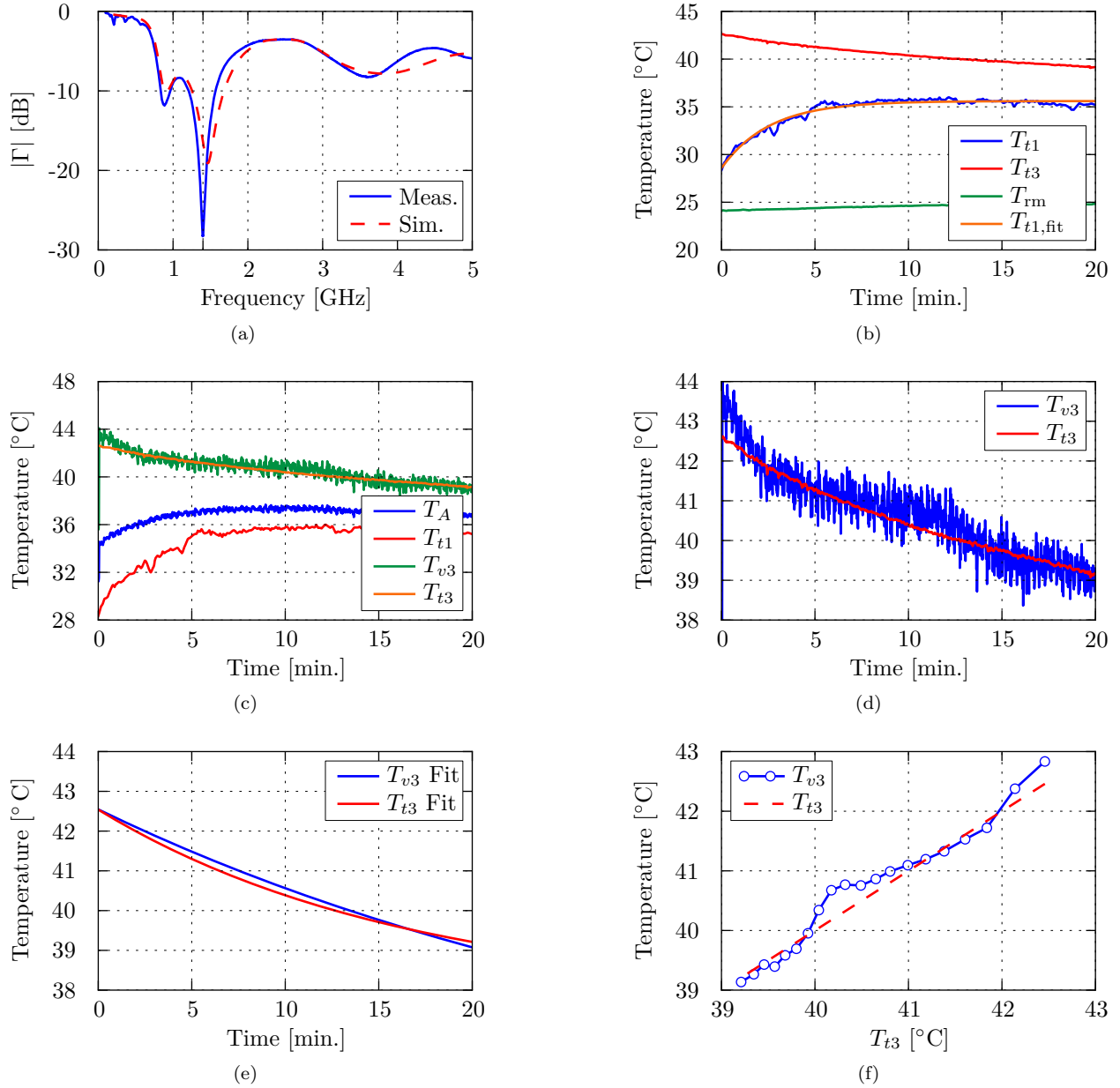


Figure 5.4: Three layer measurement with the 1.4 GHz radiometer of 10.3 mm water, 5 mm glass, and water. The measured and simulated reflection coefficient (a) of the 1.4 GHz probe. Thermocouple measurements of the two water layers and room temperature (b) along with an exponential fit for the top water layer T_{t1} . Radiometric estimate T_{v3} and thermocouple measurement T_{t3} of the subsurface water layer (c) along with the antenna temperature T_A and top water layer thermocouple measurement T_{t1} . Comparison of raw radiometer estimate and thermocouple measurement (d). Comparison of fitted radiometer thermocouple measurements (e). A comparison of the radiometer estimate vs. thermocouple temperature (f).

Next, the thermocouple data T_{t3} , and the radiometric estimate T_{v3} are fitted to the same exponential function from (5.7) using a non-linear least squares regression, and compared in Fig. 5.4e with the corresponding

unknowns from (5.7) listed in Table 5.2. The maximum difference between the fitted thermocouple data and radiometric estimate is 0.2°C as seen in Fig. 5.4e. The discrepancy between the radiometric estimate through the inversion process and the thermocouple measurement is also shown by the average of every one minute of temperature data shown vs. the thermocouple measurement in Fig. 5.4f. This demonstrates an error of up to 0.5°C. Discrepancy from the radiometric estimate and the thermocouple over time is probably due to incorrect assumption of the weighting functions which may change with temperature. Also, placement of the probe on the top layer may deviate from the assumed 10.3 mm depth used in simulation.

Table 5.2: Results of non-linear regression analysis to determine unknowns in (5.7) from thermocouple T_{t3} and radiometric estimates T_{v3} .

Parameter	T_{t3} Fit	T_{v3} Fit
A [°C]	4.73	7.93
b [s ⁻¹]	16.46	34.75
C [°C]	37.81	34.62

5.5 INVERSE PROBLEMS IN RADIOMETRY

Up to this point the inverse problem only involved determining one unknown temperature with one radiometric measurement from the formula for the antenna temperature, while the other temperatures were assumed to be known. However, if multiple frequencies are used with independent observations and different weighting functions for each probe, the measured antenna temperature may be written in matrix form in terms of the weighting functions W and the vector of layer temperatures \mathbf{T} as

$$\mathbf{T}_M = W\mathbf{T} \quad (5.11)$$

where \mathbf{T}_M and \mathbf{T} are vectors of dimension N and M respectively and W is an $N \times M$ matrix. N represents the number of frequencies or independent measurements, and M represents the number of layers or discrete regions at a constant temperature contributing to the antenna temperature.

In (5.11), \mathbf{T}_M represents a vector of noiseless measurements which, in practice, is not possible due to measurement and modeling errors. The measurements may be denoted as

$$\hat{\mathbf{T}}_M = W\mathbf{T} + \mathbf{e} \quad (5.12)$$

where \mathbf{e} is an error vector. There various inversion methods of determining an estimate for the unknown temperature profile \mathbf{T} . The solution of this problem is unstable with the addition of a small amount of experimental error and is therefore considered ill-posed [23, pp. 1294]. This section first presents the standard least-squares solution to the problem, then a statistical inversion method is considered.

5.5.1 LEAST-SQUARES METHOD

In the matrix equation above, consider that there is no solution to the problem which means no linear combination of the column vectors of W will be equal to $\hat{\mathbf{T}}_M$. The least-squares inversion technique is a solution method that aims to determine $\hat{\mathbf{T}}$ which minimizes the error function given by

$$\|\hat{\mathbf{T}}_M - W\hat{\mathbf{T}}\|^2. \quad (5.13)$$

The goal is to find a $\hat{\mathbf{T}}$ in which $W\hat{\mathbf{T}}$ is as close to $\hat{\mathbf{T}}_M$ as possible. This will happen when the error function is orthogonal to the column vectors of W . The orthogonality conditions yield

$$W^T (\hat{\mathbf{T}}_M - W\hat{\mathbf{T}}) = 0. \quad (5.14)$$

Therefore the least-squares solution to (5.11) is

$$\hat{\mathbf{T}} = (W^T W)^{-1} W^T \hat{\mathbf{T}}_M. \quad (5.15)$$

The matrix $(W^T W)^{-1} W^T$ is called the *pseudoinverse*. A more rigorous discussion of the least-squares solution may be found in [109]. The least-squares may be unstable such that the error associated with estimate $\hat{\mathbf{T}}$ is too large due to the elements of $(W^T W)^{-1}$ being large, which amplifies the error, and is often not suitable for radiometric retrieval problems [23].

5.5.2 OPTIMAL ESTIMATION METHOD

A priori constraints on the profile may be used to regularize the ill-posed problem [23]. These constraint are considered *virtual measurements* in that they provide information about the profile in the same way the actual measurements do [23, 110]. These virtual measurements may take the form of historical data or models. This method will be explained in a similar manner to that presented by Rodgers [110] and Ulaby et

al [23]. First consider combining two independent vectors \mathbf{T}_1 and \mathbf{T}_2 with error covariances S_1 and S_2 that are measurements of the vector \mathbf{T} . The combined estimate for \mathbf{T} is given by the weighted average

$$\hat{\mathbf{T}} = (S_1^{-1} + S_2^{-1})^{-1} (S_1^{-1}\mathbf{T}_1 + S_2^{-1}\mathbf{T}_2). \quad (5.16)$$

The first measurement is the virtual measurement \mathbf{T}_0 , e.g. the mean temperature profile. For the human body this may be the average or expected temperature of the skin, fat, and muscle. Additionally, there is the measured quantity from (5.12). Another estimate for $\hat{\mathbf{T}}$ is \mathbf{T}_e where $\mathbf{T}_e = D\hat{\mathbf{T}}_M$ is the exact solution where $WD = I$, the identity matrix. The covariance matrix of \mathbf{T}_e is easily found to be $S_e = (W^T S_M^{-1} W)^{-1}$ where S_M is the covariance of $\hat{\mathbf{T}}_M$. The combined estimate of \mathbf{T} from the measurement vectors \mathbf{T}_0 and \mathbf{T}_e is given from (5.16) yielding

$$\hat{\mathbf{T}} = (S_0^{-1} + W^T S_M^{-1} W)^{-1} (S_0^{-1}\mathbf{T}_0 + W^T S_M^{-1}\hat{\mathbf{T}}_M), \quad (5.17)$$

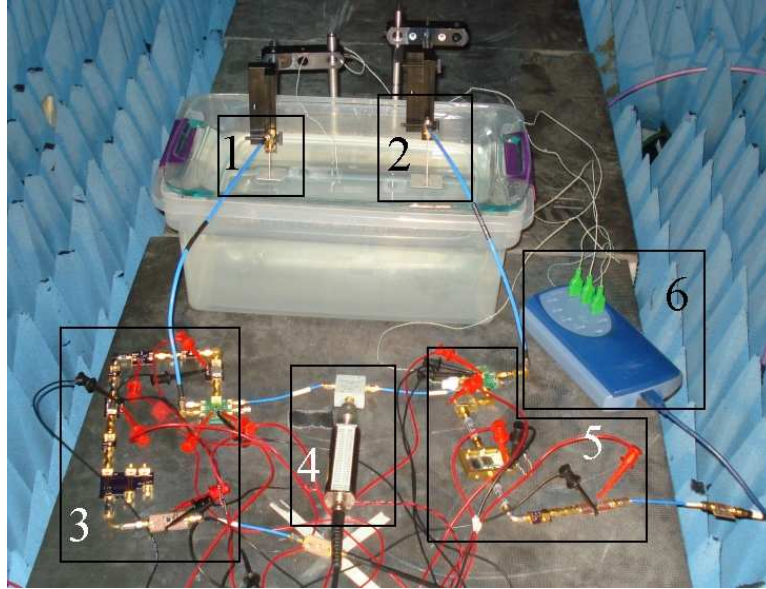
which may be put in a form more efficient for computation [110] as

$$\hat{\mathbf{T}} = \mathbf{T}_0 + S_0 W^T (W S_0 W^T + S_M)^{-1} (\hat{\mathbf{T}}_M - W\mathbf{T}_0). \quad (5.18)$$

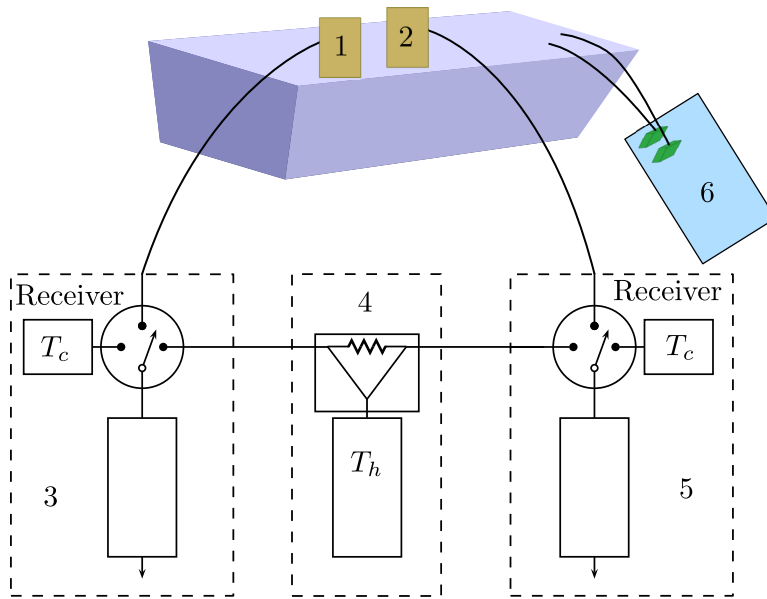
5.6 MULTI-FREQUENCY ESTIMATION OF SUBSURFACE TEMPERATURE

Utilizing the 1.4 GHz and 2.7 GHz receivers presented in Chapter 2, a two-frequency measurement was done of the three layer phantom (10.3 mm water, 5 mm glass, and water). The measurement setup and block diagram are shown in Fig. 5.5. The bottom layer of water was heated to approximately 41°C, where as the top layer of water started at 30°C. Radiometer and thermocouple measurements were taken over a 30 minute period. To determine the unknown water temperatures, the data measured by both radiometers, T_A'' in Fig. 5.1, must be corrected up to the reference plane of the probe (T_A). This was done in the same manner previously described, and the reflection coefficient of the 1.4 GHz probe is shown in along with the 2.7 GHz probe in Fig. 5.6.

For each frequency, the antenna temperature is given by (5.5). Since only two independent measurements are taken, the temperature of the upper half-space temperature is assumed to be the same as room temperature, and the feed, top water, and glass are assumed to be at the same temperature. The following equations will



(a)



(b)

Figure 5.5: Photograph of measurement setup (a), and block diagram (b) with the (1) 2.7 GHz probe, (2) 1.4 GHz probe, (3) 2.7 GHz radiometer, (4) Agilent noise source and power divider, (5) 1.4 GHz radiometer, and (6) PicoTech data logger. Both receivers were constantly calibrated and the unknown antenna temperatures measured.

be solved to determine the unknown temperature where the superscripts 1 and 2 refer to the 1.4 GHz and 2.7 GHz measured antenna temperatures and weighting functions given in Table 5.3

$$T_A^n - W_u^n T_u = (W_f^n + W_{v1}^n + W_{v2}^n) T_{v1} + W_{v3}^n T_{v3} \quad \text{for } n = 1, 2. \quad (5.19)$$

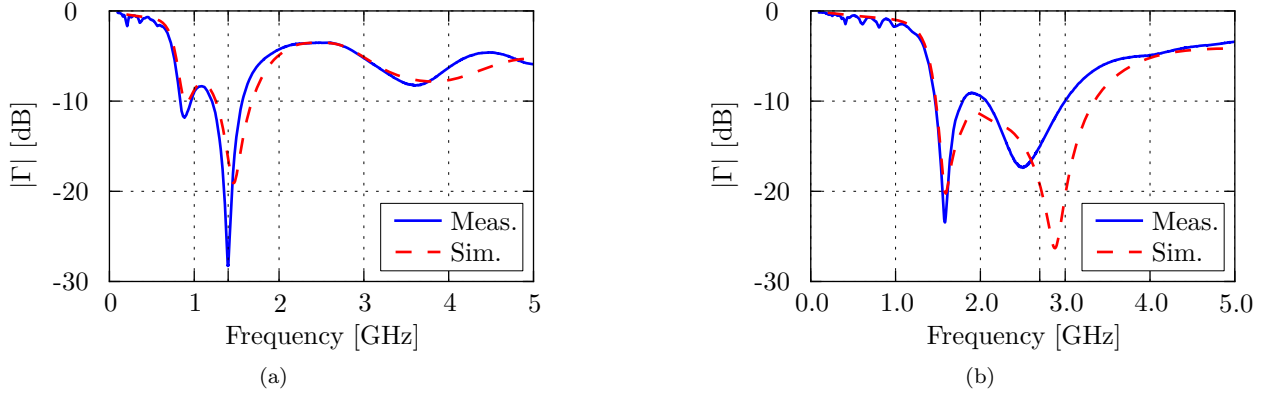


Figure 5.6: Three layer probe reflection coefficient for the (a) 1.4 GHz probe and (b) 2.7 GHz probe.

If the left hand side is considered to be T_M^n and the weighting functions in the parenthesis are summed to be W_{cv}^n , this may be written in matrix form as

$$\begin{bmatrix} T_M^1 \\ T_M^2 \end{bmatrix} = \begin{bmatrix} W_{cv}^1 & W_{v3}^1 \\ W_{cv}^2 & W_{v3}^2 \end{bmatrix} \begin{bmatrix} T_{v1} \\ T_{v3} \end{bmatrix}, \quad (5.20)$$

which may be written in a compact form as

$$\mathbf{T}_M = \mathbf{W}\mathbf{T}_v. \quad (5.21)$$

This matrix equation must be solved to determine the unknown volume temperatures. This is done using the least-squares method and optimal estimation method presented in Section 5.5.

5.6.1 LEAST-SQUARES SOLUTION TO THREE LAYER MEASUREMENT

The first, and simplest, method presented is the least-squares solution. The observations are given by T_M^n which is the portion of measured antenna temperature delivered from the unknown volume. This is adjusted by the upper half-space temperature and simulated weighting function. The upper half-space temperature is assumed to be the same temperature as the cold calibration load which is measured using a thermocouple and the PicoTech data logger. Since the data logger samples at a different rate from the measurements, the temperature is fitted to the exponential equation in (5.7). The fit is also done for the two water layers so that the error in the radiometric estimate may be determined. The thermocouple measurements and fitted curves are shown in Fig. 5.7. Since W is a square matrix, the least-squares solution is found by inverting the matrix

Table 5.3: 1.4 and 2.7 GHz probe weighting functions on 10.3 mm water, 5 mm glass, and water.

f [GHz]	Upper (W_u)	Feed (W_f)	Top Water (W_{v1})	Glass (W_{v2})	Bot. Water (W_{v3})
1.4	0.014	0.056	0.543	0.002	0.385
2.7	0.0132	0.0537	0.8590	0.0004	0.0737

and is given by

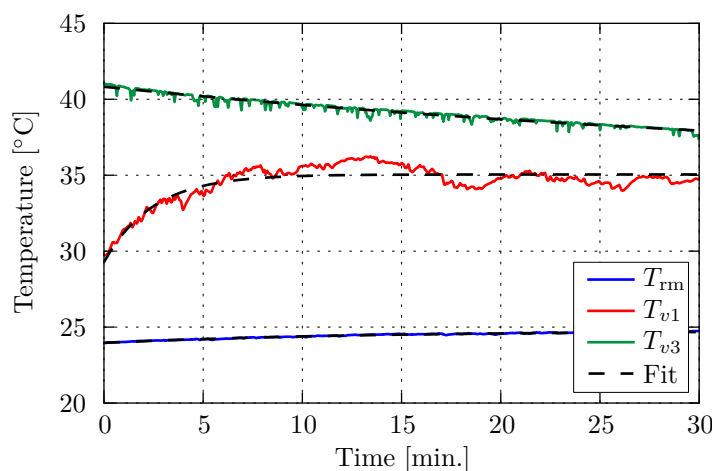


Figure 5.7: Thermocouple measurements of room temperature (T_{rm}), the top water layer (T_{v1}), and the bottom water layer (T_{v3}) along with the fitted curve (dashed black line) for each thermocouple measurement.

$$\hat{\mathbf{T}}_v = W^{-1}\mathbf{T}_M, \quad (5.22)$$

where the hat denotes an estimate.

The results from the least-squares inversion are shown in Fig. 5.8 along with a fit (dashed line) to the exponential function for both least squares estimates. To quantify the accuracy of the least-squares estimate, comparisons will be made by calculating various quantities for errors. To avoid confusion in notation, the errors in an estimate \hat{X} from the fitted thermocouple data X will be defined as

$$\begin{aligned} \text{Error} & \quad \epsilon(\hat{X}) = |X - \hat{X}| \\ \text{Relative Error} & \quad \delta(\hat{X}) = \left| \frac{X - \hat{X}}{X} \right| \\ \text{Temperature Delta} & \quad \Delta\hat{X} = \max\hat{X} - \min\hat{X} \\ \text{Error Delta} & \quad \Delta\epsilon(\hat{X}) = \max[\epsilon(\hat{X})] - \min[\epsilon(\hat{X})] \end{aligned}$$

The absolute errors in the least-squares estimate and its fit to the exponential function for both layers are shown in Fig. 5.9. The error in the fitted data is less than 0.8°C for the first layer of water, and less than

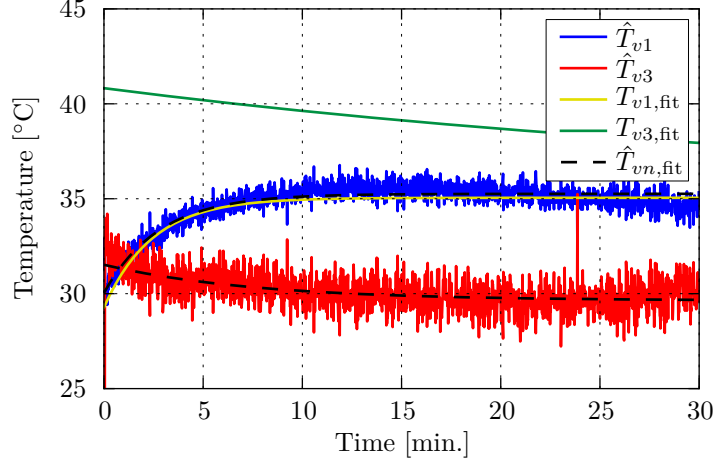


Figure 5.8: Least-squares raw estimate of the top (\hat{T}_{v1}) and bottom (\hat{T}_{v3}) water layers compared to fitted thermocouple measurements $T_{v1,fit}$ and $T_{v3,fit}$. The dashed black line shows the fit to the least-squares estimate.

9.6°C for the bottom layer of water. Although this error is large if absolute temperature is required, there are a number of applications that require only relative temperature e.g. circadian rhythm monitoring [111]. In this case, it is important that the error remain flat over time. For the fitted data, the difference between the maximum error and minimum error for the top layer is 0.7°C and 1.3°C for the bottom layer. Or if the change in temperature in each layer is considered, the fitted thermocouple data shows a change of 2.9°C for $T_{v3,fit}$ and 5.8°C for $T_{v1,fit}$. The fitted least squares estimates show changes of 1.8°C and 5.2°C for the bottom and top water layers respectively.

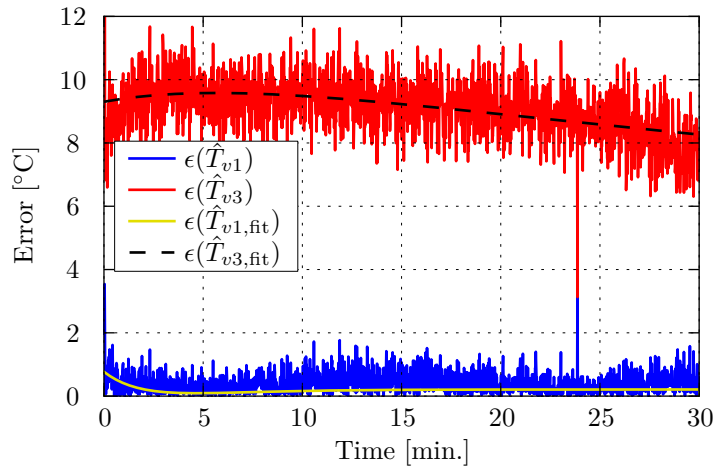


Figure 5.9: Absolute errors of the least-squares estimate for the top water ($\epsilon(\hat{T}_{v1})$) and bottom water ($\epsilon(\hat{T}_{v3})$), and the absolute error if the least-squares estimate are fitted to the exponential from (5.7) ($\epsilon(\hat{T}_{v1,fit})$, $\epsilon(\hat{T}_{v3,fit})$).

Next, the least-squares inversion is performed assuming only one unknown and two measurements. The top layer of water is assumed to be known, and the same inversion is performed. For example, it is straightforward to measure the temperature of the skin independently of radiometer estimates. The radiometric measurements T_M^n are given by the left hand side of

$$T_A^n - W_u^n T_u - (W_f^n + W_{v1}^n + W_{v2}^n) T_{v1} = W_{v3}^n T_{v3} \quad \text{for } n = 1, 2. \quad (5.23)$$

The result of the inversion and the error associated with it is shown in Fig. 5.10. The improvement in the

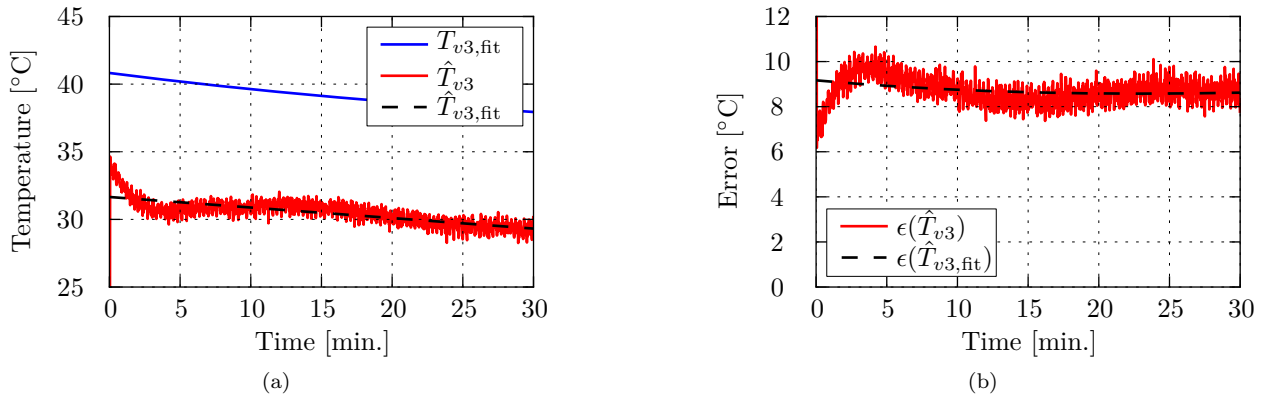


Figure 5.10: Least-squares estimate and fit (a) of the bottom water (\hat{T}_{v3} , $\hat{T}_{v3,fit}$) compared to fitted the thermocouple measurement $T_{v3,fit}$. Error (b) in the least-squares estimate ($\epsilon(\hat{T}_{v3})$) and fit ($\epsilon(\hat{T}_{v3,fit})$).

least-squares estimate for two measurements and one unknown is seen by comparing the error parameters as shown in Table 5.4.

Table 5.4: Comparison of the error in the least-squares estimate of T_{v3} for two unknowns and one unknown.

Error Parameter	Two Unknowns	One Unknown
$\max [\epsilon(\hat{T}_{v3,fit})] [^{\circ}\text{C}]$	9.6	9.2
$\Delta\epsilon(\hat{T}_{v3,fit}) [^{\circ}\text{C}]$	1.3	0.6
$\Delta(\hat{T}_{v3,fit}) [^{\circ}\text{C}]$	1.8	2.3
$\epsilon [\Delta(\hat{T}_{v3,fit})] [^{\circ}\text{C}]$	1	0.5
$\delta [\Delta(\hat{T}_{v3,fit})] [\%]$	35.9	19

5.6.2 OPTIMAL ESTIMATION OF THREE LAYER MEASUREMENT

While the least-squares method yielded results that qualitatively track the changes in temperature, the relative errors in the estimate of the temperature change were as large as 35%. To improve this estimate, the optimal estimation technique will be applied to give a weighted estimate for the temperature profile. The two weighted estimates will be a “mean” profile and the radiometric estimate. For the purpose of demonstrating how accurate the estimate could be, the mean profile is assumed to be the exact value from the fitted thermocouple data given by

$$\mathbf{T}_0 = \begin{bmatrix} T_{v1,\text{fit}} \\ T_{v3,\text{fit}} \end{bmatrix}. \quad (5.24)$$

To ensure the data is not weighted too heavily on the exact values, the covariance matrix is assumed to be

$$S_0 = \begin{bmatrix} 1 & 0 \\ 0 & 1 \end{bmatrix}, \quad (5.25)$$

and the covariance matrix for the measurements is given by

$$S_M = \begin{bmatrix} \text{var}(T_M^1) & 0 \\ 0 & \text{var}(T_M^2) \end{bmatrix} = \begin{bmatrix} 0.30 & 0 \\ 0 & 0.98 \end{bmatrix}. \quad (5.26)$$

The results from the optimal estimation utilizing the exact temperature values in the weighted inversion are shown in Fig. 5.11. A significant improvement can be seen in the error over the least-squares estimate,

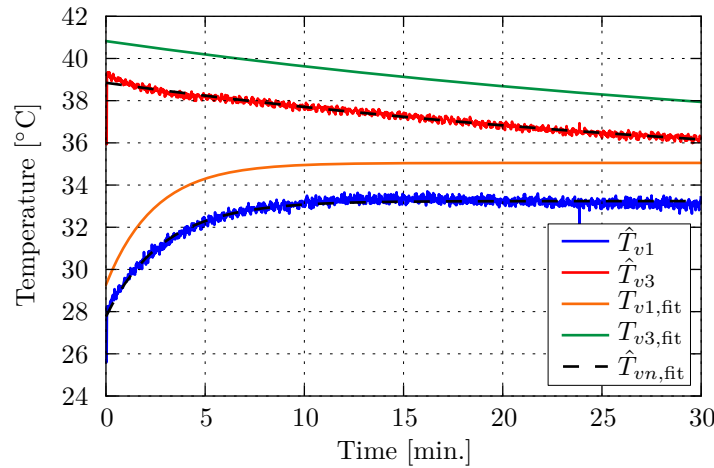


Figure 5.11: Optimal estimation of the top water (\hat{T}_{v1}) and bottom water (\hat{T}_{v3}) compared to fitted thermocouple measurements $T_{v1,\text{fit}}$ and $T_{v3,\text{fit}}$.

which is to be expected as the estimate has been weighted with the exact data as seen in Fig. 5.12. While it may seem a bit deceiving to weight the data based on the measured thermocouple data, for most applications there is historical data of the “unknown” temperature that may be used to help constrain the estimate. This estimation method will be explored in further detail in the next section for estimating human body temperatures for monitoring the circadian rhythm.

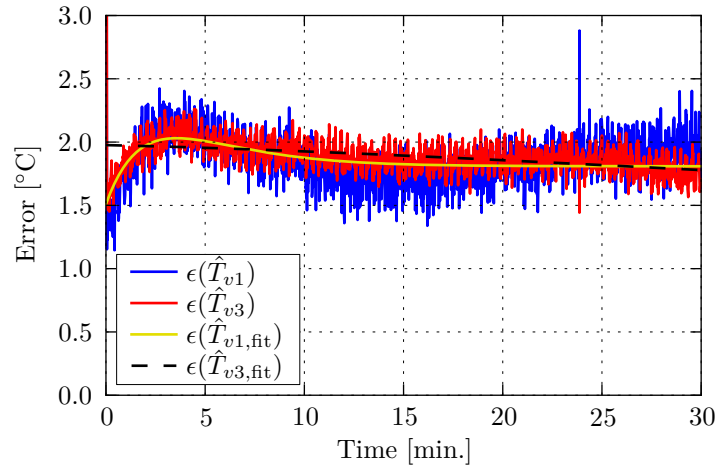


Figure 5.12: Absolute errors of the optimal estimation for the top water ($\epsilon(\hat{T}_{v1})$) and bottom water ($\epsilon(\hat{T}_{v3})$), and the absolute error if the optimal estimations are fitted to the exponential from (5.7) ($\epsilon(\hat{T}_{v1,fit})$, $\epsilon(\hat{T}_{v3,fit})$).

As was done with the least-squares estimation, the optimal estimation technique is repeated if the top layer is assumed to be known. For this inversion, the covariance matrix of the measured values from (5.23) is

$$S_M = \begin{bmatrix} \text{var}(T_M^1) & 0 \\ 0 & \text{var}(T_M^2) \end{bmatrix} = \begin{bmatrix} 0.12 & 0 \\ 0 & 0.18 \end{bmatrix}. \quad (5.27)$$

Since the variance of the measured values is lower if one unknown is assumed, the measurements will be weighted more than for two unknowns. As a result, the absolute error is larger than compared to the estimate with two unknowns. The results of the optimal estimation with one unknown are shown in Fig. 5.13, and a comparison of the optimal estimation and least-squares estimates is given for the top layer of water in Table 5.5 and for the bottom layer of water in Table 5.6.

5.6.3 MULTI-FREQUENCY ESTIMATES DISCUSSION

The results shown in Tables 5.5 and 5.6 are compared in this section and the advantages and disadvantages of each method discussed. For the estimate of the top water layer $\hat{T}_{v1,fit}$, the least-squares method yielded a

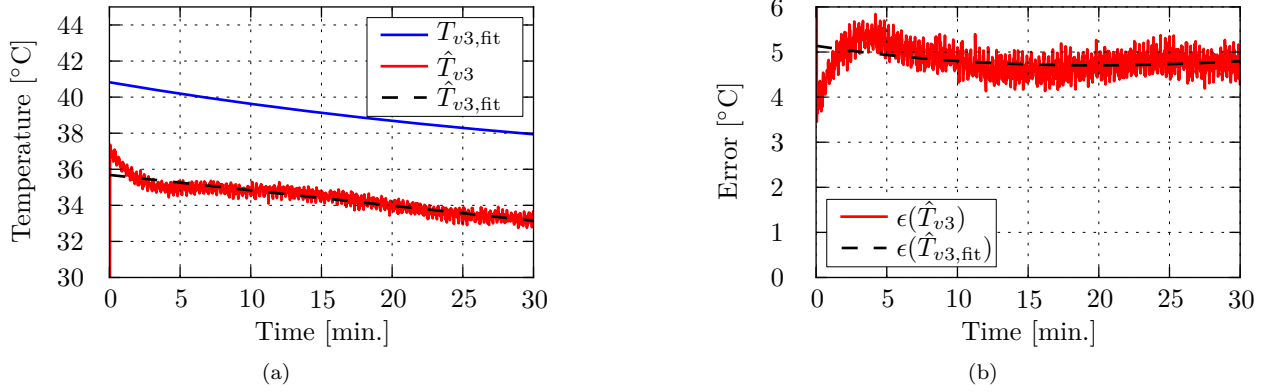


Figure 5.13: Optimal estimation and fit (a) of the bottom water (\hat{T}_{v3} , $\hat{T}_{v3,fit}$) compared to fitted the thermocouple measurement $T_{v3,fit}$. Error (b) in the optimal estimate ($\epsilon(\hat{T}_{v3})$) and fit ($\epsilon(\hat{T}_{v3,fit})$).

Table 5.5: Comparison of the error in the fitted least-squares (LS) estimate and the fitted optimal estimation (OP) of T_{v1} with two unknowns.

Error Parameter	LS	OP
$\max [\epsilon(\hat{T}_{v1,fit})] [^{\circ}\text{C}]$	0.8	2
$\Delta\epsilon(\hat{T}_{v1,fit}) [^{\circ}\text{C}]$	0.7	0.5
$\Delta(\hat{T}_{v1,fit}) [^{\circ}\text{C}]$	5.2	5.5
$\epsilon [\Delta(\hat{T}_{v1,fit})] [^{\circ}\text{C}]$	0.6	0.3
$\delta [\Delta(\hat{T}_{v1,fit})] [\%]$	9.7	5.2

Table 5.6: Comparison of the error in the fitted least-squares (LS) estimate and the fitted optimal estimation (OP) of T_{v3} with two unknowns and one unknown comparison.

Error Parameter	LS-2 Unknowns	LS-1 Unknown	OP-2 Unknowns	OP-1 Unknown
$\max [\epsilon(\hat{T}_{v3,fit})] [^{\circ}\text{C}]$	9.6	9.2	2	5.1
$\Delta\epsilon(\hat{T}_{v3,fit}) [^{\circ}\text{C}]$	1.3	0.6	0.2	0.4
$\Delta(\hat{T}_{v3,fit}) [^{\circ}\text{C}]$	1.8	2.3	2.7	2.5
$\epsilon [\Delta(\hat{T}_{v3,fit})] [^{\circ}\text{C}]$	1	0.5	0.2	0.3
$\delta [\Delta(\hat{T}_{v3,fit})] [\%]$	35.9	19	6.9	11.8

more accurate result in terms of maximum absolute error ($\max [\epsilon(\hat{T}_{v1,fit})]$). However, the optimal estimation method where the estimate is a weighted average of the mean profile (exact data in this case) and the measured estimate yielded better results if the desired measurement is to track changes. This is illustrated by the error or relative error of the change in the temperature ($\epsilon [\Delta(\hat{T}_{v1,fit})]$, $\delta [\Delta(\hat{T}_{v1,fit})]$) which was 2.5% better for the optimal estimation method.

While accurately determining the surface temperature is of interest and impacts the estimation of subsurface temperature, the true goal of this measurement is to determine subsurface temperature. For the estimate of the bottom water layer $\hat{T}_{v3,\text{fit}}$, the optimal estimation method was more accurate in terms of absolute error ($\max[\epsilon(\hat{T}_{v3})]$). While for the least-squares method the error improved if the surface temperature was assumed to be known, the optimal estimation method yielded a larger error for one unknown rather than two unknowns. This is to be expected as the measured radiometer values were weighted more heavily than if there were two unknowns (S_{Mv}^{-1} is larger if there is one unknown). If the desired goal of the device is to track changes, the optimal estimation method is also better if there are two unknowns rather than one with a relative error in the change in temperature of $\delta[\Delta(\hat{T}_{v3})] = 6.9\%$ for two unknowns as opposed to 11.8% for one unknown. However, both cases are better than the least squares inversion relative error in the change in temperature of 35.9% and 19% for two unknowns and one unknown respectively.

The mean profile \mathbf{T}_0 used in the optimal estimation method utilized the data from the thermocouples as there is no historical data for the measurement setup. While this mean profile is a best case scenario, it demonstrates how the inversion can be constrained. For the optimal estimation with one unknown the estimate for \mathbf{T} from measured data \mathbf{T}_e where $\mathbf{T}_e = D\hat{\mathbf{T}}_M$ is the exact solution where $WD = I$ is weighted approximately 0.55, where as the mean profile \mathbf{T}_0 is weighted by 0.45. However, the exact estimate depends on the weighting function W . Therefore the mean profile \mathbf{T}_0 is weighted by 0.45, but the radiometer measurements from (5.23) are weighted by 1.4 for T_M^1 and 0.2 for T_M^2 . These weights are given by

$$(S_0^{-1} + W^T S_M^{-1} W)^{-1} S_0^{-1} = \begin{bmatrix} 0.45 \end{bmatrix} \quad (5.28)$$

$$(S_0^{-1} + W^T S_M^{-1} W)^{-1} W^T S_M^{-1} = \begin{bmatrix} 1.4 & 0.2 \end{bmatrix} \quad (5.29)$$

which demonstrates that the radiometric measurement

$$T_M^n = T_A^n - W_u^n T_u - (W_f^n + W_{v1}^n + W_{v2}^n) T_{v1} \quad (5.30)$$

is weighted most heavily for the 1.4 GHz measurement, followed by the mean profile, and finally the 2.7 GHz measurement has the least weight as very little power (7.4%) is received from the bottom water layer at 2.7 GHz.

5.7 TISSUE THICKNESS VARIABILITY ANALYSIS

The previous measurements assumed that the weighting functions derived from simulation perfectly represented the problem being measured. The assumptions in the layer thicknesses used for the model may have been incorrect. This problem will arise in medical applications, as it will be difficult to measure the thickness of each tissue in an inexpensive manner. Nuclear magnetic resonance imaging (NMRI) is capable of this, but is a costly procedure. In this section, the problem of tissue thickness variability will be analyzed by generating simulated or “synthetic” radiometer data, which is often done to demonstrate the feasibility of determining temperature profiles for medical applications [11, 12, 41, 107]. Retrieval with inaccurate model data (electrical properties of tissues, skull thickness, and bolus thickness) has been investigated with artificial brightness temperature measurements for the application of hypothermal neural rescue therapy in infants by Hand et al [11]. Hand et al demonstrated deviations in bolus thickness and skull thickness lead to the largest inaccuracies. For the same application of hypothermal neural rescue, Sugiura et al [41] considered variation in the conductivity of the brain demonstrating a maximum estimation error of 0.95-1.05 K. Muzushina et al [105] considered fat thickness variability (5-25 mm) for the application of hyperthermia control. The fat thickness was assumed known, and a thickness of 15 mm gave the worst precision with a two standard deviation interval of 1 K up to a depth of 5 cm.

This motivates the question, how does error in the model used for the weighting function affect determining the temperature within the body? To investigate this problem, the application of monitoring the circadian rhythm will be considered. The circadian rhythm may be monitored by measuring core body temperature [111, 112]. Disruptions to the circadian rhythm have been linked to seasonal affective disorder (SAD) [111], Type 2 diabetes [113], and heart disease [114]. In particular, the treatment of SAD aims to increase the amplitude of the circadian rhythm [111], in which case the measure of amplitude is core temperature. The core body temperature is often measured with a rectal probe [111, 112] or a gastrointestinal (GI) pill temperature monitor [115]. In addition to monitoring core body temperature for circadian rhythm monitoring, there is interest in monitoring thermal stress by measuring core body temperature for athletic and occupational hazards [115].

Therefore, a wearable microwave radiometer could be used as a non-invasive device to measure core body

temperatures in clinical studies, and it is then necessary to know how variations in tissue thicknesses affect the estimate of important parameters for the circadian rhythm such as amplitude and phase. In this study, only effects due to incorrect weighting functions are considered, error due to change in the reflection coefficient is not considered. The variability in tissue thicknesses is studied purely in simulation for a three layer problem of skin, fat, and muscle. Weighting functions are determined for a set of probes (400 MHz, 1.4 GHz, 2.7 GHz, and 4.9 GHz) on tissues with variable thicknesses, radiometric measurements are generated in simulation, and estimates are made for the unknown core temperature.

The simulations of the probes to determine the weighting functions were carried out in Ansys HFSS. A three layer medium consisting of skin, fat, and muscle was analyzed with perfectly matched layer (PML) boundaries. The dipole was placed directly on the surface of the skin and was assumed to be a perfect electric conductor (PEC) fed with a lumped $50\ \Omega$ port. The thicknesses of the skin and fat were varied $\pm 10\%$ from the nominal values of 2 mm and 10 mm respectively in 5% increments. The dipole parameters such as frequency, length, width, and reflection coefficient (minimum and maximum for all tissue thicknesses) are shown in Table 5.7.

Table 5.7: Dipole parameters for the variability study of the three layer problem of skin, fat, and muscle.

Frequency	Length [mm],	Width [mm]	Min($ \Gamma $) [dB]	Max($ \Gamma $) [dB]
400 MHz	96	1	-18.2	-17.3
1.4 GHz	27.4	1	-27	-23.9
2.7 GHz	15	1	-23.3	-22.3
4.9 GHz	9	0.8	-19.8	-15.4

To test the variability in tissue thickness, simulated radiometric data was generated using the “correct” thickness that is within 10% of the nominal value. The goal of the analysis is to determine the unknown parameters of the muscle temperature. To create the radiometric estimates, first a temperature profile was generated for one day worth of data with temperatures corresponding to the circadian rhythm assuming the core amplitude is $0.4\ ^\circ\text{C}$ [112] (rectum measurements). The function for the skin was used to estimate the data presented in [112] for the proximal (core) skin temperature (weighted average of: infraclavicular area, mid thigh, stomach, and forehead). The fat is assumed to be an average of the two layers, and the background temperature is assumed to be $22\ ^\circ\text{C}$. The following equations describe the skin, muscle, fat, and background

temperatures as a function of time in hours as

$$\begin{aligned}
 T_{\text{skin}}(t) &= 34.5 - \left(e^{-(t-7)^2/2(0.7)^2} - e^{-(t-11)^2/2(1)^2} \right) \text{ } ^\circ\text{C} \\
 T_{\text{musc}}(t) &= 36.6 + 0.4 \cos\left(t \frac{2\pi}{24}\right) \text{ } ^\circ\text{C} \\
 T_{\text{fat}}(t) &= \frac{T_{\text{skin}}(t) + T_{\text{musc}}(t)}{2} \text{ } ^\circ\text{C} \\
 T_{\text{bgnd}}(t) &= 22 \text{ } ^\circ\text{C},
 \end{aligned} \tag{5.31}$$

which are shown for a 24 hour period in Fig. 5.14 along with measured data present by Kräuchi et al [112].

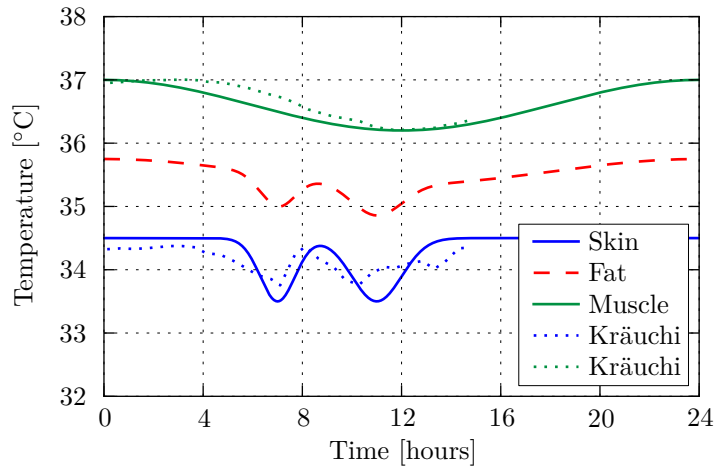


Figure 5.14: Simulated temperatures of the skin, fat, and muscle over a 24 hour period along with measured data present by Kräuchi et al [112].

The goal of this analysis is to estimate how error in the weighting function affects the estimate of the muscle temperature. This was done by creating radiometric data from a correct weighting function (W_c), then using both the correct weighting function and the nominal weighting function (W_n), an estimate of the tissue temperatures was determined. After the data was inverted, the non-linear regression tool `curve_fit` available in the Python library SciPy was used to fit to the unknown function given by

$$A \cos(Bt + C) + D. \tag{5.32}$$

This analysis was simulated in Python with the following steps:

- Select a correct weighting function W_c^i corresponding to one of the combinations of tissue thicknesses varying up to 10% from the nominal values.

- Generate a radiometric observation at one minute intervals by adding noise \mathbf{e} characterized by a normal distribution with zero mean and a standard deviation of 0.05 where the radiometric measurements are given by

$$\mathbf{T}_M = W_c^i \mathbf{T} + \mathbf{e} \quad (5.33)$$

where \mathbf{T} is a vector of the actual tissue temperature from (5.31).

- Estimate the tissue temperatures from the radiometric measurements using the least-squares method and the optimal estimation method for both the correct weighting function and nominal weighting function. The covariance matrices used in the optimal estimation were assumed to be $S_0 = I$ and $S_M = 0.0025I$ where I is the identity matrix, and the mean profile \mathbf{T}_0 was assumed to be

$$\mathbf{T}_0 = \begin{bmatrix} 36.6 \\ 35.55 \\ 34.5 \\ 22 \end{bmatrix} \text{ } ^\circ\text{C}. \quad (5.34)$$

- After 24 hours of data has been estimated, the result is fit to the function in (5.32) to determine the unknown parameters A^i , B^i , C^i , and D^i .
- For each correct weighting function repeat this process 500 times to estimate the mean value $\overline{X^i}$ of the unknown parameter and the standard deviation $\sigma(X^i)$ ($X = A, B, C$, or D).
- After all the weighting functions have been used to generate data, find the error by determining the minimum of all the values minus the corresponding standard deviation, and the maximum of all the values plus the standard deviation. The following will be considered the error bound

$$\text{Error Bound (EB)} = \begin{aligned} & +\text{Max} \left[\overline{X^i} + \sigma(X^i) \right] - X_{\text{Actual}} \\ & -\text{Min} \left[\overline{X^i} - \sigma(X^i) \right] - X_{\text{Actual}} \end{aligned} \quad (5.35)$$

and the relative error bound normalized to the actual value is

$$\text{Relative Error Bound (REB)} = \begin{aligned} & + \frac{\text{Max} \left[\overline{X^i} + \sigma(X^i) \right] - X_{\text{Actual}}}{X_{\text{Actual}}} \\ & - \frac{\text{Min} \left[\overline{X^i} - \sigma(X^i) \right] - X_{\text{Actual}}}{X_{\text{Actual}}} \end{aligned} \quad (5.36)$$

where $\overline{X^i}$ is the average from each iteration of the weighting function for $X = A, B, C$, or D .

This procedure is detailed in the code diagram shown in Fig. 5.15, and was repeated for three cases with:

- (1) Four measurements (400 MHz, 1.4 GHz, 2.7 GHz, and 4.9 GHz) and four unknowns (skin, fat, muscle, and background)
- (2) Four measurements (400 MHz, 1.4 GHz, 2.7 GHz, and 4.9 GHz) and two unknowns (fat and muscle)
- (3) Three measurements (1.4 GHz, 2.7 GHz, and 4.9 GHz) and two unknowns (fat and muscle)

The results of the simulations are shown for the nominal weighting functions in Table 5.8, where the column heading “M,U” refers to the number of measurements and unknowns along with the results if the correct weighting function is used as shown in Table 5.9. Table 5.8 shows the results of the inversion if the nominal weighting function is used instead of the correct one.

Table 5.8: Summary of analysis where various methods are used to invert the data using the nominal weighting function for radiometric observations generated by tissues properties varying 10% from the nominal values of 2 mm of skin and 10 mm of fat. The table presents the error in the estimates for the unknown muscle temperature parameters.

Method	M,U	REB(Mean) [%]	REB(Amp.) [%]	REB(Period) [%]	EB(Phase) [Hrs.]
LS	4,4	+39	+3528	+200	+25.8
		-34	-3143	-197	-21.9
OP	4,4	+1.5	+6.7	+2.9	+0.48
		-1.5	-9.7	-5.9	-0.42
LS	4,2	+1.8	+12.1	+6.6	+0.82
		-1.7	-11.3	-7.6	-0.69
OP	4,2	+1.3	+8.8	+3.3	+0.47
		-1.3	-7.9	-6.6	-0.43
LS	3,2	+2.2	+12.4	+8.3	+1.0
		-2.0	-11.5	-7.2	-0.74
OP	3,2	+1.3	+9.9	+3.1	+0.49
		-1.3	-6.8	-6.0	-0.43

It can be seen for the least-squares inversion with four measurements and four unknowns, both the correct and nominal weighting functions yield results that, due to the noise in the measurement and error in the weighting function, may vary a great deal from the correct value. For the amplitude and correct weighting function it is up to 10136%. These results would not make a useful medical device. However, if the optimal estimation technique is used, the estimate for the amplitude within 10% of the nominal value when utilizing the nominal weighting function. The least-squares estimate yields better results if there are more measurements

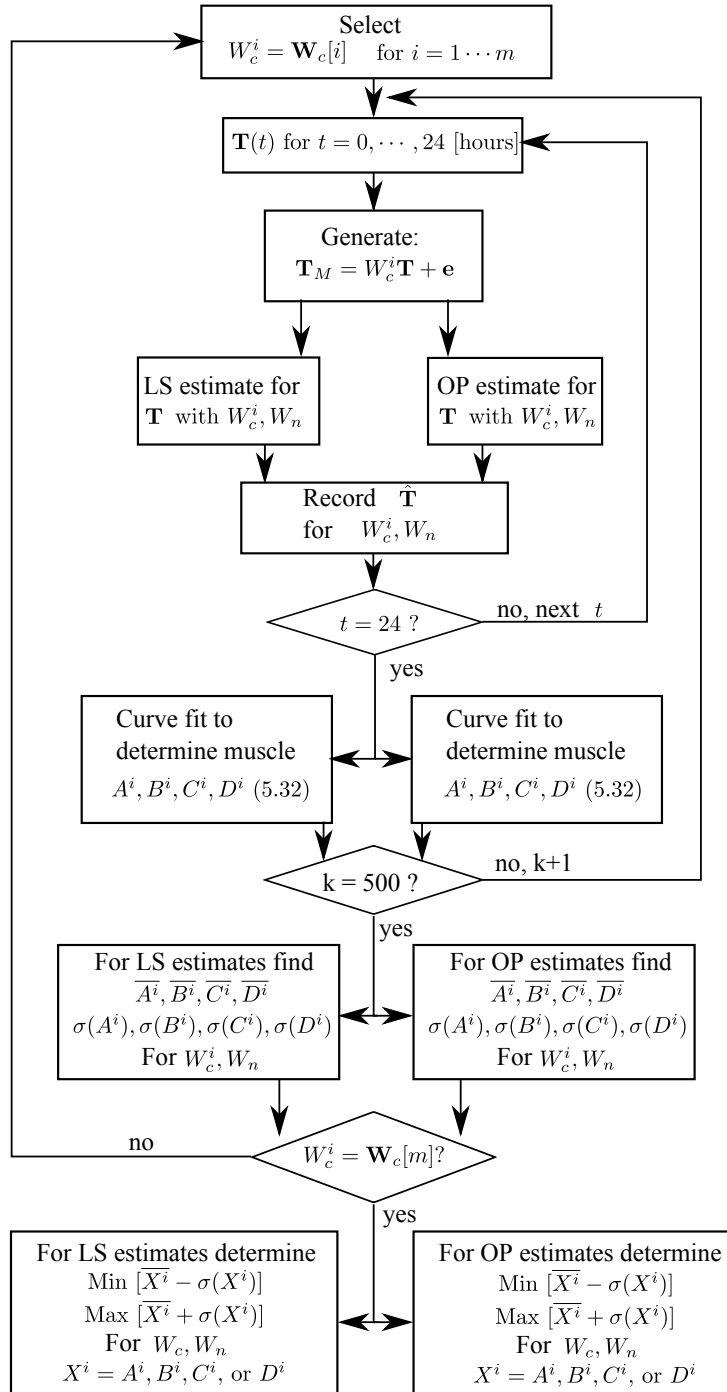


Figure 5.15: Code diagram for the tissue thickness variability analysis.

than unknowns, where value of the amplitude estimate is within 12.5% of the actual value when utilizing the nominal weighting function.

This analysis demonstrated that if tissue thicknesses vary 10% from the model used for the weighting

Table 5.9: Summary of analysis where various methods are used to invert the data using the correct weighting function for radiometric observations generated by tissues properties varying 10% from the nominal values of 2 mm of skin and 10 mm of fat. The table presents the error in the estimates for the unknown muscle temperature parameters.

Method	M,U	REB(Mean) [%]	REB(Amp.) [%]	REB(Period) [%]	EB(Phase) [Hrs.]
LS	4,4	+111	+10136	+466	+65
		-89	-8135	-455	-45
OP	4,4	+0.002	+2.6	+2.7	+0.51
		-0.1	-5.8	-5.2	-0.44
LS	4,2	+0.1	+7.4	+7.5	+0.95
		-0.1	-4.9	-6.5	-0.73
OP	4,2	+0.002	+4.8	+2.7	+0.49
		-0.1	-4.3	-5.0	-0.44
LS	3,2	+0.1	+7.7	+7.8	+0.99
		-0.1	-5.5	-6.5	-0.74
OP	3,2	+0.007	+6.3	+2.5	+0.47
		-0.1	-3.5	-5.0	-0.42

function, accurate estimates can be made for the amplitude of the core body temperature. Optimal estimation may be used to improve the estimate if there are an equal number of measurements and unknowns. The least-squares method is useful if there are more measurements than unknowns. It must be noted that this inversion analysis is specific to the probes simulated, tissue model, and noise assumed in the measurements. Additionally, the mean profile used in the optimal estimation is very close to the actual temperature as they do not vary much from their mean value. This, however, is a reasonable assumption as a body temperature less than 35°C is considered hypothermic, and greater than 38.3°C is considered hyperthermic.

5.8 CONCLUSION

The following list summarizes the contributions from this chapter.

- Demonstrated detection of temperature change for a water phantom utilizing both the 1.4 GHz and 2.7 GHz radiometers and probes.
- Using a single frequency measurement, determined subsurface temperature of a three layer medium consisting of water, glass, and water with the 1.4 GHz radiometer.
- Demonstrated multi-frequency subsurface temperature detection using both the 1.4 GHz and 2.7 GHz radiometers simultaneously.

- Discussed the least-squares and optimal estimation method and applied both to the temperature estimates from the two-frequency system measurements. The optimal estimation method helps to constrain the problem by weighting measured results with historical data.
- Analyzed the error in temperature estimates if incorrect weighting functions are used by simulating radiometer data for a model of three layer tissue model of skin, fat, and muscle, demonstrating useful results if there are more measurements than unknowns or if the optimal estimation technique is used with an accurate historical temperature profile.

CHAPTER 6

SUMMARY AND FUTURE WORK

CONTENTS

6.1	Summary	137
6.2	Future Work	138
6.3	Contributions	142

6.1 SUMMARY

In summary, this research has addressed the analysis and design of a microwave radiometer system capable of measuring subsurface temperature changes with a near-field probe. A background of radiometry specific to near-field sensing was presented. Microwave radiometers are practical for addressing medical problems in which it is necessary to determine subsurface temperature because at microwave frequencies sensing depths of up to 3-7 cm are achievable [4,5]. Microwave radiometry for non-invasive temperature measurements is based on near-field power reception and holds promise to achieve the spatial resolution and sensing depth necessary for a variety of medical applications, including cancer detection [7, 8]. Monitoring drug delivery for cancer treatment [9], hyperthermia temperature control [10], hypothermic neural rescue of infants suffering from hypoxia-ischemia [11, 12], and detection of vesicoureteral reflux in children [13, 14] also utilize non-invasive near-field radiometric measurements. Measurement of elevated joint temperature to detect arthritis by non-

invasive microwave thermometry has also been investigated [5, 15]. Quantification of *in vivo* inflammation in atherosclerotic plaques by means of non-invasive microwave radiometry has been applied to the area of vascular pathology [16, 17].

While there are a number of applications in which near-field radiometry has been investigated, monitoring the circadian rhythm, which is considered in this thesis, is a promising application for determining core body temperature, and has not previously been discussed as an application. A number of challenges must be addressed for this application: operation in a congested RF environment, compact size of the receiver and probe, subject variability. These challenges are considered in this thesis. To address operation in a congested RF environment, “quiet” frequency bands reserved for radio astronomy and remote sensing are be used. Separate dipole probes that can be light-weight and flexible not only address the size restrictions, but also help with filtering unwanted interference.

Since a dipole was the choice of probe to receive thermal emissions from the human body, the limitations on sensing depth were explored using a spectral domain analysis. While the dipole is one aspect of reducing the size of the radiometer, MMIC circuits that addressed circuitry such as calibration were presented as a way of reducing the overall size of the receiver by demonstrating on-chip circuitry.

To demonstrate the approach of using “quiet” frequency bands with dipoles as the probe, a water phantom was used to demonstrate detection of subsurface temperature changes at a depth of 1.5 cm. The measurements were made with receivers that were designed specifically to operate at 1.4 GHz and 2.7 GHz. Finally, the issue of tissue thickness variability was explored by generating simulated radiometer data to determine how error in the model used for the weighting function affects determining core body temperature variations for monitoring the circadian rhythm.

6.2 FUTURE WORK

The results from this thesis demonstrated a proof-of-concept for detecting temperature changes at a depth using a water phantom. Additionally, the sensing limitations were discussed, and variability in the model used to invert the radiometric data was analyzed for the application of monitoring the circadian rhythm. The selection of frequencies and compact dipole probes were chosen so that the radiometer system could be a

wearable device operated in a congested RF environment which may be encountered in a clinical testing application. While there are a number of applications for non-invasive temperature sensing which were briefly mentioned in the introduction, monitoring core body temperature for clinical studies would be a good candidate for demonstrating this system as a useful non-invasive medical device. Before this system can be implemented for this purpose, however, a few challenges remain. The three challenges that have the most immediate need are (1) improving the phantom model used for demonstration, (2) analyzing the affect of tissue variability, and (3) integration of the receiver to develop a compact system for use in monitoring the circadian rhythm. Each challenge is addressed below.

The current model used for the proof-of-concept was a water phantom in which the bottom water layer varied 3°C in temperature and the top layer water change 5°C over a time period of 30 minutes. While this demonstrated the measurement of subsurface temperature changes, it will be necessary to develop a more accurate phantom model that not only mimics the electric properties of tissues (e.g. [47–49]), but also the temperature changes in the body on similar time scales. This improved phantom could be further used to explore the sensing depths predicted by the formulas presented in Chapter 4.

The second issue of tissue thickness variability may be explored in further detail with the improved phantom model. Resources such as the “Virtual Population” provided by the IT’IS Foundation [30, 116] as seen in Fig. 6.1 can be a guide to developing an improved model. The probes developed for this phantom could be simulated in commercial software such as Ansys HFSS to generated a library of weighting functions. This library of weighting functions could then be used to place error bounds on the estimated temperature given the confidence in the estimated tissue layer thicknesses. The accuracy of the estimated temperature may be improved by using the optimal estimation technique as demonstrated in Chapter 5. With this measurement setup, historical data could be generated by running the experiment several times under the same controlled conditions, and then used as a more appropriate mean temperature profile in the optimal estimation method. The results of these controlled experiments may further demonstrate the applicability of the system to be used for medical applications, and will help determine where the system is insufficient.

Finally, to extend this proof-of-concept to deployment in a clinical testing facility, the radiometers must be integrated. A first step would be to integrate each receiver onto a single PCB with compact surface mount

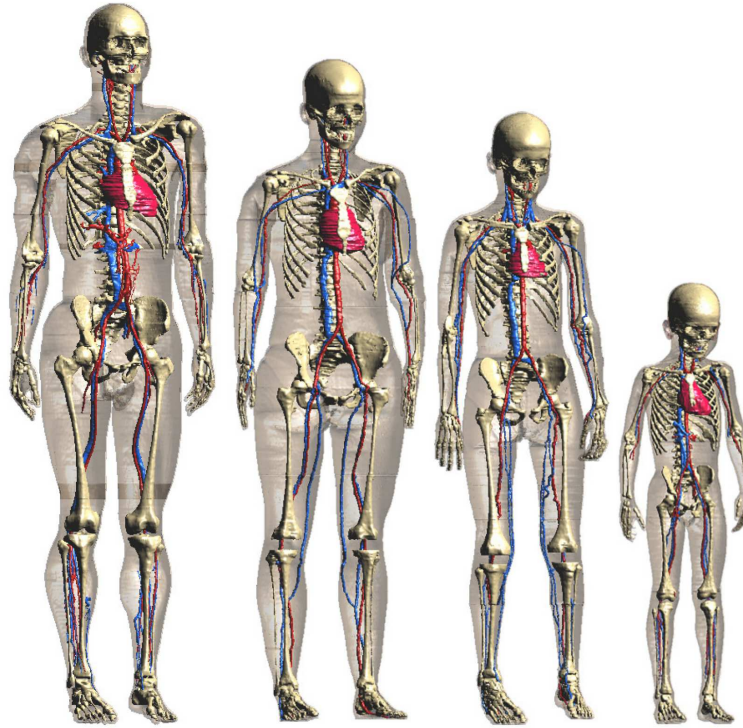


Figure 6.1: Virtual family that may be used as guide for estimating tissue variability. Image taken from [116].

parts. Fig. 6.2 demonstrates a prototype radiometer board that is the size of a credit card ($8.2\text{ cm} \times 5\text{ cm}$) neglecting the connectors. Multiple receivers at two or three different frequencies would be developed on separate boards, and then integrated into a single housing that could be worn by the patient. Cables would then extend from the receivers to the probes, and the output of the receivers would have to be measured by a compact low power microcontroller such as the MSP430 available from Texas Instruments [117].

The end goal for the system would be to accurately measure core body temperature changes as predicted by the results presented in Chapter 5 in a less invasive manner than current methods such as rectal thermistor probes [111, 112]. This could first be done by the portable hybrid boards detailed earlier, and then be implemented in an integrated system-on-a-chip. The LNAs used in the receiver can easily be integrated on chip as commercial LNAs are often just packaged MMICs. Chapter 3 addressed two circuits that can be used to help integrate the entire system onto a single chip. Integrating as many components of the receiver as possible onto a single chip will increase the usability of the system as it will interfere less with the user given the reduced size. Ultimately a CMOS process would be a great candidate for implementing a system-on-chip.



Figure 6.2: Example PCB of a radiometer integrated on a single board.

CMOS RFIC receivers in the frequency range of 1 to 5 GHz have been presented demonstrating noise figures from 4-7 dB and gain from 10-48 dB [118–121].

A clinical environment would provide the opportunity to validate estimates from radiometer measurements with data from thermistor probes. This would also provide an opportunity to further explore how variability in tissue thicknesses affects the inverse problem where weighting functions are generated by simulating a simplified model of the human body. As tissue thicknesses vary from person to person a suite of probes should be made for patients corresponding to a category of tissue thicknesses. This will ensure the probe is matched and error is not introduced due to reflection from the receiver. For each probe, a library of weighting functions can be used to invert the measurements to provide a confidence interval for the estimated value. This system, including the receivers, probe suite, and library of weighting functions could prove to be flexible to meet the needs of various patients. In addition, an array may be used to focus the sensing within the body, however, the inverse problem in this case will be more complicated and will need a more detailed model such as those from [30]. Historical data from thermistor probes could be used in the as the mean profile in the optimal estimation technique which, in Chapter 5, demonstrated how the method may be used to help constrain the inversion which will not only improve the accuracy, but also the variance of the estimate. Mean profiles in the analysis were assumed to very close to the exact value. This motivates the need for acquiring historical data

on a patient or classification of patients that may be used in as the mean profile in the optimal estimation technique.

6.3 CONTRIBUTIONS

Specific contributions from the material presented in Chapters 2-5 are summarized below.

Chapter 2 presented the background, design, and measurements of two radiometers designed for 1.4 GHz and 2.7 GHz operation. The narrow frequency bands selected were chosen because they are “quiet” bands reserved for radio astronomy and remote sensing, and at the expense of radiometer sensitivity, which, may be improved by increasing the integration time. In addition to the receiver, the probe is an essential part of the system for near-field temperature sensing, and multiple designs were presented. The following list summarizes the contributions from this chapter.

- To address the problem of operation in a congested RF environment, narrow frequency bands allocated for remote sensing and radio astronomy were utilized.
- Two radiometers capable of detecting temperatures in the range of the human body have been designed using the two-load architecture for flexibility in the mode of operation. Their performance was characterized in terms of the sensitivity to input power and frequency selectivity. In addition, the Allan variance when measuring a constant temperature water half-space was determined. The frequencies of operation for the radiometers were 1.4 GHz and 2.7 GHz.
- Two dipole probes were presented to measure temperature changes of a water phantom.
- Two multi-frequency probes were designed for measuring human tissues. The design methodology allowed for separate feeds for each frequency while maintaining SAR patterns that coincide spatially.
- A two frequency (400 MHz and 1.4 GHz) probe designed to be matched when placed on the human sternum was presented in Chapter 2 and the results were reported in [122].
- A three frequency probe (1.4, 2.7, and 4.9 GHz) was designed and measured and the results are reported in [123] that is currently under review for publication in the Transactions on Antennas and Propagation.

To address the goal of developing a compact system, Chapter 3 presents two GaAs MMICs: a tunable coupler and an active “cold” calibration standard. The first MMIC presented was the tunable coupler which may be used in a radiation balance radiometer architecture combining the fixed directional coupler and tunable attenuator into one circuit. The following list summarizes the contributions from the tunable coupler.

- Presented design procedure for a tunable coupler utilizing even and odd mode analysis.
- Designed a 2 GHz tunable coupler in a TriQuint $0.5\mu\text{m}$ GaAs process with a coupling coefficient ranging from 6.6 to 60 dB.
- Results from this paper were presented at the 2012 International Microwave Symposium [78]. The paper was selected as a finalist in the student paper competition (the top 26 out of 356 student papers were chosen as finalists).

The second MMIC presented in Chapter 3 was an active cold noise source for an on-chip calibration standard. The following list summarizes the contributions from the cold noise source.

- A design procedure for obtaining a minimum equivalent noise temperature of an active cold load was presented utilizing the equations given in [86].
- An example was shown demonstrating a minimum in $T_{s,1}$ for two different bias points of a TriQuint $0.5\mu\text{m}$ GaAs pHEMT device using TriQuint’s nonlinear TOM3 model.
- The procedure was applied to a 1.4 GHz GaAs MMIC which demonstrated a measured equivalent noise temperature of less than 90 K from 1.3 GHz to 1.5 GHz while maintaining a return loss greater than 28 dB.
- Results from this work were presented at the 2013 Compound Semiconductor IC Symposium (CSICS) [124].

Chapter 4 investigated modeling of the interaction of human tissues with a probe antenna situated on the surface of the skin. An improved sensing depth metric was presented and analyzed for a water phantom, and a three layer tissue model of skin, fat, and muscle. The results from this chapter are currently under review

for publication in the Transactions on Antennas and Propagation [123]. The following list summarizes the contributions from this chapter.

- A simplified model of a dipole in a lossy stratified medium was analyzed using a spectral-domain technique to determine the input impedance and sensing depth, defined in terms of the dipole near-field weighting functions, the total power radiometer sensitivity, and the desired temperature resolution.
- The technique was verified for the general case of a dipole on a water half-space by comparing impedance and normalized power dissipation to commercial FEM software, Ansys HFSS, with good agreement. Additional verification was presented for the input impedance of a dipole on a water half-space and a GaAs half-space by comparison to results presented in the literature.
- The analysis demonstrates simple propagation models do not accurately reflect the way power will be received from a dipole in contact with tissues.
- The results enable the design of other types of probes for a desired sensing depth by extending the theory to a three layer human tissue model of skin, fat, and muscle. The input impedance is validated with Ansys HFSS, and the sensing depth is compared for different tissue thicknesses demonstrating a difference in sensing depth for different thicknesses of skin and fat.

Chapter 5 utilized the radiometers presented in Chapter 2 to demonstrate the detection of subsurface temperature changes using a water, glass, water phantom. Additionally, the question of weighting function model validity is addressed by simulation of a radiometer measuring thermal emission from a three layer tissue medium of skin, fat, and muscle. The following list summarizes the contributions from this chapter.

- Demonstrated detection of temperature change for a water half-space phantom utilizing both the 1.4 GHz and 2.7 GHz radiometers and probes
- Using a single frequency measurement, determined subsurface temperature of a three layer medium consisting of water, glass, and water with the 1.4 GHz radiometer
- Demonstrated multi-frequency subsurface temperature detection using both the 1.4 GHz and 2.7 GHz radiometers simultaneously. The error in the absolute temperature and detection of the change in

temperature is discussed.

- Discussed the least-squares and optimal estimation method and applied to estimate the temperature of the three layer medium using the two-frequency system measurements. The optimal estimation method helps to constrain the problem by weighting measured results with historical data.
- Analyzed the error in temperature estimates if incorrect weighting functions are used by simulating a radiometer system measuring thermal emission from a three layer tissue model of skin, fat, and muscle. This analysis demonstrated useful results if there are more measurements than unknowns or if the optimal estimation technique is used with an accurate historical temperature profile.

In summary, this thesis paves a path towards a wearable microwave thermometer for core body temperature measurement. The basic principles are identified and demonstrated, showing the feasibility and opening up several areas for future research.

BIBLIOGRAPHY

- [1] J. D. Kraus, *Radio Astronomy*, 2nd ed. Cygnus-Quasar Books, 1976. [1](#), [3](#), [20](#), [23](#), [64](#)

- [2] F. T. Ulaby, R. K. Moore, and A. K. Fung, *Microwave remote sensing : active and passive Vol. 1, Microwave remote sensing fundamentals and radiometry*. Norwood, Mass.: Artech House, 1981. [1](#), [3](#), [20](#), [23](#), [90](#), [91](#), [108](#)

- [3] K. Stephan, J. Pearce, L. Wang, and E. Ryza, "Cement kiln temperature measurements using microwave radiometry," in *Microwave Symposium Digest, 2005 IEEE MTT-S International*, 2005, pp. 151–154. [1](#)

- [4] B. Enander and G. Larson, "Microwave radiometric measurements of the temperature inside a body," *Electronics Letters*, vol. 10, no. 15, pp. 317–317, 1974. [2](#), [137](#)

- [5] E. Zampeli, I. Raftakis, A. Michelongona, C. Nikolaou, A. Elezoglou, K. Toutouzas, E. Siores, and P. P. Sfikakis, "Detection of subclinical synovial inflammation by microwave radiometry," *PLoS ONE*, vol. 8, no. 5, p. e64606, May 2013. [2](#), [137](#), [138](#)

- [6] J. Edrich and P. Hardee, "Thermography at millimeter wavelengths," *Proceedings of the IEEE*, vol. 62, no. 10, pp. 1391–1392, 1974. [2](#)

- [7] K. Carr, "Microwave radiometry: its importance to the detection of cancer," *IEEE Transactions on Microwave Theory and Techniques*, vol. 37, no. 12, pp. 1862–1869, Dec. 1989. [2](#), [137](#)

- [8] S. Mouty, B. Bocquet, R. Ringot, N. Rocourt, and P. Devos, "Microwave radiometric imaging (MWI) for the characterisation of breast tumours," *The European Physical Journal - Applied Physics*, vol. 10, no. 01, pp. 73–78, 2000. [2](#), [137](#)

- [9] J. Shaeffer, A. M. El-Mahdi, A. E. Hamwey, and K. L. Carr, "Detection of extravasation of antineoplastic drugs by microwave radiometry," *Cancer Letters*, vol. 31, no. 3, pp. 285–291, Jun. 1986. [2](#), [137](#)

- [10] S. Jacobsen and P. Stauffer, "Multifrequency radiometric determination of temperature profiles in a lossy homogeneous phantom using a dual-mode antenna with integral water bolus," *IEEE Transactions on Microwave Theory and Techniques*, vol. 50, no. 7, pp. 1737–1746, Jul. 2002. [2](#), [107](#), [137](#)
- [11] J. W. Hand, G. M. J. V. Leeuwen, S. Mizushina, J. B. V. d. Kamer, K. Maruyama, T. Sugiura, D. V. Azzopardi, and A. D. Edwards, "Monitoring of deep brain temperature in infants using multi-frequency microwave radiometry and thermal modelling," *Physics in Medicine and Biology*, vol. 46, no. 7, pp. 1885–1903, Jul. 2001. [2](#), [15](#), [107](#), [129](#), [137](#)
- [12] K. Maruyama, S. Mizushina, T. Sugiura, G. Van Leeuwen, J. Hand, G. Marrocco, F. Bardati, A. Edwards, D. Azzopardi, and D. Land, "Feasibility of noninvasive measurement of deep brain temperature in newborn infants by multifrequency microwave radiometry," *IEEE Transactions on Microwave Theory and Techniques*, vol. 48, no. 11, pp. 2141 – 2147, Nov. 2000. [2](#), [88](#), [129](#), [137](#)
- [13] K. Arunachalam, P. Maccarini, V. De Luca, P. Tognolatti, F. Bardati, B. Snow, and P. Stauffer, "Detection of vesicoureteral reflux using microwave Radiometry–System characterization with tissue phantoms," *IEEE Transactions on Biomedical Engineering*, vol. 58, no. 6, pp. 1629–1636, Jun. 2011. [2](#), [137](#)
- [14] Y. Birkelund, O. Klemetsen, S. K. Jacobsen, K. Arunachalam, P. Maccarini, and P. R. Stauffer, "Vesicoureteral reflux in children: A phantom study of microwave heating and radiometric thermometry of pediatric bladder," *IEEE Transactions on Biomedical Engineering*, vol. 58, no. 11, pp. 3269–3278, Nov. 2011. [2](#), [137](#)
- [15] A. Macdonald, D. Land, and R. Sturrock, "Microwave thermography as a noninvasive assessment of disease activity in inflammatory arthritis," *Clinical Rheumatology*, vol. 13, pp. 589–592, 1994. [2](#), [138](#)
- [16] K. Toutouzas, C. Grassos, M. Drakopoulou, A. Synetos, E. Tsiamis, C. Aggeli, K. Stathogiannis, D. Klettas, N. Kavantzias, G. Agrogiannis, E. Patsouris, C. Klonaris, N. Liasis, D. Tousoulis, E. Siores, and C. Stefanadis, "First in vivo application of microwave radiometry in human carotids," *Journal of the American College of Cardiology*, vol. 59, no. 18, pp. 1645–1653, May 2012. [2](#), [138](#)
- [17] K. Toutouzas, A. Synetos, C. Nikolaou, K. Stathogiannis, E. Tsiamis, and C. Stefanadis, "Microwave radiometry: a new non-invasive method for the detection of vulnerable plaque," *Cardiovascular Diagnosis and Therapy*, vol. 2, no. 4, 2012. [2](#), [138](#)
- [18] S. Jacobsen and P. Stauffer, "Performance evaluation of various antenna configurations for microwave thermography during superficial hyperthermia," *Journal of Electromagnetic Waves and Applications*, vol. 15, no. 1, pp. 111–134, Jan. 2001. [2](#), [15](#), [17](#), [74](#)
- [19] K. D. Stephan, J. B. Mead, D. M. Pozar, L. Wang, and J. A. Pearce, "A near field focused microstrip array for a radiometric temperature sensor," *IEEE Transactions on Antennas and Propagation*, vol. 55, no. 4, pp. 1199–1203, Apr. 2007. [2](#)

- [20] J. M. Palmer and B. G. Grant, *The art of radiometry*. Bellingham, Wash: SPIE Press, 2010. 3
- [21] B. Oliver, “Thermal and quantum noise,” *Proceedings of the IEEE*, vol. 53, no. 5, pp. 436–454, 1965. 4
- [22] H. Nyquist, “Thermal agitation of electric charge in conductors,” *Phys. Rev.*, vol. 32, pp. 110–113, Jul. 1928. 5
- [23] F. T. Ulaby, R. K. Moore, and A. K. Fung, *Microwave Remote Sensing Active and Passive*. Artech House, 1986, vol. III: From Theory to Applications. 8, 118, 119
- [24] B. Bocquet, P. DeHour, A. Mamouni, J. Van De Velde, and Y. Leroy, “Near field microwave radiometric weighting functions for multilayered materials,” *Journal of Electromagnetic Waves and Applications*, vol. 7, no. 11, pp. 1497–1514, Jan. 1993. 8, 75, 88
- [25] C. Gabriel, S. Gabriel, and E. Corthout, “The dielectric properties of biological tissues: I. literature survey,” *Physics in Medicine and Biology*, vol. 41, no. 11, pp. 2231–2249, Nov. 1996. 9, 12, 74, 75, 100
- [26] S. Gabriel, R. W. Lau, and C. Gabriel, “The dielectric properties of biological tissues: II. measurements in the frequency range 10 Hz to 20 GHz,” *Physics in Medicine and Biology*, vol. 41, no. 11, pp. 2251–2269, Nov. 1996. 9, 74, 75, 100
- [27] —, “The dielectric properties of biological tissues: III. parametric models for the dielectric spectrum of tissues,” *Physics in Medicine and Biology*, vol. 41, no. 11, pp. 2271–2293, Nov. 1996. 9, 12, 74
- [28] D. Andreuccetti, R. Fossi, and C. Petrucci, “An internet resource for the calculation of the dielectric properties of body tissues in the frequency range 10 Hz - 100 GHz,” 2013, IFAC-CNR, Florence (Italy), 1997. Based on data published by C.Gabriel et al. in 1996. [Online]. Available: <http://niremf.ifac.cnr.it/tissprop/> 9, 43, 74, 75
- [29] IT’IS, “Tissue properties database,” 2013. [Online]. Available: <http://www.itis.ethz.ch/itis-for-health/tissue-properties/database/> 9
- [30] —, “The virtual population,” 2013. [Online]. Available: <http://www.itis.ethz.ch/services/anatomical-models/overview/> 9, 102, 105, 139, 141
- [31] C. A. Balanis, *Advanced engineering electromagnetics*. New York: Wiley, 1989. 10, 77
- [32] K. Foster and H. Schwan, *Handbook of biological effects of electromagnetic fields*, 2nd ed., C. Polk and E. Postow, Eds. Boca Raton: CRC Press, 1996. 10

- [33] P. Debye, *Polar Molecules*. New York: Chemical Catalog Company, 1929. 10, 91
- [34] A. Stogryn, "Equations for calculating the dielectric constant of saline water (Correspondence)," *IEEE Transactions on Microwave Theory and Techniques*, vol. 19, no. 8, pp. 733–736, Aug. 1971. 10, 13, 14
- [35] H. Schwan and K. Foster, "RF-field interactions with biological systems: Electrical properties and biophysical mechanisms," *Proceedings of the IEEE*, vol. 68, no. 1, pp. 104–113, 1980. 10
- [36] D. Miklavčič, N. Pavšelj, and F. X. Hart, "Electric properties of tissues," *Wiley encyclopedia of biomedical engineering*, 2006. 10
- [37] C. Gabriel, *Dielectric Properties of Biological Materials*, 3rd ed., F. S. Barnes and B. , Greenebaum, Eds. CRC Press, 2007. 10, 11, 12, 13
- [38] K. S. Cole and R. H. Cole, "Dispersion and absorption in dielectrics I. alternating current characteristics," *The Journal of Chemical Physics*, vol. 9, no. 4, p. 341, 1941. 12
- [39] S. Jacobsen and O. Klemetsen, "Improved detectability in medical microwave Radio-Thermometers as obtained by active antennas," *IEEE Transactions on Biomedical Engineering*, vol. 55, no. 12, pp. 2778–2785, Dec. 2008. 13, 15, 17, 74, 91
- [40] E. Cheever, J. Leonard, and K. Foster, "Depth of penetration of fields from rectangular apertures into lossy media (Short paper)," *IEEE Transactions on Microwave Theory and Techniques*, vol. 35, no. 9, pp. 865–867, Sep. 1987. 13, 75, 91
- [41] T. Sugiura, Y. Kouno, A. Hashizume, H. Hirata, J. Hand, Y. Okita, and S. Mizushina, "Five-band microwave radiometer system for non-invasive measurement of brain temperature in new-born infants: system calibration and its feasibility," in *IEMBS '04. 26th Annual International Conference of the IEEE Engineering in Medicine and Biology Society, 2004*, vol. 1, Sep. 2004, pp. 2292–2295. 13, 15, 17, 91, 129
- [42] W. Ellison, K. Lamkaouchi, and J. Moreau, "Water: a dielectric reference," *Journal of Molecular Liquids*, vol. 68, no. 2-3, pp. 171–279, Apr. 1996. 13, 91
- [43] U. Kaatze, "Complex permittivity of water as a function of frequency and temperature," *Journal of Chemical & Engineering Data*, vol. 34, no. 4, pp. 371–374, Oct. 1989. 13, 14
- [44] H. J. Liebe, G. A. Hufford, and T. Manabe, "A model for the complex permittivity of water at frequencies below 1 THz," *International Journal of Infrared and Millimeter Waves*, vol. 12, no. 7, pp. 659–675, Jul. 1991. 13, 14, 34, 40, 91, 92

- [45] R. Buchner, G. T. Hefter, and P. M. May, "Dielectric relaxation of aqueous NaCl solutions," *The Journal of Physical Chemistry A*, vol. 103, no. 1, pp. 1–9, Jan. 1999. [13](#)
- [46] C. Malmberg and A. Maryott, "Dielectric constant of water from 0° to 100° C," *Journal of Research of the National Bureau of Standards*, vol. 56, no. 1, pp. 1–8, 1956. [13](#)
- [47] A. Guy, "Analyses of electromagnetic fields induced in biological tissues by thermographic studies on equivalent phantom models," *IEEE Transactions on Microwave Theory and Techniques*, vol. 16, no. 2, pp. 205–214, Feb. 1971. [14](#), [139](#)
- [48] M. Lazebnik, E. L. Madsen, G. R. Frank, and S. C. Hagness, "Tissue-mimicking phantom materials for narrowband and ultrawideband microwave applications," *Physics in Medicine and Biology*, vol. 50, no. 18, pp. 4245–4258, Sep. 2005. [14](#), [139](#)
- [49] T. Yilmaz, T. Karacolak, and E. Topsakal, "Characterization and testing of a skin mimicking material for implantable antennas operating at ISM band (2.4 GHz-2.48 GHz)," *IEEE Antennas and Wireless Propagation Letters*, vol. 7, pp. 418–420, 2008. [14](#), [139](#)
- [50] J. Montreuil and M. Nachman, "Multiangle method for temperature measurement of biological tissues by microwave radiometry," *IEEE Transactions on Microwave Theory and Techniques*, vol. 39, no. 7, pp. 1235–1239, Jul. 1991. [15](#), [75](#)
- [51] Q. Bonds, J. Gerig, T. M. Weller, and P. Herzig, "Towards core body temperature measurement via close proximity radiometric sensing," *IEEE Sensors Journal*, vol. 12, no. 3, pp. 519–526, Mar. 2012. [15](#), [17](#)
- [52] O. Klemetsen and S. Jacobsen, "Improved radiometric performance attained by an elliptical microwave antenna with suction," *IEEE Transactions on Biomedical Engineering*, vol. 59, no. 1, pp. 263–271, Jan. 2012. [15](#), [17](#)
- [53] D. M. Pozar, *Microwave Engineering*, 3rd ed. Wiley, 2005. [20](#), [51](#), [52](#)
- [54] N. Skou and D. M. Le Vine, *Microwave radiometer systems design and analysis*. Boston: Artech House, 2006. [23](#)
- [55] A. Camps and J. M. Tarongí, "Microwave radiometer resolution optimization using variable observation times," *Remote Sensing*, vol. 2, no. 7, pp. 1826–1843, Jul. 2010. [23](#)
- [56] R. H. Dicke, "The measurement of thermal radiation at microwave frequencies," *Review of Scientific Instruments*, vol. 17, no. 7, p. 268, 1946. [23](#)

- [57] M. Goodberlet and J. Mead, “Two-load radiometer precision and accuracy,” *IEEE Transactions on Geoscience and Remote Sensing*, vol. 44, no. 1, pp. 58–67, Jan. 2006. 24, 27
- [58] FCC, “FCC online table of frequency allocations,” 2013. [Online]. Available: <http://transition.fcc.gov/oet/spectrum/table/fctable.pdf> 25, 27
- [59] C. Brewitt-Taylor, D. Gunton, and H. Rees, “Planar antennas on a dielectric surface,” *Electronics Letters*, vol. 17, no. 20, p. 729, 1981. 27, 96
- [60] M. Kominami, D. Pozar, and D. Schaubert, “Dipole and slot elements and arrays on semi-infinite substrates,” *IEEE Transactions on Antennas and Propagation*, vol. 33, no. 6, pp. 600–607, Jun. 1985. 27, 76, 92, 96
- [61] D. W. Allan, “Should the classical variance be used as a basic measure in standards metrology?” *IEEE Transactions on Instrumentation and Measurement*, vol. IM-36, no. 2, pp. 646–654, Jun. 1987. 27
- [62] J. Randa, J. Lahtinen, A. Camps, A. Gasiewski, M. Hallikainen, D. Le Vine, M. Martin-Neira, J. Piepmeier, P. Rosenkranz, C. Ruf, J. Shiue, and N. Skou, “Recommended terminology for microwave radiometry,” *NIST Technical Note TN1551*, Aug. 2008. 27
- [63] Agilent Technologies, “Noise Figure Measurement Accuracy – The Y-Factor Method,” *Application Note 57-2*, Apr. 2013. 28
- [64] J. Duncan and V. Minerva, “100:1 bandwidth balun transformer,” *Proceedings of the IRE*, vol. 48, no. 2, pp. 156–164, Feb. 1960. 33
- [65] M. Gans, D. Kajfez, and V. Rumsey, “Frequency independent baluns,” *Proceedings of the IEEE*, vol. 53, no. 6, pp. 647–648, 1965. 33
- [66] B. Climer, “Analysis of suspended microstrip taper baluns,” *IEE Proceedings*, vol. 135, no. 2, pp. 65–69, 1988. 33
- [67] S. Kim and K. Chang, “Ultrawide-Band transitions and new microwave components using Double-Sided Parallel-Strip lines,” *IEEE Transactions on Microwave Theory and Techniques*, vol. 52, no. 9, pp. 2148–2152, Sep. 2004. 33
- [68] A. Fonte, F. Alimenti, D. Zito, B. Neri, D. De Rossi, A. Lanata, and A. Tognetti, “Wearable System-on-a-Chip radiometer for remote temperature sensing and its application to the safeguard of emergency operators,” in *EMBS 2007 29th Annual International Conference of the IEEE Engineering in Medicine and Biology Society, 2007*, Aug. 2007, pp. 5715–5718. 50

- [69] F. Alimenti, D. Zito, A. Boni, M. Borgarino, A. Fonte, A. Carboni, S. Leone, M. Pifferi, L. Roselli, B. Neri, and R. Menozzi, "System-on-chip microwave radiometer for thermal remote sensing and its application to the forest fire detection," in *ICECS 2008. 15th IEEE International Conference on Electronics, Circuits and Systems, 2008*, Aug. 2008, pp. 1265–1268. [50](#)
- [70] F. Iturbide-Sanchez, S. C. Reising, and S. Padmanabhan, "A miniaturized spectrometer radiometer based on MMIC technology for tropospheric water vapor profiling," *IEEE Transactions on Geoscience and Remote Sensing*, vol. 45, no. 7, pp. 2181–2194, Jul. 2007. [50](#)
- [71] S.-M. Wang, C.-Y. Chang, and J. Lin, "A software configurable coupler with programmable coupling coefficient," in *Microwave Symposium, 2007. IEEE/MTT-S International*, 2007, pp. 185–188. [50](#), [62](#), [63](#)
- [72] S. Toyoda, "Variable coupling directional couplers using varactor diodes," in *Microwave Symposium Digest, MTT-S International*, vol. 82, no. 1, 1982, pp. 419–421. [50](#), [62](#), [63](#)
- [73] C.-S. Kim, C.-S. Yoon, J.-S. Park, D. Ahn, J.-B. Lim, and S.-I. Yang, "A design of the novel varactor tuned directional coupler," in *Microwave Symposium Digest, 1999 IEEE MTT-S International*, vol. 4, 1999, pp. 1725–1728. [50](#)
- [74] Y. Wang, Y. Zhang, L. He, F. Liu, H. Li, and H. Chen, "Tunable asymmetric composite right-/left-handed transmission line directional coupler controlled by applied voltage," in *Microwave Conference Proceedings, 2005. APMC 2005. Asia-Pacific Conference Proceedings*, vol. 1, 2005. [50](#)
- [75] M. Abdalla, K. Phang, and G. V. Eleftheriades, "A compact highly reconfigurable CMOS MMIC direction coupler," *IEEE Trans. Microw. Theory Tech.*, vol. 56, pp. 305–319, Feb. 2008. [50](#), [51](#), [62](#), [63](#)
- [76] B. Hur and W. Eisenstadt, "Tunable broadband MMIC active directional coupler," *IEEE Transactions on Microwave Theory and Techniques*, vol. 61, no. 1, pp. 168–176, Jan. 2013. [50](#), [62](#), [63](#)
- [77] U. Shah, M. Sterner, and J. Oberhammer, "High-Directivity MEMS-Tunable directional couplers for 10-18-GHz broadband applications," *IEEE Transactions on Microwave Theory and Techniques*, vol. 61, no. 9, pp. 3236–3246, Sep. 2013. [50](#), [62](#), [63](#)
- [78] R. Scheeler and Z. Popović, "GaAs MMIC tunable directional coupler," in *2012 IEEE MTT-S International Microwave Symposium Digest (MTT)*. IEEE, Jun. 2012, pp. 1–3. [63](#), [143](#)
- [79] R. Frater and D. Williams, "An active "Cold" noise source," *IEEE Transactions on Microwave Theory and Techniques*, vol. 29, no. 4, pp. 344–347, Apr. 1981. [64](#)
- [80] L. Dunleavy, M. Smith, S. Lardizabal, A. Fejzuli, and R. Roeder, "Design and characterization of FET

- based cold/hot noise sources,” in *Microwave Symposium Digest, 1997., IEEE MTT-S International*, vol. 3, Jun. 1997, pp. 1293–1296 vol.3. [64](#)
- [81] E. Leynia de la Jarrige, L. Escotte, J. Goutoule, E. Gonneau, and J. Rayssac, “SiGe HBT-based active cold load for radiometer calibration,” *Microwave and Wireless Components Letters, IEEE*, vol. 20, no. 4, pp. 238–240, 2010. [64](#)
- [82] P. Buhles and S. Lardizabal, “Design and characterization of MMIC active cold loads,” in *Microwave Symposium Digest. 2000 IEEE MTT-S International*, vol. 1, 2000, pp. 29–32 vol.1. [64](#)
- [83] S. S. Sobjaerg, J. E. Balling, and N. Skou, “Challenges in application of active cold loads for microwave radiometer calibration,” in *2012 12th Specialist Meeting on Microwave Radiometry and Remote Sensing of the Environment (MicroRad)*, Mar. 2012, pp. 1–4. [64](#)
- [84] J. Randa, L. Dunleavy, and L. Terrell, “Stability measurements on noise sources,” *IEEE Transactions on Instrumentation and Measurement*, vol. 50, no. 2, pp. 368–372, Apr. 2001. [64](#)
- [85] E. Leynia de la Jarrige, L. Escotte, E. Gonneau, and J. Goutoule, “Stability analysis of an SiGe HBT-Based active cold load,” *IEEE Transactions on Microwave Theory and Techniques*, vol. 59, no. 2, pp. 354–359, Feb. 2011. [64](#)
- [86] M. Weatherspoon and L. Dunleavy, “Experimental validation of generalized equations for FET cold noise source design,” *IEEE Transactions on Microwave Theory and Techniques*, vol. 54, no. 2, pp. 608–614, Feb. 2006. [65](#), [72](#), [143](#)
- [87] C. Gabriel, E. H. Grant, and I. R. Young, “Use of time domain spectroscopy for measuring dielectric properties with a coaxial probe,” *Journal of Physics E: Scientific Instruments*, vol. 19, no. 10, pp. 843–846, Oct. 1986. [74](#), [76](#)
- [88] J. P. Grant, R. N. Clarke, G. T. Symm, and N. M. Spyrou, “In vivo dielectric properties of human skin from 50 MHz to 2.0 GHz,” *Physics in Medicine and Biology*, vol. 33, no. 5, pp. 607–612, May 1988. [74](#), [76](#)
- [89] A. Guy, “Electromagnetic fields and relative heating patterns due to a rectangular aperture source in direct contact with bilayered biological tissue,” *IEEE Transactions on Microwave Theory and Techniques*, vol. 16, no. 2, pp. 214–223, Feb. 1971. [75](#)
- [90] K. Nikita and N. Uzunoglu, “Analysis of the power coupling from a waveguide hyperthermia applicator into a three-layered tissue model,” *IEEE Transactions on Microwave Theory and Techniques*, vol. 37, no. 11, pp. 1794–1801, Nov. 1989. [75](#)

- [91] L. Beyne and D. De Zutter, "Green's function for layered lossy media with special application to microstrip antennas," *IEEE Transactions on Microwave Theory and Techniques*, vol. 36, no. 5, pp. 875–881, May 1988. [76](#)
- [92] N. Das and D. Pozar, "A generalized Spectral-Domain green's function for multilayer dielectric substrates with application to multilayer transmission lines," *IEEE Transactions on Microwave Theory and Techniques*, vol. 35, no. 3, pp. 326–335, Mar. 1987. [76](#)
- [93] J. Galejs, "Driving point impedance of linear antennas in the presence of a stratified dielectric," *IEEE Transactions on Antennas and Propagation*, vol. 13, no. 5, pp. 725–737, Sep. 1965. [76](#), [86](#), [157](#)
- [94] ———, *Antennas in Inhomogeneous Media*. Oxford; New York: Pergamon Press, 1969. [76](#), [79](#), [86](#), [95](#), [157](#)
- [95] S. Dvorak and E. Kuester, "Fast numerical computation of the input impedance and electric field distribution for a printed strip dipole in a layered medium," Electromagnetics Laboratory, University of Colorado Boulder, Scientific Report 94, 1989. [76](#), [79](#), [86](#)
- [96] R. E. Collin, *Field theory of guided waves*. New York: IEEE Press, 1990. [76](#), [77](#)
- [97] P. Carter, "Circuit relations in radiating systems and applications to antenna problems," *Proceedings of the IRE*, vol. 20, no. 6, pp. 1004–1041, Jun. 1932. [85](#)
- [98] T. Y. Otoshi, "The effect of mismatched components on microwave noise-temperature calibrations," *IEEE Transactions on Microwave Theory and Techniques*, vol. 16, no. 9, pp. 675–686, Sep. 1968. [91](#), [108](#)
- [99] B. Coleman, "Propagation of electromagnetic disturbances along a thin wire, in a horizontally stratified medium," *Philosophical Magazine Series 7*, vol. 41, no. 314, pp. 276–288, 1950. [92](#)
- [100] B. Popović and T. Gavrilov, "Simple method for analysis of cylindrical antennas at the interface between two media," *Radio and Electronic Engineer*, vol. 46, no. 11, p. 553, 1976. [92](#), [93](#)
- [101] K. Iizuka, "An experimental investigation on the behaviour of the dipole antenna near the interface between the conducting medium and free space," Cruft laboratory, Harvard University, Scientific Report 4, 1963. [93](#)
- [102] C. A. Balanis, *Antenna theory : analysis and design*. Hoboken, NJ: John Wiley, 2005. [93](#)

- [103] F. Johansson *et al.*, *mpmath: a Python library for arbitrary-precision floating-point arithmetic (version 0.14)*, February 2010, <http://code.google.com/p/mpmath/>. 95
- [104] J. Galejs, “Power flow from a short antenna in a lossy uniaxial medium,” *Radio Science*, vol. 2, no. 12, pp. 1419–1430, Dec. 1967. 95
- [105] S. Mizushina, T. Shimizu, K. Suzuki, M. Kinomura, H. Ohba, and T. Sugiura, “Retrieval of Temperature-Depth profiles in biological objects from Multi-Frequency microwave radiometric data,” *Journal of Electromagnetic Waves and Applications*, vol. 7, no. 11, pp. 1515–1548, Jan. 1993. 107, 129
- [106] B. Stec, A. Dobrowolski, and W. Susek, “Estimation of deep-seated profile of temperature distribution inside biological tissues by means of multifrequency microwave thermograph,” in *Microwave Symposium Digest, 2002 IEEE MTT-S International*, vol. 3, 2002, pp. 2261–2264. 107
- [107] S. Jacobsen and P. Stauffer, “Nonparametric 1-D temperature restoration in lossy media using tikhonov regularization on sparse radiometry data,” *IEEE Transactions on Biomedical Engineering*, vol. 50, no. 2, pp. 178–188, Feb. 2003. 107, 129
- [108] B. N. Taylor and C. E. Kuyatt, “Guidelines for Evaluating and Expressing the Uncertainty of NIST Measurement Results,” *NIST Technical Note 1297*, 1994. 115
- [109] T. K. Moon and W. C. Stirling, *Mathematical methods and algorithms for signal processing*. Upper Saddle River, NJ: Prentice Hall, 2000. 118
- [110] C. D. Rodgers, “Retrieval of atmospheric temperature and composition from remote measurements of thermal radiation,” *Reviews of Geophysics*, vol. 14, no. 4, p. 609, 1976. 118, 119
- [111] N. E. Rosenthal, A. A. Levendosky, R. G. Skwerer, J. R. Joseph-Vanderpool, K. A. Kelly, T. Hardin, S. Kasper, P. DellaBella, and T. A. Wehr, “Effects of light treatment on core body temperature in seasonal affective disorder,” *Biological Psychiatry*, vol. 27, no. 1, pp. 39–50, 1990. 123, 129, 140
- [112] K. Kräuchi, C. Cajochen, E. Werth, and A. Wirz-Justice, “Functional link between distal vasodilation and sleep-onset latency?” *American Journal of Physiology - Regulatory, Integrative and Comparative Physiology*, vol. 278, no. 3, pp. R741–R748, 2000. 129, 130, 131, 140
- [113] J. E. Gale, H. I. Cox, J. Qian, G. D. Block, C. S. Colwell, and A. V. Matveyenko, “Disruption of circadian rhythms accelerates development of diabetes through pancreatic Beta-Cell loss and dysfunction,” *Journal of Biological Rhythms*, vol. 26, no. 5, pp. 423–433, Sep. 2011. 129
- [114] D. Jeyaraj, S. M. Haldar, X. Wan, M. D. McCauley, J. A. Ripperger, K. Hu, Y. Lu, B. L. Eapen,

- N. Sharma, E. Ficker, M. J. Cutler, J. Gulick, A. Sanbe, J. Robbins, S. Demolombe, R. V. Kondratov, S. A. Shea, U. Albrecht, X. H. T. Wehrens, D. S. Rosenbaum, and M. K. Jain, "Circadian rhythms govern cardiac repolarization and arrhythmogenesis," *Nature*, vol. 483, no. 7387, pp. 96–99, Feb. 2012. [129](#)
- [115] D. M. Wilkinson, J. M. Carter, V. L. Richmond, S. D. Blacker, and M. P. Rayson, "The effect of cool water ingestion on gastrointestinal pill temperature," *Medicine & Science in Sports & Exercise*, vol. 40, no. 3, pp. 523–528, Mar. 2008. [129](#)
- [116] A. Christ, W. Kainz, E. G. Hahn, K. Honegger, M. Zefferer, E. Neufeld, W. Rascher, R. Janka, W. Bautz, J. Chen, B. Kiefer, P. Schmitt, H. Hollenbach, J. Shen, M. Oberle, D. Szczerba, A. Kam, J. W. Guag, and N. Kuster, "The virtual family—development of surface-based anatomical models of two adults and two children for dosimetric simulations," *Physics in Medicine and Biology*, vol. 55, no. 2, pp. N23–N38, Jan. 2010. [139](#), [140](#)
- [117] Texas Instruments, "MSP430 Ultra-Low-Power Microcontrollers," *MSP430 Selection Guide*, 2013. [140](#)
- [118] D. Ozis, J. Paramesh, and D. J. Allstot, "A CMOS 5GHz Image-Reject receiver Front-End architecture," in *2007 IEEE Radio Frequency Integrated Circuits (RFIC) Symposium*, Jun. 2007, pp. 321–324. [141](#)
- [119] D. Huang, S. Kao, and Y. Pang, "A WiMAX receiver with variable bandwidth of 2.5 - 20 MHz and 93 dB dynamic gain range in 0.13- μ m CMOS process," in *2007 IEEE Radio Frequency Integrated Circuits (RFIC) Symposium*, Jun. 2007, pp. 369–372. [141](#)
- [120] G. Cafaro, T. Gradishar, J. Heck, S. Machan, G. Nagaraj, S. Olson, R. Salvi, B. Stengel, and B. Ziemer, "A 100 MHz 2.5 GHz direct conversion CMOS transceiver for SDR applications," in *2007 IEEE Radio Frequency Integrated Circuits (RFIC) Symposium*, Jun. 2007, pp. 189–192. [141](#)
- [121] F. Azevedo, F. Fortes, and M. J. Rosario, "A 1.8V/5.2GHz WLAN CMOS RFIC receiver," in *2011 IEEE EUROCON - International Conference on Computer as a Tool (EUROCON)*, Apr. 2011, pp. 1–4. [141](#)
- [122] R. Scheeler, X. Palomer, and Z. Popović, "Compact nested dipole probe for Near-Field radiometric temperature measurement of the body." Presented at the USNC-URSI National Radio Science Meeting, Jan. 2012. [142](#)
- [123] R. Scheeler, E. Kuester, and Z. Popović, "Sensing depth of microwave radiation for internal body temperature measurement," *Submitted to IEEE Transactions on Antennas and Propagation*. [142](#), [144](#)
- [124] R. Scheeler and Z. Popović, "A 1.4 GHz MMIC active cold noise source," in *2013 IEEE Compound Semiconductor Integrated Circuit Symposium (CSICS)*, 2013, pp. 1–4. [143](#)

APPENDIX A

VARIATIONAL SOLUTION TO THE INPUT IMPEDANCE

A variational solution to the input impedance can be found using the induced EMF method. This is the same as presented by Galejs [93] and Sec. 9.1 of [94] and is summarized here for clarity. To determine the input impedance the antenna current density is represented by the trial function

$$J_x(x, y) = [Af_A(x) + Bf_B(x)] f(y) \quad (\text{A.1})$$

where

$$f_A(x) = \sin [k(l/2 - |x|)] \quad (\text{A.2})$$

$$f_B(x) = 1 - \cos [k(l/2 - |x|)] \quad (\text{A.3})$$

$$f(y) = \frac{1}{W}. \quad (\text{A.4})$$

The Fourier transform of (A.1) is given by

$$\tilde{J}_x(\alpha, \beta) = \frac{k}{2\pi^2} \text{sinc}(\beta W/2) [Ag_A(\alpha) + Bg_B(\alpha)] \quad (\text{A.5})$$

where

$$g_A(\alpha) = \frac{1}{k^2 - \alpha^2} \left[\cos\left(\frac{\alpha l}{2}\right) - \cos\left(\frac{kl}{2}\right) \right] \quad (\text{A.6})$$

$$g_B(\alpha) = \frac{1}{k^2 - \alpha^2} \left[\frac{k}{\alpha} \sin\left(\frac{\alpha l}{2}\right) - \sin\left(\frac{kl}{2}\right) \right]. \quad (\text{A.7})$$

Substituting (A.5) into (4.57) yields

$$Z_{\text{in}} = \frac{A^2 \zeta_{AA} + 2AB \zeta_{AB} + B^2 \zeta_{BB}}{(A f_A(0) + B f_B(0))^2} \quad (\text{A.8})$$

where

$$\zeta_{NM} = \frac{4jk^2\omega}{\pi^2} \int_0^\infty \int_0^\infty \text{sinc}^2(\beta W/2) \tilde{F}(\alpha, \beta) g_N(\alpha) g_M(\alpha) d\alpha d\beta \quad (\text{A.9})$$

and $N, M = A$ and/or B . Dividing the numerator and denominator of (A.8) by AB yields an expression in terms of the ratio A/B

$$Z_{\text{in}} = \frac{(A/B)\zeta_{AA} + 2\zeta_{AB} + (B/A)\zeta_{BB}}{(A/B)f_A(0)^2 + 2f_A(0)f_B(0) + (B/A)f_B(0)^2}. \quad (\text{A.10})$$

The impedance is stationary such that a small change in the current about its correct value will cause a zero first order change in the impedance. The stationary nature of the impedance is utilized to find the ratio A/B by requiring $\partial Z_{\text{in}}/\partial(A/B) = 0$. Performing the differentiation and solving gives

$$\frac{A}{B} = \frac{f_A(0)\zeta_{BB} - f_B(0)\zeta_{AB}}{f_B(0)\zeta_{AA} - f_A(0)\zeta_{AB}} \quad (\text{A.11})$$

$$Z_{\text{in}} = \frac{\zeta_{AA}\zeta_{BB} - \zeta_{AB}^2}{\Delta} \quad (\text{A.12})$$

where

$$\Delta = f_B(0)^2 \zeta_{AA} - 2f_A(0)f_B(0)\zeta_{AB} + f_A(0)^2 \zeta_{BB}. \quad (\text{A.13})$$

APPENDIX B

POWER FLOW IN A STRATIFIED MEDIUM

The expression for the power flow, or real power passing through a plane in the i -th layer of a stratified medium is given from (4.59) using the transformed fields in (4.24) where

$$\tilde{E}_{xi} = [-A_i \beta \omega \mu_i (e^{-2s\gamma_i z} + \Gamma_{ai}) + js B_i \alpha \gamma_i (e^{-2s\gamma_i z} - \Gamma_{bi})] e^{s\gamma_i z} \quad (\text{B.1})$$

$$\tilde{H}_{y,-1} = [js A_i \beta \gamma_i (e^{-2s\gamma_i z} - \Gamma_{ai}) - B_i \omega \epsilon_i \alpha (e^{-2s\gamma_i z} + \Gamma_{bi})] e^{s\gamma_i z} \quad (\text{B.2})$$

$$\tilde{H}_{y,-1}^* = [-js A_i^* \beta \gamma_i^* (e^{-2s\gamma_i^* z} - \Gamma_{ai}^*) - B_i^* \omega \epsilon_i^* \alpha (e^{-2s\gamma_i^* z} + \Gamma_{bi}^*)] e^{s\gamma_i^* z}. \quad (\text{B.3})$$

Multiplying (B.1) by (B.3)

$$\begin{aligned} \tilde{E}_{xi} \tilde{H}_{y,-1}^* &= [js |A_i|^2 \beta^2 \omega \mu_i \gamma_i^* (e^{-2s\gamma_i z} + \Gamma_{ai}) (e^{-2s\gamma_i^* z} - \Gamma_{ai}^*) \\ &\quad + A_i B_i^* \omega^2 \mu_i \epsilon_i^* \alpha \beta (e^{-2s\gamma_i z} + \Gamma_{ai}) (e^{-2s\gamma_i^* z} + \Gamma_{bi}^*) \\ &\quad + A_i^* B_i \alpha \beta |\gamma_i|^2 (e^{-2s\gamma_i z} - \Gamma_{bi}) (e^{-2s\gamma_i^* z} - \Gamma_{ai}^*) \\ &\quad - js |B_i|^2 \omega \epsilon_i^* \gamma_i \alpha^2 (e^{-2s\gamma_i z} - \Gamma_{bi}) (e^{-2s\gamma_i^* z} + \Gamma_{bi}^*)] e^{2s \text{Re}\{\gamma_i\} z}. \end{aligned} \quad (\text{B.4})$$

Again using the transformed fields in (4.24)

$$\tilde{E}_{yi} = [A_i \alpha \omega \mu_i (e^{-2s\gamma_i z} + \Gamma_{ai}) + js B_i \beta \gamma_i (e^{-2s\gamma_i z} - \Gamma_{bi})] e^{s\gamma_i z} \quad (\text{B.5})$$

$$\tilde{H}_{xi} = [js A_i \alpha \gamma_i (e^{-2s\gamma_i z} - \Gamma_{ai}) + B_i \omega \epsilon_i \beta (e^{-2s\gamma_i z} + \Gamma_{bi})] e^{s\gamma_i z} \quad (\text{B.6})$$

$$\tilde{H}_{xi}^* = [-js A_i^* \alpha \gamma_i^* (e^{-2s\gamma_i^* z} - \Gamma_{ai}^*) + B_i^* \omega \epsilon_i^* \beta (e^{-2s\gamma_i^* z} + \Gamma_{bi}^*)] e^{s\gamma_i^* z}. \quad (\text{B.7})$$

Multiplying (B.5) by (B.7)

$$\begin{aligned} \tilde{E}_{yi} \tilde{H}_{xi}^* &= [-js |A_i|^2 \alpha^2 \omega \mu_i \gamma_i^* (e^{-2s\gamma_i z} + \Gamma_{ai}) (e^{-2s\gamma_i^* z} - \Gamma_{ai}^*) \\ &\quad + A_i B_i^* \omega^2 \mu_i \epsilon_i^* \alpha \beta (e^{-2s\gamma_i z} + \Gamma_{ai}) (e^{-2s\gamma_i^* z} + \Gamma_{bi}^*) \\ &\quad + A_i^* B_i \alpha \beta |\gamma_i|^2 (e^{-2s\gamma_i z} - \Gamma_{bi}) (e^{-2s\gamma_i^* z} - \Gamma_{ai}^*) \\ &\quad + js |B_i|^2 \omega \epsilon_i^* \gamma_i \beta^2 (e^{-2s\gamma_i z} - \Gamma_{bi}) (e^{-2s\gamma_i^* z} + \Gamma_{bi}^*)] e^{2s\text{Re}\{\gamma_i\}z}. \end{aligned} \quad (\text{B.8})$$

The expression for the power flow, or real power passing through a plane in the i -th layer of a stratified medium is found by subtracting (B.8) from (B.4) and combining with (4.59) yields

$$\begin{aligned} P(z) &= -2\pi^2 \omega \text{Im} \left\{ \int_{-\infty}^{\infty} \int_{-\infty}^{\infty} (\alpha^2 + \beta^2) \right. \\ &\quad \times \left[|A_i|^2 \mu_i \gamma_i^* (e^{-2s\text{Re}\{\gamma_i\}z} - \Gamma_{ai}^* e^{-2js\text{Im}\{\gamma_i\}z} + \Gamma_{ai} e^{2js\text{Im}\{\gamma_i\}z} - |\Gamma_{ai}|^2 e^{2s\text{Re}\{\gamma_i\}z}) \right. \\ &\quad \left. \left. - |B_i|^2 \epsilon_i^* \gamma_i (e^{-2s\text{Re}\{\gamma_i\}z} + \Gamma_{bi}^* e^{-2js\text{Im}\{\gamma_i\}z} - \Gamma_{bi} e^{2js\text{Im}\{\gamma_i\}z} - |\Gamma_{bi}|^2 e^{2s\text{Re}\{\gamma_i\}z}) \right] d\alpha d\beta \right\}. \end{aligned} \quad (\text{B.9})$$

APPENDIX C

UNITS

Table C.1: Table of units for various quantities used in this document.

Quantity	Symbol	Unit
Spectral Brightness	B_f	$\text{W}\cdot\text{m}^{-2}\cdot\text{sr}^{-1}\cdot\text{Hz}^{-1}$
Current density (surface)	\mathbf{J}_s	A/m
Spatial domain current density (surface)	$\tilde{\mathbf{J}}_s$	A · m
TE amplitude coefficient	A_i	A·m ³
TM amplitude coefficient	B_i	A·s· m ³ /F
x spatial transform variable	α	m ⁻¹
y spatial transform variable	β	m ⁻¹

APPENDIX D

PYTHON CODE FOR PROBE

ANALYSIS

Listing D.1: TE Reflection Coefficient Γ_{ai}

```
## Functions for solving spectral domain fields
def gamma_a(zs, ks):
    """Calculates the TE reflection coefficient.

    Parameters
    -----
    zs : array
        Locations of layer interface between i and i+1 layer
    ks : array of complex
        Array of complex propagation coefficients

    Returns
    -----
    gamma : function
        Function of the transform variables a and b for the TE reflection
        coefficient
    """
    vals = zs.shape[0]
    if vals == 0:
        return lambda a, b: 0
    else:
        z = zs[0]
        s = sign(z)
        gam0 = lambda a, b: mpmath.sqrt(((a + 0j) ** 2 + (b + 0j)**2) - ks[0] \
** 2)
        gam1 = lambda a, b: mpmath.sqrt(((a + 0j) ** 2 + (b + 0j)**2) - ks[1] \
** 2)
        Gamp = gamma_a(zs[1:], ks[1:])
        return lambda a,b: e ** (-2 * s * gam0(a, b) * z) * \
(e ** (-2 * s * gam1(a,b) * z) + Gamp(a, b) - \
(gam1(a, b) / gam0(a, b)) * (e ** (-2 * s * gam1(a, b) * z) - \
Gamp(a, b))) / \
(e**(-2 * s * gam1(a, b) * z) + Gamp(a, b) + \
(gam1(a, b) / gam0(a, b)) * (e ** (-2 * s * gam1(a,b) * z) - \
Gamp(a, b)))
```

Listing D.2: TM Reflection Coefficient Γ_{bz}

```

def gamma_b(zs, eps, ks):
    """Calculates the TM reflection coefficient.

    Parameters
    -----
    zs : array
        Locations of layer interface between i and i+1 layer
    eps : array of complex
        Array of complex permittivity for each layer
    ks : array of complex
        Array of complex propagation coefficient

    Returns
    -----
    gamma : function
        Function of the transform variables a and b for the TM reflection
        coefficient
    """
    vals = zs.shape[0]

    if vals == 0:
        return lambda a, b: 0
    else:
        z = zs[0]
        s = sign(z)
        gam0 = lambda a, b: mpmath.sqrt(((a + 0j) ** 2 + (b + 0j) ** 2) - \
            ks[0] ** 2)
        gam1 = lambda a, b: mpmath.sqrt(((a + 0j) ** 2 + (b + 0j) ** 2) - \
            ks[1] ** 2)
        Gamp = gamma_b(zs[1:], eps[1:], ks[1:])
        return lambda a, b: e ** (- 2 * s * gam0(a, b) * z) * \
            (e ** (-2 * s * gam1(a, b) * z) + Gamp(a, b) - \
            (eps[0] * gam1(a, b)) / (eps[1] * gam0(a, b)) * (e ** (-2 * s * \
            gam1(a, b) * z) - Gamp(a, b))) / (e ** (-2 * s * gam1(a, b) * z) + \
            Gamp(a, b) + (eps[0] * gam1(a, b)) / (eps[1] * gam0(a, b)) * \

```

Listing D.3: TE Amplitude Coefficient A_i

```

def amplitude_a(zs, ks, zfull, kfull, k1, G1, s):
    """Calculates the ith TE amplitude coefficient.

    Parameters
    -----
    zs : array
        Locations of layer interface between i and i+1 layer
    ks : array of complex
        Array of propagation constants for each layer
    zfull : array
        Locations of all the layers which is necessary for calculating the
        reflection coefficients
    kfull : array of complex
        Array of all the complex propagation constants for each layer which
        is necessary for calculating the reflection coefficients
    k1 : complex
        Other half-space propagation constant
    G1 : function
        Other half-space TE reflection coefficient
    s : int
        Sign defining whether to calculate upper or lower half-space

```

```

Returns
-----
25  amplitude : function
    Function of the transform variables a and b for the TE amplitude
    coefficient
    """
30  vals = zs.shape[0]
    if vals == 0:
        gamm = lambda a, b: mpmath.sqrt(((a + 0j) ** 2 + (b + 0j) ** 2) - \
            ks[0] ** 2)
        gam1 = lambda a, b: mpmath.sqrt(((a + 0j) ** 2 + (b + 0j) ** 2) - \
35  k1 ** 2)
        Gam = gamma_a(zfull, kfull)
        if s == -1:
            return lambda a, b: 1j * (1 + G1(a, b)) / (1 + Gam(a, b)) * \
                (gam1(a, b) * (1 - G1(a, b)) / (1 + G1(a, b)) + \
40  gamm(a, b) * (1 - Gam(a, b)) / (1 + Gam(a, b))) ** (-1) * \
                b / ((a ** 2 + b ** 2) * (1 + G1(a, b)))
        else:
            return lambda a, b: 1j * (gamm(a, b) * (1 - Gam(a, b)) / \
                (1 + Gam(a, b)) + gam1(a, b) * (1 - G1(a, b)) / (1 + G1(a, b))) \
45  ** (-1) * b / ((a ** 2 + b ** 2) * (1 + Gam(a, b)))
    else:
        z = zs[-1]
        Gamp = gamma_a(zfull[vals:], kfull[vals:])
        Gam = gamma_a(zfull[vals-1:], kfull[vals-1:])
50  gam0 = lambda a, b: mpmath.sqrt(((a + 0j) ** 2 + (b + 0j) ** 2) - \
            ks[-2] ** 2)
        gam1 = lambda a, b: mpmath.sqrt(((a + 0j) ** 2 + (b + 0j) ** 2) - \
            ks[-1] ** 2)
        Ai = amplitude_a(zs[:-1], ks[:-1], zfull, kfull, k1, G1, s)
55  return lambda a, b: Ai(a, b) * e ** (s * gam0(a, b) * z) / e ** \
            (s * gam1(a, b) * z) * (e ** (-2 * s * gam0(a, b) * z) + Gam(a, b)) \

```

Listing D.4: TM Amplitude Coefficient B_i

```

def amplitude_b(zs, ks, eps, zfull, kfull, epsfull, k1, eps1, G1, w, s):
    """Calculates the TM amplitude coefficient.

5  Parameters
    -----
    zs : array
        Locations of layer interface between i and i+1 layer
    ks : array of complex
10  Array of propagation constants for each layer
    eps : array of complex
        Array of complex permittivities
    zfull : array
15  Locations of all the layers which is necessary for calculating the
        reflection coefficients
    kfull : array of complex
        Array of all the complex propagation constants for each layer which
        is necessary for calculating the reflection coefficients
    epsfull : array of complex
20  Array of all the complex permittivities for each layer which is
        necessary for calculating the reflection coefficients
    k1 : complex
        Other half-space propagation constant
    eps1 : complex
25  Other half-space permittivity
    G1 : function
        Other half-space TM reflection coefficient
    w : float
        Radian frequency
30  s : int
        Sign defining whether to calculate upper or lower half-space

```

```

Returns
-----
35  amplitude : function
      Function of the transform variables a and b for the TM amplitude
      coefficient
      """
40  vals = zs.shape[0]
      if vals == 0:
          gamm = lambda a, b: mpmath.sqrt(((a + 0j) ** 2 + (b + 0j) ** 2) - \
          ks[0] ** 2)
          gam1 = lambda a, b: mpmath.sqrt(((a + 0j) ** 2 + (b + 0j) ** 2) - \
          k1 ** 2)
45  Gam = gamma_b(zfull, epsfull, kfull)
          if s == -1:
              return lambda a, b: -(1 - G1(a, b)) / (1 - Gam(a, b)) * (eps1 / \
              gam1(a, b) * (1 + G1(a, b)) / (1 - G1(a, b)) + eps[0] / \
              gamm(a, b) * (1 + Gam(a, b)) / (1 - Gam(a, b))) ** (-1) * \
              a / (w * (a ** 2 + b ** 2) * (1 - G1(a, b)) * gamm(a, b))
50  else:
              return lambda a, b: (eps[0] / gamm(a, b) * (1 + Gam(a, b)) / \
              (1 - Gam(a, b)) + eps1 / gam1(a, b) * (1 + G1(a, b)) / \
              (1 - G1(a, b))) ** (-1) * a / (w * (a ** 2 + b ** 2) * \
              (1 - Gam(a, b)) * gamm(a, b))
55  else:
          z = zs[-1]
          s = sign(z)
          Gamp = gamma_b(zfull[vals:], epsfull[vals:], kfull[vals:])
          Gam = gamma_b(zfull[vals-1:], epsfull[vals-1:], kfull[vals-1:])
60  gam0 = lambda a, b: mpmath.sqrt(((a + 0j) ** 2 + (b + 0j) ** 2) - \
          ks[-2] ** 2)
          gam1 = lambda a, b: mpmath.sqrt(((a + 0j) ** 2 + (b + 0j) ** 2) - \
          ks[-1] ** 2)
65  Bi = amplitude_b(zs[:-1], ks[:-1], eps[:-1], zfull, kfull, epsfull,
          k1, eps1, G1, w, s)
          return lambda a, b: eps[-2] / eps[-1] * Bi(a, b) * \
          e ** (s * gam0(a, b) * z) / e ** (s * gam1(a, b) * z) * \
          (e ** (-2 * s * gam0(a, b) * z) + Gam(a, b)) / \

```